Fionn Iversen

Meniscus Dynamics in Aluminium Extrusion Ingot Casting

NTNU Trondheim
Norges teknisk-naturvitenskapelige universitet

Dr. ingeniøravhandling 2002:57
Institutt for materialteknologi og elektrokjemi

IME-rapport 2002:37

Preface

This work was funded by the Research Council of Norway (NFR), Hydro Aluminium ASA and Elkem Aluminium ANS, through the PROSMAT research project. The last four months were funded by the department of Materials Technology and Electorchemistry at the Norwegian Institute of Science and Technology (NTNU).

My supervisors were professor Jon Arne Bakken at the department of Materials Technology and Electrochemistry, NTNU and professor II Stein Tore Johansen at the department of Applied Mechanics, Thermo- and Fluid Dynamics, NTNU.

Casting tests were performed at Hydro Aluminium Sunndalsøra under the supervision of Steinar Benum and Jon Erik Hafsaas of Hydro Aluminium. Dag Mortensen of the Institute for Energy Technology (IFE) provided material parameters for the casting simulations.

Parts of the work have earlier been presented at TMS conferences, with a paper published in the proceedings of the Computational Modelling conference in 2001:

> *A Marker Chain Front Tracking Method Adapted for Modelling Meniscus Dynamics in the Direct Chill Al Billet Casting Process* , Cast Shop Technology, 2001 TMS Annual Meeting.
>
> *A marker chain front tracking method for modelling meniscus dynamics in the Al ingot casting process*, Computational Modelling of Materials, Minerals and Metals Processing, TMS 2001.

Sadly, I will not be continuing the work of developing the casting process. But hopefully the results, both the development of the numerical free surface methods and the conclusions drawn regarding the casting process, will come to further use. There is a lot of work remaining to be done in both fields, and I do believe that significant improvement to the casting process through better meniscus control is possible.

I especially want to thank professor Jon Arne Bakken for always having time for a discussion, and for his patience with my enthusiasm. I also want to thank professor II Stein Tore Johansen for his valuable help and advice with model implementation in the FLUENT code.

Finally I want to thank my fiancé Gerd, and especially my eleven month old son Brage Oisín, for reminding me that there are more important things than a Dr.Ing. thesis.

Trondheim, 15. April 2002

Summary

In the modern process of continuous Direct Chill (DC) hot top casting of aluminium extrusion ingot with gas slip [25], poor surface quality of the cast ingot can still be a problem. In the worst cases pronounced *surface wrinkling* may occur coupled with periodic zones of *reduced grain size*, *macrosegregation* and *exudation* at the surface. The observed surface irregularities are believed to be linked to periodic surface oscillations or folding of the meniscus resulting in varying solidification conditions in the mould.

The focus of this work is to gain a better understanding of the dynamics of the free aluminium surface, or *meniscus*, formed in the mould, and the effect it has on ingot surface formation. Both casting experiments and numerical simulations of the casting process have been performed. In addition a brief analytical analysis of oscillations and waves that may influence the meniscus behaviour has been made, and finally a series of simple meniscus water model experiments have been performed.

The main part of the work consists of the adaption and implementation of a two-phase marker chain front tracking technique using cubic spline surface reconstruction, the Method of Tensions (MOT) [49]. This method is applied in modelling the free surface meniscus dynamics. The advantage of this type of model is its accuracy in the calculation of surface tension forces, which is especially important in the case of modelling the Al meniscus due to the high metal gas density ratio. Also, with this model wetting conditions may easily be implemented as boundary conditions on the surface spline function. Modifications have been made to marker advection, surface reconstruction, and surface force distribution algorithms of MOT to improve surface stability and phase conservation.

In the solidification modelling the effect of latent heat release is included in the heat capacity so that a direct temperature-enthalpy relation is preserved. Further a simple model for the solidification contraction is implemented to correctly model both the heat flow across and the slip gas flow through the air gap.

The modified MOT is implemented together with the solidification model

in the FLUENT CFD solver, which uses the SIMPLE algorithm [47] together with the Power Law [1] in the Finite Volume discretization.

The work has lead to two important contributions:

> Firstly, a functional numerical method for modelling meniscus dynamics in the casting process has been developed.
>
> Secondly, added insight into the casting process has been achieved, primarily though the casting tests and casting simulations.

The most important result, indicated by both casting tests and simulations, is that the meniscus oscillations are coupled with significant upward bubbling through the melt inlet in the mould. This conclusion is based on both visual observations of bubbling at the melt surface in the mould and from simulated upward bubbling from the meniscus. Also, the high stability of the section of the meniscus closest to the mould wall, observed in the casting experiments and recreated in casting simulations, imply a large meniscus with at least periodic contact with the melt inlet corner. The results also indicate that a significant upward gas discharge is necessary to induce the rapid meniscus collapse observed in the casting tests. It is believed that the momentum of the fluid flow induced by upward bubbling induces the collapse.

Based on the results achieved, some suggestions are made for process modifications. Firstly, to achieve as smooth a behaviour as possible, the geometry of the inside of the hot top should be smooth. And improved control of the meniscus may be achieved with a modified mould geometry so that meniscus oscillations are reduced. Possible modifications are suggested.

To further develop mould geometry and slip gas control, casting tests should be performed with the modified mould geometry. Also, numerical simulations should be performed with surface breakup and merging techniques implemented in the simulation program, so that bubble formation and coalescence may be included. Subsequently, the upward discharge of slip gas, which is believed to be linked to meniscus collapse, may be properly simulated.

To conclude, the modified Method of Tensions is shown to be accurate and stable enough to be applied to modelling of the meniscus dynamics. And for the casting process, by altering mould geometry and improving slip gas control, it should be possible to achieve a more stable meniscus, and subsequently a more stable casting process, which should result in improved cast ingot surface quality.

Contents

Chapter 1

Al ingot casting

1.0.1 A brief history of aluminium ingot casting

The history of Al ingot casting stretches back to approximately 100 years ago. At this time the process of casting steel and copper ingots was already well developed. The ingots were solidified in permanent moulds (book-moulds) into which the molten metal was poured. Initially this technique was also used for production of aluminium ingot, but because of the dangers of the reactivity of the molten aluminium with the atmosphere modifications had to be made. A technique of tilting the mould [9] was developed (see figure 1.1). By using this technique a gentler melt flow was achieved making for a safer casting process.

Increasing industrialization in the early 20th century, and especially the rapidly growing aviation industry, resulted in a need for increased ingot size. Larger ingots allowed for production of larger parts so larger planes could be made. These larger ingot dimensions, however, led to new problems in the casting process. The considerable air gap produced by shrinkage of the casting lead to poor heat transfer, slow solidification, and resulted in extremely coarse grain structures. Large intermetallic particles in the coarse structure could cause fracture during rolling and forging, or if cracks were avoided in this process then fractures could appear later in the finished product.

The consequence of the problems connected to large ingot size was the development of the Direct Chill (DC) ingot casting process [16]. The basic idea of DC casting is cooling the ingot by a jet of running water as the ingot emerges from an open mould. Through this open casting technique many of the problems connected to the slow solidification were avoided and the ingot quality was greatly improved.

As requirements for ingot quality further increased new casting techniques were sought to better control the properties of the castings. An important

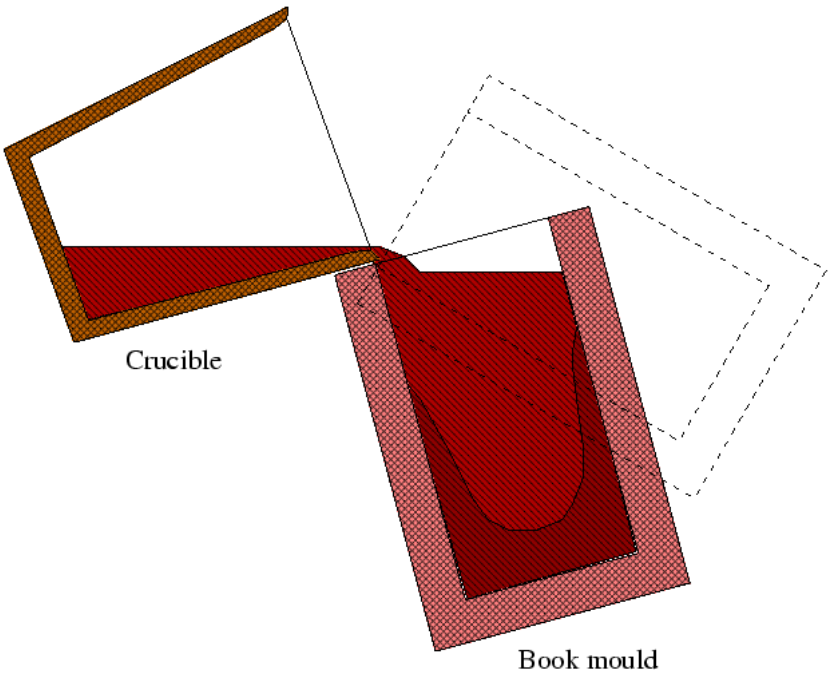

Figure 1.1: Permanent mould casting; tilting-mould technique.

factor in ingot quality was found to be the height of the metal head in the mould. A lower metal surface lead to a shortening of the air gap between the mould wall and ingot surface and subsequently reduced heat extraction through the mould wall. Thereby the properties of the ingot were made less dependent on the primary cooling (see below), which is difficult to control, and thus improving ingot quality [44]. One of the best ways to achieve a lower metal surface in the mould was found to be by the use of a header box of insulating material, a 'hot top', on the top of a short mould [7]. The method was further developed in the late 1960's and early 1970's resulting in a similar geometry to the one used in hot top moulds today. With such good control of metal height, ingot quality could be further improved. Also simultaneous casting of multiple ingots in a multistrand unit was made possible.

Another problem which needed to be dealt with was the poor surface quality of the ingots cast with the hot top DC casting process. For ingots used for rolling poor surface quality is not a problem, since ingots are normally scalped before the rolling process [5]. But for extrusion ingots, which are generally not scalped, better surface quality would greatly influence the finished product. Further developments towards solving the problem of poor surface quality were suggested by Showa in the late 1970's. By injecting gas into the top of the mould a better control of the shape and position of the free

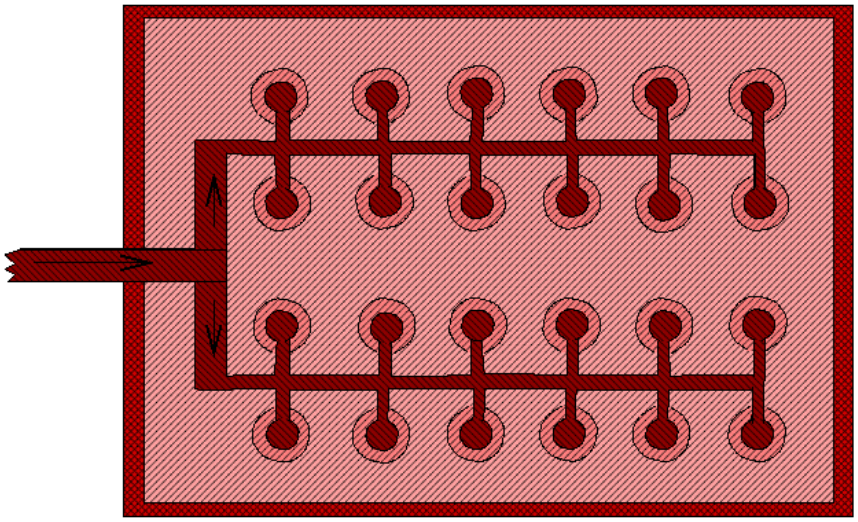

Figure 1.2: Casting table seen from above. 24 moulds.

melt surface in the mould (also known as the meniscus) could be achieved. With this technique it was possible to further reduce the air gap and consequently reduce the heat transfer over the gap, thereby further improving the ingot quality. The technique is known as gas slip or air slip casting.

Several different casting techniques have been developed in parallel with the development of the process described above. The three other techniques used today [5] are conventional open DC moulds, air/gas slip moulds with the original Showa-Denko design, and electromagnetic moulds.

The casting method considered in this work is the hot top DC air/gas slip method. A better understanding of the meniscus dynamics and solidification in the mould is sought mainly through mathematical modelling and subsequent numerical simulation. The motivation for this work is to further improve the cast ingot surface quality. The process is described more thoroughly in the following section. Through this description the current general understanding of the casting process is presented. And some new models are suggested.

1.1 Process description

The contemporary continuous Al hot top DC gas slip extrusion ingot casting process is schematically described in figures 1.2 to 1.4(b). The molten metal flows from the holding furnace onto the casting table (figure 1.2) where it is distributed through channels into a matrix of open moulds. A typical casting

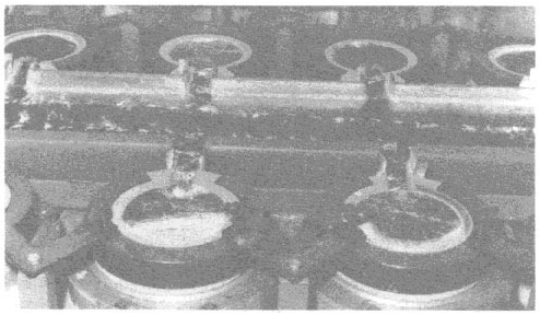

Figure 1.3: Hot top casting of extrusion ingots.

mould is presented in figure 1.4(a). The melt flows into the mould where it is initially supported by the mould wall and a bottom block. As the metal solidifies the bottom block is withdrawn and as the solid ingot emerges it is further cooled by a water spray which hits the ingot directly below the mould wall (figure 1.4(b)). This is referred to as *Direct Chill*. A picture of an actual casting process is shown in figure 1.3.

1.2 Solidification

The characteristics of the solidification depend on a multitude of variables such as alloy content, cooling efficiency, mould geometry, melt flow and casting velocity. The influences and effects of these most important factors are considered below.

1.2.1 Hot top

As described above the hot top controls the level of the melt in the mould, thereby improving ingot quality and also stabilizing the casting process. The hot top is made of an insulating material so that the heat extraction from the ingot through the hot top will be minimal.

1.2.2 Mould geometry

Several different types of mould geometry are used in the casting process. The geometry presented here (figure 1.4(a)) is chosen partly to facilitate gridding of the computational domain in the numerical simulations. One important aspect of the geometry is the extra space for the gas pocket above the meniscus. Through developments of the casting process one has found

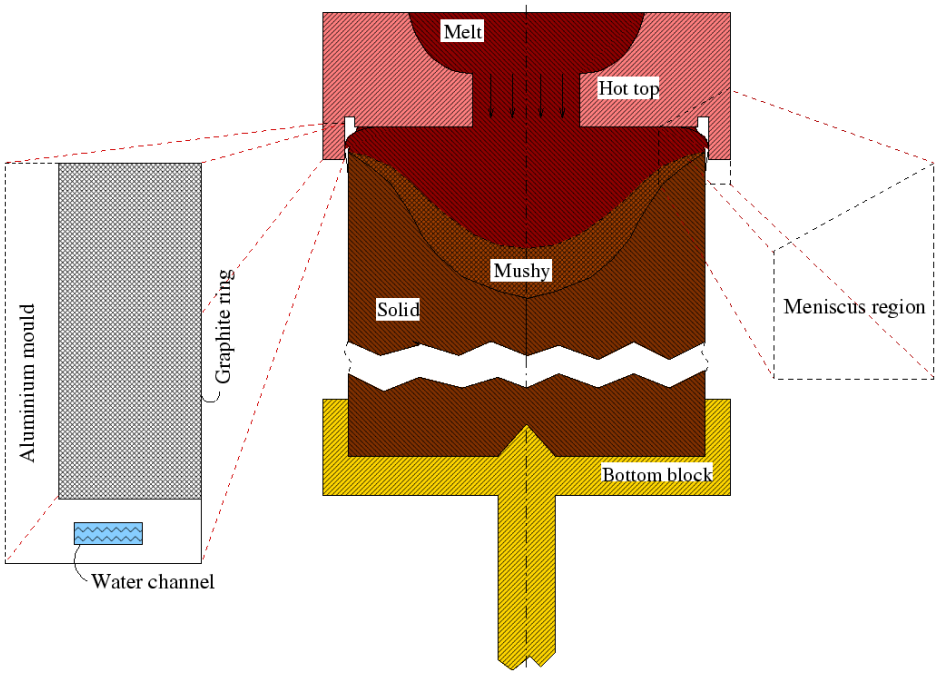

(a) Cross section of casting with enlarged mould wall and definition of meniscus region. Melt flow direction indicated in melt inlet.

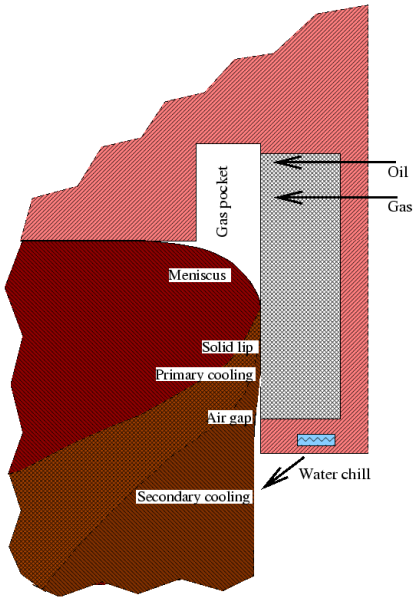

(b) Cross section of meniscus region. Closed air gap, free meniscus.

Figure 1.4: Ingot casting with meniscus.

that extra space above the meniscus stabilizes the primary solidification. A partly sloping bottom surface of the hot top is often used.

1.2.3 Lubrication and gas injection

Lubrication systems were developed in parallel with the development of DC casting [42]. During casting lubricating oil is injected into the top of the mould to lubricate the mould wall, thereby allowing the ingot to slip. New methods have gradually been developed for the injection of both gas and oil into the mould. In the specific process considered here the air and oil are introduced into the mould through a porous graphite ring (figure 1.4(a)) in the mould wall. The gas is injected through the upper part of the ring while the air is injected through the lower part. This technique is used in both the Wagstaff AirSlip [33] and Hydro Air Cushion techniques, among others.

1.2.4 Cooling

There are two main sources of cooling: the mould wall and the direct water chill.

The mould wall is composed of two separate regions: a porous graphite ring and an aluminium casing encapsulating it (figure 1.4(a)). Both these regions are cooled by a water reservoir inside the mould. As the metal comes into thermal contact with the mould wall it is cooled and a solid shell may form, known as the *solid lip*. This cooling by the mould wall is known as the *primary cooling*.

The second and main source of cooling is the Direct Chill. As the ingot emerges below the mould it is sprayed with water (figure 1.4(b)). The water cools the ingot as it runs down along its surface. This region of water cooling is known as the 'secondary cooling' zone. The water chill efficiency determines the properties of the bulk of the cast ingot while the primary cooling mainly effects the ingot surface properties.

1.2.5 Mushy zone

Alloy elements induce a broadening of the solidification temperature range. Pure aluminium goes from complete liquid to complete solid at a specific temperature, whereas aluminium alloys, due to segregation, solidify over a finite temperature range. The temperature range of solidification increases with the amount of alloy elements added. This is the reason for the so called 'mushy zone' between the liquid and solid (see figure 1.4(a)). At the top of the region where the temperature is at its highest, fine 'equiaxed' grains with

no preferred growth direction are formed which float freely in the melt. The extent of grain formation in the melt depends on the particular aluminium alloy considered. At the lower part of the mushy region dendrites grow from the solid region extending out into the mushy. Dendrites will also form in the primary cooling zone growing inward from the mould wall. As the grains formed in the mushy zone grow and settle around the dendrites growing at the bottom of the zone the metal grows in strength and eventually becomes rigid. The temperature at which the solidified metal forms a connected structure is known as the *point of dendrite coherency*. Solidification contraction (see 1.2.7) will start at some temperature below this point, depending on the properties of the specific aluminium alloy.

1.2.6 Heat transfer

Primary cooling

The heat transfer from the melt to the hot top is negligible compared to the primary and secondary cooling described above. So normally the ingot will start solidifying only after making thermal contact with the mould wall (figure 1.4(b)), resulting in the solid lip described above. The heat transfer from the ingot to the mould in the primary cooling zone will depend on the amount of physical contact between the ingot and the mould, the width and length of the air gap, the composition of gas and oil in the air gap and the emissivity of the mould and ingot surfaces. If the ingot is in physical contact with the mould then the heat transfer in the region of contact will dominate the other heat transfer from ingot to mould. In this case the air gap is closed (as in figure 1.4(b)). When there is no contact between mould wall and ingot the air gap is open. In this case slip gas passes through the gap and exits below the mould. Gas flow is discussed in section 1.3.4. The heat conduction across the air gap is determined by the gap width and the composition of the oil/gas mixture in the gap. Increased oil content will result in increased conduction. The emissivity of the mould and ingot surfaces will influence the radiative heat transfer across the gap. Another factor which might influence the heat transfer over the air gap could be surface oxide passing through it. Formation of aluminium oxide (alumina) is discussed below (1.3).

Secondary cooling

With given alloy properties, the direct water chill , being the main cooling source, determines the solidification rate and extent of the mushy zone in the bulk of the ingot. The water impingement area can be seen in figure 1.4(b). In

addition, the secondary cooling can to a lesser extent effect the temperature field, and consequently the solidification, in the primary cooling zone.

The effect of the secondary cooling depends on the mechanism of heat transfer between the ingot and the cooling water and on the temperature difference between the ingot surface and bulk water temperatures. Film boiling will often occur in the upper area of contact between water and ingot. This type of boiling produces an insulating layer of water vapour on the surface of the ingot, thereby reducing the cooling effect of the water. The transitions from nucleate boiling to unstable film or transitional boiling, and further to film boiling, [43] are dependent on water properties (see [29]). Therefore the quality of the water can greatly influence the efficiency of the secondary cooling.

1.2.7 Contraction

As pure aluminium solidifies it will contract to a considerable extent because of the reordering of atoms into the metallic crystal lattice structure. Excessive contraction can cause serious problems in castings, such as large cracks in the center (hot tearing) or bottom of the ingot (see [19]). Therefore alloy elements are normally added. Through the formation of eutectic/peritectic/hypoeutectic the crystal lattice is split up into sections ([19]). Some alloy elements form compounds which contract less than the aluminium. Consequently the total contraction is reduced. The alloy content will to a great extent determine the total radial contraction of the ingot.

The radial contraction in the mould is determined by the balance between the force of solidification contraction in the solid lip, the force of the total metallostatic head in the mould and possibly also the pressure in the gas pocket , which determines the pressure drop through the open air gap. The mean pressure of the metallostatic head is determined by the mean metal level at the top of the mould. The instantaneous metal height will however vary due to both waves on the casting table and to variations in gas pocket volume. This leads to variations in air gap width. The radial contraction in the mould also depends on the thickness of the solid lip, which is determined by the intensity of the primary and secondary cooling. Since the amount of primary cooling is partly determined by the radial contraction in the mould this system constitutes a feedback loop, which may lead to a physically unstable air gap. The thickness of the solid in the vertical cross section directly below the primary cooling zone, which is mainly determined by secondary cooling, will also influence the radial contraction, and hence the air gap, in the mould, since the solid lip is supported by the solid metal below. Consequently the strength and radial contraction in the in the secondary cooling zone will

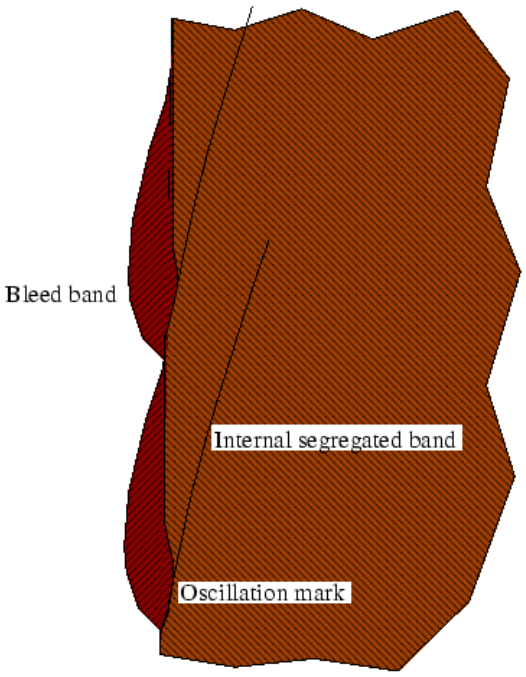

Figure 1.5: Intersection of cast ingot surface showing irregularities.

influence the contraction in the mould.

1.2.8 Segregation

Several kinds of macrosegregation can occur in the surface region of the cast ingot. The four main types (again from [5]) are *periodic segregation*, segregation linked to *exudation*, *depleted bands*, and a *continuous surface segregation* layer. The characteristic periodic segregation occurs in alloys with a short solidification temperature range. The effect is probably linked to periodic

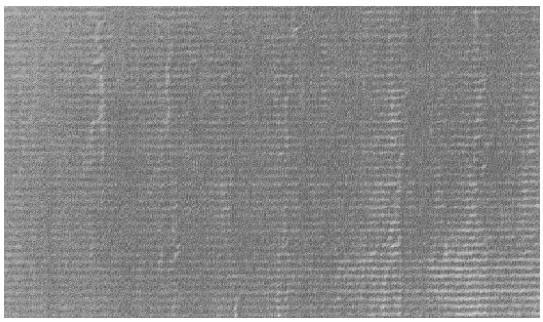

Figure 1.6: Typical oscillations marks on surface of cast ingot.

remelting of the solid lip, described in [16]. The second type, exudation, is linked to alloys with a broad solidification range. This effect might also be linked to remelting, but here with resulting bleeding or exudation through the semi-solid surface. Another possible cause is folding of the meniscus, also leading to exudation. The third type of segregation, banding, is probably also linked to meniscus behaviour. The second and third type of exudation are discussed further below in section 1.3 . The fourth type, the continuous segregation layer, is a naturally occurring enriched layer appearing in ingots of all alloy types, created by diffusion of alloy elements and melt flow during solidification. Also see [65].

1.2.9 Grain structure

The grain structure might or might not be linked to segregation. The banded segregation described above often occurs coupled with a finer grain structure. A possible explanation for this phenomenon is solidification of the meniscus, again discussed below (1.3).

1.2.10 Solidified surface

There are at least three typical physical irregularities that occur on the cast ingot surface. These are *oscillation marks* (also known as *surface marks* [2]), *bleed bands*, and the *grain refined segregated bands*. These faults are presented schematically in figure 1.5. The oscillation marks are regular periodic grooves in the ingot surface. The bleed bands, caused by exudation (or bleeding) mentioned above, form segregated bulges on the ingot surface, and will often cover the oscillation marks (see [5]). Both the oscillation marks and the bleed bands have the same period as the bands of finer grain structure, suggesting that these periodic defects are all formed by the same mechanism, which is discussed further below (1.3). Also see [62] and [2]. A typical cast ingot surface with oscillation marks is shown in figure 1.6.

1.3 Meniscus dynamics

The meniscus geometry and dynamic properties will greatly influence the solidification in the primary cooling zone. The mean geometry of the meniscus is mainly determined by the mould geometry (particularly the level of the hot top), the slip gas flow rate, and the casting velocity. The geometry influences the metal level at the mould wall and consequently also the length of the air gap. It also influences the periods of open and closed air gap.

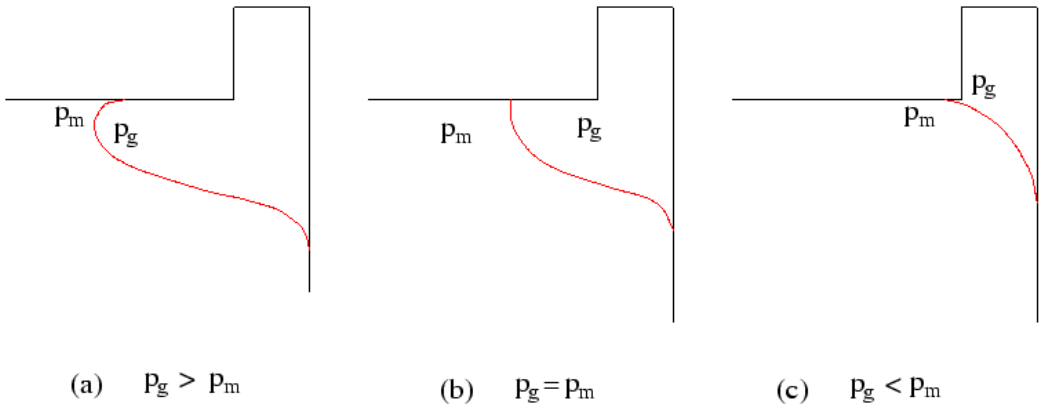

Figure 1.7: Pressure difference related to curvature at top of meniscus. Gas pressure p_g, metallostatic head pressure p_m.

By the discussion above (section 1.2), the air gap influences the amount of primary cooling, and consequently also the ingot surface quality. Therefore controlling the meniscus is of primary importance in the casting process.

Many factors influence the meniscus properties and dynamics. These include wetting boundary conditions at the mould wall and hot top, surface tension coefficient and oxidation on the meniscus. Both the solid lip and the extent of the mushy zone below the meniscus will influence its movement. Subsequently meniscus dynamics and ingot solidification is a two-way interaction. If there is solidification up onto the meniscus the movement is constrained, otherwise the meniscus is here defined as a *free meniscus* (see figure 1.4(b)).

1.3.1 Surface tension and Wetting

The curvature of the free molten metal surface is determined by the surface tension forces and the pressure difference over the surface (by Laplace's formula [40]). An increase in surface tension coefficient will give a decreased surface curvature with other parameters equal. A fixed wetting angle between the molten metal surface and the mould puts an extra constraint on the meniscus shape. However, in order for the pressure difference between the gas pocket and the metal pressure at the bottom of the hot top to vary freely, the curvature at the contact point between the molten meniscus free surface and the hot top must be free to balance the arbitrary pressure difference (see figure 1.7). To avoid an extra constraint on curvature the wetting angle at this point must also be free.

Tests have shown that the static wetting angle between liquid aluminium

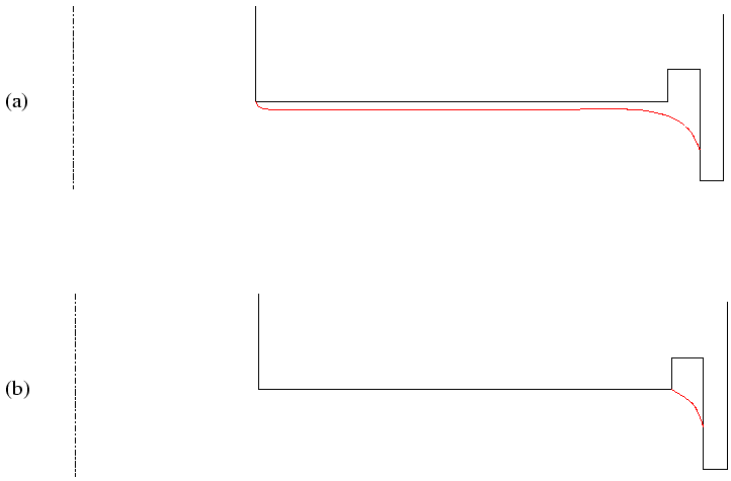

Figure 1.8: Extreme upper meniscus contact points.

and ceramics (as in the ceramic hot top) is quite small (see [22]). However, in a dynamic system the wetting behaviour may differ from that of the static case.

Also it might be possible that the meniscus could be hanging on a corner of the hot top, thereby allowing it to have free wetting. There are two possible corners to hang from on the hot top bottom: next to the melt inflow and next to the gas pocket. Meniscus dynamics should differ considerably for these two cases (see figure 1.8). Wetting conditions are made subject to analysis in the following modelling work to gain a better understanding of the process.

1.3.2 Oxidation

Aluminium oxide or alumina, Al_2O_3, forms on molten aluminium in contact with an oxygen-rich atmosphere. In the hot top gas slip casting process the molten aluminium is in contact with air on the casting table. As the aluminium flows into the mould the oxide formed can be pulled down and thereby effect the surface formation of the cast ingot. If there is oxygen in the slip gas then oxide will also form on the meniscus surface. Both the oxide pulled into the mould and the oxide formed on the meniscus will influence the dynamic properties of the meniscus. Resolving the free meniscus dynamics will in this case be a three phase problem, with gas, oxide, and molten metal phases present, and the applied free surface approximation (see chapter 4) might not any longer be valid. The following discussion is however based on free meniscus surface movement (unless it is constrained by solidification). Effects of oxidation will be considered in the later discussion. For now it can

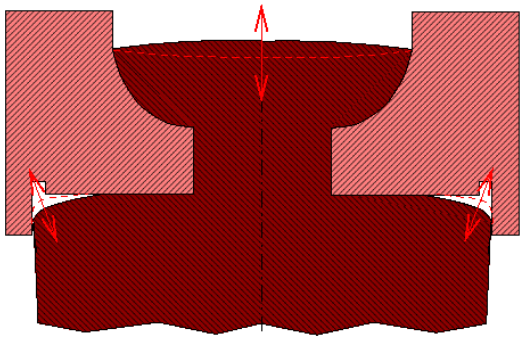

Figure 1.9: Gravity induced oscillations in casting column.

be stated that a lot of oxidation can make the meniscus more rigid and may also lead to highly irregular meniscus behaviour.

1.3.3 Meniscus oscillations

Several observations have been made of meniscus dynamics in the mould ([2], [68], [67], [14]). Based on these results and results of observations made during this work (see 2), some models for meniscus dynamics and interaction with solidification are suggested in the following.

Waves on meniscus surface

Oscillations of the meniscus can take several forms. The dynamic properties of the free surface are partly influenced by gravity, surface tension forces (or capillary forces), and wetting. One form of oscillation that might occur is *capillary waves*, i.e. waves provoked by surface instability where the dominating restoring force is the surface tension force. Or if the restoring forces are the combined surface tension and gravity forces then gravity-capillary waves occur. *Gravity waves* in the casting column might also occur. In this case the upper surface of the molten metal in the mould oscillates in combination with the meniscus surface (see figure 1.9). The reason for this type of oscillation can be surface waves propagating on the molten metal surface on the casting table, or the oscillation might be induced by gas escaping intermittently from the gas pocket. The amplitude and sustainability of these gravitational oscillations will depend on the damping in the gas pocket, which is dependent on the compressibility of the gas and the flow of gas through the open air gap or bubbling through the mould inlet. An analysis of the influence of the different types of waves is analyzed in chapter 3.

Solidification of the meniscus can also be linked to oscillations.

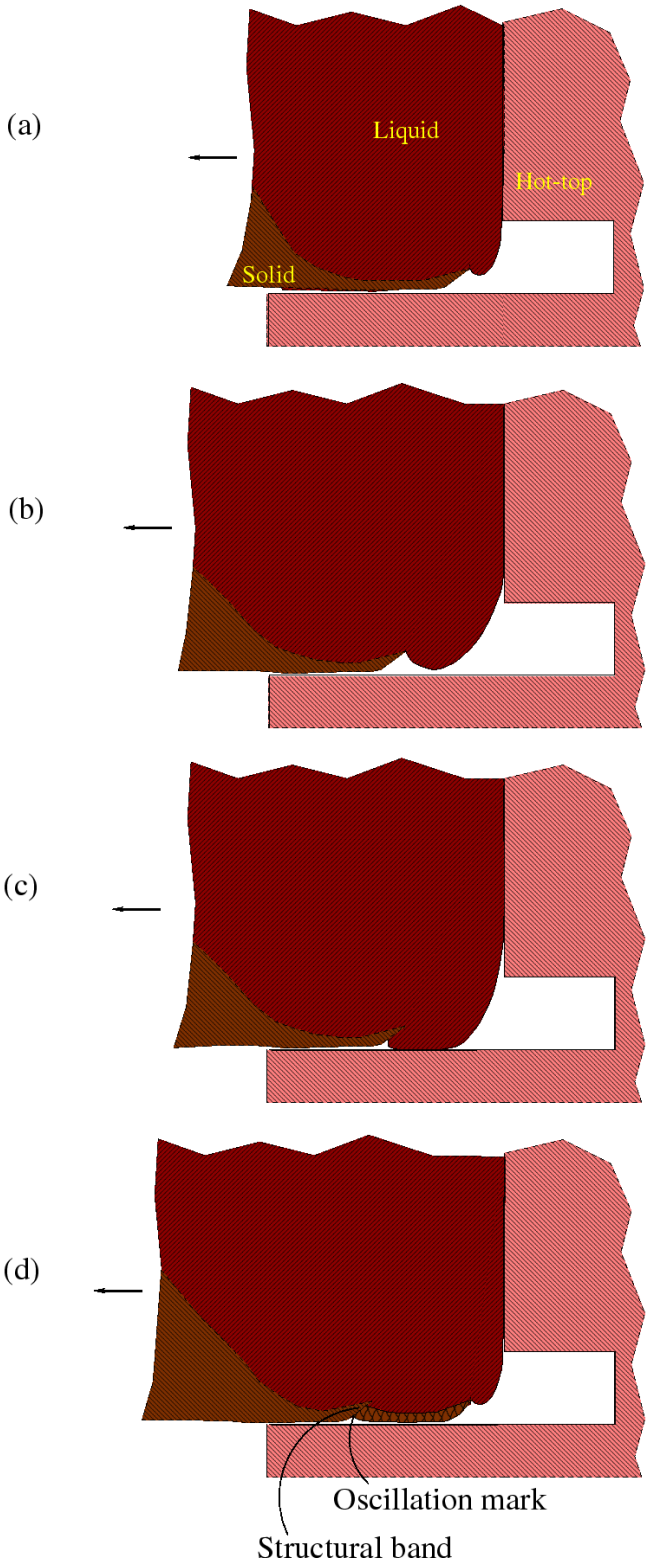

Figure 1.10: Collapsing meniscus model.

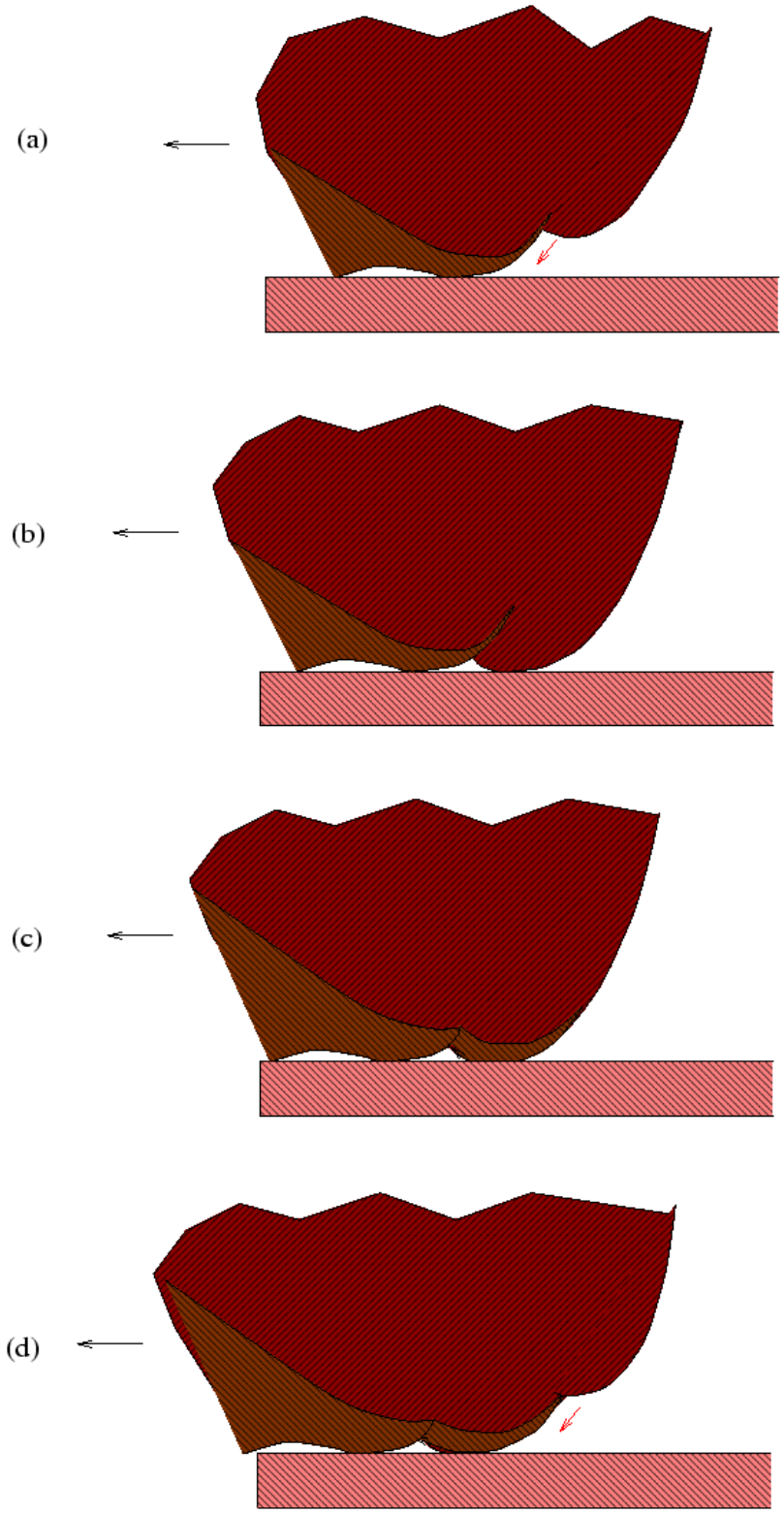

Figure 1.11: Surface mark formation model of Ackermann et al.

Solidification and collapse of the meniscus

Molten meniscus If there is no meniscus solidification the molten meniscus must be supported by the mould wall. However, the slip gas injected must have some form of escape. And if there is no downward escape route it must bubble up through the melt inlet. So with a molten meniscus intermittent upward gas discharge is to be expected.

Meniscus solidification

With sufficient primary cooling, solidification of the lower part of the meniscus can occur, as shown in figure 1.10(a). In this case meniscus oscillations might be connected to formation of surface irregularities. The extent of the solidification will determine the amplitude of the meniscus oscillations and resulting surface faults. The complete process is illustrated in figure 1.10.

Four stages of an oscillation period are shown. The casting direction is towards the left (compare to figure 1.4(b)). The initial state is shown in 1.10(a), where the lower part of the meniscus is solid. When there is solidification on the meniscus a geometry as in figure 1.4(b) is mechanically unstable because the surface forces are not balanced according to Young's equation [58]. To achieve mechanical equilibrium a partial overflow of the melt over the solidified lower part of the meniscus is necessary. (A similar case which can easily be observed is the meniscus formed when a glass is overfilled with water). The wetting angle at the lower point of the liquid meniscus is then determined by Young's equation. The meniscus surface shape for a given gas pocket volume is consequently determined by the boundary conditions and the balance of forces through the extent of solidification, the wetting angle at the lower point of the liquid meniscus, the surface tension coefficient, the profile of the pressure jump across the surface and the gravitational forces pulling on the molten metal.

As the ingot is pulled down during casting the solid lip follows, thereby lengthening and deforming the meniscus. Now two things may happen: the meniscus may collapse, or the meniscus may solidify because of thermal contact with the mould wall.

Collapsing meniscus model If the forces over the meniscus can no longer be balanced at some point due to dominating gravitational forces, it will collapse as shown in 1.10(b) - 1.10(c). Subsequently a new meniscus is formed above the old solidified lower part of the meniscus, and the new meniscus surface in contact with the wall solidifies and forms a new solid shell, as shown in 1.10(d). This brings us back to the initial state in 1.10(a).

Solidification or surface tension forces or both may hinder the new meniscus from completely filling the gap between the old meniscus and the mould wall. Curvature and consequently surface tension forces at the lower point of the liquid surface will increase as it collapses toward the wall. The increased curvature and the resulting surface tension forces could prevent complete regaining of wall contact at the lower point of the old meniscus. And also solidification of the collapsing meniscus, stopping its downward movement, might prevent complete filling of the gap. The result will then be a small groove or oscillation mark in the cast ingot surface as shown in figure 1.5.

Internal structural bands might be coupled with the oscillation marks. The upper part of the solidified meniscus solidifies quickly, leading to a fine grain structure . The metal that runs over the old meniscus when the meniscus collapses solidifies more slowly. After the collapse of the meniscus the regions above and below the thin surface shell of the old meniscus solidify due to increased heat transfer from contact with the mould wall. Consequently a coarser grain structure is formed in these regions. Different alloy content due to different segregation on the solidified surface and inside the ingot may also influence the grain structure. In this way the irregular grain structure described in 1.2.9 might occur, possibly coupled with varying segregation.

Semi steady state A combination of the collapsing meniscus and the molten meniscus models might also occur. After the collapse of the meniscus the formation of the solid shell might not be instantaneous. In the phase before the solid shell grows sufficiently strong to pull the meniscus down, the meniscus dynamics could be as described for the molten meniscus above. Once the solid shell has gained enough strength to pull the meniscus down the collapsing meniscus phase is again initiated. And so on. Oscillation marks and structural bands (figure 1.5) would probably not be as distinct by this process, but more bleed bands might form, due to a longer period before solidification.

Surface mark formation model of Ackermann et al The second mechanism for oscillation mark formation, which gives similar results to the collapsing meniscus model described above, is the 'Surface mark formation model' presented in [2]. In this case the free lower contact point of the meniscus, driven by the gravitational pull on the melt, moves down the old solid meniscus surface until it touches the mould wall and solidifies. The cycle is illustrated in figures 1.11(a) to 1.11(d). In this case more remelting of the old meniscus would be expected than for the case of the collapsing meniscus. So the internal structural bands might be less distinct. The oscillation marks

should however be of approximately the same size as for the case of meniscus collapse.

It is very possible that the process of oscillation mark formation can be a combination of the 'collapsing meniscus' and 'surface mark formation' models.

Exudation In the case of meniscus solidification oscillations there is a much greater chance of exudation leading to the bleed bands (figure 1.5). After the new meniscus has collapsed or started resolidification the new ingot surface will not be solid. If there is a groove or oscillation mark below the partly solidified new surface the metal head may force melt out through pores in the metal surface into the groove, causing exudation, possibly thereby covering the oscillation marks. If there is an open air gap between the old meniscus and the wall the exuded liquid metal may partly flow down into the gap. This effect may create the characteristic bleed bands shown in figure 1.5. It would both explain the periodicity of the bands and the fact that they are in phase with the internal structural bands. A similar explanation is suggested in [5].

1.3.4 Slip gas flow

Gas discharge from the gas pocket is determined by the meniscus dynamics and solidification. A common technique during casting startup is increasing injected gas flow until the gas starts bubbling up through the melt inlet and then decreasing the gas flow until bubbling is no longer visible. As already described, the meniscus reduces the ingot to mould contact in the primary cooling zone, thereby improving casting control. Making the gas pocket volume as large as possible results in a large meniscus and small ingot/mould contact area. This effect is sought through the startup procedure. In the proceeding casting process it is important to maintain a large gas pocket. Therefore knowledge and control of gas flow in and out of the gas pocket is important for controlling the cast ingot surface quality.

The injected gas has two possible ways of exiting the gas pocket. The gas can either flow down through the air gap, if it is open, or the gas can escape upwards bubbling through the melt inlet at the top of the mould.

Downward discharge

If the lower part of the meniscus is solidified then the air gap will open a clear passage between the mould wall and the ingot through which the gas escapes from the gas pocket. If the meniscus is completely molten, then there

is no free passage and the air from the gas pocket can not escape downwards. But if the meniscus dynamics are like those described in either the collapsing meniscus model or the surface mark formation model, then gas flow from the pocket through the air gap should be possible, at least intermittently.

As figure 1.10 illustrates, for the collapsing meniscus model, the passage down along the mould wall is only blocked for a short period after the meniscus collapse. At all other stages the air gap is open. In the case of the surface mark formation model, either the passage is open continuously or there is periodic blocking due to contact between the new meniscus and the mould wall before the meniscus solidifies. So both mechanisms include either intermittent or continuous downward gas discharge.

Upward discharge

If the gas pocket fills to such an extent that the upper contact point of the meniscus passes the lower corner of the melt inlet then the gas will bubble upward through the melt inlet.

Slip gas balance

The injected gas flow rate will determine what fraction of gas flows up and what fraction flows down for each particular solidification mechanism described above. If the injected and downward gas flow rates are not balanced then two things may happen. If the mean injected flow rate is larger than the mean downward flow rate the gas pocket will grow until there is upward gas discharge and the process will repeat itself. If the mean injected gas flow rate is smaller than the mean downward flow rate then the gas pocket will empty, and the casting might freeze to the mould. There might be mechanisms which compensate for the imbalance in injected and downward flow rate, perhaps changing the thickness of the solidified shell, thereby decreasing the length or width of the air gap, and consequently changing downward gas flow rate. It would be very surprising to find that the solidification process could stabilize itself in this fashion, but it should not be ruled out. The most probable casting situation would however seem to be a nonzero mean downward discharge combined with an excess of injected gas leading to periodic gas discharge up through the mould. A better understanding of slip gas flow will be sought in the current work.

Chapter 2

Casting experiments

A series of test castings were performed using pure aluminium and Al 6082, with both pure Argon and a mixture of 90% argon and 10% oxygen for injection in the mould. Casting velocities used were 90mm/min, 100mm/min, 120mm and 160mm/min. The ingot diameter was 200mm.

The casting set-up is displayed in figure 2.1. There were six pairs of moulds. The test mould is indicated.

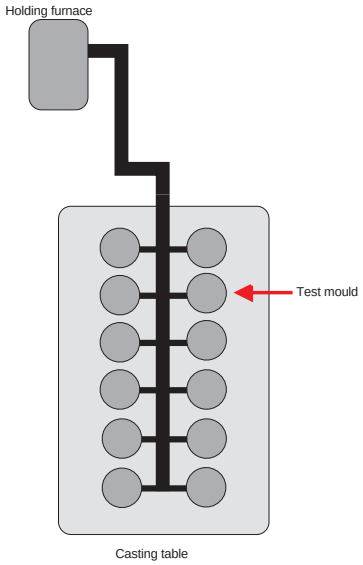

Figure 2.1: Casting setup.

The placing of the thermocouples for temperature measurements are shown in figures 2.2 and 2.3. The temperature was measured in four different regions; at several points close to the surface of the graphite ring in the mould, at the bottom of the hot-top, in the aluminium mould encapsulating the graphite (*mould temperature*) and at the melt surface in the mould (*bath temperature*). Thermocouples 1 and 3 in the graphite were not functioning during the tests.

The pressure in the gas pocket was measured using a Fischer Porter differential pressure transmitter. The meniscus was also videotaped during the experiments through an endoscope. Holes were made through the hot top for the pressure measurements and videotaping. The movement of the melt

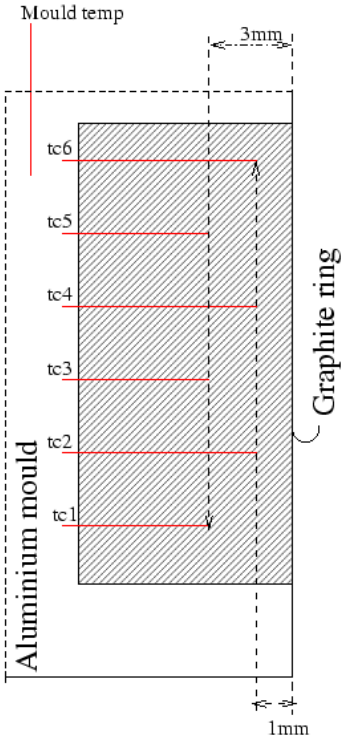

Figure 2.2: Positioning of thermocouples in cross section of graphite ring and mould wall.

surface in the moulds was observed visually. Frequencies of oscillations were measured with the aid of a stopwatch. To facilitate visual observations a mould other than the test mould was observed.

Chemical analysis of pure Al and the Al 6082 alloy (weight %) is shown in the following table.

	Al	Fe	Si	Mg	Mn	other
Pure Al	99.68	.15	.13	.006	.03	.004
Al 6082	97.70	.18	.96	.62	.52	.02

2.1 Tests

A total of seven test castings were performed. Initially the aim was to cast four ingots with all four combinations of alloy and gas. Each ingot was to be cast in three 1- meter sections with casting velocities of 90mm/min, 120mm/min and 160mm/min. Due to problems experienced during the tests three castings were made for the case with pure Al, Ar10%O_2 and

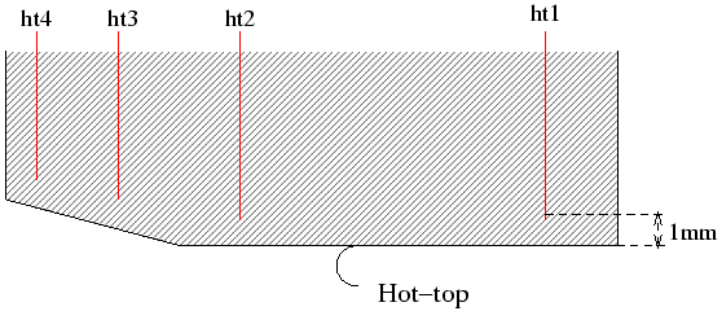

Figure 2.3: Placing of thermocouples in hot-top cross section (1mm from bottom surface).

two castings were made with Al 6082, Ar10%O_2. The following table gives an overview of castings. Cast ingots are numbered from 1 to 7.

Alloy	90mm/min	100mm/min	120mm/min	160mm/min	Gas
Pure Al	1	-	2/3	2/3	Ar10%O2
-	-	-	4	4	Ar
Al 6082	5	6	6	6	Ar10%O2
-	-	7	7	7	Ar

It was observed that for 160mm/min casting velocity the oscillatory behaviour in the test mould differed significantly from that of the other moulds. So at this casting velocity the setup seemed to influence the casting more than at the lower casting velocities. Raw data for a section of ingot 6 are plotted in figure 2.4.

2.2 Frequency analysis

A frequency analysis of the temperature and pressure measurements were performed using the Fast Fourier Transform. Results for ingot 6 are presented in appendix A. From the frequency analysis the following higher characteristic frequencies [Hz] were found.

Alloy	90mm/min	100mm/min	120mm/min	160mm/min	Gas
Pure Al	0.89	-	*0.62*	*0.93*	Ar10%O2
-	-	-	0.68	0.81	Ar
6082	-	*0.45* *0.89*	*0.49* *0.98*	0.90	Ar10%O2
-	-	-	*0.55* (*1.08*)	-	Ar

The figures in italics are common modes of oscillation for temperature and

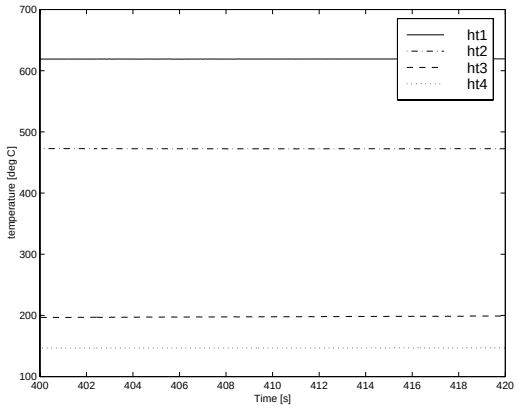

(a) Hot-top temperature.

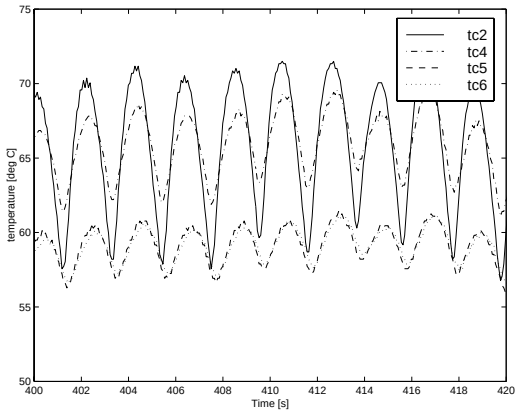

(b) Graphite ring temperature.

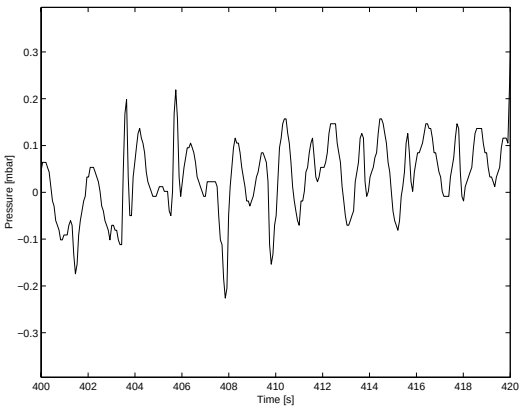

(c) Gas pocket pressure variation.

Figure 2.4: Raw data, Al 6082, 90% Ar 10% O_2, 120mm/min

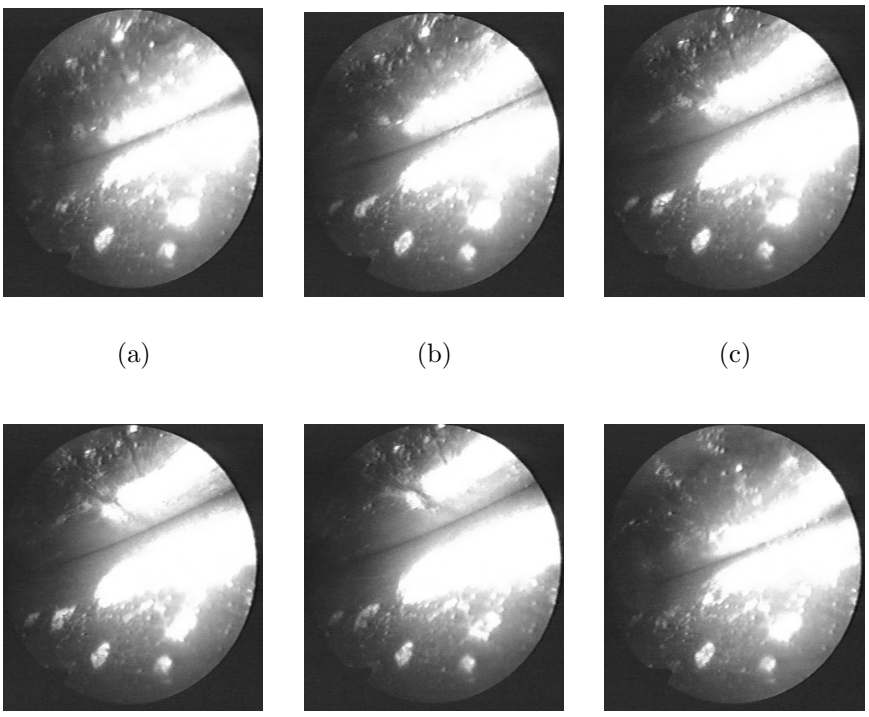

(a) (b) (c)

(d) (e) (f)

Figure 2.5: One period of oscillation ($\sim 2s$) for Al6082 with $90\%Ar$ $10\%O_2$.

pressure. Modes only appearing in the pressure signal are displayed in normal font.

The lower frequencies observed (of order 0.1Hz and lower) are not discussed here, since they represent a time scale that will not be used in the numerical simulations. These slow variations are possibly due to thermomechanical coupling between the ingot contraction and secondary cooling. And variations in the temperature field will affect the properties of the molten aluminium at the meniscus, so they will influence meniscus behaviour on the time scale of the casting. For simplicity the variations will however be neglected in this thesis, where constant thermal boundary conditions are applied for the secondary cooling.

Characteristic period with meniscus collapse

A series of pictures for a period of meniscus oscillation for Al6082 with $90\%Ar$ $10\%O_2$ at 120mm/min casting velocity is shown in figure 2.5. The

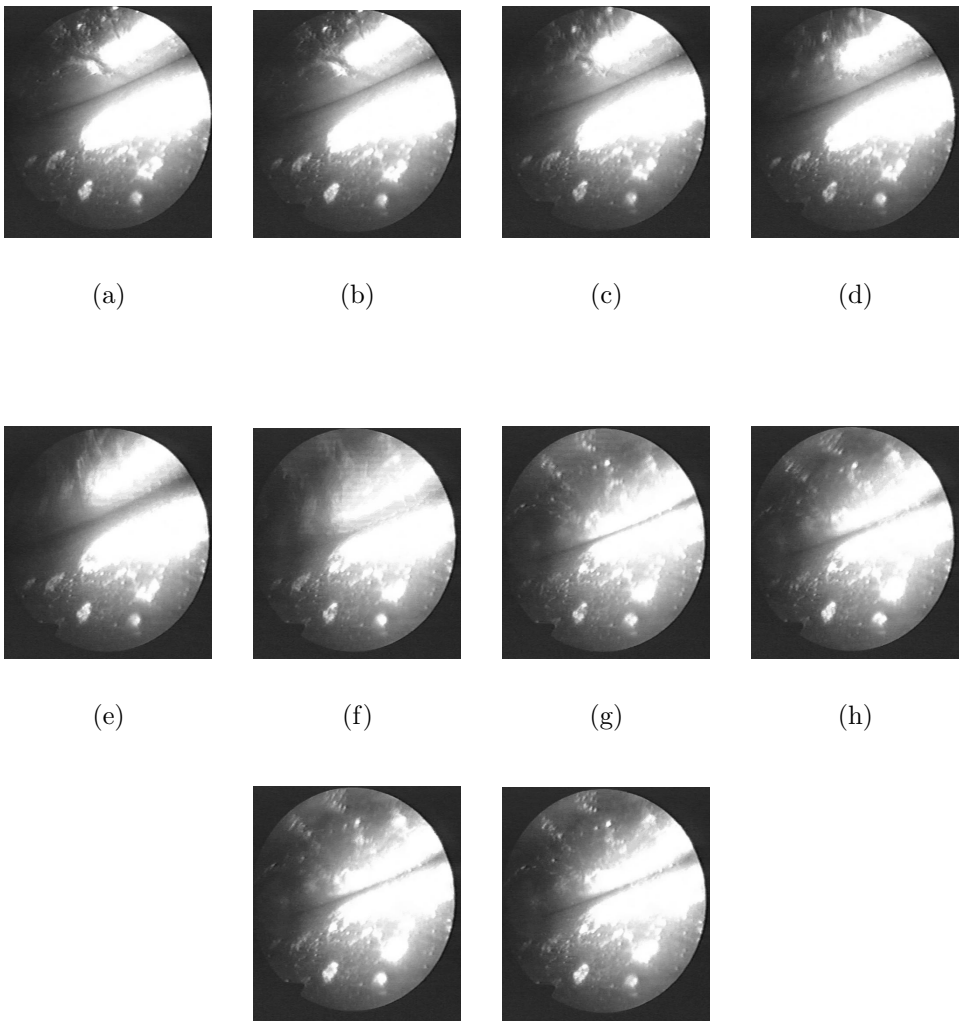

(a) (b) (c) (d)

(e) (f) (g) (h)

(i) (j)

Figure 2.6: Meniscus collapse ($\sim .1s$) for Al6082 with $90\%Ar$ $10\%O_2$.

meniscus collapse at the end of the period is shown in series 2.6. In the pictures the meniscus is viewed from above. The mould wall is seen below right while the meniscus surface is above left. Patches of lubricating oil can be seen on the mould wall and some fissures in the surface oxide layer may be discerned on the meniscus. These fissures disappear down along the mould wall as the meniscus collapses. There is approximately equal time spacing between the pictures in the individual series.

During a period (figure 2.5) the meniscus can be seen to move slowly downwards along the mould wall, 2.5(a) to 2.5(e), before it rapidly moves back up to its highest level, 2.5(f). At the end of this rapid upward movement the meniscus folds, or collapses. This collapse is seen in 2.6(f) to 2.6(i), where the resolution is poorer than in the other pictures due to the rapid folding process.

Surface oscillations

The frequencies of oscillation [Hz] of the visually observed melt surface in the mould are summarized in the following table. The oscillations were timed with a stopwatch.

Alloy	90mm/min	100mm/min	120mm/min	160mm/min	Gas
Pure Al	3.00	-	0.66	0.81	Ar10%O2
-	-	-	0.59	1.00	Ar
Al 6082	-	0.43	0.50	0.71	Ar10%O2
-	-	-	0.43	1.11	Ar

The frequencies coincide quite well with the modes common to pressure and graphite temperature oscillations for casting velocities of 100mm/min and 120mm/min (again apart from the pure Ar cases, where the oscillatory signals are weak). But the modes only appearing in the pressure signal do not correspond very well to the manually measured frequencies.

2.3 Discussion

Common modes

It can be seen that the common modes exist mainly for medium casting velocity (120mm/min). With a casting velocity of 160mm/min the noise is greater than for the lower casting velocities and characteristic frequencies are more difficult to discern.

Significant oscillatory modes common to mould temperature, graphite temperature and gas pocket pressure only occur in Al 6082. They correspond

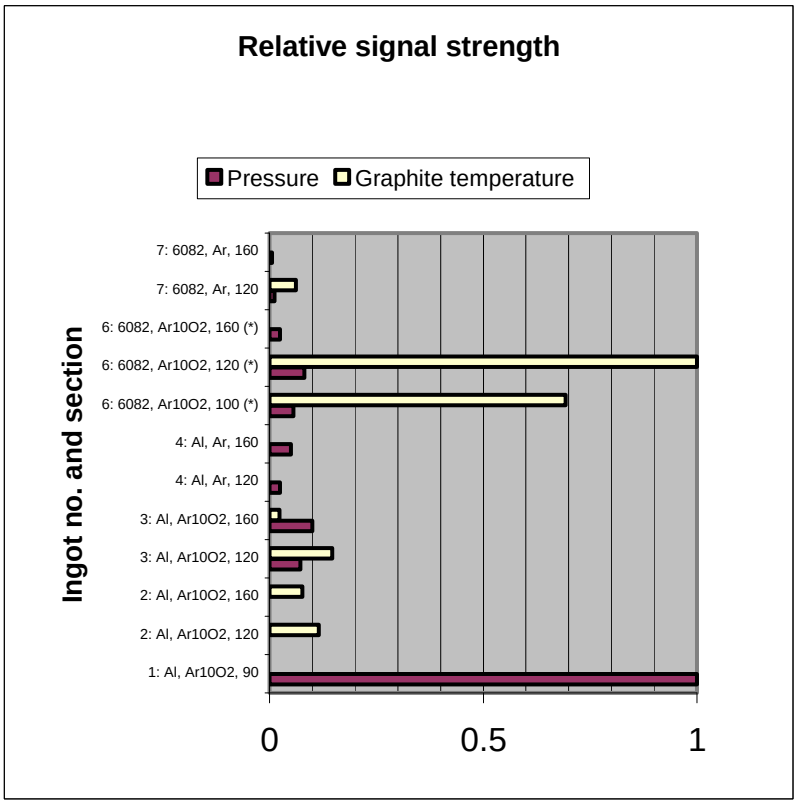

Figure 2.7: Relative peak signal strength of oscillations in pressure and graphite temperature.

to the modes with high signal strengths for graphite temperature oscillations for ingot 6.

The common temperature oscillations observed for mould and graphite temperature are to be expected considering the frequency and the signal strength of these oscillations in the graphite. They occur however only for the ingots with alloy 6082, indicating more contact at the bottom of the mould, where the ingot is in thermal contact with the Aluminium part of the mould (see figure 2.2). The reason for the difference in contact is probably the difference in contraction experienced by 6082 and pure aluminium at this point.

Temperature oscillations

Figure 2.7 shows that in relation to the casting velocity the peak graphite temperature signal strengths are strongest for the 120mm/min castings, be-

ing an order of magnitude greater than for the 100 and 160 mm/min sections of ingot 6 (Al 6082, Ar1%O2). Graphite temperature peak signal strength is generally low for castings with no oxygen, with the only significant peak for ingot 7 (Al 6082, Ar) at 120mm/min. These results imply that both oxygen and alloying elements enhance the periodicity and dampen the noise, with the oxygen possibly having a larger influence than the alloy elements. And the combined effect gives oscillations an order of magnitude stronger than that due to only oxygen or alloy elements.

Pressure oscillations

The peak signal strengths of the pressure oscillations (figure 2.7) have smaller variations (except for the 1 ingot, which froze in the mould). The pressure mode peaks for 160mm/min casting velocity are the largest for the pure aluminium ingots, while the peaks for 120mm/min are the largest for the Al 6082 ingots. Also, for the Al 6082 ingots there are dual pressure mode peaks for the 120mm/min sections. These dual peaks may imply higher harmonics.

The higher harmonic modes observed may be linked to a wave propagating on the meniscus. And the first mode could be coupled with the gravitational oscillations observed on the melt surface in the mould (see above). No observed higher harmonic modes at 160mm/min could be due to lowering of the contact point of the meniscus, giving reduced thermal contact with the wall. A smaller primary cooling area will also stabilize the process.

The peak signal strength of the graphite temperature oscillations is significantly stronger than the signals for mould temperature and pressure oscillations in the analysis (figure 2.7). This can also be observed in the raw data. And the oscillations in pressure are a lot more erratic than the oscillations in the graphite temperature (figure 2.4).

Pressure spikes It is possible that the effect of the dual pressure peak is an artificial effect caused by regular interruption of the natural pressure signal following a meniscus collapse by the next collapse. An indication of this is the regularly appearing spike at the local temperature minima. This is assumed to be the point of the meniscus collapse (see figure 2.8). This being the case, a new characteristic pressure signal might be initiated, indicated by a spike[1], a sharp peak or through, at each point of collapse.

The direction of the pressure spike might be an indication of the gas pocket behaviour during folding, a strong upward spike indicating significant

[1]These spikes are seemingly not due to singular experimental error, since the width of a spike is several times the sampling interval.

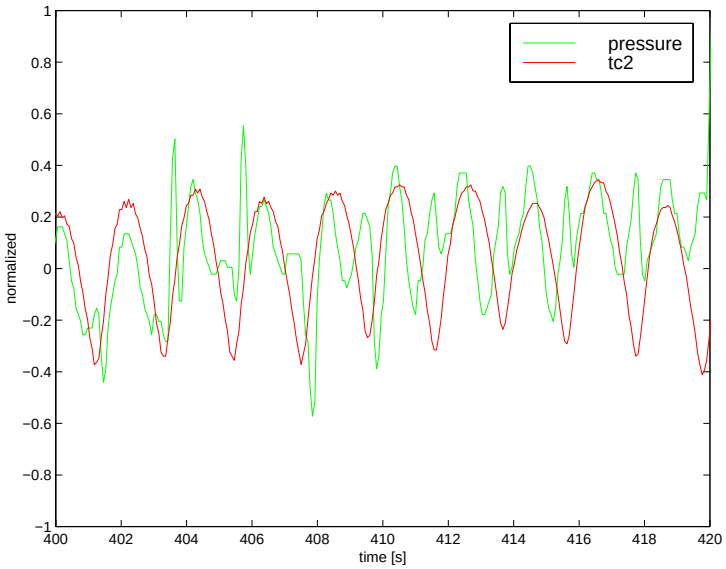

Figure 2.8: Comparison of normalized pressure in gas pocket and temperature for second thermocouple.

upward bubbling and a strong downward spike indicating folding without upward bubbling. To understand these effects the behaviour of the metal head must be considered in the collapsing process. As the meniscus collapses the metal head will decrease due to increased velocity of metal flow into the mould, and the extra metal momentum will displace gas in the pocket.

Now if the gas can escape quickly upwards the volume in the gas pocket can decrease without pressure buildup. The pressure in the gas pocket may therefore drop proportionally with the drop in metallostatic head. After the collapse, the reduced metal level will quickly fill. Thereby a negative spike in pressure is created. Gravity waves may be excited by the variations in metal level, resulting in further pressure variations, but now of a more sinusoidal nature.

In the opposite case, where there is no upward gas discharge, the gas can not escape quickly as the volume of the gas pocket is reduced by the momentum of the collapse. In this case the pressure will quickly build up as the gas volume is decreased by the metal momentum and then fall again as the gas expands by the force of its own pressure. So a positive pressure spike is created.

If the interpretation above is correct the type of gas discharge can be directly observed from a comparison of the pressure and temperature signals, giving an effective experimental method for observing meniscus behaviour.

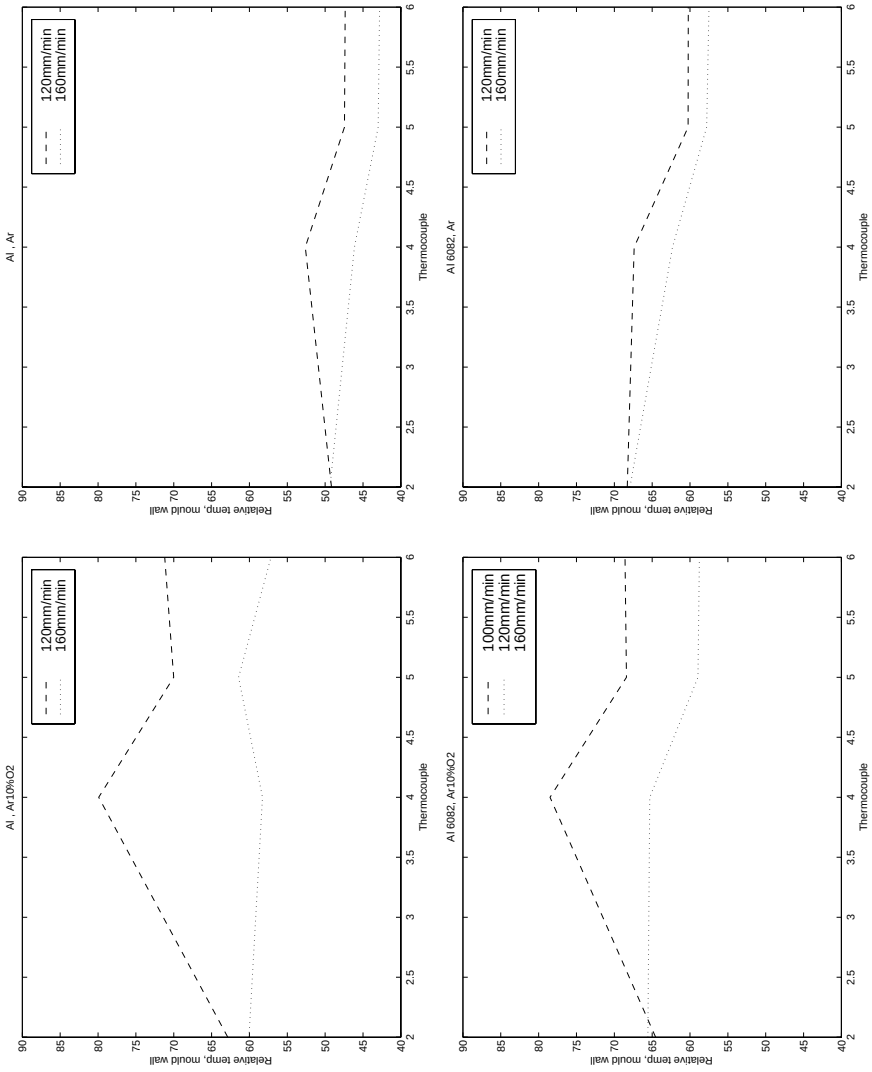

Figure 2.9: Mean mould wall temperatures.

Graphite temperature profile

The test data imply good thermal contact between graphite and ingot surface up to thermocouple 4 (see figures 2.9) for 120mm/min with pure aluminium. For 160mm/min the contact is lower.

When Al 6082 is used, there appears to be contact up above thermocouple 2 for 120mm/min. With 160mm/min casting velocity the temperature gradient implies contact below the lowest thermocouple but the measured temperatures are exceptionally high when oxygen is used.

The indication of lowering of the meniscus at the mould wall coincides

with observations in the mould during casting. In general, the lower meniscus contact point is lowered when casting velocity is increased. And both added oxygen in the slip gas and added alloy elements increase thermal contact with the mould wall, the former to a greater extent. This might also be explained by increased oscillations with larger amplitudes causing more thermal contact with the mould wall.

Elastic eigenmodes

If the mushy zone reaches above the lower point of the meniscus the movement will become more elastic than Newtonian. Consequently eigenfrequencies coupled to the elasticity might appear. The oxide layer on the surface of the melt could also influence eigenmodes. The combined effect is a lot stronger, and obviously not linear (see figure 2.7). This effect is not yet understood.

Chapter 3

Analysis of wave phenomena

3.1 Introduction

In the experimental measurements of the temperature oscillations close to the meniscus in direct chill casting of aluminium ingot (see [17]), the characteristic frequencies are found to be around 0.5 and 1.0 Hz. These results are for castings of aluminium ingot with a radius of 200mm and casting velocity of 90 to 160 mm/s.

In this chapter different types of wave phenomena are analyzed to ascertain which wave phenomena could induce the observed characteristic frequencies. For different types of wave phenomena are analyzed. These are:

capillary waves on a meniscus of spherical section

coupled *capillary gravity waves* on a meniscus of spherical section

gravitational oscillations in casting column

coupled *gravity pressure oscillations*

The assumption of a steady state meniscus of cylindrical cross section is quite rough, since the curvature of a steady state meniscus will increase monotonously with the metal depth. However, for a small enough meniscus, this assumption will become valid. Ideally a solution for gravity/capillary waves should be sought for the type of meniscus, or free surface, obtained in the simulations (as in for example figures9.9(b)). But here the analysis will be restricted simple geometries and to the phenomena listed above. The stability of the solutions will also be considered.

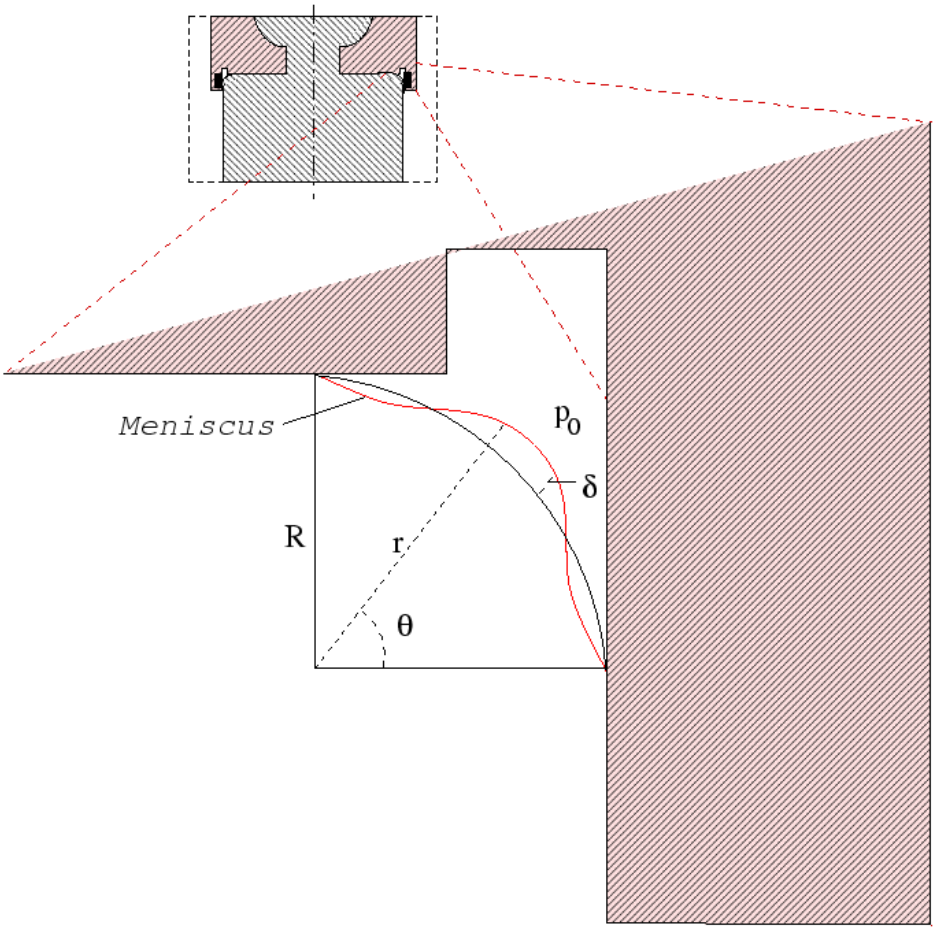

Figure 3.1: Coordinate system and capillary wave on the meniscus.

3.2 Capillary waves on meniscus

Laplace equation

With the assumption of incompressibility and potential or irrotational flow, the velocity potential ψ in the meniscus region must fulfill the 2D Laplace equation:

$$\frac{\partial^2\psi}{\partial r^2} + \frac{1}{r}\frac{\partial\psi}{\partial r} + \frac{1}{r^2}\frac{\partial^2\psi}{\partial\theta^2} = 0. \tag{3.1}$$

See figure 3.1 for description of coordinate system. The velocity components are

$$v_r = \frac{\partial\psi}{\partial r} \text{ and } v_\theta = \frac{\partial\psi}{\partial\theta}. \tag{3.2}$$

Boundary conditions (wave equation)

The boundary condition on the meniscus can be found by a variational analysis (as is done for the derivation of the spherical capillary wave equation in Landau and Lifshitz [40]). The change in meniscus surface area A will correspond to

$$A = \iint \sqrt{r^2 + \left(\frac{\partial r}{\partial\theta}\right)^2}\, d\theta dz. \tag{3.3}$$

Here a cylindrical coordinate system is applied with axis at $z = 0$ (normal to the plane shown in figure 3.1), then for variations of small amplitudes ζ (compared to wavelength), we have $r = R + \zeta$ on the meniscus, where R is the constant average radius, i.e. $\zeta \ll R$. Using a truncated binomial series, and neglecting terms of order ζ^2 and higher, gives the approximate result

$$A \approx \iint \left(r + \frac{1}{2R}\left(\frac{\partial\zeta}{\partial\theta}\right)^2\right) d\theta dz. \tag{3.4}$$

The change in surface area du to wave motion can subsequently be expressed by (see [23]):

$$\iint \left(\frac{\partial I_\zeta}{\partial\zeta} - \frac{d}{d\theta}\frac{\partial I_\zeta}{\partial\dot{\zeta}}\right)\delta\zeta\, d\theta\, dz, \tag{3.5}$$

where I_ζ and $\dot{\zeta}$ are defined by $I_\zeta = r + \frac{1}{2R}\left(\frac{\partial\zeta}{\partial\theta}\right)^2$ and $\dot{\zeta} = \frac{\partial\zeta}{\partial\theta}$. As a result,

$$\delta A = \iint \left(1 - \frac{1}{R}\frac{\partial^2\zeta}{\partial\theta^2}\right)\delta\zeta\, d\theta\, dz. \tag{3.6}$$

In [40] it is shown that

$$\delta A = \int\int \delta\zeta \left(\frac{1}{R_1} + \frac{1}{R_2}\right) r\, d\theta\, dz, \tag{3.7}$$

with R_i as the principle radii of curvature. For an ideal fluid, neglecting the influence of gravity and defining σ as the uniform surface tension coefficient, p as the pressure in the fluid and p_0 as the pressure outside the fluid (above the meniscus, see figure 3.1), then by [40]:

$$p - p_0 = \sigma \frac{1}{R} \tag{3.8}$$

For capillary waves with incompressible fluids and adiabatic conditions we have, again by [40],

$$p = -\rho \partial\psi/\partial t, \tag{3.9}$$

where ρ is the density of the fluid. Equating the integrands in expressions 3.6 and 3.7, applying $r = R + \zeta$, and including relations 3.8 and 3.9 we get to the first order in ζ

$$-\left(\rho \frac{\partial\psi}{\partial t} + p_0\right) = \sigma \left(\frac{1}{R} + \frac{\zeta}{R^2} - \frac{1}{R^2}\frac{\partial^2\zeta}{\partial\theta^2}\right). \tag{3.10}$$

Taking the derivative with respect to time, linearizing and using the relation $\frac{\partial\zeta}{\partial t} = v_r = \frac{\partial\psi}{\partial r}$, the boundary condition on $r = R$ becomes:

$$\rho\frac{\partial^2\psi}{\partial t^2} + \frac{\sigma}{R^2}\frac{\partial\psi}{\partial r} - \frac{\sigma}{R^2}\frac{\partial}{\partial r}\frac{\partial^2\psi}{\partial\theta^2} = 0, \qquad r = R. \tag{3.11}$$

Eigenfunction solution

The Laplace equation for the velocity potential can be solved using the method of eigenfunction expansions, or separation of variables. Since this corresponds to a regular Sturm-Liouville problem, the eigenfunctions are orthogonal and linearly independent. With the separation

$$\psi = T(t)Q(\theta)P(r), \tag{3.12}$$

the resulting equations are

$$\frac{\partial^2 Q}{\partial\theta^2} = -\nu^2 Q, \tag{3.13}$$

$$r^2\frac{\partial^2 P}{\partial r^2} + r\frac{\partial P}{\partial r} = \nu^2 P. \tag{3.14}$$

The following boundary condition is imposed:

$$\frac{\partial \psi}{\partial r} = 0\,;\, \theta = 0\,, \theta = \frac{\pi}{2}. \tag{3.15}$$

The eigenfunction equation for P is known as the Euler-Cauchy equation. A solution can be found using the Extended Power Series Method [37]. By substituting r^γ for P it can be seen that the eigenfunctions are

$$P_\nu = b_1 r^\nu + b_2 r^{-\nu}. \tag{3.16}$$

The eigenfunctions Q become

$$Q_\nu = a_1 e^{i\nu\theta} + a_2 e^{-i\nu\theta}. \tag{3.17}$$

Applying boundary conditions 3.15, Q becomes

$$Q_\nu = A_\nu \sin(\nu\theta), \tag{3.18}$$

$$\nu = 2n,\ n = \pm 1, \pm 2, \pm 3, ... \tag{3.19}$$

The coefficients may also depend on ν. If the amplitude is to be largest at the meniscus surface one needs to choose $b_1(\nu) = 0$ for ν negative and $b_2(\nu) = 0$ for ν positive. Then with positive ν

$$P_\nu = b_1 r^\nu. \tag{3.20}$$

For the temporal part

$$T_\nu = B_\nu e^{i\omega t} \tag{3.21}$$

are used as eigenfunctions, where frequency of oscillation is $f = \omega/2\pi$. The solution ψ then becomes

$$\psi = \sum_\nu \mathcal{A}_\nu e^{i\omega t} \sin(\nu\theta) r^\nu \tag{3.22}$$

With the boundary condition 3.11 the *dispersion relation* becomes

$$f = \pm \frac{1}{2\pi} \sqrt{\frac{\sigma|\nu|}{\rho R^3}\,(1+\nu^2)}. \tag{3.23}$$

Stability If the coefficients b_i are not chosen as above, the amplitude increases toward $r = 0$, leading to a singularity at $r = 0$, and ω becomes imaginary - see expression 3.22). The conclusion must be that pure capillary waves can not lead to instabilities, unless there also exist singularities, which is unphysical.

Eigenfrequencies The eigenfrequencies f may be now be related to the radius of curvature R through (3.23). The applied material properties are (as in the simulations of Al 6082 in chapter 9):

$$\sigma = 0.9N/m,$$
$$\rho = 2700kg/m^3.$$

For a given eigenfrequency the dispersion relation (3.23) then gives the relation between mode n (by (3.19) and radius of curvature. For the lowest mode ($|\nu| = 2$) the radius of curvature $R = 0.045m$ corresponds to an eigenfrequency of $0.96Hz$ and the radius of curvature $R = 0.0275m$ corresponds to an eigenfrequency of $2.02Hz$. These frequencies are close to the ones measured in the casting experiments (chapter 2). These radii of curvature are significantly larger than the experimentally observed meniscus curvature, and the radii increase with increasing modes. Therefore, with a meniscus geometry as in figure 3.1, it can be concluded that this type of capillary waves can not be directly linked to the experimentally observed oscillations.

3.3 First order coupled capillary gravity waves

For an extended equation containing gravity terms, effects such as damping and instabilities might occur. And the geometry of the meniscus might influence its dynamic properties. Therefore the effect of gravity and meniscus dimension is analyzed here. The geometry of the meniscus applied in this case is shown in figure 3.2.

Including gravity terms the internal pressure p in 3.8 becomes

$$p = -\rho g \Delta z - \rho \partial\psi/\partial t, \tag{3.24}$$

where $\Delta z = \zeta \sin\theta$. figure 3.2.

The boundary condition 3.11 becomes

$$\rho \frac{\partial^2\psi}{\partial t^2} - \rho g \left\{ \sin\theta \, \frac{\partial\psi}{\partial r} + \cos\theta \, \frac{1}{R}\frac{\partial\psi}{\partial\theta} \right\} + \frac{\sigma}{R^2}\frac{\partial\psi}{\partial r} - \frac{\sigma}{R^2}\frac{\partial}{\partial r}\frac{\partial^2\psi}{\partial\theta^2} = 0, \quad r = R. \tag{3.25}$$

If we consider only the first term added, neglecting the $\frac{\partial\psi}{\partial\theta}$ term, which will be small for θ close to $\frac{\pi}{2}$, we see that the result of including gravitational effects will be to reduce the frequency of oscillations. This can be analyzed further by expanding the $\cos\theta$ term around $\pi/2$; $\theta = \pi/2 - \theta'$, where $\theta' \epsilon [0, \theta_0]$.

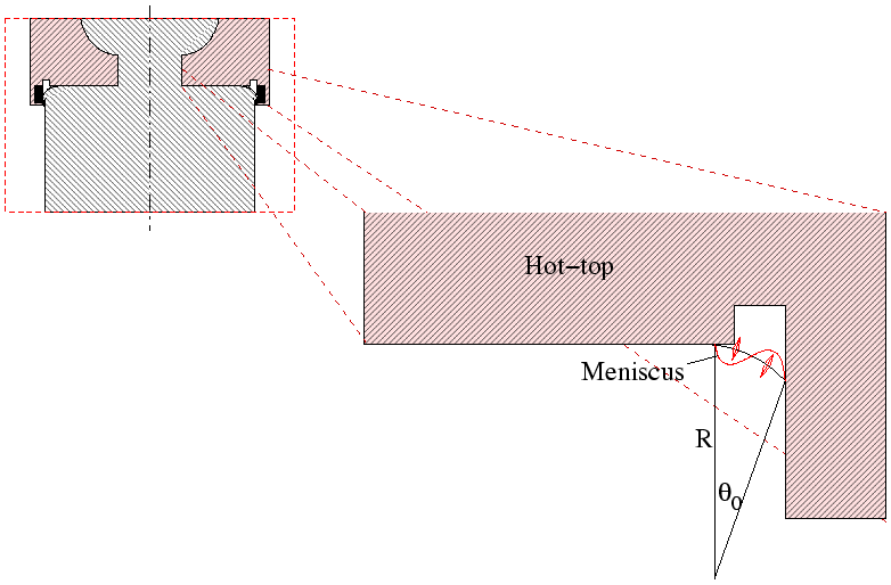

Figure 3.2: Meniscus configuration for perturbed solution, second mode of oscillation for solution of first order. Amplitude greatly exaggerated

Thus getting $\cos\left(\frac{\pi}{2}+\theta'\right)\frac{1}{R}\frac{\partial\psi}{\partial\theta} \approx 0$, since θ' is chosen to be $\ll \frac{\pi}{2}$ and $\partial\psi/\partial\theta$ is also small. Also, $\sin\left(\frac{\pi}{2}+\theta'\right) \approx 1$. The wave equation becomes

$$\rho\frac{\partial^2\psi}{\partial t^2} - \rho g\frac{\partial\psi}{\partial r} + \frac{\sigma}{R^2}\frac{\partial\psi}{\partial r} - \frac{\sigma}{R^2}\frac{\partial}{\partial r}\frac{\partial^2\psi}{\partial\theta^2} = 0, \qquad r = R. \tag{3.26}$$

The applied boundary conditions are

$$v_r = \frac{\partial\psi}{\partial r} = 0;\ \theta = \frac{\pi}{2} \tag{3.27}$$
$$v_\theta = \frac{1}{r}\frac{\partial\psi}{\partial\theta} = 0;\ \theta = \frac{\pi}{2} - \theta_0.$$

The motivation for these boundary conditions is that the contact point at the hot-top is always at the same level, while the angular velocity at the mould wall (or corresponding to the velocity perpendicular to a possible solid lip formed at the wall) is zero. The allowed values for ν are then given by applying these boundary conditions with the eigenfunction (3.17):

$$a\,e^{i\nu\frac{\pi}{2}} + b\,e^{-i\nu\frac{\pi}{2}} = 0,$$
$$i\nu\left(a\,e^{i\nu\left(\frac{\pi}{2}-\theta_0\right)} - b\,e^{-i\nu\left(\frac{\pi}{2}-\theta_0\right)}\right) = 0.$$

The condition on ν becomes

$$\nu = \frac{\pi}{2\theta_0} + n\frac{\pi}{\theta_0}, \qquad n = 0, \pm 1, \pm 2, \pm 3, ... \tag{3.28}$$

For simplicity θ_0 will be chosen so that the set of values ν consists only of integers. This gives the eigenfunctions

$$Q(\theta, \nu) = A(\nu) \sin(\nu\theta)\,,\ \nu odd, \tag{3.29}$$

$$Q(\theta, \nu) = A(\nu) \cos(\nu\theta)\ \nu even. \tag{3.30}$$

With the other eigenfunctions (3.21 and 3.20) the same as before, the dispersion relation becomes:

$$f = \pm\frac{1}{2\pi}\sqrt{\frac{|\nu|}{R}\left(\frac{\sigma(1+\nu^2)}{\rho R^2} - g\right)}. \tag{3.31}$$

Eigenfrequencies and stability For the test case, $\theta_0 = \frac{\pi}{16}$. Then for the lowest order solution, where $n = 0 \leftrightarrow \nu = 8$, a radius of curvature from $R = 0.045m$ to $R = 0.047m$ gives frequencies ranging from 2 Hz to 0.2 Hz for aluminium with $\sigma = 0.9\,N/m$, $\rho = 2700\,kg/m^3$ and $g = 9,8m/s^2$. This value of the radius of curvature corresponds to a meniscus length of $10mm$, a reasonable value. So with this shape of the meniscus it is possible to find a solution with a frequency corresponding to the experimental results referred to in the introduction (3.1). The second order solution ($n = 1 \leftrightarrow \nu = 24$) will in this case have frequencies in the order of $20Hz$, a frequency which is assumed to be of lesser importance. For only slightly larger radius of curvature ($R > 0.047m$), the first order solution will either be dampened or become unstable. So this case is right on the border of stability.
If the second order solution is to have a period of $2\,s$ the corresponding radius of curvature is approximately $0.14m$. With this radius of curvature the first order frequency will be imaginary. Thus it is either dampened or becomes unstable.
An important aspect to consider here is how the amplitude decreases inwards from the meniscus. The wave solution on the assumed circular meniscus is an approximation since there is solidification in the domain of the solution (figure (3.2)), while the solution is for a liquid of homogeneous density. If the amplitude of the waves decreases rapidly downwards the approximation will be a good one. The radial eigenfunction solution (equation 3.20) shows that the velocity goes as $v_r = \frac{\partial}{\partial r}\psi \sim r^{\nu-1}$. If $R = 0.046m$ at the meniscus surface with $\nu = 8$, as above, then the amplitude is decreased by a factor ten at $r = 0.034m$. So if the point of dendrite coherency is $1.2cm$ beneath the meniscus surface or lower, the solution is physically possible.

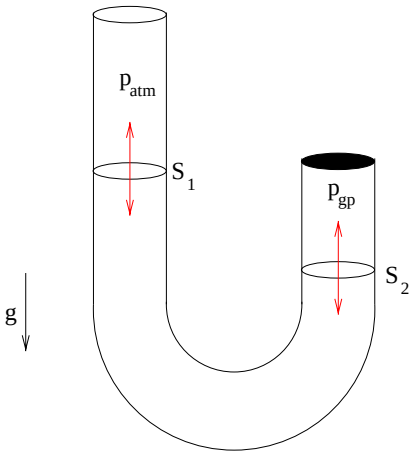

Figure 3.3: Gravitational oscillations in tube, diameter Ø=10cm.

3.4 Oscillations in casting column

3.4.1 Gravitational oscillations in casting column

To analyze the effect of gravity induced oscillations of the melt surface above the hot-top discussed in 1.3.3, the behaviour of the melt under the influence of gravity is approximated by the behaviour of fluid in a tubular section like that in figure 3.3. The gravity oscillations in the casting column (figure 1.9) are analogue to oscillations in the tube. The surface S_1 corresponds to the molten metal surface at the top of hot-top with atmospheric pressure p_{atm} above it while surface S_2 corresponds to the meniscus surface under gas pocket pressure p_{gp}. It will be assumed that no compression in the gas pocket above the meniscus occurs due to the oscillations. If this is to be the case for the meniscus, then the gas inflow and outflow must balance the variations in gas pocket volume.

The area of the surfaces S_1 and S_2 in the tube should roughly correspond to the free surface area at the top of the hot-top and the surface area of the meniscus, respectively. Since this might be quite a rough approximation this should be considered a tentative analysis.

Analysis produces the following equation for the position x of a surface in the column (where x is parameterized displacement along the tube):

$$\frac{\partial^2 x}{\partial t^2} = -\frac{2\,g}{L}x, \tag{3.32}$$

where L is the length of the liquid column. So the equation is independent

of both fluid density and the diameter of the tube. It is now assumed that the gravity oscillations are harmonic:

$$x = A\cos(2\pi f t). \tag{3.33}$$

Then the frequency of oscillations becomes

$$f = \frac{1}{2\pi}\sqrt{\frac{2g}{L}}. \tag{3.34}$$

In this case the frequency only depends on the metal height and the diameter of the cast ingot. With a typical fluid length $L = 0.3m$ (corresponding to the distance from melt surface to meniscus surface in mould) the frequency of gravitational oscillations becomes $f = 1.3Hz$. This frequency is very close to the characteristic frequencies observed in the casting experiments described in the previous chapter.

3.4.2 Gravity pressure oscillations

A similar analysis to the one above is performed, but now with the constraint of no flow in or out of the gas pocket . With this constraint the pressure variations in the gas pocket must be included in the wave equation.

Pressure variations Δp in the gas pocket are calculated by the ideal gas law:

$$\Delta p = \frac{nRT}{V + \Delta V} - p, \tag{3.35}$$

for gas pocket volume V containing n moles at temperature T. With small volume variations ΔV a Taylor expansion in ΔV gives the approximate pressure variation

$$\Delta p \approx -\Delta V \frac{nRT}{V^2}. \tag{3.36}$$

Then the balance of forces leads to the wave equation

$$\frac{\partial^2 x}{\partial t^2} = -\left(\frac{2\,g}{L} + \frac{\pi r^2 RT}{2MVL}\right) x, \tag{3.37}$$

where M is the molar mass $\rho V/n$ and r is the radius of the tube (with area πr^2 corresponding to meniscus surface area). Solving for harmonic oscillations as in (3.33) the frequency f becomes

$$f = \frac{1}{2\pi}\sqrt{\frac{2g}{L} + \frac{\pi r^2 RT}{2MVL}}. \tag{3.38}$$

The maximum gas pocket volume V is in the order of $1l$[1]. For air $M = 0.029kg/mol$, and the temperature is approximately $500K$. The radius r is $5cm$, as before. Under these conditions the effect of the pressure variations dominates the effect of gravitational pull, thereby determining the frequency of oscillations. The frequency becomes $f \approx 218Hz$.

Oscillations of a frequency as high as $184Hz$ can not be sustained at significant amplitudes. The energy required for the variation in momentum is not available. Therefore oscillations in the column can not exist when the air pocket is closed.

[1]This corresponds to a meniscus with upper contact point at the melt inlet corner and with 1 cm spacing from hot-top

Chapter 4

Numerical methods of free surface modelling

To model the meniscus dynamics a method is needed which can correctly describe both folding and wave propagation on the surface of the meniscus, while preserving a sharply defined surface on a relatively coarse grid. The meniscus is assumed to behave as a free surface, for which dynamics are determined by the balance of surface tension forces, gravitational forces, and the pressure jump across the meniscus surface. Specificly the effects of surface advection influenced by the acting surface tension forces must be dealt with in the modelling of flow in the combined gas and molten metal phases. This chapter gives a brief overview of methods for modelling the dynamics of such a free surface in a regular Eulerian grid. The applicability of the various models to simulating the meniscus in the casting process is also discussed.

Advection techniques The methods of multiphase modelling can be divided into two main groups; *interface tracking* and *interface capturing* methods. The interface tracking methods track the surface by marker particles or line segments, as in the *Marker and Cell* (MAC) method [71] and the *Method of Tensions* (MOT) [49]. Thus the surface representation is Lagrangian. The flow equations are solved on an Eulerian grid. Therefore these methods are also known as *Lagrangian Eulerian* methods. The original Lagrangian Eulerian method was the MAC method.

The interface capturing methods keep track of the surface either by some form of geometrical reconstruction by use of the *volume fraction* ([26], [77], [3]) or calculate the advection and surface tension forces by purely algebraic methods ([56], [39]). The algebraic models are generally easier to implement in numerical algorithms than the models where surface reconstruction is applied in the advection calculation. The interface capturing methods are also

known as Eulerian Eulerian methods or simply *Eulerian* methods. The basic interface capturing methods, developed in the 1970's were based on the Donor-Acceptor Cell technique. Variants of this technique were developed by Ramshaw and Trapp [51], Noh and Woodward [46] and the *Volume of Fluid* (VOF) method of Hirt and Nichols [26].

Surface tension techniques Several models for modelling surface tension forces have been developed in the last decade. One type applies reconstruction of the surface ([71], [49]) while others calculate a continuous surface force distribution from a smoothed interface ([10], [39], [36], [56]).

Flow solvers The Navier-Stokes (NS) solvers have been developed in parallel with the development of surface advection and surface tension techniques. In the application of the flow solvers attention must be payed to conditions of stability. Some references to the development of flow models are made in the discussion. The basic MAC and VOF methods are presented here together with the respective solvers.

4.1 The Marker and Cell (MAC) method

The fundamental work on computational multiphase methods was done by the CFD research group at Los Alamos Scientific Laboratory. Through this work, Eddie Welch, Frances Harlow, John Shannon and Bart Daly developed the MAC Method, the first numerical multiphase method in 1965 [71]. It was a 2D two-phase method. As this was the first method of its kind, the method is here described to create a basis for the understanding of two-phase flow methods.

Marker field

The MAC method uses massless Lagrangian marker particles spread evenly over the whole computational domain to trace the fluid flow and to mark the separate fluids. The computational domain is spanned by a regular and uniform Eulerian grid. The marker particles are advected with the fluid. Because of the large computing capacity needed to handle a 3D marker particle model, the basic MAC model was in 2D. Today, as computing capacity has greatly increased, 3D MAC models can be applied in multiphase flow, but the marker advection will still need a lot of computing power.

Volume averaging

Cell mean density and cell mean viscosity are applied in the flow calculations in MAC. In this way continuity in the cells containing the fluid interface can be fulfilled. Subsequently the Navier-Stokes equations can be applied over the whole computational domain. The averaging is performed with the use of the marker particle distribution. With n_1 particles of phase 1 and n_2 particles of phase 2 in a cell, mean density ρ and mean viscosity μ are given by

$$\rho = \frac{n_1\rho_1 + n_2\rho_2}{n_1 + n_2} \tag{4.1}$$

$$\mu = \frac{n_1\mu_1 + n_2\mu_2}{n_1 + n_2}. \tag{4.2}$$

ρ_i and μ_i are respectively cell mean density and cell mean viscosity of phase i. Periodic redistribution of the marker particles is necessary to maintain even marker distribution and consequently correct averaging. Marker distribution influences both stability and mass conservation, so in this type of model redistribution of the markers is an important issue.

Uniform staggered grid

The NS solver developed for the MAC method was named SOLA, for Solution Algorithm. This method uses a regular and uniform *staggered grid*, presented in figure 4.1. The 2D staggered grid model consists of three grids, one for each of the flow velocities and one for the pressure. The pressure, and generally all other flow variables, are stored in the *pressure grid*. And the nodes of the *velocity grids* are staggered in relation to the pressure grid by placing the nodes midway between pressure nodes (see figure). This configuration solves the problem of pressure checkerboarding that can occur in a single grid system (see Patankar [47]).

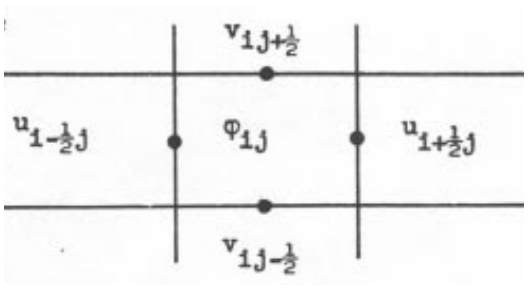

Figure 4.1: MAC staggered grid configuration, $\phi = \frac{p}{\rho}$

Pressure equation/Time Cycle

Central differences and time integration explicit in velocity **u**, implicit in pressure p, are applied in the discretization in SOLA. The pressure is computed by imposing incompressibility on the velocity field, resulting in a Poisson equation for the pressure.

The equations of continuity and momentum are:

$$\nabla \cdot \mathbf{u} = 0 \tag{4.3}$$

$$\frac{\partial \mathbf{u}}{\partial t} = -\nabla \cdot (\mathbf{uu}) - \nabla\phi + \nu\nabla^2\mathbf{u} + \mathbf{g} \tag{4.4}$$

u is the velocity vector, ϕ is p/ρ for pressure p and constant density ρ (or for small density changes $\delta\rho/\rho \ll 1$, corresponding to low Mach number, making the equation a lowest order approximation), ν is the kinematic coefficient of viscosity and **g** is gravity. The momentum equation is applied on divergence form. This facilitates conservation of momentum when discretizing the equations. The first term in the momentum equation can be discretized by central differences in time:

$$\frac{\partial \mathbf{u}}{\partial t} \rightarrow \frac{\mathbf{u}^{n+1} - \mathbf{u}^n}{\delta t}, \tag{4.5}$$

where δt is the time step. Using 4.4 and 4.3 together with 4.5 the Poisson equation in pressure may be derived:

$$\frac{\mathbf{u}^{n+1} - \mathbf{u}^n}{\delta t} = -\nabla \cdot (\mathbf{uu})^n - \nabla\phi^{n+1} + \nu\nabla^2\mathbf{u}^n + \mathbf{g}, \tag{4.6}$$

$$\Downarrow \; incompressibility \rightarrow \nabla \cdot \mathbf{u}^{n+1} = 0$$

$$\frac{\nabla \cdot u^n}{\delta t} = -\nabla\nabla : (\mathbf{uu})^n - \nabla^2\phi^{n+1} + \nu\nabla \cdot \nabla^2\mathbf{u}^n. \tag{4.7}$$

The Poisson equation 4.7 is subsequently discretized using linear interpolation and central differences.

Velocities calculated in the previous time step are inserted in the discretized Poisson equation which is subsequently solved for new pressures. These new pressures are inserted in the discretized momentum equations 4.6 which are then solved for the new velocities. This idea is basically the same as the original *projection method* described by Fortin et al [20].

Conservation properties and surface tension in the MAC method

With the MAC method, volume conservation should be maintained for small density ratio, according to Welch et al. Normal and tangential stress conditions at the interface should theoretically also be satisfied. It is however

difficult to achieve continuity of pressure at the interface 'when the fluids have markedly different densities'.

In the free surface modelling the pressure is not continuous, so a pressure correction model is needed. It is possible to incorporate such a technique in the MAC method. But the surface reconstruction which would be needed for calculation of the surface tension forces is a complicated process. If the surface is to be reconstructed an ordering of the markers is needed, which would take up a lot of computing time. A diffuse surface tension model like the Continuous Surface Force model CSF could however be applied [10][1]. Then surface reconstruction would not be necessary, but accuracy would be poorer due to the diffusive surface representation in CSF.

A problem with the SOLA solver is the low order of approximation in the momentum equation. The density is assumed approximately homogeneous. This is true within each phase for low Mach numbers, but the density change across the interface causes problems. So for phases of markedly different phase densities, as in our case, the use of this solver will lead to significant error.

To conclude, the MAC method together with the SOLA algorithm may be applied for free surface modelling with a pressure jump and surface tension force calculations without the need for ordering of markers. But because of the insufficiencies of the SOLA algorithm, a different solver taking into account the pressure jump and inhomogeneous density and allowing for a non-uniform grid would be preferable. The large memory requirements and CPU time needed for the calculation of marker advection also make the MAC method awkward. Some other method should therefore be sought.

4.2 Hirt & Nichols Volume of Fluid (VOF) method

Based on the ideas of the combined MAC and SOLA methods this method was developed by by Hirt and Nichols, also at Los Alamos in 1981 [26]. Improvements were made to the SOLA code to include limited compressibility, producing the SOLA-VOF method. Many variations of the VOF method exist. Therefore this VOF method is here referred to as *Hirt and Nichols' VOF*. It contains the basics of all the VOF methods (except for surface tension calculations) and is therefore here presented as an introduction to these types of methods.

[1] This model is discussed at a later point

Fractional volume

The most important contribution in the VOF method is the introduction of the phase function F which distinguishes the phase at each point. F is used slightly ambiguously in the paper, being simultaneously used as its own volume average. To avoid this ambiguity two new values are introduced here. The first is the *phase function* $C(x, y, z)$, which takes the value 1 for (x, y, z) in phase 1 (f.ex. the slip gas) and 0 for (x, y, z) in phase 2 (the molten metal). The second is the volume average of C, denoted by α, known as the *volume fraction*. In a two-phase liquid gas system the convention is that α is the volume fraction of gas, while the volume fraction of the individual phases is denoted by a postscript, with α_L for liquid volume fraction. By applying the VOF method marker particles are made superfluous by an advection algorithm for the volume fraction α. This decreases usage of computer memory and saves calculation time. The model may also be applied in three dimensions because of the low demand on CPU time.

Volume fraction advection

The volume fraction field is advected together with the fluid flow according to the equation for conservation of phase:

$$\frac{\partial \alpha}{\partial t} + \frac{\partial \alpha u}{\partial x} + \frac{\partial \alpha v}{\partial y} = 0. \tag{4.8}$$

The velocities here represent the velocity field of the volume averaged fluid quantities. In the discretization of this equation several considerations are taken into account[2]. Since upstreaming is numerically stable, a certain amount of upstreaming is required. However, the unstable downstreaming helps to keep the surface sharply defined. Therefore a combination of both discretization methods should be used. Another important point is that neither the fluxed gas volume should not be larger that the gas volume contained in the upstream cell . This would lead to unphysical consequences. All the mentioned considerations are taken into account in the Donor-Acceptor volume fraction advection method in the VOF-SOLA algorithm.

Donor-Acceptor algorithm In the Donor-Acceptor algorithm the type of discretization is determined by the mean surface orientation. The surface

[2]Note that two types of discretization must be considered for the algebraic models: the ordinary discretization of the NS equations, and in addition the discretization concerning the choice of which volume fraction to use in phase advection across cell faces, i.e. the discretization of the conservation equation of volume fraction (4.8). The discretization in discussion here is the latter.

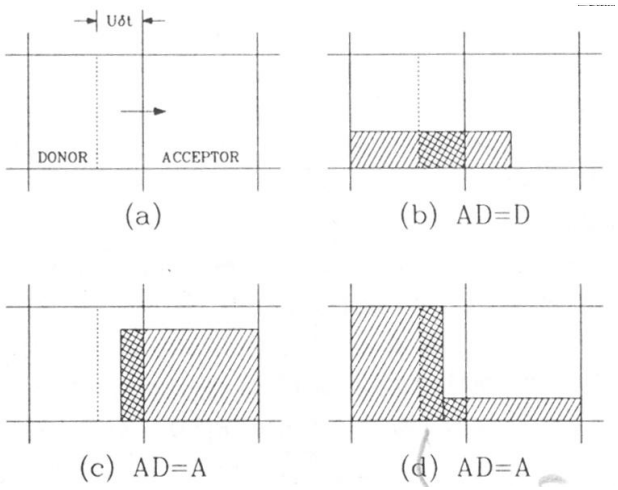

Figure 4.2: Donor acceptor modelling.

orientation is found by an interpolative algorithm which uses the volume fraction values in a nine cell scheme (as shown in figure (C.1) in the appendix). Upwinding is used when the surface is advected mostly parallel to itself (i.e. the volume fraction of the upwind cell is applied at the cell face in the discretization) while downwinding is used in the opposite case. Taking into account the conditions of no overfilling or over emptying of cells, resulting in volume fractions respectively larger than one or negative, the algorithm can be graphically illustrated by figure 4.2.

In the figure the downstream cell of the cell face is called the *donor* cell and the upstream cell is called the *acceptor* cell. The total advected volume for one time step is indicated in 4.2(a). In the first example (4.2(b)) the surface is advected mainly parallel to itself, so the donor (upstream) volume fraction is used as the volume fraction flux across the cell wall. In the second case (4.2(c)) the surface is advected mainly normal to itself, so the acceptor (upstream) value is used. However, in this case the donor cell is empty before the time step is over. So no fluid can be advected across the cell face after this point, meeting the condition of no over emptying of the donor cell. In the last case (4.2(d)) the advection is also mainly normal to the surface, so the upstream volume fraction is applied as the cell face flux. However, here the donor cell fills up before the time step is over, so the rest of the flux must be determined by the downstream volume fraction. Thereby the condition of no overfilling is met.

Two more conditions are set for the advection. If the acceptor cell is empty, or if the cell upstream of the donor cell is empty, then the acceptor

cell volume fraction determines the flux. Thus a donor cell must fill with liquid before it can advect any liquid to a downstream empty cell. This condition decreases smearing of the surface, thus helping to keep the surface sharply defined.

Phase conservation

An analysis of phase conservation is made in appendix C. The analysis shows that inaccuracy in phase conservation may be a significant problem due to errors in the interface advection. For one-dimensional advection (either in the x or y direction) the method is phase conserving, but when the mean velocity is not parallel to any of the grid lines phase conservation is not ensured due to the advection of the same fluid elements twice in one time step. By the analysis (C) this problem seems to be most apparent for significant curvature of the interface. Thus for a smaller ratio of grid spacing by surface curvature the problem would not be as prominent. However, as long as there are significant changes in volume fraction value over few cell spacings, i.e. a sharply defined surface, this is a problem that probably will occur. A solution to this problem might be using a diffuse surface during advection. This is however contradictory to the wish of keeping the surface sharply defined, which is also necessary if a good approximation of surface tension effects are to be found. It would seem that an unnecessarily small time step is here needed to achieve good phase conservation, compared to the resolution needed to solve for the fluid flow in the independent phases.

The conclusion is that phase fluxes should be calculated for all cell faces of a cell simultaneously, and flux correction methods should be applied to solve the problem of overfilling or over emptying. This technique will produce the most accurate phase conservation. Such methods are discussed in the next section (4.3).

Non-uniform grid

A non-uniform staggered computational grid is introduced in the SOLA-VOF model, allowing for a more complex geometry and multiple size scales. In the case of a non-uniform grid, analysis shows that care must be taken to ensure accuracy in the discretization. Upstreaming is normally applied in the discretization to improve stability. But if upstreaming is used in a regular nonuniform grid it can be shown [26] that discretization of the convective term $\frac{\partial(u^2)}{\partial x}$, which appears in the momentum equation on divergence form, is

to the first order equal to

$$\frac{1}{2}\left(\frac{3\delta x_i + \delta x_{i+1}}{\delta x_i + \delta x_{i+1}}\right)\frac{\partial(u^2)}{\partial x} + O(\delta x). \tag{4.9}$$

δx is width of computational cell and u is velocity in x-direction. So the first order term is incorrect unless $\delta x_i = \delta x_{i+1}$. However if we do not use any upstreaming, the stability of the solution deteriorates. Therefore, using upstreaming together with some correction of the advection terms is a preferable solution in this case.

Non-divergence momentum

In the SOLA-VOF the momentum equations are not applied on divergence form (equation 4.12), so conservation of momentum may be significantly inaccurate. However, with this technique, upstreaming results in no loss of formal accuracy on a nonuniform grid.

Continuity equation

As already mentioned, limited compressibility is included in the continuity equation in Hirt and Nichols VOF. The fluid pressure is assumed to depend only on the density, thus giving the relation,

$$\frac{dp}{d\rho} = c^2 \tag{4.10}$$

where c is the adiabatic speed of sound, i.e. the entropy is here assumed constant. Assuming small density changes $\rho = \rho_0 + \delta\rho$, where $\delta\rho/\rho_0 \ll 1$, implying a small Mach number ($U/c \ll 1$), together with equation 4.10, the continuity equation for constant entropy becomes to the lowest order

$$\frac{1}{c^2}\frac{\partial p}{\partial t} + \rho_0 \nabla \cdot \mathbf{u} = 0. \tag{4.11}$$

Condition 4.10 corresponds to the assumption of an ideal fluid [40]. So for a gas of low viscosity this is a valid assumption. For liquids of higher viscosity however, the validity of the assumption is not as good. However, the approximation is consistent with neglecting the work of viscous and pressure forces in the energy equation.

Discretization of momentum equations

The basic momentum equations in Hirt and Nichols VOF are

$$\frac{\partial u}{\partial t} + u\frac{\partial u}{\partial x} + v\frac{\partial u}{\partial y} = -\frac{\partial \phi}{\partial x} + g_x + \nu\left[\frac{\partial^2 u}{\partial x^2} + \frac{\partial^2 u}{\partial y^2}\right]. \tag{4.12}$$

$$\frac{\partial v}{\partial t} + u\frac{\partial v}{\partial x} + v\frac{\partial v}{\partial y} = -\frac{\partial \phi}{\partial y} + g_y + \nu\left[\frac{\partial^2 v}{\partial x^2} + \frac{\partial^2 v}{\partial y^2}\right]. \tag{4.13}$$

The momentum equations are discretized by central differencing in time and explicit time integration in the other terms. And the continuity equation is integrated implicitly in time. Subsequently no Poisson equation for the pressure is applied in the SOLA-VOF method (although it is inherent in the applied set of flow equations). The remaining discretization of the momentum equation is performed by applying a combination of upstreaming and central differencing. As an example, the convective term $u\frac{\partial u}{\partial x}$ is discretized as

$$\begin{aligned} u\frac{\partial u}{\partial x} \rightarrow \left(u_{i+1/2}/\delta x_\gamma\right)&\left[\delta x_{i+1} DUL + \delta x_i DUR + \right. \\ &\left. \gamma\ \mathrm{sgn}(u)\left(\delta x_{i+1} DUL - \delta x_i DUR\right)\right], \end{aligned} \tag{4.14}$$

where

$$\begin{aligned} DUL &= \left(u_{i+1/2,j} - u_{i-1/2,j}\right)/\delta x_i, \\ DUR &= \left(u_{i+3/2,j} - u_{i+1/2,j}\right)/\delta x_{i+1}, \\ \delta x_\gamma &= \delta x_{i+1} + \delta x_i + \gamma\ \mathrm{sgn}(u)\left(\delta x_{i+1} - \delta x_i\right). \end{aligned}$$

where γ determines the amount of upstreaming. For $\gamma = 0$, there is only central differencing and for $\gamma = 1$ there is complete upstream differencing. Since central differencing is more accurate while upstreaming is more stable, γ is chosen between 0 and 1 to give optimal results. The same discretization technique is applied to the other convective terms in the momentum equation. The set of volume averaged flow equations (4.11), (4.12) and (4.13) are subsequently solved iteratively, based on the updated volume fraction α by (4.8).

Pressure correction

A pressure correction method is introduced in the SOLA-VOF solver. In this technique the corrected pressure is an interpolation between the *surface cell* pressure and a neighbouring liquid cell pressure (see figure 4.2). The correction algorithm is based on the surface configuration, so some form of surface reconstruction must be applied. Based on the surface geometry, each

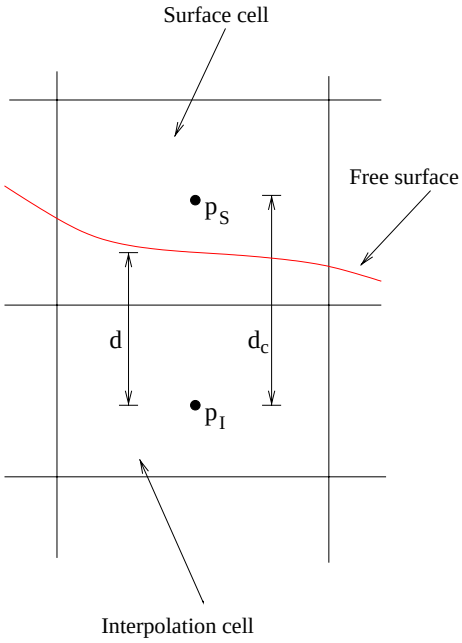

Figure 4.3: Pressure correction in VOF.

surface cell is assigned a neighbour *interpolation cell* inside the liquid, and the pressure correction is determined by an interpolation between these two cells[3]:

$$p_{i,j} = (1-\eta)p_I + \eta\, p_S,$$
$$\eta = \frac{d}{d_c}, \tag{4.15}$$

where d is the distance from the interpolating cell centre to the free surface and d_c is the distance between the surface and interpolating cell centres. p_I is the mean pressure in the interpolating cell and p_S is the mean pressure in the surface cell. This correction is included in the iterative solution of the flow equations.

Stability considerations

Analysis shows that to avoid movement of parts of the same fluid element across more than one cell wall during a time step the Courant condition (also

[3]There is an error in this formula in the paper of Hirt and Nichols where they define $\eta = d_c/d$. With this definition the correction will not work

called the Courant-Friedrichs-Levy or CFL condition)

$$\delta t < \min\left\{\frac{\delta x_i}{|u_{i,j}|}, \frac{\delta y_j}{|v_{i,j}|}\right\} \tag{4.16}$$

must be fulfilled. It is common to apply a stronger constraint than this condition given by

$$\frac{1}{c} = \frac{1}{\delta t}\min\left\{\frac{\delta x_i}{|u_{i,j}|}, \frac{\delta y_j}{|v_{i,j}|}\right\} \geq \frac{1}{\gamma}; \quad \gamma < 1, \tag{4.17}$$

where c is known as the Courant number. To avoid diffusion through more then one cell during a time step the following condition should also be fulfilled (based on the discretized momentum equation):

$$\nu\delta t < \frac{1}{2}\frac{\delta x_i^2 \delta y_j^2}{\delta x_i^2 + \delta y_j^2}. \tag{4.18}$$

These criteria apply to all two-phase models.

Also, for stability and to avoid too much steepening of the surface an appropriate value of γ must be chosen in the discretization in SOLA-VOF.

Properties of Hirt and Nichols VOF

Advection Flux correction methods must be implemented if mass conservation is to be achieved with the donor-acceptor model. And due to the piecewise horizontal or vertical surface applied in the model special discretization methods must be applied to the advection equation (4.8) to achieve sufficient accuracy and stability in the advection. So compared to the MAC method the negative side effects of the less time consuming VOF surface advection is the loss of accuracy and stability. However, adjustments to the VOF method may help to improve these defects. An improved VOF advection method developed by Johansen [31] is described in the following section.

NS solver Adjustments have been made to the original SOLA algorithm. The momentum equations are not applied on divergence form, thereby improving discretization accuracy, but loosing conservation properties. Limited compressibility is introduced, which facilitates the implementation of the solver. Also, improved discretization methods are introduced which control the balance between accuracy and stability of the solver, a conflict which is an issue in all the two-phase models. So this technique is an improvement to the SOLA. And a pressure correction model is introduced which decreases the error due to the pressure jump across the surface.

Surface tension forces A diffuse surface tension force model such as the CSF method [10] may also be included in Hirt and Nichols SOLA-VOF. The CSF is discussed in the next section.

Hirt and Nichols VOF model combined with the improved SOLA-VOF solver are more applicable to the current problem than the MAC/SOLA method. However, the diffuse interface in the VOF method may lead to problems with numerical diffusion of the interface, causing unphysical effects such as uncontrolled droplet formation. The poor surface definition inhibits proper modelling of dynamics such as surface folding and bubble formation, both effects which may occur in the meniscus dynamics.

4.3 Developments

The methods of Welch et al [71] and Hirt and Nichols [26] respectively introduce the basics in Lagrangian Eulerian and Eulerian multiphase modelling methods. A lot of work has been put into development of multiphase modelling in recent years, and a brief discussion on the application of some of these developments to our problem of meniscus modelling is given here. The papers considered are by topic:

Interface reconstruction; Zaleski et al [78], Rudman [55] [56] with *FCT* and *FGVT*, Gueyffier et al [24], Youngs et al [77] with *Youngs method*, Ashgriz et al [3] with *FLAIR*, Lafaurie et al [39] with *SURFER*, Rider et al [52] and Unverdi et al [69].

Advection methods; Welch and Harlow [71] with *MAC*, Hirt and Nichols [26] with *VOF*, Noh and Woodward [46] with *SLIC*, Johansen [31], Ashgriz et al [3], Sussman et al [63], Lafaurie et al [39] , Rider et al [52], Rudman [55] and Gueyffier et al [24]

Flux correction; Hirt and Nichols [26], Zaleski et al [78], S. T. Johansen [32], Rudman [55] [56] and Popinet et al [48] with *MOT*

Surface tension force calculation; Brackbill et al [10] with *CSF*, Rieber et al [54], Popinet and Zaleski [48] and Rudman [56].

Mass and momentum conservation ; more or less all of the above

4.3.1 Interface reconstruction

All applied fluid properties in the homogeneous multiphase flow model are volume averages. Some form of discrete surface interface reconstruction is

therefore necessary to calculate the volume fraction change due to interface advection. Either a stepwise non-physical interface as an analogy to the algebraic method that is used (VOF [26]), a piecewise linear reconstruction of the interface as in Youngs method [77][4], or a higher order interface reconstruction as the cubic spline interpolation applied in the MOT of Popinet and Zaleski [49] may be applied. The interface reconstruction may also be applied in calculating the effect of surface tension forces.

The advection techniques will here be grouped according to the type of surface reconstruction that is applied. Algebraic methods where the surface representation is parallel to one of the grid line directions are defined as *zero order advection methods*. Piecewise linear models are defined as *first order advection methods*. And the remaining methods are the *higher order advection methods*.

In the higher order methods some sort of surface marking is normally used. In the MAC model, marker particles are distributed over the whole fluid domain. Thus a surface reconstruction can be performed by interpolation once the surface markers are ordered. For the cubic spline surface reconstruction in the MOT, marker particles are only applied on the interface. So the method requires less computer memory and CPU time than the MAC. It does however require more memory than the Eulerian VOF methods. The advantage of the spline reconstruction with marker particles is that the accuracy is a lot better than for other reconstruction techniques. This facilitates accuracy in computation of surface tension forces (see 6). Flux correction is however more difficult for the higher order surface interpolation methods.

Of the zero order methods a variation on the Donor-Acceptor VOF model, SLIC, was developed by Noh and Woodward in 1975 [46]. This model uses the same basic ideas as in Hirt and Nichols VOF (figure 4.4(d)), but here the surface reconstruction is dependent on the sweep direction (see figure 4.4(b) and (c)), so it is a type of split operator method.

Youngs method [77], is generally referred to as the basic PLIC model. The interface reconstruction is piecewise linear, linear for each cell (see figure 4.4(e)). In another first order method, FLAIR [3], the reconstruction is made over two cells, where the linear segments are bisected by the cell face they intersect, as shown in figure 4.4(f). The surface reconstruction applied in FLAIR improves on the accuracy of the phase flux calculation compared to that of Youngs method.

[4]This type of methods are also known as PLIC methods, for *Piecewise Linear Interface Construction*.

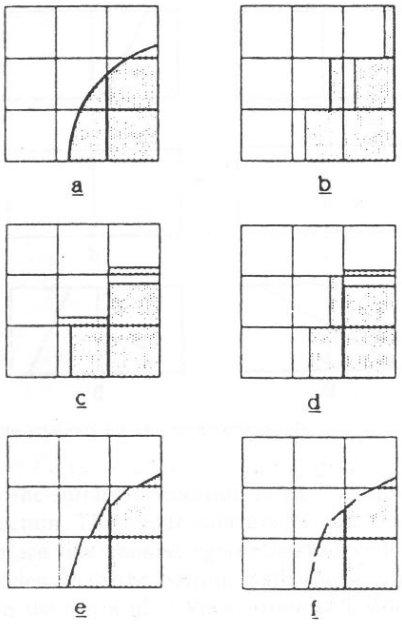

Figure 4.4: Different types of interface reconstruction. (a) actual interface, (b) and (c) SLIC [46], (d) VOF donor acceptor [26], (e) PLIC [77] and (f) FLAIR reconstruction [3]. The figure is from [3]

4.3.2 Advection

The methods used for advecting the interface between two regions of different phase are closely linked to the type of surface representation applied, as described above. Examples of advection techniques are given here for the different types of surface reconstruction.

'Zero order' or algebraic methods

In these methods algebraic expressions involving the volume fraction determine the surface advection. Therefore graphical imaging of the method (as in figure 4.4(d) for Hirt and Nichols VOF) does not picture the physical surface. The physical surface may be constructed by interpolating from the volume fraction field, but it is not directly applied in the the advection calculations.

An important problem with all multiphase flow models is error in mass conservation due to imbalance in phase fluxes. Several contributions have been made to solve this problem for the VOF method.

SLIC The SLIC method [46] solves the problem of advection by using a split operator method where the surface is reconstructed differently for each

flux direction, independent of the mean surface orientation (see figure 4.4(b) and (c)). This makes the advection algorithm of SLIC somewhat simpler than for Hirt and Nichols VOF, and the split operator technique hinders unphysical cell volume fractions.

Johansen's VOF [31] method applies an improved flux correction algorithm. The phase flux across a computational cell face is here expressed by an algorithm using the volume fraction of the two closest upwind cells and the downwind cell. The technique is a variation of the donor-acceptor method, but here the mean surface orientation is not applied, again simplifying the calculations. With this technique the control of phase conservation is improved. For cases of volume fraction larger than 1 or smaller than 0 a correction is applied[5] This method is shown by Johansen to produce good phase conservation.

SURFER A third algebraic advection method, SURFER, is presented by Lafaurie et al [39]. As explained earlier, using upwinding improves stability but also leads to numerical diffusion. Downwinding, on the other hand, causes steepening (or sharpening) of the surface, but leads to instability. In this model a combined differencing scheme is used, as in the original VOF (4.2). In this method the relative upwinding/downwinding is determined by the angle between the direction of fluxing and the surface normal. So as in the original VOF, the mean surface orientation is calculated. For small angles mostly downwinding is used, while for large angles mostly upwinding is applied. This keeps a steep surface steep and a more horizontal surface more horizontal. A flux correction algorithm is also implemented in SURFER, which takes into account symmetry properties between the two phases. In the original VOF method a correction is used so that fluxing of gas over two cell faces in one time step is avoided. By the symmetry of SURFER this correction is also made for fluxed liquid phase.

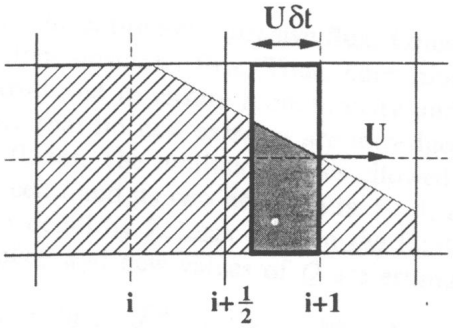

Figure 4.5: Advection in FCT

[5]Operator splitting as for SLIC will also solve this problem, but operator splitting generally leads to significant errors in phase conservation.

FCT Finally Rudman [55] presents a modified VOF method where the volume fraction is calculated on a subgrid half the size of the velocity grid (shown in figure 4.5). This improves consistency in mass and momentum advection. A flux correction algorithm FCT (*Flux Corrected Transport*) is again applied to improve conservation properties. This algorithm works in much the same way as the relaxation method. A low order flux term is first calculated and then corrected by a higher order term (the *anti-diffusive flux*). It is however the use of the subgrid for the volume fraction that is the most important contribution to phase conservation. The application of the subgrid and iterative flux correction results in a more CPU time consuming model than the other VOF methods.

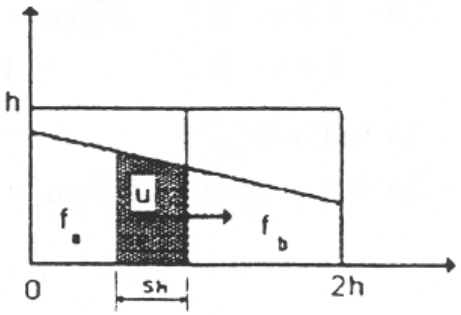

Figure 4.6: Flux calculation method in FLAIR. Shaded region indicates fluxed area.

First order methods

In these methods piecewise linear reconstruction of the surface is applied. The reconstructed surface subsequently gives the advected phase volumes across the computational cell face, as shown in figure 4.6. These methods are also known as piecewise linear interface construction (PLIC) methods.

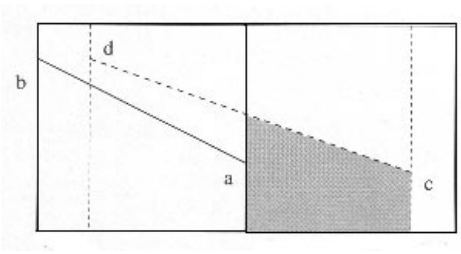

Figure 4.7: Advection method of Gueyffier et al

Youngs method The original method in this group was developed by Youngs et al [77]. In this method a piecewise linear reconstruction is determined by interpolation on a 9 cell scheme. An example of the reconstructed surface is shown in figure 4.4(e). The method uses a uniform and regular grid. And the advection is performed by operator splitting.

FLAIR The FLAIR algorithm [3] is basically a modification of Youngs method. Instead of reconstructing the surface linearly in each cell the re-

construction is linear across cell faces, as in figures 4.4(f) and 4.6. In this way a more correct slope for the surface at the cell face is found and the flux calculation is thereby improved.

Gueyffier Gueyffier [24] et al also present a variation on Youngs method. Here reconstruction of the surface is performed in the same manner as in the Youngs model. However, the volume fraction flux is now determined by advecting the sides of the element of 'liquid phase' with the mean cell face velocities. Thereby the original geometrical phase element is deformed in accordance with the velocity gradient of the flow (see figure 4.7). The result is an improved advection model, without much extra work involved (since algebraic relations determine the deformation). This idea is somewhat similar to the use of marker particles in the surface advection (see below), although surface reconstruction is not as accurate as for the higher order marker chain methods.

Advection tests

A comparisons of the advection properties of some of the models presented here is made by Rudman [55]. In figure 4.8 a test is shown for an initial 2D 'spherical' free surface placed in a homogeneous fluid with a vorticity field. The flow is given by the stream function

$$\Psi = \frac{3}{\pi} \sin\left(\frac{\pi}{3}x\right) \sin\left(\frac{\pi}{3}y\right). \tag{4.19}$$

All the compared methods except Youngs are algebraic (or zero order).

Rudman's FCT-VOF [55] gives nearly as good results as Youngs model. Youngs model does however require more calculation, since the surface needs to be linearly reconstructed for each iteration. The other algebraic models give much poorer results.

Higher order methods

For the MAC method [71] surface reconstruction is only needed for calculation of the effects of surface tension. In this case the advection is determined purely by Lagrangian advection of the markers.

For surface *marker chain* methods (see figure 4.9), such as the Method of Tensions (MOT), surface interpolation is applied both in volume fraction calculation and for the calculation of surface tension forces. In MOT the surface advection is calculated by marker advection followed by surface reconstruction. Subsequently the new phase field may be found. The additional work needed for surface

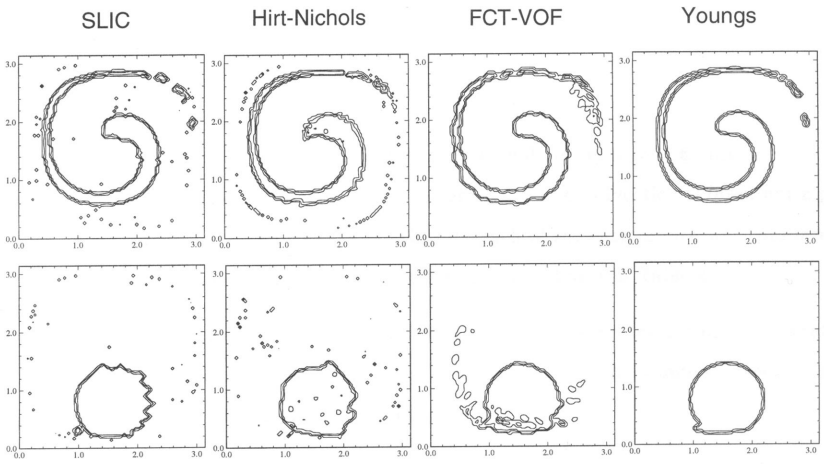

Figure 4.8: Comparison of standard advection test in a vortex field after 2000 steps forward (top) and after another 2000 steps backward (bottom).

reconstruction in MOT is generally negligible compared to the work needed for advection of the marker field in the MAC method. Therefore MOT is a preferable technique, even when there is no need for surface tension calculations.

The issues of stability and phase conservation in discretization of advection for the first order VOF methods also apply to some extent in the higher order methods. In this case the type of velocity interpolation for the marker particles influences stability and conservation. This factor needs consideration, especially in systems with high density ratios.

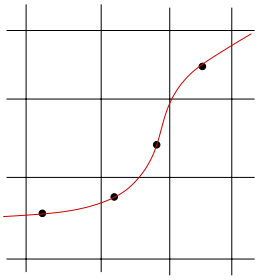

Figure 4.9: Reconstructed surface on computational grid with massless marker particles: a marker chain.

In the higher order methods flux correction may not be implemented algebraically. Some tests have been performed on flux correction using different types of cubic splines for surface reconstruction and subsequent redistribution of marker particles (see chapter 6). The results are promising.

4.3.3 Surface tension forces

In order to calculate pressure boundary conditions at the interface between two phases the effects of surface tension must be included. The general surface stress boundary condition at an interface can be expressed (from [40])

$$(p_1 - p_2 + \sigma\kappa)\,\mathbf{n} = (\boldsymbol{\tau}_1 - \boldsymbol{\tau}_2)\cdot\mathbf{n} + \nabla\sigma. \tag{4.20}$$

Here σ is the surface tension coefficient , p_i is the interface pressure in fluid i, $\boldsymbol{\tau}_i$ is the viscous stress tensor in fluid i, $\mathbf{n}$ is the surface unit normal and κ is the surface curvature. The surface stress boundary condition represents a balance of forces per unit area of the interface.

For the MAC model [71] and subsequent markers particle models, reconstruction of the interface can be interpolated between surface markers, from which the surface curvature and unit normal can be calculated. For the lower order methods volume fraction interpolation must be applied to find the curvature and surface normal.

Error sources and spurious currents Inaccuracy in the calculation of surface tension forces can be caused by several factors. Both the order of the reconstruction method and the applied surface tension force model influence accuracy. The higher the order of reconstruction the more accurately the surface tension forces may be calculated (depending on which surface tension model is applied). And the less diffuse the surface is made in the calculation of surface tension forces the less the surface tension forces are spread. The distribution of the surface tension forces greatly effects the stability of the flow, especially in flows with large density ratios. Also, the discretization of the NS equations leads to error in the numerical solution where the size of the error depends on the order and type of the applied discretisation. Error in the calculation of pressure due to incorrect modelling of the pressure jump across the surface is also an important factor. And finally the quality of surface definition depends on the ratio between grid size and radius of curvature. The larger the ratio the poorer the definition.

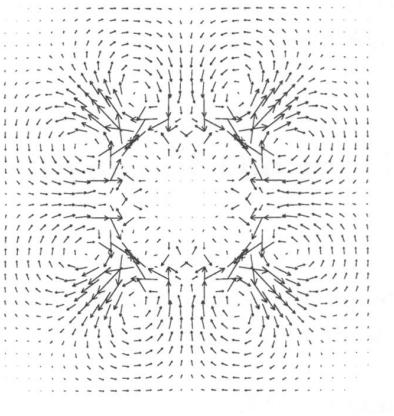

Figure 4.10: Spurious currents for bubble simulation by Hirt and Nichols VOF using the CSF model. Calculated by Popinet and Zaleski[49]

All the factors described above may contribute to the creation of artificial currents known as *spurious currents*, which normally develop into vortexes. These currents are driven by the energy created by the imbalance in the modelled surface tension forces. For a static surface situation as in figure 4.10 the erroneous representation of the acting surface tension forces leads to diverging flow, as the spurious currents will increase without bound. Therefore

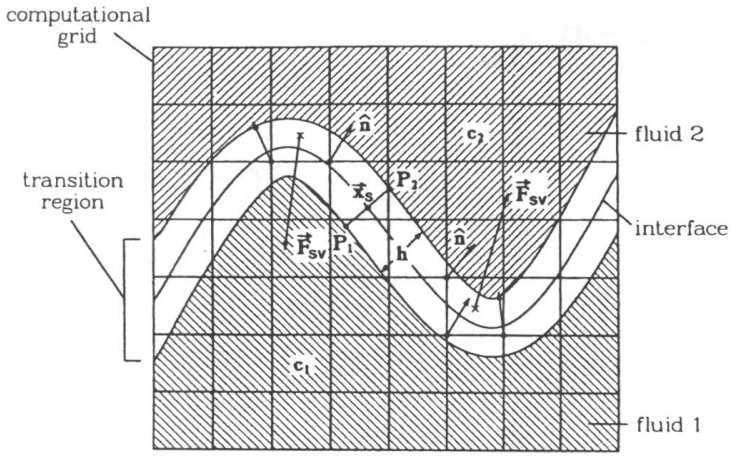

Figure 4.11: Continuous Surface Force model. Interface treatment

these methods should only be applied where no steady state configuration is possible, or the calculation should be interrupted when a steady state situation is reached. In the case of a time dependent flow, the spurious currents may lead to irregular behaviour like unphysical surface waves or surface folding. The dimensions of these waves will be characteristically of the same order as the grid size, since they are related to error in the surface tension force field, which again is linked to the grid size. Therefore the characteristic dimension of the grid should be smaller than the characteristic dimension of the surface effects one wishes to model.

Continuous surface force (CSF) model

The basic surface tension force model is the CSF model, developed by Brackbill et al in 1992 [10]. This model calculates a surface force distribution centered at the interface between two fluids. The model assumes the fluids to be inviscid and incompressible, and the surface tension coefficient is assumed constant. Thus the surface boundary condition becomes

$$p_2 - p_1 = \sigma\kappa. \tag{4.21}$$

In the CSF, the surface tension term in the surface boundary condition is reformulated as a volume force, which subsequently is included in the continuous volume averaged momentum equation. This reformulation is performed by applying the colour function c [10], representing the surface discontinuity, convolved with a distribution $\mathcal{L}$ (known as the *convolution kernel*);

$$\tilde{c} = \frac{1}{V}\int_V c(\mathbf{x}')\mathcal{L}(\mathbf{x}' - \mathbf{x})d\mathbf{x}' \tag{4.22}$$

which results in a continuous smoothed colour function $\tilde{c}$ (see figure 4.11). $\tilde{c}$ is then nonconstant in a transitional region across the surface, as shown in figure 4.11. A natural choice of the color function is the phase function, defined earlier (4.2). The smoothed colour function is subsequently applied in the calculation of the surface tension volume force per unit volume $\mathbf{F}_{SV}$:

$$\sigma\kappa\mathbf{n} \rightarrow \sigma\kappa\frac{\Delta\tilde{c}}{[c]} = \mathbf{F}_{SV}, \tag{4.23}$$

where $[c]$ is the jump in the colour function c across the interface. This volume force can subsequently be included in the balance of volume forces, i.e. the momentum equation:

$$\rho\frac{d\mathbf{u}}{dt} = \nabla p + \mathbf{F}_{SV} + \rho\mathbf{g} \tag{4.24}$$

The mean curvature κ may also be found from $\tilde{c}$ (see [10]).

Conservative CSF

In SURFER [39] a modified version of the CSF model is applied. In this case a surface tension volume force is applied on divergence form (i.e. as a potential force), thus improving the conservation properties of the momentum equation. The momentum equation then becomes

$$\begin{gathered}\frac{\partial\rho\mathbf{u}}{\partial t} = \\ -\nabla p - \nabla\cdot(\rho\mathbf{\Pi} - \mu\mathbf{S} + \mathbf{T}), \\ \mathbf{\Pi} = \mathbf{uu}, \\ \mathbf{T} = \sigma(\mathbf{I} - \mathbf{nn}) \mid \nabla\tilde{c} \mid, \\ \mathbf{n} = \frac{\nabla\tilde{c}}{\mid \nabla\tilde{c} \mid}, \\ \mathbf{S} = \frac{\partial u_j}{\partial x_i} + \frac{\partial u_i}{\partial x_j}.\end{gathered} \tag{4.25}$$

Here viscous forces are included, i.e. the fluid is not assumed ideal, as in the original CSF, so the corresponding surface stress boundary condition is given by equation 4.20. But the balance of volume forces in the momentum equation is still valid. The improved conservation properties lead to a reduction in spurious currents compared to the original CSF.

Method of tensions (MOT)

In the 2D Method of Tensions Popinet and Zaleski [49] also use the idea of surface tension forces implemented as a volume force. The incompressible momentum equation is applied on the weak form

$$\frac{\partial \rho \mathbf{u}}{\partial t} + \nabla \cdot (\rho \mathbf{\Pi}) = -\nabla p - \nabla \cdot \mu \mathbf{S} + \sigma \kappa \delta_s \mathbf{n}. \quad (4.26)$$

δ_s is here the delta function across the interface. $\mathbf{\Pi}$ and $\mathbf{S}$ are as defined above. The surface tension term $\sigma \kappa \delta_s \mathbf{n}$ comes from the integral relation

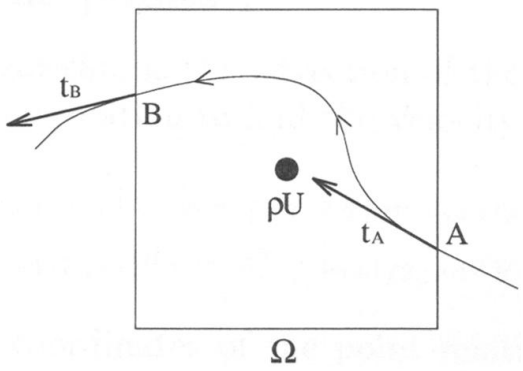

Figure 4.12: Surface reconstruction and tension calculation in MOT [49]

$$\int_A \sigma \kappa \mathbf{n} \, dA = \int_V \sigma \kappa \mathbf{n} \, \delta[\mathbf{n}(\mathbf{x}_S) \cdot (\mathbf{x} - \mathbf{x}_S)] \, dV, \quad (4.27)$$

where the last integrand is the surface tension volume force term for zero interface width, defined in the weak sense (as shown in [10]). Here $\mathbf{x}_S$ maps the interface in 3D. So the surface delta function δ_s corresponds to the distribution kernel $\mathcal{L}$ used is the CSF model when the transitional region goes to zero. Again viscous forces are included in the momentum equation, as in SURFER.

In MOT surface marker particles are applied to track the surface as described earlier. Reconstruction of the surface is performed by interpolation between the markers using cubic splines (see figure 4.9). The surface tension forces are found by applying the curvature of the reconstructed surface. It can be shown by Stokes theorem and the Frenet-Serret formulae that for a computational volume Ω:

$$\int_\Omega \sigma \kappa \delta_S \mathbf{n} dV = \sigma(\mathbf{t}_B - \mathbf{t}_A), \quad (4.28)$$

where $\mathbf{t}_A$ and $\mathbf{t}_B$ are the surface unit tangent vectors (see figure 4.12) at the intersection between the interface and the boundaries of the computational volume. This relation is applied in the finite volume discretisation of the momentum equation (4.26).

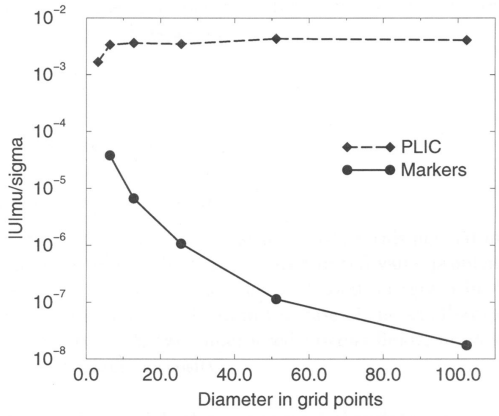

Figure 4.13: Amplitude of spurious currents versus spatial resolution for PLIC method [77] and the method of tensions [49]

In figure 4.13 a comparison between MOT and a PLIC/CSF method is shown. For the Method of Tensions the nondimensional amplitude of the spurious currents ($|U|\mu/\sigma$) decreases greatly as a function of grid size over curvature while for the PLIC model there is no marked change in the amplitude of spurious currents. This effect is due to the direct link between physical surface geometry and surface tension force calculation in MOT (which increases in accuracy as grid size/curvature ratio decreases). For the lower order advection methods this effect can not be achieved.

A method of pressure correction, similar to the one used in Hirt and Nichols VOF, is also included in the MOT (see [49]).

Rudman FGVT

Rudmans FGVT model [56] also includes a modified CSF method. A point is here made that the *smoothing length* needs to be large compared to grid size in order to obtain a smooth convolved colour function field, facilitating stability and convergence of the solution. A cubic B-spline kernel, as applied in the smoothed particle hydrodynamics (SPH) method of Monaghan [30], is applied in the convolution. With r as the normal distance (distance in normal direction) from the surface, the kernel is given by

$$K(r,h) = \frac{1}{h^2}\begin{cases} \frac{40}{7\pi}\left(1 - 6\left(\frac{r}{h}\right)^2 + 6\left(\frac{r}{h}\right)^3\right) & \text{if} \frac{r}{h} < \frac{1}{2} \\ \frac{80}{7\pi}\left(1 - \frac{r}{h}\right)^3 & \text{if} \frac{r}{h} < 1 \\ 0 & \text{otherwise} \end{cases} \tag{4.29}$$

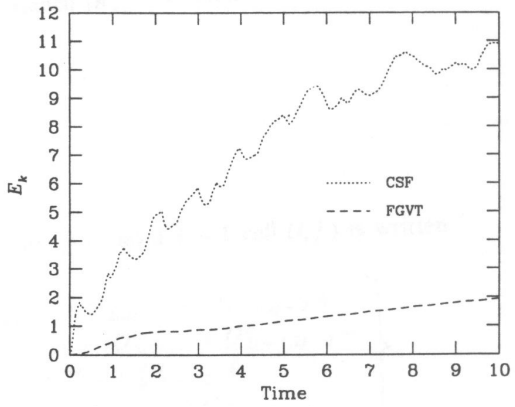

Figure 4.14: Growth of kinetic energy of parasitic currents vs time for CSF and FGVT surface tension models.

The smoothing length h is arbitrary and can be adapted to the specific grid. The normalized version of this kernel can be used to find the the interface distribution function (or convolution kernel) and subsequently the surface unit normal and the curvature. From here one proceeds as in the ordinary CSF model [10]. Again Rudman applies a subgrid for the volume fraction calculations, as in the FCT.

A comparison between the original CSF model and the FGVT model is shown in figure 4.14 for a static cylindrical drop. As can be seen, the FGVT model gives results far superior to that of the original CSF model. The amount of work per iteration is larger for the FGVT than for the CSF, but to achieve a stable result the number of iterations per time step is much larger for the CSF. So the FGVT is generally preferable.

4.3.4 Wetting

RIPPLE

A method for modelling the contact angle of a free surface at a solid physical boundary is introduced in the *RIPPLE* model [36]. The method is expressed graphically in figure 4.15. The vectors at the grid points ($\hat{n}_{i+1/2,j+1/2}$, $\hat{n}_{i+1/2,j-1/2}$, etc) indicate the normal to the surface of the phase containing the points (wall or fluid phase in the figure). The equilibrium angle θ_{eq} and the equilibrium surface normal $\hat{n}$, corresponding to the imposed boundary condition, are also indicated. If the fluid surface normal, interpolated from $\hat{n}_{i-1/2,j+1/2}$ and $\hat{n}_{i-1/2,j-1/2}$, differs from the set boundary condition, a force is imposed on the free surface pulling it towards the equilibrium configura-

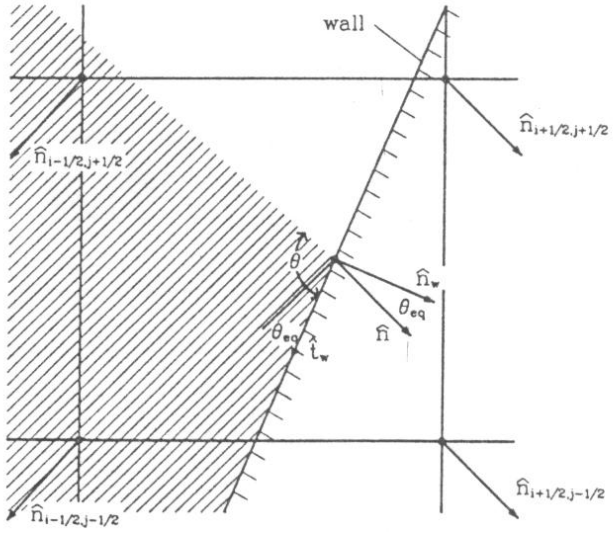

Figure 4.15: Wetting angle in RIPPLE

tion set by the boundary conditions. The forces pulling on the surface act a distance of two cells out from the wall.

MOT

In the Method of Tensions the wetting angle can be implemented directly as a boundary condition on the spline function (see appendix E). Computing time is therefore saved compared to RIPPLE. Also the surface behaviour close to the wall is more physical than in the RIPPLE model due to the resulting smoothness of the interpolated spline surface.

4.4 Selected model - The Method of Tensions

The Method of Tension (MOT) is chosen for modelling of the meniscus dynamics. The model has both advantages and disadvantages compared to the other models considered, but in total it seems to be the best alternative. The main reasons for choosing this model are the surface smoothness, control of spurious currents, accuracy of and simplicity in implementing wetting boundary conditions and reasonable CPU time.

MOT can simulate both surface wave propagation and folding with good accuracy. Uncontrolled surface breakup, which might occur in the lower order methods, will not occur, since the surface is always discretely defined by the surface marker particles. The method will also function on a relatively

coarse grid, due to the discretely defined surface, although accuracy in surface advection will be poor. Again the lower order methods are too diffuse to give useful results on too coarse a grid.

A pressure correction algorithm is included in MOT, facilitating convergence at the surface boundary, similar to the correction applied in Hirt and Nichols VOF. Due to the discretely defined surface this correction works better in MOT. Staggered grid is also applied to avoid pressure checkerboarding.

Generally conservation of phases is not very accurate with MOT. But flux correction is not necessary to reduce the effect of spurious currents in this model, due to the consistency of the surface tension force calculations by application of 4.28, which ensures fulfillment of Newton 3. This balance of surface tension forces is not ensured in the other surface tension models (as an example, see figure 4.13). With the simple marker advection and no flux correction the CPU time is also significantly reduced compared to techniques applying iterative flux correction.

Memory requirements for MOT are comparable to those of Hirt and Nichols VOF. Additional memory is needed for storage of marker positions and surface spline and the staggered phase fields needed for surface force calculations. So the increase in memory requirement compared to the lower order methods is not significant.

Although simple bilinear interpolation is applied for marker velocities in the original MOT, discretization of the phase conservation, or advection equation (4.8), may be controlled by the type of interpolation applied for the marker particle velocities in MOT, as is done for the lower order methods. Thereby the fine balancing between stability and accuracy, which is an important issue for the large density ratio system of liquid metal and gas, can be taken care of.

Variation in the surface tension coefficient (as in the conservative CSF) is not included in MOT. A constant surface tension coefficient is a rough approximation, but experimental measurements have shown that for molten metal the surface tension coefficient does not vary significantly with temperature and is also not significantly altered by surface oxide formation. The change in bulk metal properties due to solidification is more important to meniscus dynamics.

The importance of distribution of surface tension forces through application of a large smoothing length, as in the FGVT, or by applying a broad convolution kernel as in the CSF, may also be accounted for in MOT. By the original MOT the calculated surface tension forces are only nonzero in computational cells intersected by the free surface. However, these forces may also be spread into neighbour cells so as to facilitate stability of the surface. This is done in our adaption of the method (see chapter 6).

The SIMPLE algorithm will be applied together with the multigrid technique in the Navier-Stokes solver. These methods are described in chapter 8.

Chapter 5

Two phase meniscus modelling

An analysis of the averaged equations

In general, at least three phases are present in the meniscus system; Liquid metal, aluminium oxide on the melt surface (when air is applied as the slip gas), and gas. It has been shown [15] that surface behaviour has a strong dependence on the surface oxide layer. Measurements have also shown that the surface tension coefficient is not influenced greatly by the oxide layer (see [64]). Subsequently the surface tension forces are not altered by the oxide layer, but the oxide constrains the meniscus movement, since the dynamic properties of the oxide phase influence the dynamics of the system. In future work a model for the oxide formation and rheology should be included. However, here the model is restricted to a two phase model describing the system of the gas pocket and aluminium melt. It is assumed to be a system of two distinct separate phases with a free surface boundary without any diffusion or reaction between the two phases.

Several different approaches are taken to modelling flow in this kind of system. The simplest method is to consider the two phase fluid as a homogeneous mixture in each computational cell, also known as the *homogeneous model*. The most complex is to consider each phase separately with a set of equations for each phase, a *two-fluid model*. Several modelling schemes exist which lie somewhere between these two in complexity (see [13], [76] and [74]). The model applied here, which is based on the Method of Tensions of Popinet and Zalesky [49], is among this group. It is basically a homogeneous model, but with corrections to flux and pressure terms.

An analysis of the volume averaged flow and internal energy equations is performed in this chapter, pointing out the problem areas of the method. Incompressibility is assumed and each phase is assumed homogeneous.

The validity of some of the assumptions made here are discussed further in appendix D.

5.1 Governing equations

In a two phase system with an interfacial boundary the condition of continuity is not fulfilled. Several variables may be discontinuous over the interface, such as density, viscosity, velocity, heat capacity, etc. If the heat and fluid flow equations are to be solved without defining separate computational domains for the two phases, then some form of averaging or smoothing of the dependent variables must be applied. Smoothing can be performed by averaging variables over finite regions of volume.

The general condition of validity of volume averaging in a system with disperse flow was shown by Whitaker [72] to be:

$$\begin{gathered}\text{characteristic dimension of phases or pores} \ll \\ \text{characteristic dimension of averaging volume} \ll \\ \text{characteristic dimension of physical system.}\end{gathered} \tag{5.1}$$

In the case of the modelling of two unmixed separate phases, as in the gas pocket / molten aluminium system, this condition can not be fulfilled, since the dimension of both phases are of the same order as the dimension of the physical system . The effect of volume averaging of this system should therefore be properly analyzed to assess its applicability.

Two types of volume averaging are generally used for multiphase flow[61], extensive averages and intrinsic averages. For the definitions of the averages the colour function C_k is used, which is defined by

$$C_k(x,y,z) = \begin{cases} 1, \, (x,y,z) \, \text{inside phase k} \\ 0, \, (x,y,z) \, \text{not inside phase k} \end{cases} \tag{5.2}$$

Three conceptual coordinate spaces are applied in the system of volume averaging used here. The coordinate field spanning the space of exact physical values is denoted by (x,y,z), the field of averages is denoted by (X,Y,Z) and the field spanning a computational volume is denoted (α,β,γ). The averaging volume Ω centered on (X,Y,Z) may then be defined as

$$\Omega = \{(\alpha,\beta,\gamma); \alpha \, \epsilon \, [X-\delta x, X+\delta x], \beta \, \epsilon \, [X-\delta y, X+\delta y], \gamma \, \epsilon \, [Z-\delta z, Z+\delta z]\} \tag{5.3}$$

for small increments δx, δy and δz. So the averaging volume may be a computational cell volume, or any other fixed geometric volume in the computational domain. The phase volume Ω_k is defined:

$$\Omega_k = \{\Omega; C_k = 1\}. \tag{5.4}$$

Based on the definition of the averaging volumes above the volume averages may then be defined as follows:
The *extensive average* of variable ψ in phase k is

$$< \psi_k > (X, Y, Z) = \frac{1}{V} \int_{\Omega_k} \psi \, dV, \tag{5.5}$$

and the *intrinsic average* is

$$^i< \psi_k > (X, Y, Z) = \frac{1}{V_k} \int_{\Omega_k} \psi \, dV. \tag{5.6}$$

Here Ω_k is the section of the averaging volume containing phase k. The volume of Ω is V, defined as

$$V(X, Y, Z) = \int_{\Omega} dV \tag{5.7}$$

Correspondingly, V_k is the volume of Ω_k. Then by (5.5) and (5.6):

$$< \psi_k >= \alpha_k \, ^i< \psi_k >, \tag{5.8}$$

where the volume fraction α_k of phase k is defined as

$$\alpha_k = \frac{V_k}{V}. \tag{5.9}$$

The mean values thus defined are continuous in the whole computational domain (X, Y, Z). By Soo [61], volume averaging should only be applied to quantities per unit volume or area, such as density, momentum per unit volume, energy per unit volume and gradients of stresses and fluxes. Only then will the mean values have physically meaningful properties. With a constant density specific values, i.e. properties per kg, may also be averaged. In our case there is however a large jump in density at the phase interface, so such averaging may not be applied.

5.1.1 Equation of continuity

The equation for conservation of mass in a volume Ω is derived based on the mean values defined in 5.5 and 5.6. The continuity equation within a continuous phase k is

$$\frac{\partial \rho_k}{\partial t} + \nabla \cdot \rho_k \vec{u}_k = 0. \tag{5.10}$$

Two theorems are applied in the further analysis, both derived from Reynolds transport theorem. Whitaker's averaging theorem [72] states that for an averaging volume containing phase interfaces the volume average of the derivative of ψ in phase k with respect to time can be expressed as

$$< \frac{\partial \psi_k}{\partial t} >= \frac{\partial}{\partial t} < \psi_k > -\frac{1}{V} \int_{\delta\Omega_k} \psi_k \vec{u}_s \cdot \vec{n}_k \, dA, \tag{5.11}$$

where $\vec{u}_s$ is the velocity of the boundary $\delta\Omega_k$ of phase k with outer unit normal $\vec{n}_k$.
And Slattery's averaging theorem [60] states that for a scalar field ψ:

$$< \nabla \psi_k >= \nabla < \psi_k > + \frac{1}{V} \int_{\delta\Omega_k} \psi_k \vec{n}_k \, dA. \tag{5.12}$$

Correspondingly, for a vector field $\vec{\xi}$

$$< \nabla \cdot \vec{\xi}_k >= \nabla \cdot < \vec{\xi}_k > + \frac{1}{V} \int_{\delta\Omega_k} \vec{\xi}_k \cdot \vec{n}_k \, dA. \tag{5.13}$$

Incompressibility and no mass transfer between the phases is assumed in our system of liquid metal and gas. Then by taking the volume average (5.5) and applying Whitaker's (5.11) and Slattery's (5.13) theorems, the mean continuity equation for each phase k becomes

$$< \frac{\partial \rho_k}{\partial t} > + < \nabla \cdot \rho_k \vec{u}_k >= \frac{\partial < \rho_k >}{\partial t} + \nabla \cdot < \rho_k \vec{u}_k >= 0. \tag{5.14}$$

In the framework of averages the intrinsic mean phase velocity ${}^i< \vec{u}_k >$ may be defined by the mean momentum per unit volume as

$${}^i< \vec{u}_k > \equiv \frac{{}^i< \rho_k \vec{u}_k >}{{}^i< \rho_k >} = \frac{< \rho_k \vec{u}_k >}{< \rho_k >}. \tag{5.15}$$

In the homogeneous model the intrinsic velocities are by approximation given the same value in the two phases

$$\begin{aligned} {}^i< \vec{u}_L > &\equiv < \vec{u} >, \\ {}^i< \vec{u}_G > &\equiv < \vec{u} > . \end{aligned} \tag{5.16}$$

$< \vec{u} >$ becomes the velocity field in the domain of volume averaged variables. Then adding the equations of continuity for the liquid and gas phases and applying (5.18), the continuity equation is

$$\frac{\partial \sum_k < \rho_k >}{\partial t} + \nabla \cdot \sum_k < \rho_k >< \vec{u} >= 0. \tag{5.17}$$

In our system of liquid (L) and gas (G) the volume average density $< \rho >$ may be expressed as:

$$< \rho >= \sum_{k=L,G} < \rho_k >= \sum_{k=L,G} {\alpha_k}^i < \rho_k >. \tag{5.18}$$

Where L denotes liquid phase and G denotes gas phase. This leads to the homogeneous model momentum equation:

$$\frac{\partial}{\partial t} < \rho > + \nabla \cdot < \rho >< \vec{u} >= 0. \tag{5.19}$$

Note that the homogeneous fluid corresponding to equation 5.19 will have pseudo-fluid properties and will differ in behaviour from that of a discontinuous two-fluid system in the vicinity of the interface.

Pseudo-fluid properties The stresses and fluxes in the homogeneous formulation are generally expressed as mean values $< \psi_k >= {\alpha_k}^i < \psi_k >$, thereby giving the fluid pseudo-fluid properties. The physical meanings of the mean terms are expressed through the volume averaged equations, such as the mean velocity in the mean continuity equation (5.19). Consequently a mean stress or flux value $< \psi_k >$ is not necessarily directly related to the corresponding physical property field ψ in the averaging volume in the region of the phase interface.

If the equation of continuity is to give a good approximation to the system's behaviour in the vicinity of a phase interface, the difference between the mean intrinsic phase velocities at the interface must be small (making (5.1.1) a good approximation). Restraints are placed on the solution process by this condition on the intrinsic velocities. Our system is particularly sensitive to this type of volume averaging due to the large density ratio between liquid metal and gas.

This aspect is discussed further in appendix D.

5.1.2 Equation of momentum

The momentum equation for a continuous phase k is

$$\frac{\partial \rho_k \vec{u_k}}{\partial t} + \nabla \cdot \rho_k \vec{u_k} \vec{u_k} = -\nabla p_k + \mu_k \left[\nabla \vec{u}_k + (\nabla \vec{u}_k)^T \right] + \vec{F_k}. \tag{5.20}$$

Temporal and convective terms

Taking the extensive average (5.5) of the left hand of the phase momentum equation and applying Whitaker's and Slattery's theorems we get:

$$< \frac{\partial \rho_k \vec{u_k}}{\partial t} > + < \nabla \cdot \rho_k \vec{u_k} \vec{u_k} > = \frac{\partial}{\partial t} < \rho_k \vec{u_k} > + \nabla \cdot < \rho_k \vec{u_k} \vec{u_k} > . \tag{5.21}$$

As in the continuity equation, the mean momentum per volume term can be rewritten using the definition of intrinsic velocity (5.15). From the second term the intrinsic mean product of velocities ${}^i< \vec{u}_k \vec{u}_k >$ is defined in a similar way:

$${}^i< \vec{u}_k \vec{u}_k > \equiv \frac{{}^i< \rho_k \vec{u}_k \vec{u}_k >}{{}^i< \rho_k >}, \tag{5.22}$$

Leading to the following relation:

$$< \frac{\partial \rho_k \vec{u_k}}{\partial t} > + < \nabla \cdot \rho_k \vec{u_k} \vec{u_k} > = \frac{\partial}{\partial t} < \rho_k > {}^i < \vec{u_k} > + \nabla \cdot < \rho_k > {}^i< \vec{u_k} \vec{u_k} >. \tag{5.23}$$

Again the use of common mean intrinsic velocities gives us a pseudo-fluid with properties differing from the physical system modelled in the region of the interface.

Local deviations The intrinsic product of velocities ${}^i< \vec{u}_k \vec{u}_k >$ can be related to the intrinsic velocity ${}^i< \vec{u}_k >$ by introducing local deviations from averages $\delta\psi_k$ within each averaging volume Ω centered on (X, Y, Z):

$$\psi_k(\alpha, \beta, \gamma) = < \psi_k > (X, Y, Z) + \delta\psi_k(\alpha, \beta, \gamma). \tag{5.24}$$

Then

$$\frac{1}{V} \int_{\Omega_k} \psi_k dV =$$

$$\frac{1}{V} \int_{\Omega_k} [< \psi_k > (X, Y, Z) + \delta\psi_k(\alpha, \beta, \gamma)] \, d\alpha \, d\beta \, d\gamma =$$

$$\frac{1}{V} \int_{\alpha=X-\delta x}^{\alpha=X+\delta x} \int_{\beta=Y-\delta y}^{\beta=Y+\delta y} \int_{\gamma=Z-\delta z}^{\gamma=Z+\delta z} C_k(\alpha, \beta, \gamma) \, [< \psi_k > (X, Y, Z) + \delta\psi_k(\alpha, \beta, \gamma)] \, d\alpha \, d\beta \, d\gamma =$$

$$< \psi_k > (X, Y, Z), \tag{5.25}$$

since

$$< \delta\psi_k >= 0 \tag{5.26}$$

by definition. It is assumed that the size of each volume Ω is chosen to be small enough for the deviations to be negligible[1], $\delta\psi_k \ll< \psi_k >$. The local deviations $\delta\psi_k$ within the averaging volume Ω will here depend on the way Ω is defined, i.e. they will depend on the grid size in the numerical simulations.

Subsequently the intrinsic product of velocities can be expressed

$$\begin{aligned} {}^i< \vec{u}_k\vec{u}_k >= {}^i< (< \vec{u}_k > +\delta\vec{u}_k)^2 > = \\ {}^i< \vec{u}_k >{}^i< \vec{u}_k > + {}^i< \delta\vec{u}_k\delta\vec{u}_k > + \frac{{}^i< \delta\rho_k\delta\vec{u}_k\delta\vec{u}_k >}{< \delta\rho_k >}. \end{aligned} \tag{5.27}$$

The volumetric Reynolds stress like terms formed by the averages of the product of the local deviations lead to the need of extra closure relations if they are to be included.

Cell wall averages In the Method of Tensions the phase interface is interpolated by a cubic spline function (see chapter 6). So the interface is at all times uniquely defined by the spline function. Consequently the exact volume fraction can be found on cell walls, and when incompressibility and homogeneous density is assumed the mean wall density $< \rho_k >_w$ given by the spline surface can be found for each phase and applied in the discretization. This improves on the accuracy of the homogeneous model.

Velocity averaging When cell walls are not intersected the density is constant and the only error in the mean convective term is due to local deviations in velocities (secant term on the right hand side in (5.27)). With a continuous velocity field and first order discretization (as in the method of finite volume discretization used here) the error in velocity at the cell wall will be of second order in δx, δy and δz (by the dimensions of the computational cell Ω, definition (5.3)), so the intrinsic product of the velocity deviations ${}^i< \delta\vec{u}_k\delta\vec{u}_k >$ will be of fourth order.

With the intrinsic velocity defined as in (5.15), it does not depend on the density in a homogeneous incompressible phase. However, when two phases are present, a common mean intrinsic velocity will depend on the density distribution (by 5.15). So even if a mean cell density is not applied directly in the interface flux term a mean density is applied by definition in the mean

[1] With the condition that a sufficiently fine grid is applied.

intrinsic velocity, resulting in error when the intrinsic phase velocities are different, and particularly in our case of large phase density ratio. This problem may be partly resolved by introducing a *semi-homogeneous* velocity scheme where differences in mean velocity are accounted for. A method that has been developed to deal with this problem is presented by Wörner et al [74]. Adaptive grid techniques as applied by Unverdi and Tryggvason [69] would also help to solve the problem. Here it will however be assumed that with a sufficiently small grid size differences in mean phase velocities are negligible. Then the assumption of approximately equal intrinsic phase velocities (5.1.1) can be applied, the intrinsic product of velocity deviations can be neglected and the sum of the individual mean momentum phase equations becomes

$$\sum_k \left[< \frac{\partial \rho_k \vec{u}_k}{\partial t} > + < \nabla \cdot \rho_k \vec{u}_k \vec{u}_k > \right] \approx$$
$$\frac{\partial}{\partial t} \sum_k < \rho_k > < \vec{u} > + \nabla \cdot \sum_k < \rho_k >< \vec{u} >< \vec{u} > . \qquad (5.28)$$

Reynolds stresses

For a complete analysis time averaging should also be considered in relation to the discretization in time. This will only be done for the convective term here. The error in time averaging of the other terms in the momentum equation is assumed to be of minor importance.

According to Whitaker [72] the time averaging should be performed after the volume averaging, since a priori time averaging eliminates the identity of the dynamic phases, making subsequent volume averaging unphysical. And according to Soo [61], the purpose of time averaging is to express averages of products, such as intrinsic product of velocities, in terms of products of averages and to account for high frequency fluctuations (i.e. turbulence). Note however that to express volume averages of products as products of volume averages, some form of local deviations must be introduced. Partly because the volume and time averaging are not commutative. So either local deviations must be applied separately before the time averaging, as above, or combined temporal and local deviations must be applied to express averages of products as products of averages. Here combined deviations will be applied in the analysis.

With a time increment Δt time averaging of a volume averaged phase variable $< \psi_k >$ can be defined as

$$^t \ll \psi_k \gg = \frac{1}{\Delta t} \int_{\Delta t} < \psi_k > \, dt. \qquad (5.29)$$

With this definition the time and volume averaged product of the convective term is:

$$^{t} \ll \rho_k \vec{u}_k \vec{u}_k \gg = \frac{1}{\Delta t} \int_{\Delta t} \frac{1}{V} \int_{\Omega_k} \rho_k \vec{u}_k \vec{u}_k \, dV \, dt. \tag{5.30}$$

Combined temporal and spacial deviations Local deviations in both time and space can be defined by

$$\psi_k = ^{t}\ll \psi_k \gg (X, Y, Z, \mathcal{T}) + \delta\psi_k(x, y, z, t), \tag{5.31}$$

so that

$$\begin{gathered} ^{t} \ll \rho_k \vec{u}_k \vec{u}_k \gg = \\ \frac{1}{\Delta t} \int_{\Delta t} \frac{1}{V} \int_{\Omega_k} (^{t}\ll \rho_k \gg + \delta\rho_k)(^{t}\ll \vec{u}_k \gg + \delta\vec{u}_k)(^{t}\ll \vec{u}_k \gg + \delta\vec{u}_k), dV \, dt = \\ ^{t} \ll \rho_k \gg ^{t}\!\!<\!\!^{i}\!\!< \vec{u}_k \gg ^{t}\!\!<\!\!^{i}\!\!< \vec{u}_k \gg + \mathcal{O}(\delta^2). \end{gathered} \tag{5.32}$$

The higher order terms consist of combined local and temporal deviations, producing Reynolds stress terms

$$^{t} \ll \rho_k \gg ^{t}\ll \delta\vec{u}_k \delta\vec{u}_k \gg . \tag{5.33}$$

For an incompressible homogeneous fluid this is the only term containing products of deviations that is nonzero. However, in the two-fluid regions the fluid is not homogeneous. So when a turbulence model is applied to model the Reynolds stresses the error is of third order in the homogeneous regions, but only of second order in the interface region.

Here a *Large Eddy Simulation* turbulence model is applied to model the combined temporal fluctuations and local deviations.

Large Eddy Simulation (LES) turbulence model

The LES model [18] attempts to model the effect of turbulence by its influence on the shear viscosity. The subgrid scale Reynolds stress tensor (by equations 5.32 and 5.33)

$$\overline{\overline{\tau}}^{s} = \sum_{k}^{t} \ll \rho_k \gg ^{t}\ll \delta\vec{u}_k \delta\vec{u}_k \gg \tag{5.34}$$

is attempted modelled by the assumption

$$\tau_{ij}^{s} - \frac{1}{3}\tau_k k \delta_{ij} \equiv \mu_t \left(\frac{\partial < u_i >}{\partial x_j} + \frac{\partial < u_j >}{\partial x_i}\right) = 2\mu_t \overline{S}_{ij}, \tag{5.35}$$

where μ_t is the eddy viscosity. By dimensional analysis the eddy viscosity may be derived as

$$\mu_t = C_S^2 \rho \Delta^2 (\overline{S_{ij}}\,\overline{S_{ij}})^{\frac{1}{2}}, \tag{5.36}$$

where Δ is the length scale of the filter kernel (see [18]), corresponding to the dimension of the averaging volume (5.1). C_S is a model parameter. Models for isotropic turbulence generally use a value in the region of $C_S \approx 0.2$.

Pressure term

By Slattery's theorem (5.12) the pressure term in phase k can be expressed

$$< \nabla p_k >= \nabla < p_k > + \frac{1}{V} \int_{\delta\Omega_k} p_k \vec{n}\, dA. \tag{5.37}$$

It can also be shown by Slattery's theorem that

$$\frac{1}{V} \int_{\delta\Omega_k} \vec{n}\, dA = -\nabla \alpha_k. \tag{5.38}$$

In the homogeneous model the concept of local deviations (5.24) the may be applied, and the pressure term becomes

$$< \nabla p_k >= -\alpha_k \nabla^i < p_k > + \frac{1}{V} \int_{\delta\Omega_k} \delta p_k \vec{n}\, dA. \tag{5.39}$$

Since pressure is a measure of an entity (force) per unit area this averaging produces a physical meaningful property (see [61]).

By the assumption of small local deviations the δp_k term is neglected. In the homogeneous model the intrinsic pressures are assumed to be equal in the same manner as was done for the intrinsic velocities:

$$\begin{aligned} {}^i< p_L > &\equiv < p >, \\ {}^i< p_G > &\equiv < p > . \end{aligned} \tag{5.40}$$

which together with (5.39) gives the pressure term in the homogeneous model. This assumption is however not necessarily applicable in our case of stratified flow with separate phases. Whitaker's conditions (5.1) are also not fulfilled in this case. The pressure jump across a curved surface must somehow be included in our model.

If the interface is assumed to be diffuse and spread over several computational cells with the surface tension as a volume force spread over the same

region, then the pressure gradient over the cells containing the surface can balance the surface forces, and the homogeneous approximation (5.40) can be applied. The diffuse surface is of course unphysical, but the sum of forces acting over the surface remain the same, and for a sufficiently fine grid the properties of the system should approximate the physical behaviour of the meniscus dynamics. These considerations directly relate to the type of convolution kernel applied in the surface force models discussed in the previous chapter (4.3.3).

In the original MOT the surface forces are only distributed in cells containing the phase interface. So the pressure gradient over a single cell must therefore balance the surface tension forces across the surface. The required sharp pressure gradient results in poor stability and convergence in the solution of the pressure Poisson equation. To deal with this problem a pressure correction method (see 6.6) is applied in MOT. Here a further distribution of surface forces is also introduced (see 6.6) to improve stability and convergence. The effect of the surface force distribution is similar to the effect of a convolution kernel with a smoothing length stretching over several computational cells. The additional smoothing is here needed due to the large density ratio in the system of gas and molten metal.

Through these adaptions the homogeneous model may be applied, and the momentum equation pressure term becomes

$$-\sum_k \alpha_k \nabla^i < p_k > = -\nabla < p > \sum_k \alpha_k = -\nabla < p > . \tag{5.41}$$

Volume forces

The volume forces $\mathcal{F}$ consist of gravitational pull and surface tension forces. Again, due to the large density ratio care must be taken in the implementation of surface tension forces, as discussed above. The surface tension force model is described in chapter 6.

Note that in a purely homogeneous two phase model body forces might lead to poor accuracy in fluid behaviour through fluxing of mean density with the mean velocity across cell walls. However, when the mean wall densities are applied through the Method of Tensions instead of interpolated densities in the discretization this problem should be avoided.

A remark should also be made on the temperature dependence of the density in the molten aluminium. This temperature dependence leads to buoyancy in the liquid, causing natural convection.

The importance of the effect is analyzed in appendix D.

Viscous stresses

The extensive volume average of the viscous stress term is by Slattery's theorem (5.12)

$$< \nabla \cdot \overline{\overline{\tau}}_k >= \nabla \cdot \alpha_k \, {}^i< \overline{\overline{\tau}}_k > + \frac{1}{V} \int_{\delta\Omega_k} \vec{\tau}_k \, dA, \tag{5.42}$$

where $\vec{\tau}_k$ is the shear force along the interface. To split the mean stress tensor local deviations in both the viscosity and the velocity gradients may be applied. Then

$$\overline{\overline{\tau}}_k = (< \mu_k > + \delta\mu_k) \left[{}^i< \nabla \vec{u}_k > + \delta(\nabla \vec{u})_k + {}^i< \nabla \vec{u}_k >^T + \delta(\nabla \vec{u})_k^T \right], \tag{5.43}$$

and

$$\nabla \cdot \alpha_k \, {}^i< \overline{\overline{\tau}}_k > = \nabla \cdot \alpha_k \, {}^i< \mu_k > \left({}^i< \nabla \vec{u}_k > + {}^i< \nabla \vec{u}_k >^T \right) + \mathcal{O}(\delta^2). \tag{5.44}$$

$\mathcal{O}(\delta^2)$ symbolizes the terms of second order in local deviations[2], which are neglected in consistency with neglecting mean products of deviations for the convective term. By defining the intrinsic velocity gradient tensor

$${}^i< \nabla \vec{u}_k > = \frac{< \rho \nabla \vec{u}_k >}{< \rho >} \tag{5.45}$$

and applying Slattery's theorem and local deviations it can be shown that

$$\begin{aligned} {}^i< \nabla \vec{u}_k > = \nabla \, {}^i< \vec{u}_k > - \frac{1}{< \rho_k >} \frac{1}{V} \int_{\delta\Omega_k} \rho_k \vec{u}_k \vec{n}_k dA - \\ \frac{< \delta \nabla \rho_k \delta \vec{u}_k >}{< \rho_k >} - \frac{< \delta\rho_k \delta \nabla \rho_k \delta \vec{u}_k >}{< \delta\rho_k >< \rho_k >}, \end{aligned} \tag{5.46}$$

leading to the mean viscous forces

$$\begin{aligned} \nabla \cdot \alpha_k \, {}^i< \overline{\overline{\tau}}_k > = \\ \nabla \cdot \alpha_k \, {}^i< \mu_k > \left(\nabla \, {}^i< \vec{u}_k > + (\nabla \alpha_k \, {}^i< \vec{u}_k >)^T \right) - \\ \nabla \cdot \, {}^i< \mu_k > \frac{1}{< \rho_k >} \frac{1}{V} \int_{\delta\Omega_k} \rho_k \vec{u}_k \vec{n}_k dA + \frac{1}{V} \int_{\delta\Omega_k} \vec{\tau}_k \, dA. \end{aligned} \tag{5.47}$$

In summation of the viscous stresses for the liquid and solid phases the last integral term vanishes by the balance of shear forces across the phase boundary, when no slip is assumed. The second term does not. It is a

[2]These are similar to local deviation terms in the convective term (5.27).

more complicated friction term arising from the conversion from mean shear tensor to the shear tensor of the mean velocities (by equation 5.46). The term is however obviously quite small. It is therefore assumed that it can be neglected.

Then with the assumption of approximately equal intrinsic velocity fields as in (5.1.1), and assuming the interfacial integral terms to be negligible, the homogeneous model is applied, and the mean viscous forces can be expressed as

$$< \nabla \cdot \bar{\bar{\tau}} > \approx < \mu > \left[\nabla < \vec{u} > + (\nabla < \vec{u} >)^T \right], \tag{5.48}$$

with the viscosity in the homogeneous model defined as

$$< \mu > = \sum_k \alpha_k{}^i < \mu_k >. \tag{5.49}$$

By applying the homogeneous model the momentum equation finally takes the form

$$\frac{\partial < \rho >< \vec{u} >}{\partial t} + \nabla \cdot (< \rho >< \vec{u} >< \vec{u} >) = -\nabla < p > + \nabla \cdot \bar{\bar{\tau}} + \vec{\mathcal{F}}, \tag{5.50}$$

where the vector $\vec{\mathcal{F}}$ represents the mean body forces, and the stress tensor $\bar{\bar{\tau}}$ is

$$\bar{\bar{\tau}} = < \mu > \left[\nabla < \vec{u} > + (\nabla < \vec{u} >)^T \right], \tag{5.51}$$

Two-fluid model

If a separate phase model as mentioned in the introduction were to be applied, the separate phase velocity, pressures and stresses could be modelled independently of each other. The higher order terms neglected in the homogeneous model in the convective, stress and pressure terms would then be included as boundary conditions at the phase interface. In this case two sets of momentum equations should be solved, coupled by these boundary conditions in addition to coupling by the balance of the pressure jump and surface tension forces. The Method of Tensions could also be applied in such a two phase model, where the pressure jump in a cell intersected by a phase interface could be derived from the calculated surface force. Substantial work has already been done on such models (see [28] and [75]).

5.1.3 Internal energy equation

Two boundaries must be considered in the analysis of the energy equation: the gas-metal surface boundary and the diffuse liquid-solid boundary in the

solidifying ingot. The temperature range of the liquid solid boundary is dependent on the type of alloy being cast. For pure Al the boundary is at its narrowest, so it is harder to model than the more alloy rich castings. Here the effects of the discontinuity of the gas-metal surface are analyzed. The effect of the liquid-solid interface is discussed in the presentation of the solidification model in the next chapter.

The equation for internal energy e per unit mass is

$$\frac{\partial \rho e}{\partial t} + \nabla \cdot \vec{u}\rho e = -\nabla \cdot \vec{q} + \overline{\overline{\tau}} : \nabla \vec{u} + \mathcal{S}. \tag{5.52}$$

The equation can be expressed in terms of enthalpy per unit mass h by

$$e = h - \frac{p}{\rho}, \tag{5.53}$$

leading to the equation for enthalpy per unit mass

$$\frac{\partial \rho h}{\partial t} + \nabla \cdot \vec{u}\rho h = -\nabla \cdot \vec{q} + \frac{dp}{dt} + \overline{\overline{\tau}} : \nabla \vec{u} + \mathcal{S}. \tag{5.54}$$

$\frac{d}{dt}$ is the material derivative and $\mathcal{S}$ is the source terms, discussed later. The individual phase enthalpy equations can subsequently be expressed

$$\frac{\partial \rho_k h_k}{\partial t} + \nabla \cdot \vec{u}_k \rho_k h_k = -\nabla \cdot \vec{q}_k + \frac{dp_k}{dt} + \overline{\overline{\tau}}_k : \nabla \vec{u}_k + S_k. \tag{5.55}$$

Temporal and convective terms

Similar to the treatment of the linear momentum equation, by using Whitaker's and Slattery's theorems, local deviations, and with the condition of incompressibility and no mass exchange the volume averaged left hand side of the enthalpy equation becomes

$$\begin{aligned} &< \frac{\partial \rho_k h_k}{\partial t} > + < \nabla \cdot \rho_k h_k \vec{u_k} > = \\ &\frac{\partial}{\partial t} < \rho_k > {}^i\!< h_k > + \nabla \cdot < \rho_k > {}^i\!< h_k > {}^i\!< \vec{u_k} > + \\ &\nabla < \rho_k > \left({}^i\!< \delta h_k \delta \vec{u}_k > + \frac{{}^i\!< \delta \rho_k \delta h_k \delta \vec{u}_k >}{< \delta \rho_k >} \right). \end{aligned} \tag{5.56}$$

Homogeneous model In the homogeneous model the higher order deviation terms are again assumed negligible. And the mean intrinsic enthalpy of the phases are assumed to be equal: ${}^i\!< h_G > = {}^i\!< h_L > \equiv < h >$. With equal

mean phase velocities (as in 5.1.1) adding the temporal and convective terms for the two phases gives

$$\sum_k \left(< \frac{\partial \rho_k h_k}{\partial t} > + < \nabla \cdot \rho_k h_k \vec{u_k} > \right) \approx$$
$$\frac{\partial}{\partial t} \sum_k < \rho_k >< h > + \nabla \cdot \sum_k < \rho_k >< h >< \vec{u} > . \tag{5.57}$$

Relevance to two phase system Using a common mean phase enthalpy is a similar source of error as the use of a common mean pressure in the momentum equation. The enthalpy is as the pressure, discontinuous across the liquid-gas interface, due to the difference in heat capacity of the gas and metal: the temperature is continuous and by definition,

$$h = \int_T c_p dT. \tag{5.58}$$

Therefore to achieve a good result an enthalpy correction method similar to the pressure correction model might be applied. Such a model is not applied here, but it should be considered in future work.

Conductive term

Fourier's law is applied to describe the heat conduction. Also, to facilitate the solution the temperature gradient is expressed in terms of the enthalpy gradient at constant pressure by (5.58) so that

$$\nabla T = \frac{1}{c_p} \nabla h. \tag{5.59}$$

Then

$$\nabla \cdot \vec{q} = -\nabla \cdot k \nabla T = -\nabla \cdot \frac{k}{c_p} \nabla h. \tag{5.60}$$

The volume averaged conductive term then becomes (by Slattery's theorem and using local deviations)

$$< \nabla \cdot \vec{q}_k >= - < \nabla \cdot \left(\frac{k}{c_p}\right)_k \nabla h_k >=$$
$$-\nabla \cdot \alpha_k {}^i< \left(\frac{k}{c_p}\right)_k \nabla h_k > - \frac{1}{V}\int_{\delta\Omega_k} \left(\frac{k}{c_p}\right)_k \nabla h_k \cdot \vec{n}_k dA =$$
$$-\nabla \cdot \alpha_k {}^i< \left(\frac{k}{c_p}\right)_k >^i< \nabla h_k >$$
$$-\nabla \cdot \alpha_k \left({}^i< \delta \left(\frac{k}{c_p}\right)_k \delta\nabla h_k > + \frac{{}^i< \delta\rho_k \delta \left(\frac{k}{c_p}\right)_k \delta\nabla h_k >}{< \delta\rho_k >} \right)$$
$$-\frac{1}{V}\int_{\delta\Omega_k} \left(\frac{k}{c_p}\right)_k \nabla h_k \cdot \vec{n}_k dA. \tag{5.61}$$

Again using Slattery's theorem and local deviations we may define

$${}^i< \nabla h_k > = \frac{< \rho\nabla h_k >}{< \rho >} =$$
$$\nabla {}^i< h_k > - \frac{1}{< \rho_k >}\frac{1}{V}\int_{\delta\Omega_k} \rho_k h_k \vec{n}_k dA -$$
$$\frac{< \delta\nabla\rho_k \delta h_k >}{< \rho_k >} - \frac{< \delta\rho_k \delta\nabla\rho_k \delta h_k >}{< \delta\rho_k >< \rho_k >}. \tag{5.62}$$

Subsequently the conductive term in the energy equation becomes

$$< \nabla \cdot \vec{q}_k >= - < \nabla \cdot \left(\frac{k}{c_p}\right)_k \nabla h_k >=$$
$$-\nabla \cdot \alpha_k {}^i< \left(\frac{k}{c_p}\right)_k > \nabla {}^i< h_k > +$$
$$\nabla \cdot \alpha_k \frac{{}^i< \left(\frac{k}{c_p}\right)_k >}{< \rho_k >}\frac{1}{V}\int_{\delta\Omega_k} \rho_k h_k \vec{n}_k dA -$$
$$\frac{1}{V}\int_{\delta\Omega_k} \left(\frac{k}{c_p}\right)_k \nabla h_k \cdot \vec{n}_k dA + \mathcal{O}(\delta^2). \tag{5.63}$$

The products of deviations are again assumed to be small, and the individual phase terms

$$\int_{\delta\Omega_k} \left(\frac{k}{c_p}\right)_k \nabla h_k \cdot \vec{n}_k dA = \int_{\delta\Omega_k} k_k \nabla T_k \cdot \vec{n}_k dA \tag{5.64}$$

will cancel in the summation when there is no energy source or drain on the gas-metal interface.

Homogeneous model In the homogeneous model the mean enthalpy of the two phases are assumed to be approximately equal so that ${}^{i}< h_L >= {}^{i}< h_G > \cong < h >$. Then the sum of the individual phase energy equations becomes

$$-\sum_k < \nabla \cdot \vec{q}_k >= -\nabla \cdot \sum_k \alpha_k {}^{i}< \left(\frac{k}{c_p}\right)_k > \nabla < h > + \nabla \cdot \sum_k \alpha_k \frac{{}^{i}< \left(\frac{k}{c_p}\right)_k >}{< \rho_k >} \frac{1}{V} \int_{\delta\Omega_k} \rho_k h_k \vec{n}_k dA + \mathcal{O}(\delta^2). \tag{5.65}$$

The second term to the right in (5.65) represents a heat transfer across the phase interface. It is assumed to be negligible compared to the mean heat transfer. With the assumption of equal intrinsic average temperatures this leads to the homogeneous conductive term equation

$$-\sum_k < \nabla \cdot \vec{q}_k > \approx -\nabla \cdot \left(\sum_k -\alpha_k {}^{i}< \left(\frac{k}{c_p}\right)_k > \right) \nabla < h > . \tag{5.66}$$

Relevance to two phase system Again the application of a common phase enthalpy is a rough approximation. An enthalpy correction method would improve stability and convergence, as discussed above.

If the heat flux is assumed to be normal to the interface, and the temperature on each side of the interface is known or can be approximated, then a more accurate expression for the heat conduction across the interface can be found: this is done by introducing a harmonic mean conductivity and directly applying the phase temperature gradients. Such a method is applied in the model for solidification contraction (see chapter 7).

Friction and pressure

The heat generated by friction and pressure work is normally quite small, and the corresponding terms in the heat equation are therefore neglected.

Source term and solidification

Since the model must be capable of modelling phase change between liquid and solid aluminium, the latent heat of melting must be accounted for in the energy equation. This can be achieved by including the latent heat release per unit mass in the source term S_k. Another possibility is including the latent heat in an enthalpy/temperature model. The latter technique, presented in

section 7.1.1 is applied in our model. Problems connected to a steep enthalpy gradient in the region of solidification are discussed in this section.

Another term that might be included here is the radiation between the meniscus and ingot surface and the mould wall. It is however shown in 7.2.7 that the effect of radiation is negligible compared to the conductive heat flow from ingot to mould.

Chapter 6

Developments in Method of Tensions

A 2D marker chain method is applied for tracking the interface between the gas and metal phases. The method is based on earlier work by Popinet and Zaleski [49]. The original method, the Method of Tensions (MOT), models a free moving interface with surface tension forces in a 2D Cartesian system, using a cubic spline function to interpolate the interface (shown in figure 4.9). Since the original MOT is not very applicable to systems with both large density ratio and small Weber numbers some modifications have been made to the model.

The main advantages of the Method of Tensions are accuracy of surface interpolation and direct application of wetting properties as boundary conditions (see chapter 4). The surface construction is performed using cubic splines, of which the accuracy is a lot higher than for the lower order surface tracking and capturing methods (see chapter 4). Thereby control of spurious currents is greatly improved and consequently also the stability of the solution. The wetting conditions at the surface contact points with the walls is applied as boundary conditions at the ends of the interpolating spline. Compared to models of lower order this improves the dynamics close to wall contact points in the numerical simulations.

The Method of Tensions has been adapted to the cylindrically symmetric coordinate system and further to a system with large density ratio (as in our case of a metal gas interface). Modifications have been made to the marker advection algorithm, the method of marker redistribution, and the method of distribution of surface tension forces in order to improve stability and conservation of individual phase mass at the interface. Also for simplicity the SIMPLE NS solver (described in 8.1) already implemented in FLUENT V3.04 has been applied instead of the variation on the explicit projection

method described in the original Method of Tensions paper [49]. Attempts have further been made to improve the conservation properties of the marker chain advection method.

Navier-Stokes equations

The dynamics and thermodynamics of three separate phases (gas, liquid metal, and solid metal) are coupled in the casting simulations. There are three kinds of discontinuity or interfaces in the system; the gas-liquid interface, the gas-solid interface and the liquid-solid interface. To fulfill the condition of continuity all coefficients and dependent variables are defined as volume averages in the applied equations, as described and analyzed in the previous chapter.

2D cylinder symmetry, incompressibility, Newtonian viscosity and a constant surface tension coefficient are assumed. The Navier-Stokes equations [8] are expressed in conservative form, as in the original SOLA algorithm, to facilitate conservation of mass and energy in the discretization. The volume averaged NS equations are as follows.
Continuity equation;

$$\frac{\partial}{\partial t}\rho + \frac{1}{r}\frac{\partial}{\partial r}(r\rho v_r) + \frac{\partial}{\partial z}(\rho v_z) = 0. \tag{6.1}$$

Momentum equations;

$$\begin{aligned}
\frac{\partial}{\partial t}(\rho v_r) + \frac{1}{r}\frac{\partial}{\partial r}(r\rho v_r^2) + \frac{\partial}{\partial z}(\rho v_r v_z) &= -\frac{\partial}{\partial r}P \\
&- \left(\frac{1}{r}\frac{\partial}{\partial r}(r\tau_{rr}) - \frac{\tau_{\theta\theta}}{r} + \frac{\partial}{\partial z}\tau_{rz}\right) + S_r, \\
\frac{\partial}{\partial t}(\rho v_z) + \frac{1}{r}\frac{\partial}{\partial r}(r\rho v_z v_r) + \frac{\partial}{\partial z}(\rho v_z^2) &= -\frac{\partial}{\partial z}P \\
&- \left(\frac{1}{r}\frac{\partial}{\partial r}(r\tau_{rz}) + \frac{\partial}{\partial z}\tau_{zz}\right) + \rho g + S_z,
\end{aligned} \tag{6.2}$$

where surface tension forces per unit volume are defined as $\mathbf{S} = (S_r, S_z)$.

The Newtonian stress tensor components are

$$\begin{aligned}
\tau_{rr} = -\mu 2\frac{\partial v_r}{\partial r},\ \tau_{\theta\theta} = -\mu 2\frac{v_r}{r},\ \tau_{zz} = -\mu 2\frac{\partial v_z}{\partial z}, \\
\tau_{zr} = \tau_{rz} = -\mu\left[\frac{\partial v_z}{\partial r} + \frac{\partial v_r}{\partial z}\right],
\end{aligned} \tag{6.3}$$

and by the condition of incompressibility

$$\nabla \cdot \mathbf{v} = \frac{1}{r}\frac{\partial}{\partial r}(rv_r) + \frac{\partial v_z}{\partial z} = 0.$$

6.1 Surface tension forces

The basics of the surface force calculation in the Method of Tensions are described in section 4.3.3. With surface tension coefficient σ, surface curvature κ and surface unit normal $\mathbf{n}$, the total surface tension forces acting on a surface S can be expressed (by Landau [40]);

$$\int_S \sigma\kappa\mathbf{n}\, dA. \tag{6.5}$$

And by relation 4.27 shown by Brackbill et al [10]:

$$\int_S \sigma\kappa\mathbf{n} dA = \int_\Omega \delta_s\sigma\kappa\mathbf{n}\, dV. \tag{6.6}$$

where δ_s is the surface δ-function as defined by Brackbill (equation 4.27). So the surface tension term in the momentum equations (6.2) can be expressed as a force per unit volume by

$$\mathbf{S} = \delta_s\sigma\kappa\mathbf{n}.$$

Assuming a constant surface tension coefficient σ it can be shown by the Frenet-Serret formulae that:

$$\int_\Omega \delta_s\sigma\kappa\mathbf{n}\, dV = \sigma \oint_{\delta S} d\mathbf{t}, \tag{6.7}$$

where δS is the border of the surface S and $\mathbf{t}$ is the surface unit tangent vector. This relation is applied in the finite volume discretization of the momentum equations.

Discretization in cylindrical coordinates Parameterizing the surface boundary by s[1] the contribution from the surface tension forces to the equations of momentum can then be expressed as (see figure 6.1);

$$\begin{aligned}\sigma \oint_{\delta S} d\mathbf{t} = \sigma[\oint_{\delta S_1} (\mathbf{t}_3 - \mathbf{t}_1)ds \; + \Delta\theta(r_4\mathbf{t}_4 - r_2\mathbf{t}_2)] \approx \\ \sigma[\,(\overline{\mathbf{t}}_3 - \overline{\mathbf{t}}_1) \oint_{\delta S_1} ds \; + \Delta\theta(r_4\mathbf{t}_4 - r_2\mathbf{t}_2)].\end{aligned} \tag{6.8}$$

$\overline{\mathbf{t}}_1$ and $\overline{\mathbf{t}}_3$ are mean surface values of $\mathbf{t}_1$ and $\mathbf{t}_3$ at the computational cell wall. The tangent vectors in (6.8) may be calculated from the surface spline function.

[1] Parameterization by a single parameter is applicable since the surface is defined by a curve in the rz plane.

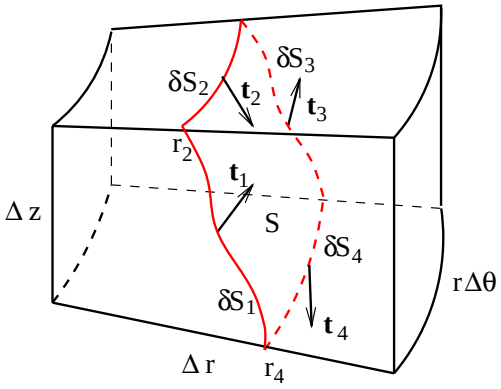

Figure 6.1: Computational volume Ω. Surface segment S with sides δS_i with normal surface tangent vectors $\mathbf{t}_i$ displayed in volume.

6.2 Deriving points of intersection

In order to calculate both the volume fraction and the surface tension forces one must obtain the points of intersection between the spline surface and the computational grid. Intersections are sought by searching sequentially along the spline a small segment ($s = (s_i, s_{i+1}]$) of the spline surface at a time. If a segment crosses several grid lines it is halved and intersections are sought on each segment half. A numerically robust procedure combining Newton-Rhapson and the bisection method is used to find the intersections for each segment. Parameterizing the curve with s a vertical intersection is found by

$$r_i - r(s_{int}) = 0, \tag{6.9}$$

where r_i is the radial value at the vertical computational cell wall i being intersected. The root s_{int} then gives the point of intersection $(r(s_{int}), z(s_{int}))$. The horizontal intersections are found in the same fashion at a horizontal cell wall j by

$$z_j - z(s_{int}) = 0. \tag{6.10}$$

The five possible types of intersections are shown in figures 6.3 to 6.7.[2] The segment for which an intersection is sought is indicated in each figure.

[2]It is assumed that the curvature is restricted so that these are the only possible cases.

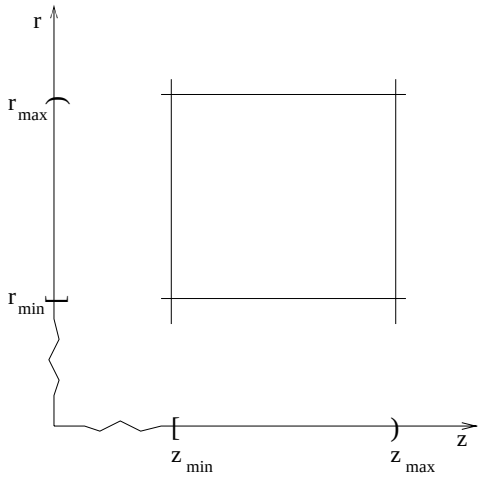

Figure 6.2: Definition of region of computational cell.

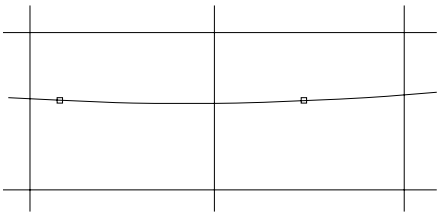

Figure 6.3: Single intersection, computational cells, markers and spline.

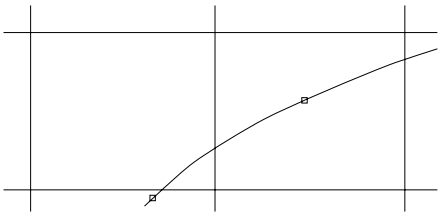

Figure 6.4: Simple double intersection.

Simple single and double

Figure 6.3 shows a *single intersection* on the segment while figure 6.4 shows a *double intersection*. All intersections are easily determined in these types of cases. To find which walls are intersected the cell position of the segment end points are first calculated, where the region of a computational cell L is defined as in figure 6.2:

$$(r, z) : \{r \,\epsilon\, [\, r_{min}(L), r_{max}(L)\,), z \,\epsilon\, [\, z_{min}(L), z_{max}(L)\,)\}. \tag{6.11}$$

In this way any overlap between cells is avoided. If the end points are found to be in different cells an intersection has occurred on the cell wall common to the two cells containing the segment end points. The root s_{int} indicating the intersection is then sought by either (6.9) or (6.10), for respectively vertical or horizontal intersection . If there is a double intersection, as in figure 6.4, a check is performed to determine the order of the intersections since it is necessary to know the ordering of the intersections for volume fraction calculation. Subsequently the intersections are determined as before.

Common double

A common double intersection (of neighboring horizontal and vertical cell walls) occurs when the spline intersects a cell corner, as in figure 6.5. This case is treated as a single intersection where the spline crosses directly between diagonal neighbour cells.

Triple intersection

In figure 6.6 a case is shown with a *triple intersection* on the segment. In this case, the intersection on the vertical wall between the particles will be on a cell face neighbouring the one between the segment end points. So a check is performed to see whether this is the case. If it is, the spline segment is split at the point of vertical intersection so that the two horizontal intersections may be found. Again similar for vertical intersections.

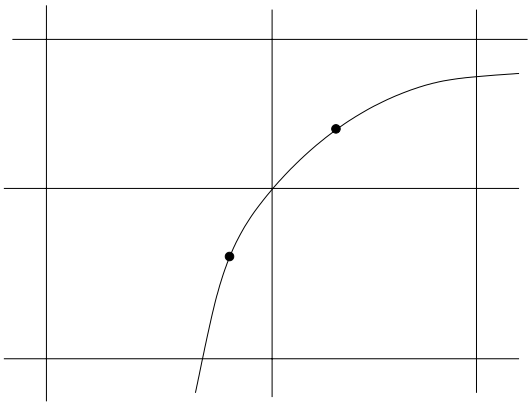

Figure 6.5: Common double intersection.

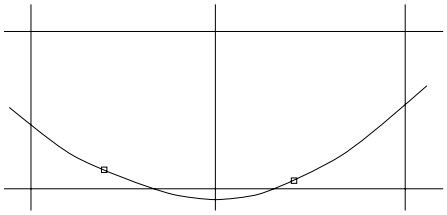

Figure 6.6: Triple intersection.

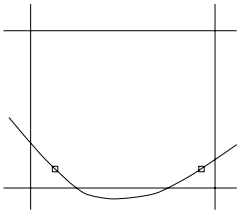

Figure 6.7: 'Hidden' double intersection.

Hidden double

Figure 6.7 shows the case of a hidden double intersection. No intersections will be sought by our algorithm in this case, since the segment end points are in the same computational cell. No check for this kind of error has been included. For limited spline curvature the problem is however not considered to be of much consequence, since the resulting error in calculated volume fraction will be small.

6.3 Calculation of volume fraction

The volume fraction of each phase in a computational cell (figure 6.1) must be computed in order to derive the volume averaged variables applied in the Navier Stokes and energy equations. The method of integration of volume fraction described in [49] is here adapted to cylindrical coordinates.

Figure 6.8 shows an intersection of the computational volume Ω. The surface spline function is parameterized by s; $(r, z) = (r(s), z(s))$. Again referring to [49] and by Stokes theorem: For a surface Σ with boundary $\delta\Sigma$;

$$\int_{\Sigma} r\, dr\, dz = \oint_{\delta\Sigma} \frac{1}{2} r^2 dz. \tag{6.12}$$

This comes from the relation that for a piecewise-smooth simple closed curve $\delta\Sigma$,

$$\int_{\Sigma} \frac{\delta P}{\delta r} dr dz = \oint_{\delta\Sigma} P dz,$$

by the fundamental theorem of calculus And for the computational volume Ω in figure 6.1 with $r = R$ at the centre of the volume (see figure 6.8):

$$\int_{\Omega} r\, d\theta\, dr\, dz = R\Delta\theta\, \Delta r\, \Delta z.$$

By applying (6.12), the volume fraction of the phase to the left of the spline surface can be expressed as;

$$\alpha = \frac{1}{R\Delta r\, \Delta z} \int_{\Sigma} r\, dr\, dz = \frac{1}{R\Delta r\, \Delta z} \oint_{\delta\Sigma} \frac{1}{2} r^2\, dz, \tag{6.13}$$

where the part of the boundary integral along the spline $\delta\Sigma(s) = (r(s), z(s))$, can be expressed as;

$$\int_{\delta\Sigma(s)} \frac{1}{2} r^2\, dz = \int_{\delta\Sigma(s)} \frac{1}{2} r^2(s)\, z'(s)\, ds. \tag{6.14}$$

With the interface defined by the spline function the integral in (6.14) can be derived, thereby giving the volume fraction α by (6.13).

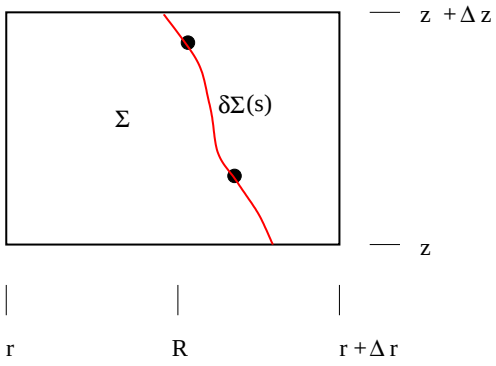

Figure 6.8: Surface of computational volume Ω. Interface spline $\delta\Sigma(s) = (r(s), z(s))$ bounds the surface Σ. Two markers are shown on the spline.

6.4 Bubble pressure test

Tests of the surface tension force model were carried out for a 2D bubble in a cylindrically symmetric coordinate system. In this coordinate system a 2D bubble centered on the symmetry axis corresponds to a real 3D bubble while a 2D bubble removed from the axis is a 3D taurus.

Three tests were performed for a bubble with radius 2mm with centre respectively on the symmetry axis, removed 2mm from the axis, and removed 7.5mm from the axis. The value of the applied surface tension coefficient was $\sigma = 0.07$, corresponding to a water-air interface. Gravity was set to zero, so phase density was of no influence (except for having an influence on stability). The uniform grid size was 1/10 of the bubble diameter, as can be seen in figure 6.9(d).

In the simulations the surface was held static and the NS equations were solved for the flow. The resulting pressure distributions are shown in figure 6.9. The modelling results may be compared to the analytical solution for the pressure jump across the interface given by Landau and Lifshitz [40]:

$$p = \sigma(\kappa_1 + \kappa_2), \tag{6.15}$$

where κ_1 and κ_2 are the principal curvatures.

By this formula the pressure jump for a 3D bubble with radius of $2mm$ is $140Pa$. Such a bubble is simulated in figure 6.9(a). Here the pressure jump Δp is $125Pa$, somewhat lower than for the analytical solution. The difference is partly due to problems with modelling the effects of surface tension at the symmetric axis boundary, and may also be due to the low resolution of the grid. Another possible cause is trying to force the cubic spline to maintain constant curvature.

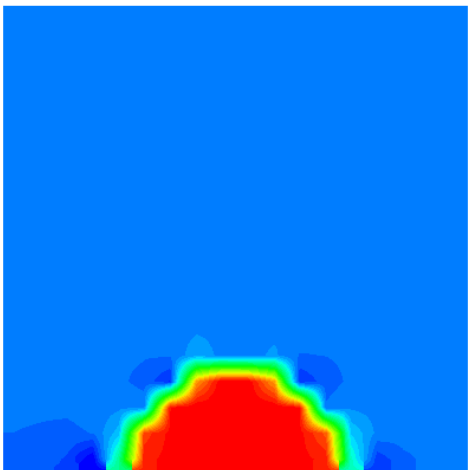

(a) Bubble test. Real 3D bubble. $\Delta p = 125Pa$.

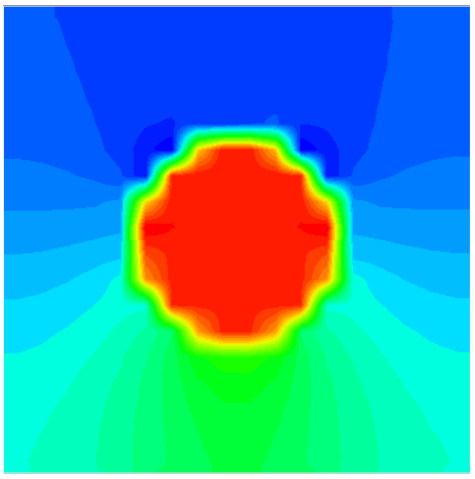

(b) Bubble test. 2D bubble with centre 2mm from symmetry axis. $\Delta p = 84Pa$.

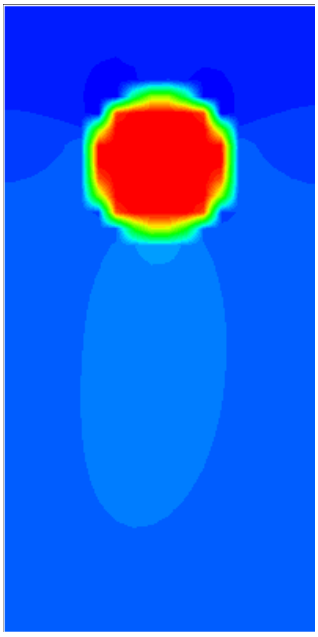

(c) Bubble test. 2D bubble with centre 7.5mm from symmetry axis. $\Delta p = 70,2Pa$.

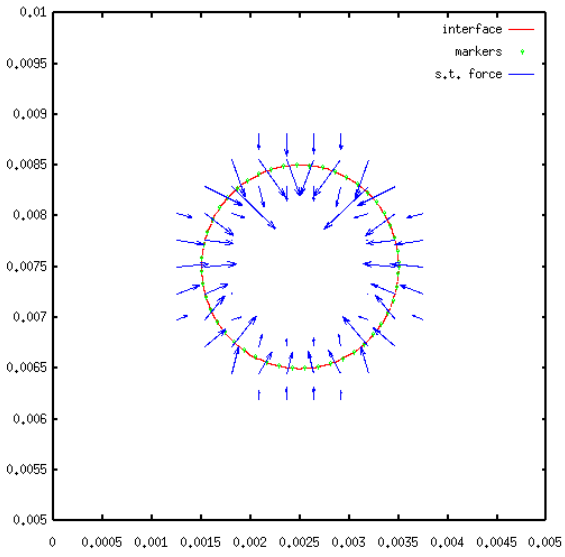

(d) Surface tension forces in computational grid for 2D bubble at 7.5mm radius.

Figure 6.9: Bubble pressure tests. Symmetry axis at bottom of figures (except for in figure 6.9(d)). 2mm bubble diameter. The given pressure jump Δp is the difference between lowest and highest pressure.

For a 2D bubble (corresponding to a taurus) the pressure jump is $70Pa$ by (6.15). The cylindrical bubble is approximated by the test in figure 6.9(c), where the effect of the toroidal curvature is small. The pressure jump shows good agreement with the analytical calculation at $70,2Pa$, indicating that for a connected surface the model gives good results.

The intermediate case in figure 6.9(b) shows the influence of the toroidal curvature on the pressure field by the increased pressure inside the taurus. The pressure jump lies between the extreme cases in figures 6.9(a) and 6.9(c).

To conclude, the bubble pressure tests shows quite good agreement with the analytical model for pressure jump across a surface. Boundary conditions at walls and grid resolution will however probably both influence the result, particularly the former. This indicates that behaviour of the model close to a wall boundary for a disconnected surface might deviate somewhat from correct physical behaviour. Here the behavior will also be partly determined by the applied wetting boundary conditions.

6.5 Grid refinement

Another cause of instability in MOT is the fact that a surface of constant curvature (circular segment) can not be exactly modelled by a third order spline function. Irregularities in the surface tension force field along the interpolated surface will therefore occur. However, it can be shown that for MOT there is a linear relation between the amplitude of the spurious currents and the gridsize (see section 4.3.3 and [49]). So with sufficient grid refinement the spurious currents can be significantly reduced.

6.6 Redistribution of surface tension forces

As discussed in 4.3.3, high density ratios ρ_1/ρ_2 between phases lead to considerable difficulties in simulating multiphase systems. The resulting spurious currents lead to vortexes at the interface, causing erroneous surface behavior (also see [56] and [53]). In the case of modelling the meniscus interface, the ratio between liquid Al density and air density is close to 3000:1. This constitutes a serious problem to stability.

The instabilities are partly caused by large surface tension forces on the side of the low density gas phase, since the forces are distributed symmetrically across the interface. In the original MOT a pressure correction technique similar to that applied in Hirt and Nichol's VOF (section 4.2) is applied to improve stability. Here a redistribution of surface tension forces is applied.

The force calculated in a cell is distributed over all its neighboring cells, where the distribution is weighted by the mean cell density. Define

$$F_{k,k} = \int_{\Omega_{k,k}} \mathbf{S}\, dV.$$

And the applied computational cell surface forces are denoted $\Gamma_{i,j}$. The change in $\Gamma_{i,j}$ due to rearrangement of the surface forces $F_{k,k}$ calculated in cell (k,k) can be expressed as;

$$\Delta\Gamma_{i,j} = F_{k,k}\,\hat{\rho}^{\gamma}_{i,j} / \left(\sum_{i=k-1}^{k+1} \sum_{j=k-1}^{k+1} \hat{\rho}^{\gamma}_{i,j} \right). \tag{6.16}$$

The parameter γ determines the strength of the weighting. The ideal value of γ should depend on both density ratio and curvature/gridsize ratio. By using this rearrangement of surface tension forces, the forces acting in cells with low density will be reduced. Thereby stability should be improved. The resulting force field with CMOT in the case of an air bubble in aluminium melt for $\gamma = 5$ is shown in figure 6.10(a). The generated spurious currents are shown in figure 6.10(b).

In applying this model to simulations an ideal value for γ was found to be around 1. For larger γ the redistribution increases instability due to loss in smoothness in the redistributed surface forces Γ along the interface.

6.7 Marker advection

In the original MOT marker advection is performed by bilinear interpolation of velocities ([49]). A problem with this technique is that velocities in the gas affect the flow of the free aluminium melt surface to the same extent as the velocities within the molten metal. So in general, the binomial interpolation is unphysical, since for a phase interface the velocity field is normally nonlinear with a discontinuous gradient at the interface. The interpolation should therefore be dependent on the shear and subsequently the viscosity at each side of the interface.

Here the meniscus surface is modelled as a free surface , i.e. only the pressure and not the flow in the gas influences surface marker advection. This is done by applying density weighting in the velocity interpolation. Then the interpolated horizontal marker velocity u_m for marker m (see figure 6.7) is

$$u_m = \frac{\sum_{i=k}^{k+1} \sum_{j=n}^{n+1} u_{i,j}\rho_{i,j}}{\sum_{i=k}^{k+1} \sum_{j=n}^{n+1} \rho_{i,j}}. \tag{6.17}$$

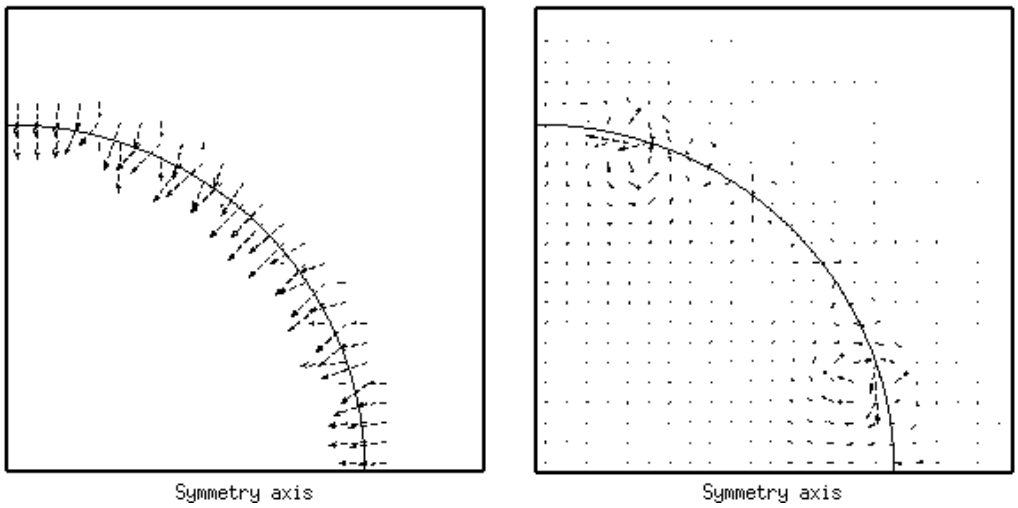

(a) Surface tension force field. (b) Spurious currents.

Figure 6.10: Static air bubble in Al melt. Bubble radius 3mm.

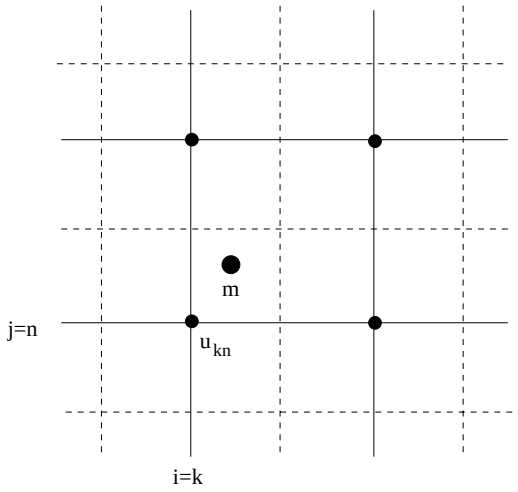

Figure 6.11: Marker m in computational u-grid (solid line). Computational cells also indicated (dashed line).

The density weighting is chosen for generality. The larger the density ratio the stronger the decoupling of marker velocity from the phase with smaller density. In the case here with density ratio 3000:1, this technique gives a close approximation to advection at a free surface.

6.8 Redistribution and spline interpolation

The Method of Tensions uses massless markers on the interface together with cubic spline interpolation for reconstruction of the interface. The markers are regularly redistributed on the surface for stability. The process is described in [49].

After advection of marker particles the interface is reconstructed using cubic spline interpolation. Popinet and Zalesky [49] apply regular cubic splines for reconstructing the surface. However, when applying this method, problems of stability and phase conservation are observed. Therefore an analysis has been performed using varying redistribution frequency and also cubic B-spline for reconstruction. Varying redistribution and surface reconstruction in this way may improve both phase conservation and stability.

6.8.1 Advection tests

Tests were performed for the case of a constant stream function Ψ:[3].

$$\Psi = \frac{1}{\pi}\sin[\pi(x-0.5)]\sin[\pi(y-0.5)]. \tag{6.18}$$

In the tests bilinear interpolation is applied for the marker advection[4]. Advection is performed at a Courant number

$$c = \frac{\delta t\, U}{\delta x} \tag{6.19}$$

of 0.1, where δt is time increment, δx is computational cell dimension and U is velocity. The initial surface configuration is shown in figure 6.12(a), with the surface after 2500 time steps in figure 6.12(b)[5].

[3]Only advection and subsequent calculation of volume fraction was performed. With the stream function given it is not necessary to solve the Navier-Stokes system.

[4]For a static velocity field the fluid properties are of no consequence for the flow.

[5]This result was achieved by only advecting markers, no redistribution of markers was used.

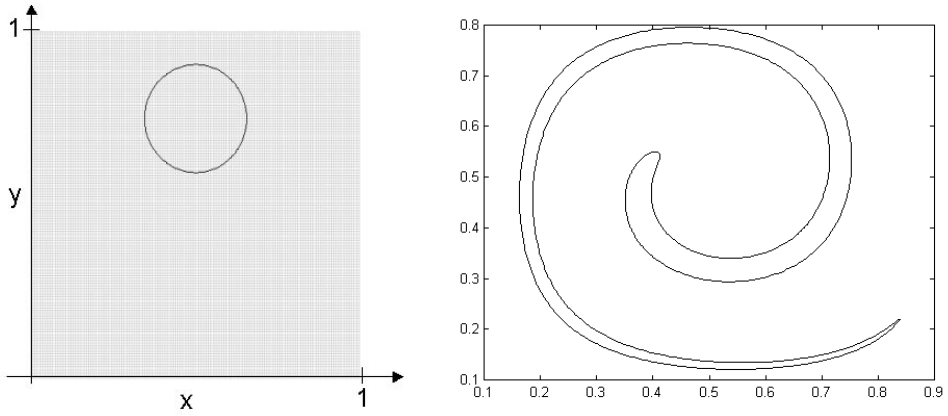

(a) Initial surface configuration on computational grid.

(b) Correct surface after 2500 time steps, Courant no = 0.1

Figure 6.12: Correct initial and advected surface.

Reference simulation 2500 time steps were performed, the velocity was reversed, and 2500 time steps were subsequently performed with reversed velocity. Redistribution is here performed as suggested in MOT [49], where new markers are placed on the old spline at regular intervals. Figure 6.13(a) shows the spline initially, after 2500 time steps and after 5000 time steps. After 2500 forward time steps irregularities appear at the tail, and after 5000 time steps the surface is partly folded and irregular, in addition to a mean shift to the right (compare figure 6.12(a)).

Past 2500 time steps waves start to form on the surface, as shown in figure 6.14. In addition to this instability, an increase in total volume of the inner phase is observed (see figure 6.13(b)). This is due to the combined effect of cubic spline reconstruction of the surface and redistribution of markers.

B-spline reconstruction and rate of redistribution

To attempt to solve the problem of instability and poor phase conservation a cubic B-spline surface interpolation is applied (see [21]). Because of the parameterization, a cubic spline reconstruction must be applied after the B-spline redistribution in order to calculate the volume fraction, but this does not effect the position of the markers, and can therefore not cause instability. The B-spline reconstruction reduces the volume in the inner phase. A B-spline redistribution is therefore applied each time the volume of the internal phase grows larger than its initial volume. Application of the cubic B-spline

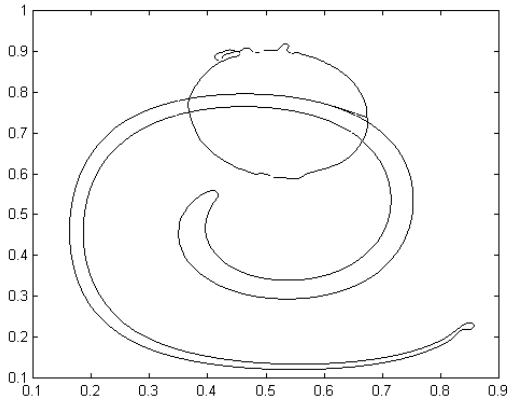

(a) Splines at initial state, at 2500 steps with Courant no 0.1, and at time = 0 after reversal

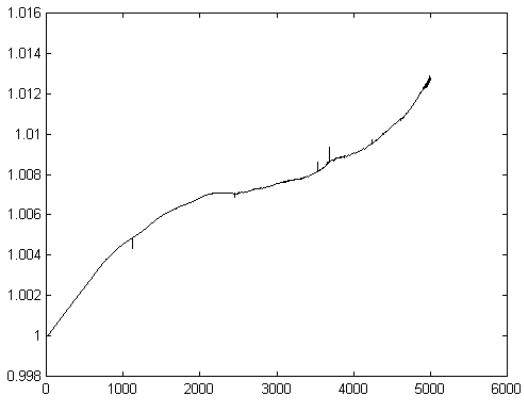

(b) Total volume relative to initial volume, reversal at 2500 time steps with Courant no 0.1.

Figure 6.13: Test run with regular cubic splines.

also improves stability by its smoothing properties. So in this fashion the total volume is conserved and stability improved at the same time.

Advection tests are presented in the following figures. The redistribution rate *Rds* denotes the number of time steps between redistribution of marker particles. Rds is a parameter which greatly influences both volume conservation and stability.

Test 1 The results of the first test case are shown in figure 6.15. As in the test with MOT (section 6.8), from the initial 2D bubble a run is made iterating 2500 time steps. The flow is then reversed and the program and another 2500 time steps are performed.

The tests in figures 6.13 and 6.15 are compared. Cubic B-spline interface reconstruction and redistribution is applied each time the ratio of internal volume to initial internal volume grows larger than unity. Thereby the volume is kept within 10^{-3} of the initial volume in this case (figure 6.15(b)).

The spline function is also more regular when the B-spline method is used. The interface is highly irregular after the flow reversal when only regular cubic splines are used (6.13(a)), while the surface is smooth in the improved version (6.15(a)). A larger time between redistribution of markers also improves surface stability.

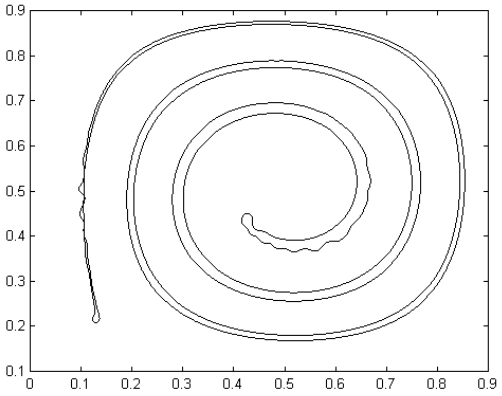

Figure 6.14: Unstable surface after 5000 time steps with Courant no = 0.1 using regular cubic spline reconstruction.

Test 2 A similar test to that in figure 6.15 is shown in figure 6.16. Here 5000 time steps are performed before flow reversal. By applying the same technique as for test 1 the internal volume ratio (figure 6.16(b)) is also mainly within 10^{-3}. The spline surface is fairly smooth both after 5000 time steps and after complete reversal (see figure). The surface after complete reversal is however somewhat distorted compared to the initial surface.

Test 3 Finally, a run is made of 50000 time steps for Courant number $c = 0.01$. The spline surface is still quite even after 50000 iterations (figure 6.17(a)). The relative total volume is however more irregular in this case, owing to the large number of time steps. The time rate of change of relative volume is however smaller than for the runs with larger Courant number in the semi-stable regions of the curve (apart from the jumps), so less corrections by B-spline reconstruction and redistribution are needed for volume conservation.

6.8.2 Application of spline reconstruction to meniscus simulations

The tests above show that using a combination of regular cubic spline and cubic B-spline reconstruction together with a low frequency of marker redistribution considerably improves interface stability. Also, B-spline reconstruction can be used to improve phase conservation. With this technique problems with surface instability still arise after traversing a large number of cells, but now at a much later stage than when using the original MOT of

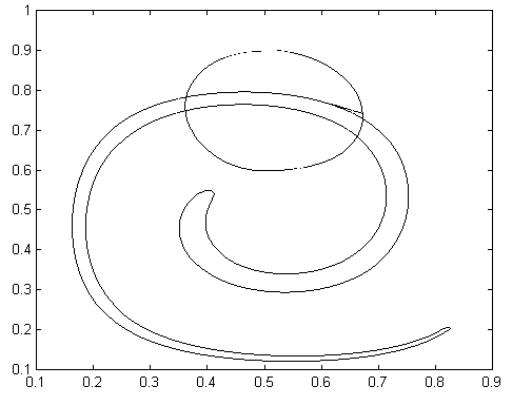

(a) Spline surface after 2500 time steps, and at time = 0 after reversal.

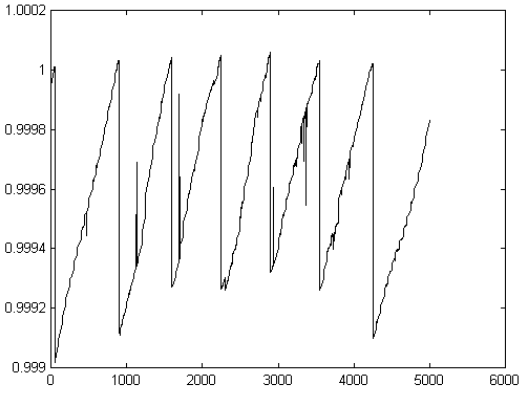

(b) Total volume relative to initial total volume

Figure 6.15: Test case 1 with volume correction. Time: 0-2500-0, Courant no: 0.1, Rds: 50

Popinet and Zalesky.

Although this redistribution technique shows good promise, some adaption is still necessary to achieve accurate volume conservation through spline reconstruction. The volume change from a B-spline reconstruction depends locally on the spline curvature. Therefore the effect on total volume by applying the B-spline depends on surface geometry. Also, the volume conservation achieved in the tests above is a total volume conservation, which does not ensure flux balancing on the local scale (i.e. in each surface cell).

Other types of splines could also be applied to the problem, such as cubic tension splines or higher order splines. The cubic tension splines have only continuous first derivative at the points of interpolation, and subsequently the surface tension forces will be discontinuous for this type of surface. A tension spline of a higher order might however be a good candidate, since the curvature of the spline could be controlled while at the same time keeping the curvature continuous. Therefore it should be interesting to try to apply a fourth order tension spline to the problem.

However, for simplicity a regular cubic spline has been applied to the meniscus problem, where the method of reconstruction has been adapted so as to achieve an adequately stable method on the required non-uniform grid (see 8.1).

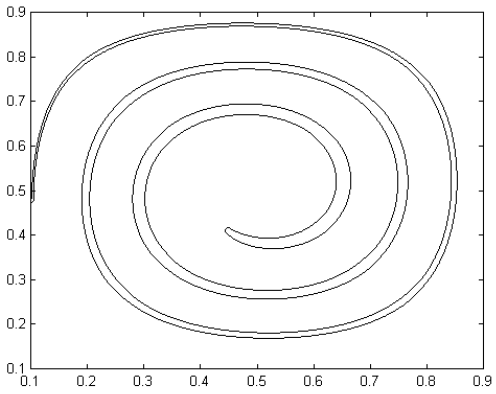

(a) Spline function after 5000 time steps

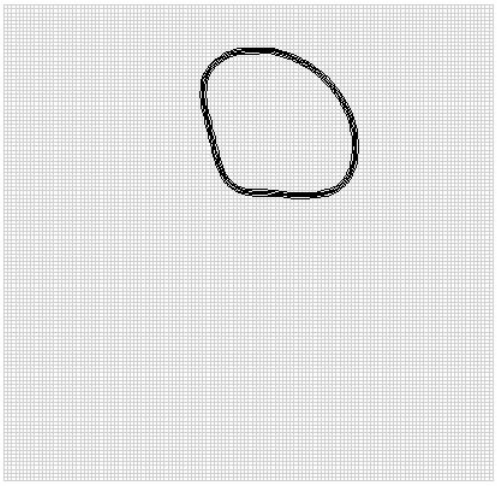

(b) Volume fraction at time = 0 after reversal

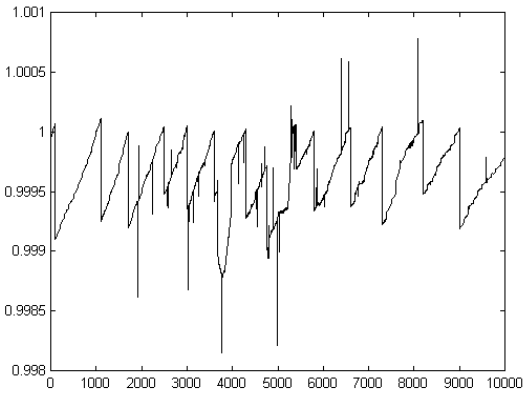

(c) Total volume relative to initial total volume

Figure 6.16: Test case 2 with volume correction. Time: 0-5000-0, Courant no: 0.1, Rds: 100

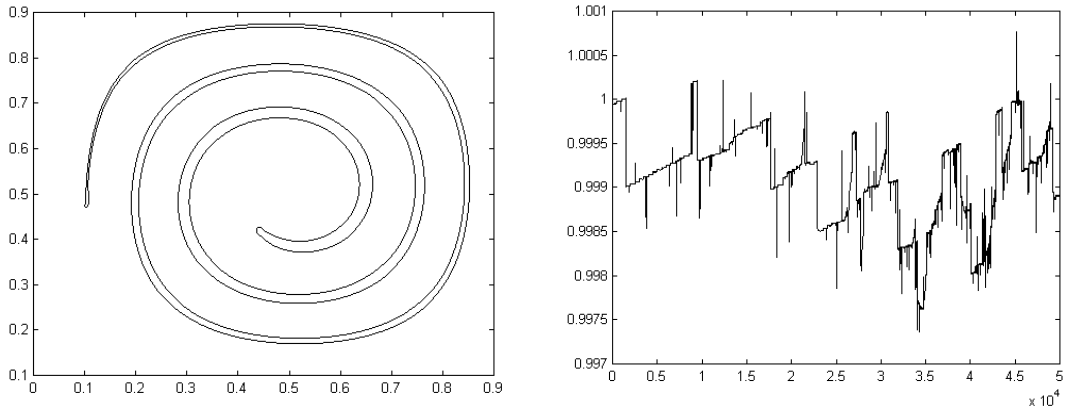

(a) Volume fraction after 5000 time steps

(b) Total volume rel. to initial volume

Figure 6.17: Test case 3 with volume correction. Time: 0-5000, Courant no: 0.01, Rds: 500

6.8.3 Alternating midway redistribution

In the tests above an even spaced redistribution of markers was applied. However, in the case of large density ratio between metal and gas density this type of redistribution proved unstable. The markers were not displaced enough from their original positions to provide a sufficient stabilizing effect[6]. Another problem with this technique is that the amount of markers per cell is not controlled for the non-uniform grid. Applying more than one marker per cell may lead to instability (see [49]), while too sparsely distributed markers leads to low accuracy of surface interpolation.

The most stable redistribution method proved to be alternating between distribution of markers midway between intersections between spline and computational and distribution of markers midway between old markers. In this way the local marker spacing was ensured to be in the order of the local grid size while the varying of redistribution could give sufficient smoothing. It is here important to note that redistribution also leads to error in the advected surface, so an ideal rate of redistribution is both low enough to ensure sufficient accuracy of advected surface and high enough to ensure sufficient smoothing and stability of the surface.

[6]Varying marker positions leads to smoothing of the interpolated spline, although to a smaller degree with regular cubic than for cubic Bspline

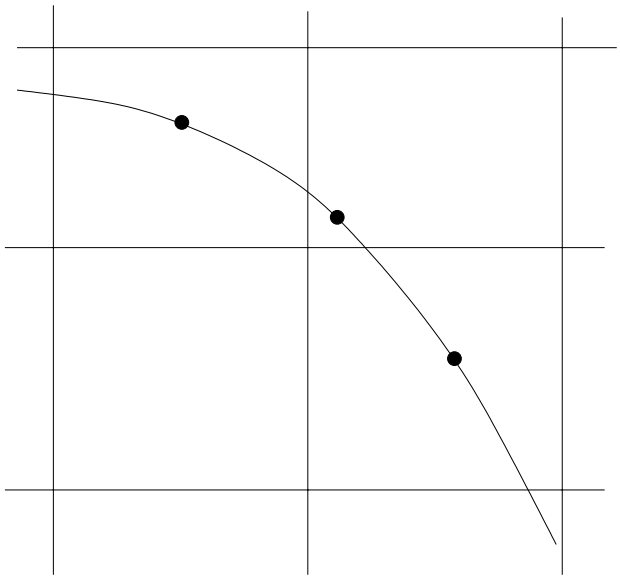

(a) First distribution: Midway between grid intersections.

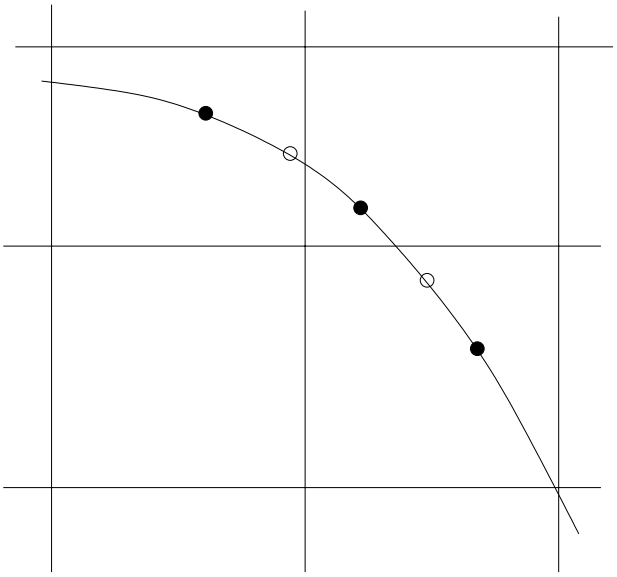

(b) Redistribution after surface advection: New markers (empty) midway between old markers (filled). Old markers are deleted.

Figure 6.18: Marker redistribution alternation.

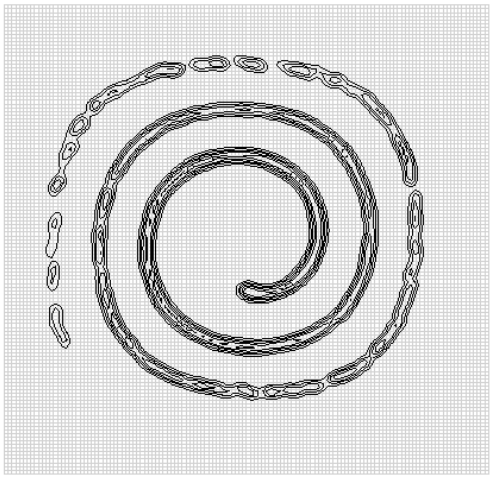

Figure 6.19: Advection test with Hirt and Nichols' VOF. 5000 time steps, Courant no 0.1.

6.9 Advection test with Hirt & Nichols' VOF

To compare the advection properties for the Method of Tensions to the original Volume of Fluid an advection test was also performed using the VOF method. Again the flow field given by the stream function in (6.18) was applied. Figure 6.19 shows the result for 5000 iterations with a Courant number of 0.1. The test is comparable to the one shown in figure 6.16 for the Method of Tensions. It is quite apparent that problems of instability are much greater for the VOF method, leading to uncontrolled breakup of the surface. This shows quite clearly that a higher order model like MOT is preferable when stability of surface is of great importance, as when modelling the meniscus, where the number of time steps required may be of the order of 100000 or larger.

6.10 Summary

The combined effects of a fine grid, redistribution of surface tension forces and velocity weighting are all needed to achieve sufficiently stable modelling of the meniscus. Depending on the amount of viscous dissipation, the spurious currents will either converge to a stable oscillation or else diverge. Therefore the model is not suitable for modelling static systems. But to achieve reliable results when modelling the dynamic meniscus the only necessary criterion is that the amplitude of the spurious currents is of a lower order than the mean

value of the flow in the gas and melt.

Chapter 7

Mathematical modelling of casting

7.1 Casting process

The casting process is described in detail in chapter 1. Applications are described in [6] and [34]. The ingot is cast vertically applying the gas slip method. The melt flows into the mould through an open ceramic top, the hot top, which covers the mould. The inner wall of the aluminium mould is covered by a graphite ring through which gas and oil are injected for lubrication and slip. Water cooling is applied in the secondary cooling zone below the open mould as the ingot is pulled downward[29]. In the process the melt surface forms a meniscus in the upper corner formed by the hot top and mould wall (figure 7.1).

The following factors are assumed to have an influence on the meniscus dynamics: Mould and ingot geometry, surface tension forces, casting velocity, primary cooling, secondary cooling, metallostatic head, slip gas flow rate, oxidation on the melt surface, lubrication, alloy content, and wetting between melt surface and mould wall.

It will be assumed that the lubricant oil forms a continuous layer and that small variations in this layer are unimportant in the casting process. As long as the ingot does not freeze to the mould the effects of variation in oil flow are assumed negligible. The effect of the lubricant on wetting in the mould, air flow and air gap is assumed to be constant.

Casting velocity and bath temperature are assumed constant in the casting simulations. Significant variations in bath temperature were observed during the casting experiments (chapter 2), but the variations were quite small.

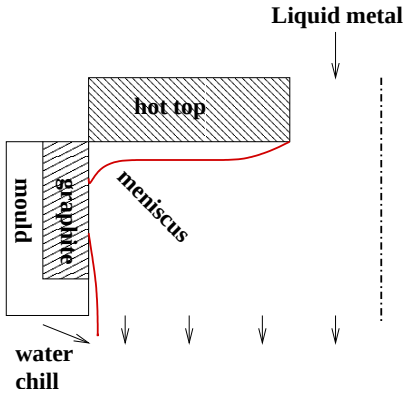

Figure 7.1: Meniscus and air gap in mould.

7.1.1 Internal energy equation in terms of enthalpy

The internal energy equation expressed in enthalpy per unit mass h is given in 5.1.3:

$$\frac{\partial \rho h}{\partial t} + \nabla \cdot \vec{u} \rho h = -\nabla \cdot \vec{q} + \frac{dp}{dt} + \overline{\overline{\tau}} : \nabla \vec{u} + \mathcal{S}, \tag{7.1}$$

where $\mathcal{S}$ represents the source terms. Then applying Fourier's law and assuming constant pressure (in consistency with (5.58)):

$$\frac{\partial \rho h}{\partial t} + \nabla \cdot \vec{u} \rho h = \nabla \cdot \frac{k}{c_p} \nabla h + \overline{\overline{\tau}} : \nabla \vec{u} + \mathcal{S}. \tag{7.2}$$

The latent heat will be included in the enthalpy, so the source term in (7.2) is therefore zero. Then by further assuming cylindrical symmetry, Newtonian flow, and incompressibility:

$$\begin{aligned} \rho \left(\frac{\partial h}{\partial t} + v_r \frac{\partial h}{\partial r} + v_z \frac{\partial h}{\partial z} \right) &= \frac{1}{r} \frac{\partial}{\partial r} \left(r \frac{k}{c_p} \frac{\partial h}{\partial r} \right) + \frac{\partial}{\partial z} \frac{k}{c_p} \frac{\partial h}{\partial z} \\ +2\mu \left[\left(\frac{\partial v_r}{\partial r} \right)^2 + \left(\frac{v_r}{r} \right)^2 + \left(\frac{\partial v_z}{\partial z} \right)^2 \right] &+ \mu \left(\frac{\partial v_z}{\partial r} + \frac{\partial v_r}{\partial z} \right)^2 . \end{aligned} \tag{7.3}$$

Relation between enthalpy and temperature

During solidification the latent heat of melting is released. The temperature dependent latent heat content is here expressed by ΔH, where L is the latent

heat of melting. Heat content in a mixture of solid and liquid at constant pressure is then expressed by

$$H = h + \Delta H = \int_{T_{ref}}^{T} c_P dT + \Delta H \tag{7.4}$$

H is total enthalpy and h is sensible heat. Since a mixture of phases are considered the values of ΔH and c_P used in the calculations are averaged values. Consider a volume element with fraction solidified f_s. Then

$$c_P(T) = (1 - f_s(T))c_P^l(T) + f_s(T)c_P^s(T), \quad T_s < T < T_l. \tag{7.5}$$

The latent heat content ΔH can be expressed as

$$\begin{aligned} \Delta H(T) &= L, T \geq T_l \\ \Delta H(T) &= L(1 - f_s(T)),\ T_s < T < T_l \\ \Delta H(T) &= 0, T \leq T_s \end{aligned} \tag{7.6}$$

Using the lever rule (complete diffusion in both solid and liquid phase) and assuming linear solidus and liquidus lines, the solid fraction and the temperature in a binary alloy can be expressed by the initial (C_0) and liquid (C_l) alloy concentrations [19];

$$\begin{aligned} f_s &= \frac{1}{1-k}\left(1 - \frac{C_0}{C_l}\right), \\ T &= T_l + \frac{C_l - C_0}{m}. \end{aligned} \tag{7.7}$$

Here m is the liquidus slope and k is the equilibrium distribution coefficient C_s/C_l, where C_s is the alloy concentration in the solid (see [38]). Expressing solid fraction by temperature:

$$f_s = \frac{1}{1-k}\left(1 - \frac{C_0}{C_0 + m_l(T - T_l)}\right). \tag{7.8}$$

The solid fraction f_s here varies inversely with the temperature T. So the latent heat term ΔH also varies inversely with temperature. The absolute value of the gradient $\partial f_s/\partial T$ is initially at T_l quite large and decreases rapidly as the temperature approaches T_s and $\Delta H \to 0$. An example is shown for an AlSi alloy with 0.96% Si in figure 7.2. In this case more than half the latent heat has been released when the temperature has fallen only 10% of the solidification temperature range. Both higher alloy content and non-equilibrium

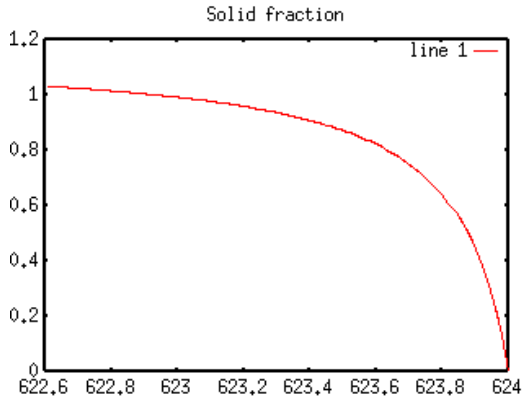

Figure 7.2: Solid fraction vs temperature (^{o}C) for Al0.96%Si.

conditions increases the effect of high initial release of latent heat. In the case of multiple alloy elements the solid fraction dependence on temperature gets more complicated. The conclusion is that using a linear relation between solid fraction and temperature can lead to considerable error in heat flow calculations. A more advanced nonlinear model is therefore applied.

The heat term (7.4) can by (7.5) and (7.6) be expressed as

$$\begin{aligned} H &= h + \Delta H \\ &= \int_{T_{ref}}^{T} \left[(1 - f_s(T))c_P^l(T) + f_s(T)c_P^s(T)\right] dT \\ &\quad + L(1 - f_s(T)) \end{aligned} \tag{7.9}$$

Then the latent heat content becomes

$$\Delta H = L - L \int_{T_{ref}}^{T} \frac{df_s}{dT}\, dT; \tag{7.10}$$

By relation (7.4) the *total heat capacity* can therefore be expressed as

$$\tilde{c}_P = c_P - L\frac{df_s}{dT}, \tag{7.11}$$

and

$$H = L + \int_{T_{ref}}^{T} \tilde{c}_P(T) dT. \tag{7.12}$$

With the enthalpy defined in this way the relation

$$\frac{\partial H}{\partial \eta} = \tilde{c}_P \frac{\partial T}{\partial \eta} \tag{7.13}$$

is valid for any variable η.

In the simulations of the casting process the Newtonian viscosity is made temperature dependent to model the rheology of the solidifying metal (see chapter 9). However, the gain of internal energy due to viscous work is negligible compared to the conductive term in the energy equation. The relation between viscous dissipation and thermal conduction can be expressed by the Brinkman number Br:

$$Br = \frac{\mu(\Delta v)^2}{k\Delta T}, \tag{7.14}$$

where Δv is characteristic velocity difference and ΔT is characteristic temperature difference. In the aluminium melt the temperature range in the sump is in the order of $100K$ while velocity differences are of the order of $0.1m/s$. Then by the applied viscosity and conductivity (see chapter 9) the Brinkman number is of the order of 10^{-11}, so the viscous dissipation may be neglected.

Under the conditions of cylindrical symmetry, negligible viscous dissipation, constant pressure, incompressibility, and with $\tilde{c}_P$ defined as in (7.11), relation (7.13) can be applied and the energy equation [8] can be expressed as;

$$\frac{\partial \rho H}{\partial t} + v_r \frac{\partial \rho H}{\partial r} + v_z \frac{\partial \rho H}{\partial z} = \frac{1}{r}\frac{\partial}{\partial r}\left(r \frac{k}{\tilde{c}_P}\frac{\partial H}{\partial r}\right) + \frac{\partial}{\partial z}\frac{k}{\tilde{c}_P}\frac{\partial H}{\partial z} \tag{7.15}$$

The heat capacity $\tilde{c}_P$ and the thermal conductivity k depend on the temperature T. So a relation giving the temperature as a function of enthalpy is needed. The relation is found by using Newton-Rhapson interpolation [35] on relation (7.12).

7.2 Solidification and air gap flow

In the Direct Chill casting process water cooling of the ingot is applied. The water is sprayed under pressure onto the ingot below the mould from a water channel, or reservoir, which is in contact with the mould (see figure 7.3). Consequently the mould is cooled by heat loss to both the water reservoir

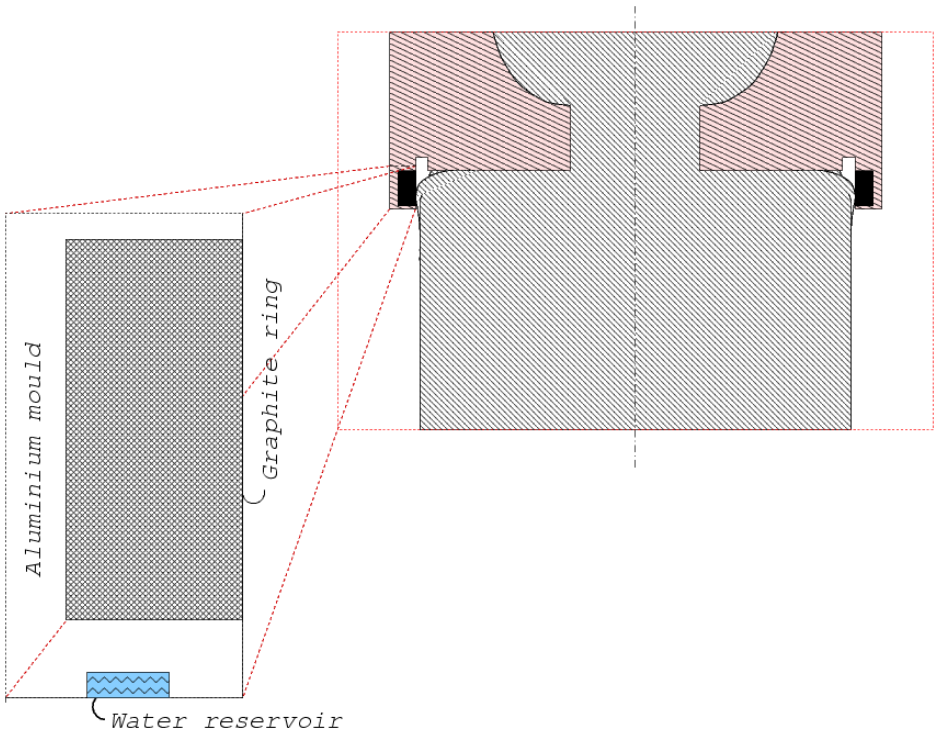

Figure 7.3: Intersection of mould wall with graphite ring and water channel.

and the air surrounding the mould. This compound heat loss constitutes the primary cooling, which cools the ingot in the upper part of the mould, as defined in 1.2.
Cooling water flows from the reservoir through spouts at the bottom of the mould, forming jets hitting the ingot surface right below the bottom of the mould. The region of impingement of the water jet and below is the secondary cooling zone.

7.2.1 Shrinkage

Some degree of radial contraction of the ingot will always occur during solidification due to shrinkage of the Al alloy as it solidifies. Pure Aluminium will decrease in volume by approximately 12% when it goes from liquid to solid (by [11] and [27]). The alloy elements can both increase and reduce the contraction, the most important being Si, which expands around 8% when going from liquid to solid. Most of the alloy elements will solidify separately in eutectic/peritectic/hypereutectic phases, thereby forming their own regular crystal structures and thus influencing the density of the solid to a greater degree than in the melt. Solid aluminium alloy densities can range

from $2600\,kg/m^3$ to $2900\,kg/m^3$ (by [11]). The density of the liquid Al alloys vary to a much smaller degree.

7.2.2 Solid lip and air gap

The cooling process described above leads to a characteristic ingot profile in the mould. A solid lip forms next to the mould wall in the primary cooling zone in the upper part of the mould (see 1.2). If the slid lip is strong enough, i.e. thick enough, solidification contraction will cause it to withdraw from the mould wall, thereby reducing heat transfer from the melt to the mould. In the secondary cooling zone, which can reach up above the bottom of the mould, the thickness of the solidified shell will lead to significant radial contraction. The contraction may lead to an air gap between the ingot and mould wall. The amount of contraction induced in the primary and secondary cooling zones are primarily determined by the casting velocity, the volume flow rate of cooling water, and the content of alloy elements.

7.2.3 Gas flow

In the modelling the gas inlet is placed above the meniscus to simulate the gas flow into the mould in the gas-slip process. The gas introduced must have some form of escape, and the possibilities are either upward discharge through the melt inlet in the hot-top or downward flow between the mould wall and the ingot surface. The amount of contraction, especially in the primary cooling zone, will effect the downward gas flow rate. At the same time the shape of the meniscus will effect the heat transfer in the mould, thus influencing the solidification rate of the metal in the mould. The process in the mould is therefore a complicated and unstable coupled thermo mechanical system. Both a model for the solidification contraction and a model for the gas flow rate must therefore be included in our modelling system.

7.2.4 Contraction model

A simple contraction model is applied. The radial contraction is assumed proportional to the width of the solid cross section. The assumption is made that the contraction starts at a certain solid fraction f_{sc} for temperature T_{sc}[1]. The total fractional contraction from liquid to solid is denoted by C. The

[1]This idea can be related to the concept of the point of coherency

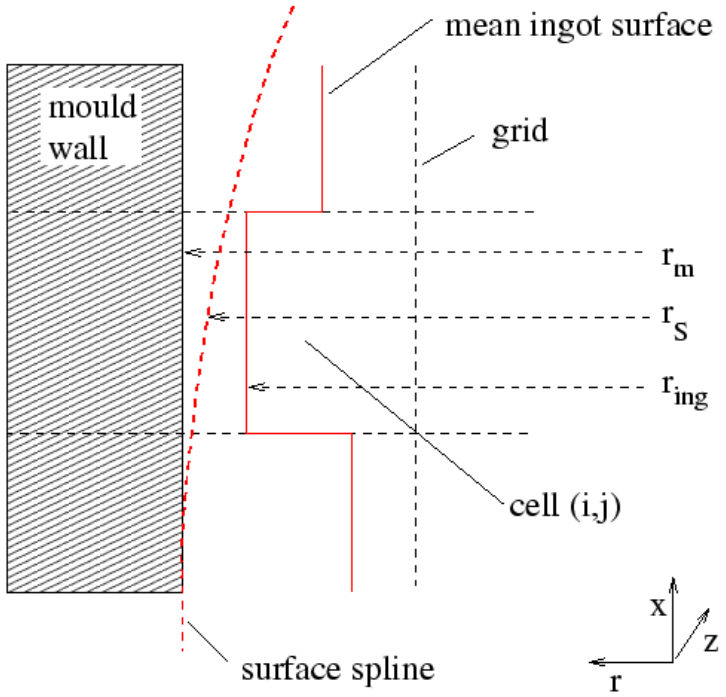

Figure 7.4: Geometry in air gap calculation.

radial contraction Δr at height x_i can then be expressed (see figure 7.4)

$$\Delta r(x_i) = C \int_0^{\overline{r_S(x_i)}} H(T_{sc} - T(r, x_i)) \frac{f_s(T(r, x_i)) - f_{sc}}{1 - f_{sc}}\, dr, \tag{7.16}$$

where H is the Heaviside or step function and $\overline{r_S(x_i)}$ is mean spline surface radial value at level x_i. Then the mean ingot surface at level x_i (see figure 7.4) is

$$r_{ing}(x_i) = r_m(x_i) - (\overline{r_S(x_i)} + \Delta r(x_i)). \tag{7.17}$$

7.2.5 Air gap flow rate model

The calculation of the gas flow rate from the air pocket through the gap is based on the contraction model described above. The flow of the gas through the air gap is assumed to be fully developed Poiseuille flow. The ratio of pressure to gravitational forces driving the flow (the product of the Euler and Froude numbers $Eu \times Fr$) is of the order of 10^2. Therefore the effect of gravity can be neglected. Combining the equation of continuity 6.1 and equations of momentum 6.2, the flow equation for gas flow in an air gap

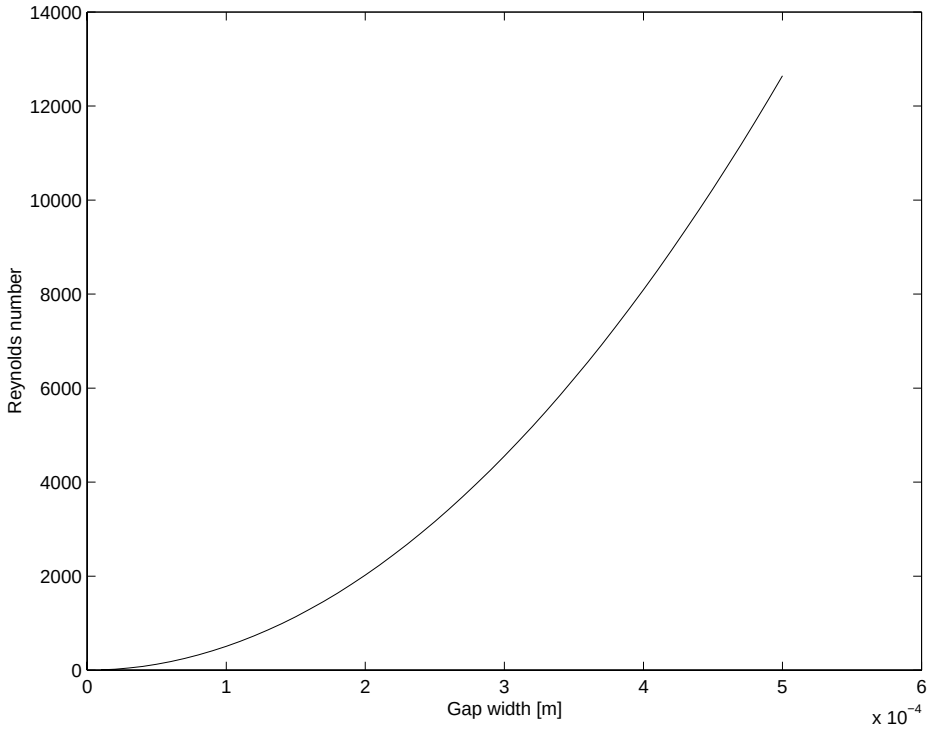

Figure 7.5: Reynolds number vs. gap width at mould wall.

cell becomes (see figure 7.4)

$$\frac{1}{r}\frac{d}{dr}\left(r\frac{d}{dr}u(r,x_i)\right)=\frac{1}{\mu}\frac{dp}{dx_i}=const. \tag{7.18}$$

With r_m as the inner radius of the mould wall and $r_{ing}(x_i)$ as the outer radius of the ingot, the corresponding boundary conditions are

$$u(r_m)=0, \tag{7.19}$$

$$u(r_{ing}(x_i))=0. \tag{7.20}$$

Here it is assumed that the ingot casting velocity is negligible in comparison to the velocity of the slip gas flow.

The solution is (by [73])

$$u(r,x_i)=\frac{1}{4}\left[\left(r_m^2-r^2\right)-\left(r_m^2-r_{ing}(x_i)^2\right)\frac{\ln\frac{r}{r_m}}{\ln\frac{r_{ing}(x_i)}{r_m}}\right]\frac{1}{\mu}\frac{dp}{dx_i}, \tag{7.21}$$

giving the cell mean gas velocity

$$\overline{u(x_i)}=\left[\frac{1}{6}\left(r_m^2+r_{ing}(x_i)^2+r_m r_{ing}(x_i)\right)+\frac{1}{4}\frac{r_m^2-r_{ing}(x_i)^2}{\ln\frac{r_{ing}(x_i)}{r_m}}\right]\frac{1}{\mu}\frac{dp}{dx_i}. \tag{7.22}$$

The logarithmic term in 7.22 will lead to numerical error. Therefore the Taylor expansion of the logarithm is applied. Through a subsequent binomial expansion the result is

$$\overline{u(x_i)}=-\frac{1}{\mu}\frac{dp}{dx_i}\frac{1}{24}\left[\frac{3}{2}+\frac{1}{2}\frac{r_{ing}(x_i)}{r_m}\right](r_m-r_{ing}(x_i))^2+\mathcal{O}\left((r_m-r_{ing}(x_i))^3\right). \tag{7.23}$$

At very small air gaps ($r_{ing}/r_m\approx 1$), the flow will approximately correspond to Poiseuille flow between two parallel plates.

The total pressure drop Δp over the air gap

$$\sum_i\frac{dp}{dx_i}=\Delta p, \tag{7.24}$$

is assumed to equal the metallostatic head at the upper contact point of the meniscus (at the level of the bottom of the hot top). And the volumetric flow rate V_f through the gap can be expressed:

$$V_f=\overline{u(x_i)}(r_m-r_{ing}(x_i))\Delta z, \tag{7.25}$$

where Δz is the depth of the computational cell (see figure 7.4).

Continuity gives the condition of equal cell volumetric gas flow for all cells in the air gap. Equations 7.23, 7.24, and 7.25 then give a complete set of equations for the gas volume flow rate in the gap.

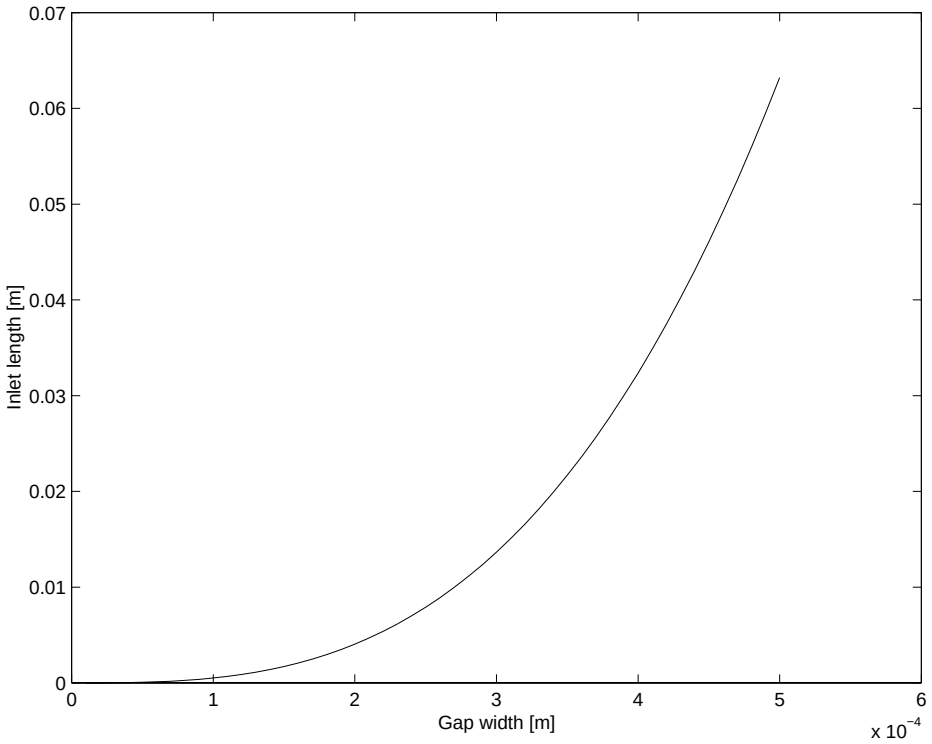

Figure 7.6: Inlet length vs. gap width at mould wall.

Turbulence The turbulent limit for this model can be seen in figure 7.5, which displays Reynolds number vs gap width for a gap of length 18mm and with a metallostatic head of 150 mm, characteristic values in our casting process. The Reynolds number Re is here

$$Re = \frac{2U\rho^g(r_m - r_{ing})}{\mu}, \tag{7.26}$$

where U is air gap velocity and ρ^g gas density. For gaps of width smaller than 0.1mm the Reynolds number is less than 1000. So the laminar Poiseuille flow model is valid for gaps of width smaller than this. From the fluid mechanical inlet length

$$L_{ev} \approx 0.01Re(r_m - r_{ing}), \tag{7.27}$$

the flow will be fully developed before 1 mm (figure 7.6), so for laminar flow the condition of fully developed Poiseuille flow in the gap is also fulfilled.

7.2.6 Melt flow

Stress model

A Newtonian flow model is used in the domain of the melt. The viscosity $\mu(T)$ is made temperature dependent to simulate the rheology of the solidifying metal. For temperatures above the onset of solidification a normal temperature dependent viscosity is applied. Beyond this point the viscosity increases rapidly with temperature up to the point of onset of contraction T_{SC} (as defined in the contraction model 7.2.4). For temperatures lower than T_{SC} the velocity is set constant and equal to the ingot casting velocity. This is quite a simple model. The nature of the metal becomes first elastic/plastic as it solidifies. These flow regimes can not be properly modelled by the Newtonian viscous model. Incorporating other models such as Hooke's law [57] for elasticity would improve on the result. However, the simulation results show that using the Newtonian flow model with temperature dependent viscosity is sufficient to study meniscus dynamics.

Buoyancy

To facilitate mass conservation the density of the aluminium is held constant in the simulations. If this was not done the stability of the solution would be worsened and more iterations would need to be performed to achieve convergence at each time step. With a Rayleigh number of $\sim 10^1$, as observed in the casting simulations (chapter 9), some natural convection is to be expected. The natural convection is however assumed to have negligible effect on meniscus dynamics. The flow in the meniscus region is dominated by the effects of the meniscus movement.

7.2.7 Radiation considerations

Radiation between the mould and the ingot will be present in the airgaps. To assess the effect the radiation has on the heat flow we apply the relation for radiation between non-black bodies at different temperatures [8]. Q_{12} is the heat flow rate between surfaces 1 and 2 of areas A_1 and A_2. F_{12} is the view factor, σ is the Stefan-Bolzmann constant, e is emissivity and T is temperature. Then

$$Q_{12} = A_1 \mathcal{F}_{12} \sigma (T_1^4 - T_2^4), \tag{7.28}$$

$$\frac{1}{A_1 \mathcal{F}_{12}} = \frac{1}{A_1 F_{12}} + \frac{1}{A_1}\left(\frac{1}{e_1} - 1\right) + \frac{1}{A_2}\left(\frac{1}{e_2} - 1\right).$$

With a small gap of width $r_m - r_{ing} \ll r_m$ (see figure 7.4) the surface areas are approximately equal: $A_1 \approx A_2$. By [8], the view factor F_{12} is in this case approximately 1. The emissivity e_1 of the graphite surface is close to 1, assuming an approximately black surface. The emissivity e_2 of the oxidized aluminium surface is assumed to be in the region of 0.1. Then an approximation to the heat flux q_{12} between the ingot and the mould can be expressed as

$$q_{12} \approx \frac{\sigma}{10}(T_1^4 - T_2^4). \tag{7.29}$$

During measurements the temperature of the graphite ring in the mould was in the region of $400K$. To check the influence of radiation on heat loss the temperature of the ingot is assumed to be at the solidus level. The radiation calculated will then be above the actual radiation present. The resulting radiative heat flux is $q_{12} \approx 2 \cdot 10^3\ W/m^2$. This flux is equal to the heat flux owing to conduction between the ingot surface and the mould through an airgaps of approximately 5mm. For the laminar Poiseuille flow model the air gap must be $<< 1mm$. Since the conductive heat flux has an inverse linear dependence on the air gap the conductive flux will be at least one order of magnitude larger than the radiative flux for this air gap size. Also, the lubricative oil present in the gap can possibly reduce the radiation, since some of the radiative energy will be spent heating the oil. So neglecting radiation is consistent with the assumption of fully developed laminar air gap flow.

7.2.8 Numerical implementation

Heat flow

The heat transfer from the ingot to the mould wall is adjusted by altering the conductivity according to the contraction calculated by equation (7.16). The computational cells inside the resulting gap are given the thermal conductivity of the gas and a density weighted heat capacity. The heat capacity at constant pressure in computational cell L with density $\rho(L)$ is designated $c_P(L)$. The constant heat capacity and density of gas are respectively c_P^g and ρ^g. Then the weighted heat capacity is expressed as $c_P(L) = c_P^g\, \rho^g/\rho(L)$.

In the cells containing the new ingot surface at $r(x) = R(x)$, a harmonic mean value is used for the thermal conductivity and an averaged and density weighted heat capacity are used (see figure 7.7). Maximum radius in the cell is r_{max} and minimum is r_{min}. Cell width is r_w. With air at $r > R$, g denoting gas phase and a denoting aluminium phase, the conductivity in cell number

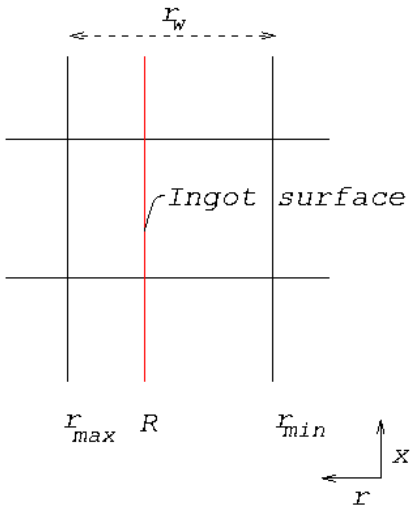

Figure 7.7: Ingot surface intersecting grid cell.

L is defined

$$k(L) = \hat{k}(L) = 1/\left(\frac{r_{max}(L) - r_i}{r_w k^g(L)} + \frac{r_i - r_{min}(L)}{r_w k^a(L)}\right); \tag{7.30}$$
$$r_i = r_{max}(L) \; for \; R < r_{min}(L),$$
$$r_i = r_{min}(L) \; for \; R > r_{max}(L),$$
$$r_i = R \; otherwise.$$

The corresponding altered heat capacity c_P is

$$c_P(L) = \overline{c_P(L)}\frac{\overline{\rho(L)}}{\rho(L)}, \tag{7.31}$$
$$where \; for \; a \; value \; \phi : \tag{7.32}$$
$$\overline{\phi(L)} = (r_{max} - r_i)\phi^g(L) + (r_i - r_{min})\phi^a(L).$$

with r_i defined as in equation (7.31). To see that the energy is still conserved we need to study the equation of enthalpy and its definition. With the definition (7.12) the enthalpy is

$$H = L + \int_{T_{ref}}^{T} \overline{c_P(T)}\,\overline{\rho}/\rho \; dT. \tag{7.33}$$

In the region of application of the contraction model there is only aluminium alloy phase, so $\rho = \rho^a = const.$ Shifting the reference point ($H = H - L =$

$\int_{T_{ref}}^{T} \overline{c_P(T)}\,\overline{\rho}/\rho\; dT$), we can therefore define enthalpy per volume H_V as

$$H_V = \rho H = \int_{T_{ref}}^{T} \overline{c_P(T)}\,\overline{\rho}\; dT. \tag{7.34}$$

Defining the heat capacity per volume as $c_{PV} = \overline{c_P}\ \overline{\rho}$, and applying the new definitions (7.31) and (7.33) to the enthalpy equation (7.15), we get the equation for enthalpy per volume:

$$\frac{\partial H_V}{\partial t} + v_r\frac{\partial H_V}{\partial r} + v_z\frac{\partial H_V}{\partial z} = \frac{1}{r}\frac{\partial}{\partial r}\left(r\frac{\hat{k}}{c_{PV}}\frac{\partial H_V}{\partial r}\right) + \frac{\partial}{\partial z}\frac{\hat{k}}{c_{PV}}\frac{\partial H_V}{\partial z}, \tag{7.35}$$

which is a physically sound equation. So we may assume that the energy is conserved through the alteration made in (7.31) and (7.33).

Ingot temperature

In the multiphase model the temperature at each grid point will be the a mean cell temperature where the temperature is found by implicit numerical integration of relation 7.13:

$$T = T_{ref} + \int_{H_{ref}}^{H} c_P(T(H)))\; dH, \tag{7.36}$$

where the heat capacity c_P is given by 7.33. So the calculated temperature in an intersected cell will be unequal to the average temperature of the metal in the cell. This difference will lead to an error in the calculation of solidification contraction in 7.16. Therefore a model is needed to calculate the mean metal temperature in the intersected cell. The calculation of approximate average metal temperature can be made using the one dimensional condition of energy conservation. For a mean ingot surface configuration as in figure 7.8 the heat flux is assumed to be horizontal. This assumption is only accurate for vertical isotherms, so it is quite a rough approximation. However, because of the mould cooling the isotherms at the ingot surface will be more horizontal than vertical. So the error due to non-vertical isotherms is probably not very large. Another possibly larger source of error is the release of latent heat as the metal solidifies. But both sources of error will increase with the coarseness of the grid, and since we use a fine grid in the meniscus area we will assume the approximation of constant horizontal energy flux at the ingot surface to be valid. This can be expressed:

$$\begin{aligned} q = k_{Al}(T_W)\frac{T_w - T_W}{r_w - r_W} &= k_{Al}(\overline{T_P})\frac{T_S - T_w}{r_S - r_w} \\ &= k_g\frac{T_e - T_S}{r_e - r_S} = k_{wall}\frac{T_E - T_e}{r_E - r_e}, \end{aligned} \tag{7.37}$$

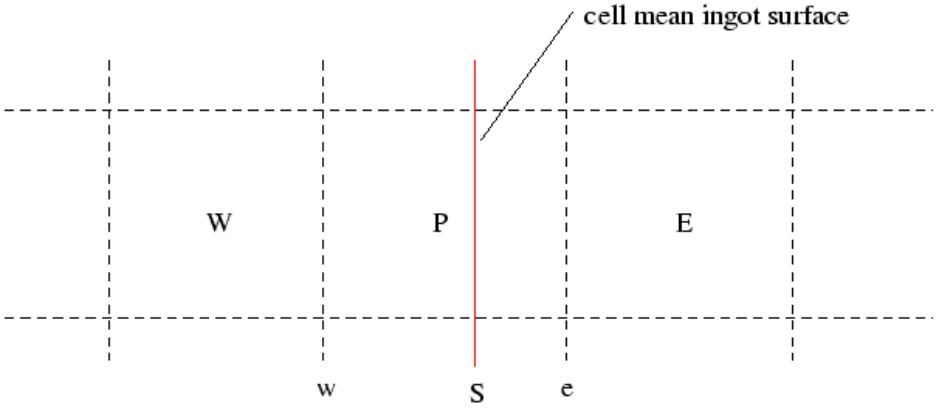

Figure 7.8: Mean ingot surface in computational grid.

giving the matrix equation for the unknown temperatures

$$\begin{bmatrix} \frac{k_{Al}(T_W)}{r_w - r_W} + \frac{k_{Al}(\overline{T_P})}{r_S - r_w} & -\frac{k_{Al}(\overline{T_P})}{r_S - r_w} & 0 \\ \frac{k_{Al}(T_W)}{r_w - r_W} & \frac{k_g}{r_e - r_S} & -\frac{k_g}{r_e - r_S} \\ \frac{k_{Al}(T_W)}{r_w - r_W} & 0 & \frac{k_{wall}}{r_E - r_e} \end{bmatrix} \begin{bmatrix} T_w \\ T_S \\ T_e \end{bmatrix} = \begin{bmatrix} \frac{k_{Al} T_W}{r_w - r_W} \\ \frac{k_{Al} T_W}{r_w - r_W} \\ \frac{k_{Al}(T_W) T_W}{r_w - r_W} + \frac{k_{wall} T_E}{r_E - r_e} \end{bmatrix} \tag{7.38}$$

And the mean metal temperature in the intersected cell P is:

$$\overline{T_P} = \frac{T_S + T_w}{2}. \tag{7.39}$$

Since the thermal conductivity of the aluminium is dependent on temperature, the equation set 7.38 and 7.39 must be solved iteratively.

Melt flow

A normal volume mean calculation of the isotropic viscosity in a computational cell will give too high a viscosity in cells containing both gas and aluminium melt. Then the transfer of momentum between melt and gas will be too great. To avoid this effect harmonic mean is applied on the form:

$$\mu = \left(\frac{\alpha}{\mu_g} + \frac{1 - \alpha}{\mu_{Al}} \right)^{-1}. \tag{7.40}$$

The physical basis for the use of a harmonic mean viscosity can be found by looking at a horizontal shear flow with shear in equilibrium. In the flow is a flat interface parallel to the flow, as in figure 7.9. At equilibrium, by

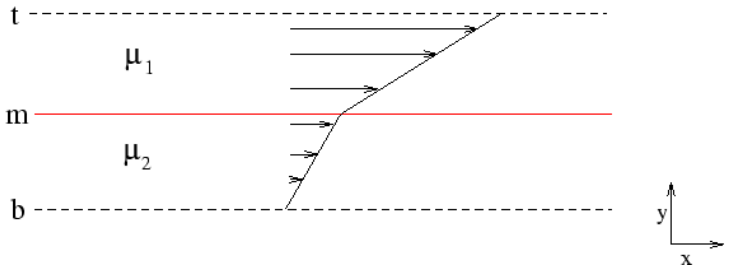

Figure 7.9: Shear flow with parallel interface.

Newton's third law, the shear force is constant. Therefore, defining mean shear force as $\hat{\mu}\frac{\Delta u}{\Delta y}$ with mean viscosity $\hat{\mu}$:

$$F = \hat{\mu}\frac{u_t - u_b}{y_t - y_b} = \mu_1\frac{u_t - u_m}{y_t - y_m} = \mu_2\frac{u_m - u_b}{y_m - y_b}$$
$$\Downarrow$$
$$\hat{\mu} = \frac{y_t - y_b}{\frac{y_t - y_m}{\mu_1} + \frac{y_m - y_b}{\mu_2}}.$$

In the simulations the angle of the surface varies, but small sections of surface are approximately linear. And the flow is mainly parallel to the surface. Then a transformation of variables will give the same conditions as in figure 7.9, so the calculation above is applicable to our free surface model. With the void fraction α corresponding to $(y_t - y_m)/(y_m - y_b)$ the result is the function 7.40.

Gas flow

In the simulation the inflow of gas (see 7.2.3) is adjusted according to the volume flow rate of gas through the contraction gap. With v_{in} as the initial gas inflow velocity in the inlet region of width Δx_{in} the modified inflow velocity $\tilde{v}_{in}$ becomes

$$\tilde{v}_{in} = v_{in} - \frac{V_f}{\Delta x_{in}\Delta z}. \tag{7.41}$$

Chapter 8

Numerical implementation in FLUENT

The numerical implementation of the mathematical models presented in the previous chapters is described here. The FLUENT CFD solver has been applied into which the cylindrical Method of Tensions has been implemented.

8.1 Solution process

As described in the chapter on mathematical methods (chapter 7), the governing equations are expressed in cylindrical coordinates. So 3D effects are neglected. Both the NS equations (6.1 - 6.2) and the energy equation (7.15) are applied on conservative (or divergence) form, facilitating the conservation properties of the method (see 4.1). The stability problems that might result are attempted resolved by more stable interpolation techniques in the discretization (see previous chapters).

Implicit in time The governing equations are integrated implicitly in time, giving unconditional stability and a more robust solver. However, since this technique is only accurate to the first order in time, small time steps are needed to ensure accuracy.

Power law The spacial discretization of the momentum and heat equations ((6.2) and (7.15)) is performed using Finite Volume discretization ([1]) together with the Power Law by Patankar [47] for interpolation. The Power Law takes into account the relation between advection and diffusion, repre-

sented by the cell Peclet number:

$$Pe = \frac{\rho U}{\Gamma/\delta x}, \tag{8.1}$$

where Γ is the diffusion coefficient and δx is characteristic cell size. For $Pe > 10$, when advection dominates the flow, upwind differencing is applied, while for smaller Pe the amount of upwinding decreases with decreasing Pe. The scheme is accurate only to the first order in space, but is much more stable than higher order methods such as QUICK [41].

Computational domain The computational domain is shown in figure 8.1. The height of the melt inflow channel (distance from top of domain to bottom of hot-top - 129mm) is comparable to the metal height in the experimental test case (so that differences in melt inflow properties do not have a significant effect on the flow in the meniscus region). The surface of the melt at the top of the channel is however not included, so melt surface dynamics at the top of the mould are not included in the modelling simulations[1]. The geometry of the computational domain goes far below the impingement zone so that the bottom boundary conditions have little influence on the solidification and melt flow. Otherwise the dimensions of the domain are approximately the same as in the experimental casting tests.

Computational grid Staggered grid is applied in FLUENT, as in the original MAC method (4.1). To model the meniscus dynamics with sufficient accuracy it is necessary to have a finer grid in this region than in the rest of the ingot, where only heat and metal flow are modelled. Therefore a regular non-uniform grid is applied. The computational grid is shown overlying the domain outline in figure 8.2.

Discretized momentum equations With (I, J) denoting the pressure grid and (i, j) denoting the staggered grid (see figure 8.3), the discretized momentum equations can be expressed as

$$\begin{aligned} a_{i,J}u_{i,J} &= \sum a_{nb}u_{nb} + (p_{I-1,J} - p_{I,J})A_{i,J} + b_{i,J}, \\ a_{I,j}v_{I,j} &= \sum a_{nb}v_{nb} + (p_{I,J-1} - p_{I,J})A_{I,j} + b_{I,j}. \end{aligned} \tag{8.2}$$

Here the a and A are coefficients depending on material parameters and old velocities while the b terms contain source terms such as body forces and a

[1]Including variations in pressure linked to surface oscillations might however be attempted by varying the reference pressure

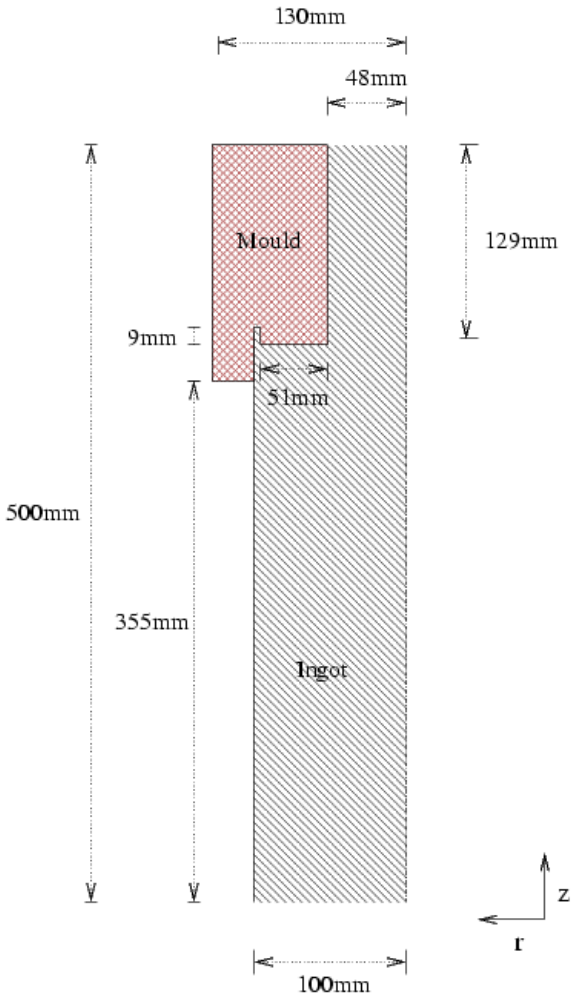

Figure 8.1: Computational domain.

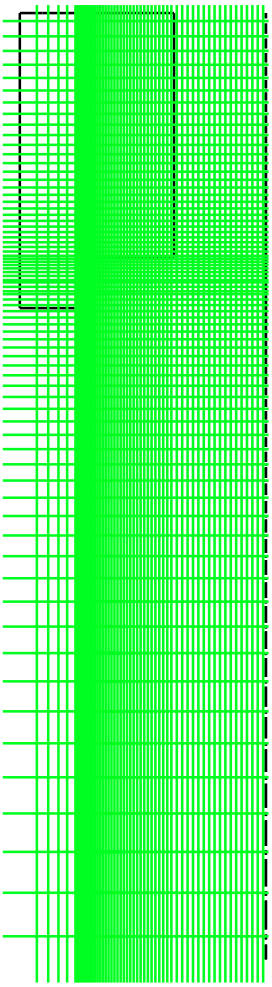

Figure 8.2: Computational (pressure) grid (50×75 cells) overlying domain outline. Finer grid in meniscus region.

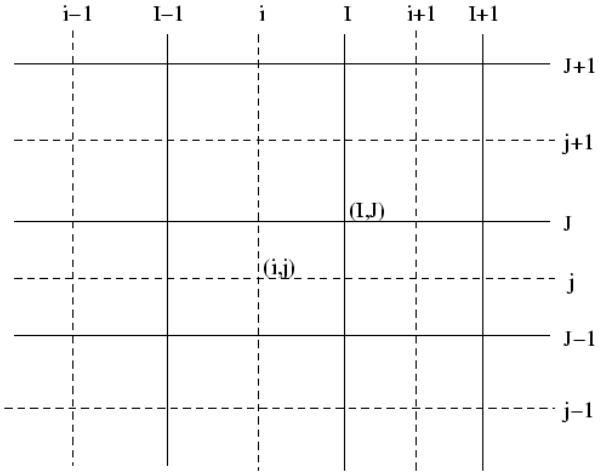

Figure 8.3: Staggered grid. Grid points (I,J) and (i,j) indicated.

term dependent on the old velocity. *nb* denotes neighbour cells. Included in the coefficients is also the effect of sub-grid turbulence, simulated by applying the Large Eddy Simulation model (see description in 5.1.2).

SIMPLE

Patankar's Semi Implicit Method for Pressure-Linked Equations (SIMPLE) is applied to solve the set of discretized Navier-Stokes equations. The SIMPLE algorithm may now be explained as follows: A initial pressure field p^* is guessed from which the velocity components u^* and v^* are found by solving the set of discretized momentum equations (8.2). The correct fields may now be expressed as

$$\begin{aligned} p &= p^* + p', \\ u &= u^* + u', \\ v &= v^* + v', \end{aligned} \tag{8.3}$$

where p' u' and v' are corrections to the estimated values. With the matched p^*, u^* and v^* the momentum equations may be expressed

$$\begin{aligned} a_{i,J}u'_{i,J} &= \sum a_{nb}u'_{nb} + (p'_{I-1,J} - p'_{I,J})A_{i,J} + b_{i,J}, \\ a_{I,j}v'_{I,j} &= \sum a_{nb}v'_{nb} + (p'_{I,J-1} - p'_{I,J})A_{I,j} + b_{I,j}. \end{aligned} \tag{8.4}$$

An adjustment is now made. The equations are solved under the constraint that the terms $\sum a_{nb}u'_{nb}$ and $\sum a_{nb}v'_{nb}$ are zero. In a converged velocity field

this is true by definition, but in the correction equations this constitutes an inaccuracy. Therefore this approximation destabilizes the system of equations.

With the assumption of negligible sum of neighbour velocity terms the correction equations become:

$$\begin{aligned} a_{i,J}u'_{i,J} &= (p'_{I-1,J} - p'_{I,J})A_{i,J} + b_{i,J}, \\ a_{I,j}v'_{I,j} &= (p'_{I,J-1} - p'_{I,J})A_{I,j} + b_{I,j}, \end{aligned} \tag{8.5}$$

and subsequently (by 8.3)

$$\begin{aligned} a_{i,J}u_{i,J} &= a_{i,J}u^*_{i,J} + (p'_{I-1,J} - p'_{I,J})A_{i,J} + b_{i,J}, \\ a_{I,j}v_{I,j} &= a_{I,j}v^*_{I,j} + (p'_{I,J-1} - p'_{I,J})A_{I,j} + b_{I,j}, \end{aligned} \tag{8.6}$$

giving the correct velocities in terms of approximate velocities and pressure corrections.

The expressions for the correct velocities may now be substituted into the discretized continuity equation (6.1) which may subsequently be solved for the pressure corrections. Then the correct pressure is calculated by (8.3) and correct velocities are found by (8.6). The process is normally iterated until the residuals become smaller than a chosen small parameter.

Relaxation To stabilize the solution process under-relaxation (with under-relaxation factors w_ϕ between 0 and 1) of the correction equations is therefore applied:

$$\begin{aligned} p^{new} &= p^* + w_p p', \\ u^{new} &= w_v u^n + (1 - w_v)u^{n-1}, \\ v^{new} &= w_v v^n + (1 - w_v)v^{n-1}. \end{aligned} \tag{8.7}$$

u^n and v^n are the corrected velocity components without relaxation after the n^th iteration in time.

Discretization and solution of energy equation

The internal energy equation in enthalpy (7.15)[2] is integrated implicitly in time, and again the power law is applied for velocity interpolation in the finite volume discretization. The solution method applied to the discretized energy equation is the same as the one used for the discretized pressure correction equation, as the equations are of the same type.

[2]The equation may be applied on conservative form by the assumption of incompressibility.

Tri-diagonal matrix algorithm (TDMA)

The direct TDMA[3] method [66] is applied in the iterative solution of the discretized equation. One row of computational cells is solved at a time for the dependent variables. Each row of cells gives a set of coupled equations constituting a tri-diagonal matrix equation which is solved by TDMA.

Multigrid (MG) acceleration

The number of iterations necessary for convergence increases with the amount of nodes in a line, and is quite slow for the elliptical equations for pressure correction and enthalpy. The multigrid method [18] solves the discretized equations on multiple grid sizes. By increasing grid size the boundary information is spread more quickly through the computational domain, facilitating convergence. Subsequent iterations with a smaller grid then improves the accuracy. By applying this technique the solution process becomes a lot faster without loss of accuracy.

With Multigrid the sweep direction is arbitrary, since the boundary conditions are quickly spread across the computational domain when coarse grids are applied.

8.1.1 Boundary conditions

Fluid flow

Fluid flow into or out of the computational domain is imposed by velocity boundary conditions. The temperature and phase (gas or metal) are also specified at these boundaries.

Metal flow For differing casting velocities the appropriate metal velocity boundary conditions are chosen at the top of the melt inlet channel and at the bottom of the domain. To improve stability outlet cells are included in the upper boundary cells next to the mould (see figure 8.1). Outlet boundary conditions impose zero gradient normal to the boundary for all flow variables.

Gas flow Gas flow into or out of the gas pocket (determined by 7.2.3) is imposed by gas velocity boundary conditions on the mould wall above the meniscus or at the top of the groove under the hot top.

[3]TDMA is also known as the Thomas algorithm

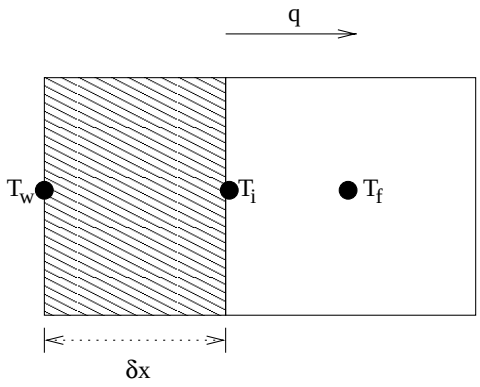

Figure 8.4: External heat transfer boundary. Boundary cell at left.

Heat flow

Hot-top The hot-top is modelled as a conducting wall , for which the 2D conduction equation is solved:

$$\rho_w c_w \frac{\partial T}{\partial t} = \nabla \cdot k_w \nabla T + Q, \tag{8.8}$$

where Q is the volumetric heat source and ϕ_w is the value of ϕ in the wall. Harmonic mean conductivity is applied at the interfaces between wall cells and fluid cells. At the upper boundary of the hot-top the heat flux is set to zero[4], and a heat transfer boundary is applied at the exterior of the hot-top. External heat transfer boundary conditions calculate the heat flux q by the set of equations

$$q = \frac{k_w}{\delta x}(T_w - T_i) = h_f(T_i - T_f), \tag{8.9}$$

$$k_w/\delta x = h_w. \tag{8.10}$$

The position of the variables are explained by figure 8.4. Heat transfer across the wall h_w and outer wall temperature T_w are given as boundary condition. With temperature T_f known the set of equations (8.10) can be solved for the heat flux q which may be substituted into the discretized internal energy equation.

Mould wall Both the graphite ring and encapsulating aluminium are modelled as conducting walls. Resistance to heat transfer between the graphite

[4]Zero heat flux imposes zero temperature gradient normal to the boundary

and aluminium is modelled by inserting a boundary of cells with appropriately chosen conductivities. An external heat transfer boundary is applied at the exterior of the mould wall as was done for the hot-top.

The effect of the water reservoir in the mould wall (see figure 1.4(b)) is modelled by imposing appropriate an appropriate heat transfer boundary at the bottom of the mould wall. Further, the amount of primary cooling is controlled by the contraction model presented in section 7.2.

Secondary cooling The secondary cooling is modelled by imposing external heat transfer boundary conditions on the ingot wall.

The numerical values applied in the thermal boundary conditions are found empirically by adapting the values so that the experimentally measured temperatures are achieved on the ingot boundaries. Initiation of the temperature field is discussed in 9.1.3.

Chapter 9

Casting simulations

9.1 Initiation

9.1.1 Meniscus shape

The initial meniscus shape is calculated by a method described by Mortensen [45]. The method is based on parameterization of the meniscus by arc length s, as in the spline interpolation. The second order Taylor expansion of the slope θ along the meniscus (see figure 9.1) is:

$$\theta_{i+1} = \theta_i + \frac{d\theta}{ds}_{s=s_i} \Delta s + \frac{1}{2} \frac{d^2\theta}{ds^2}_{s=s_i} \Delta s^2. \tag{9.1}$$

Assuming a constant surface tension coefficient σ and hydrostatic metal pressure $\rho g z$, the relation between curvature and pressure jump Δp may be expressed

$$\Delta p = p_0 + \rho g z - p_e = \sigma \left(\kappa_1 + \kappa_2 \right). \tag{9.2}$$

Here p_0 is the atmospheric pressure, p_e is the pressure in the gas pocket above the meniscus and the κ_i are the principal curvatures.

By the definition of curvature [70] the principal curvatures are (again see figure 9.1)

$$\begin{aligned} \kappa_1 &= \frac{d\theta}{ds}, \\ \kappa_2 &= \frac{sin\theta}{r}. \end{aligned} \tag{9.3}$$

Then by (9.2) and (9.3)

$$\frac{d\theta}{ds} = \frac{p_0 + \rho g z - p_e}{\sigma} - \frac{\sin\theta}{r}. \tag{9.4}$$

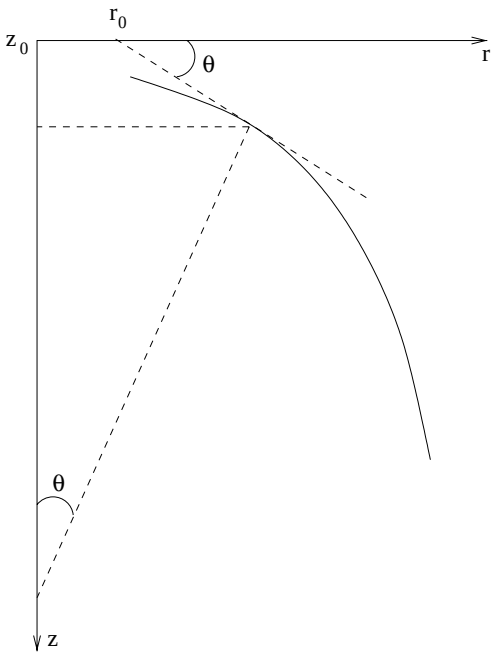

Figure 9.1: Meniscus angle.

The radial distance r and the depth z along the meniscus may be calculated by the following integrals:

$$r = r_0 + \int_0^s \cos\theta ds \qquad (9.5)$$

and

$$z = z_0 + \int_0^s \sin\theta ds. \qquad (9.6)$$

Boundary conditions needed are the contact angle at the upper contact point (θ_0) of the meniscus and the liquid depth z_0[1] and radial distance (r_0) at this point. The subsequent development of radius and depth along the meniscus may be calculated by taking the second order expansions of (9.5) and (9.6):

$$r_{i+1} = r_i + \cos\theta_i \Delta s - \frac{\sin\theta_i}{2} \frac{d\theta}{ds}_{s=s_i} \Delta s^2, \qquad (9.7)$$

$$z_{i+1} = z_i + \sin\theta_i \Delta s + \frac{\cos\theta_i}{2} \frac{d\theta}{ds}_{s=s_i} \Delta s^2. \qquad (9.8)$$

The set of equations (9.1), (9.4), (9.7) and (9.8) together with the appropriate boundary conditions may now be solved to obtain the meniscus shape. The system of equations giving the meniscus shape is not very stable, and physically valid solutions can only be found for a narrow range of parameters when the method above is applied. This is however sufficient for initiation of a meniscus shape. A more extensive analysis on equilibrium or static meniscus shapes has been performed by Baker and Grandfield [4].

Nondimensionalization of meniscus shape

Based on the equation for meniscus slope (9.1) the Π theorem is here applied to find the non dimensional parameters governing the static meniscus

[1] The metal surface in the mould is at $z = 0$

shape. The shape is given by the curvature $d\theta/ds$ which has the following non dimensional dependence

$$\frac{d\theta}{ds} = \kappa_1 = f(z_0, r_0, g, \Delta p, \rho, \sigma, s), \tag{9.9}$$

$$\Delta p = p_e - p_0. \tag{9.10}$$

By the Π theorem, there is a minimum of five independent dimensionless parameters (number of dimensional parameters minus number of fundamental dimensions). In this case the following five independent dimensionless parameters may be constructed:

$$\Pi_1 = z_0\kappa_1 = f(\Pi_2, \Pi_3, \Pi_4, \Pi_5) = f(\frac{\Delta p}{\rho g z_0}, \frac{\sigma}{\rho g z_0^2}, \frac{r_0}{z_0}, \frac{s}{z_0}). \tag{9.11}$$

Properties of dimensionless parameters The first dimensionless parameter Π_1, is the scaled first principal curvature[2]. The second parameter, Π_2, indicates the relation between hydrostatic forces and gas pressure difference. This parameter subsequently has a strong influence on the meniscus profile. The third parameter, Π_3, indicates the strength of the surface tension forces relative to the metallostatic head, so this parameter influences the curvature. The fourth parameters indicates scaling of the system while the last parameter indicates scaling along the meniscus.

For large Π_3 small variations in curvature are needed to balance the pressure difference, while for small Π_3 the case is the opposite. On the other hand, for large Π_2 (i.e. significantly larger than 1), the meniscus profile will be less smooth than for smaller Π_2. So for a smooth and stable meniscus it would seem that a small Π_2 and large Π_3 is preferable. In our case the density, surface tension coefficient and gravitational constant are set. The only non-constant parameter influencing both Π_2 and Π_3 is the metallostatic depth z_0 in the mould. p_e is also variable, but in the case of steady state (or static meniscus) this pressure would be determined by the metallostatic height and the curvature at the initial point of the meniscus (figure 9.1). Based on these considerations it would seem that an ideal height z_0 might exist. Further analysis would have to be performed to determine an analytical relation for an ideal z_0.

9.1.2 Velocity field

The melt flow field initiation is performed with a static meniscus and without heat flow. The metal is given a uniform temperature of 960K (thus making

[2]The curvature due to the cylindrical shape of the ingot is neglected here. It is assumed to be small compared to the 2D meniscus curvature

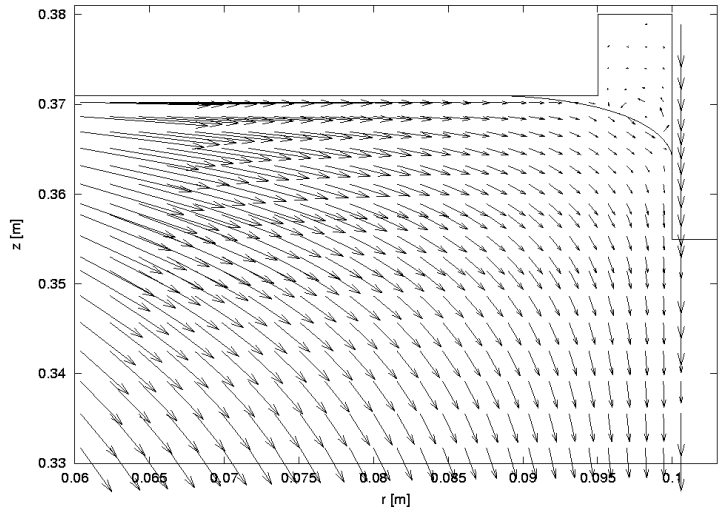

Figure 9.2: Initial velocity field in meniscus region for ingot cast at $120mm/min$. Velocity scaled by $M/5 \times 10^{-4}$, M is minimum computational cell dimension.

it liquid) and an appropriate initial meniscus shape is found by the technique described above. The gas inflow into the meniscus air pocket is also turned off. An initial flow field is subsequently found by solving the fluid flow equations with imposed melt inlet boundary conditions (given in section 8.1.1). The calculated initial flow field in the meniscus region for a casting velocity of $120mm/min$ is shown together with the meniscus in figure 9.2, and for the whole computational domain in figure 9.3. The flow field depends on ingot geometry, boundary inlet velocities and meniscus shape, in addition to the melt parameters of density and viscosity.

9.1.3 Temperature field

Based on the initial velocity field calculated in the previous section, an approximate initial temperature field may be found. The solidification and contraction models described in chapter 7 are applied and the energy equation is solved for the temperature field on the constant initial velocity field.

To heat transfer boundary conditions are found by solving the inverse heat transfer problem based on the temperature measurements in the mould from the casting experiments described in chapter 2. Appropriate heat transfer coefficients are found in the mould and along the ingot, i.e. for the primary and secondary cooling. The obtained initial temperature profile on the mould wall for Al6082 parameters is compared with mean experimental values (see

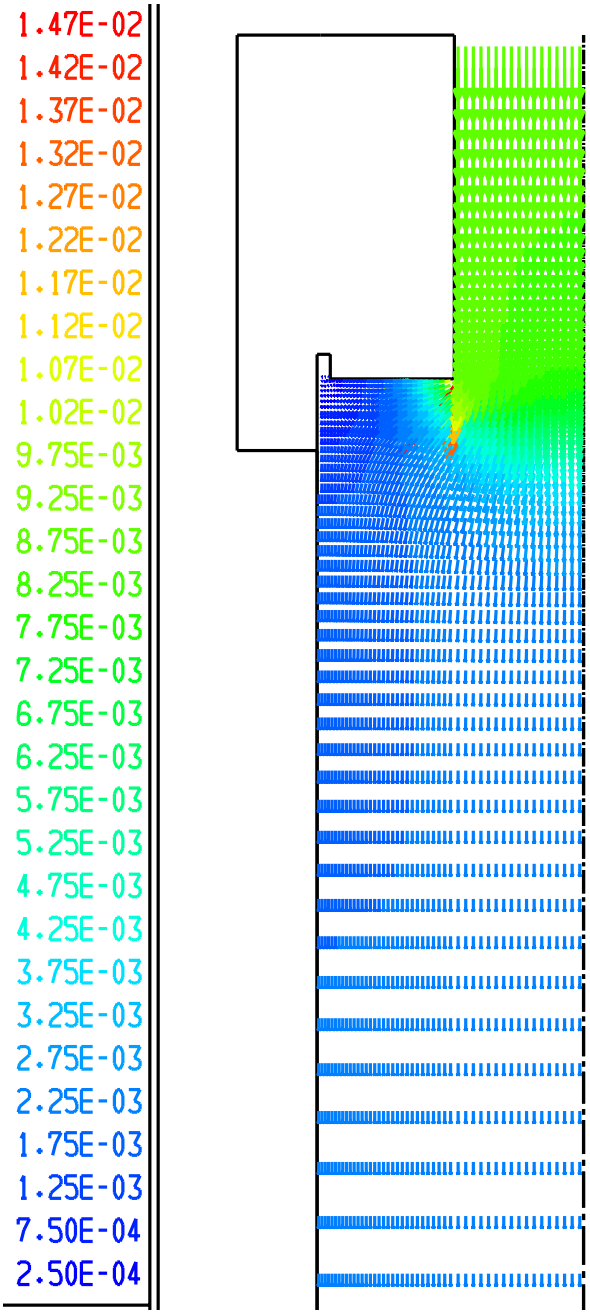

Figure 9.3: Initial velocity field (m/s).

A) in figure 9.4(a). The initial temperature profile is well within the range of experimental values (the graphite ring starts at $z = 0.355m$).

The initial ingot temperature profile is shown in figures 9.6(a) and 9.6(b). The initial temperature profile in the bottom surface of the hot top (not displayed) show a poorer correlation with the experimental measurements, which are a lot lower (see tables in the appendix (A.1)). This difference is assumed to be due to the positioning of the meniscus. For a large air pocket there will be less contact between the bottom of the hot-top and the molten aluminium, thereby leading to a lower hot-top surface temperature. This tendency is seen in the simulations where the gas pocket expands beneath the hot-top (see figure 9.7).

9.1.4 Filling of gas pocket

At the startup of the casting process the gas is normally allowed to fill the volume below the hot-top before the gas flow rate is turned down (as described in section 1.3.4). After this initiation it is believed that there should ideally be insignificant upward gas flow from the gas pocket out of the mould. The filling process is simulated here.

To assess the stability of the model during the filling process tests have been performed with varying time step and varying wetting conditions (corresponding to varying Courant number and varying boundary conditions for the cubic spline meniscus surface).

In the first set of tests (figure 9.9) the time step is $\delta t = 10^{-3}s$ and in the second set (figure 9.8) the time step is $\delta t = 10^{-4}s$. It should however be pointed out that a condition is set on the Courant number in the simulation program. If the chosen time step causes a breach of the Courant condition (Courant number smaller than a certain value), then the time step is automatically shortened to fulfill the Courant condition. In these simulations the Courant condition is chosen to be $c \leq 0.1$, where c is the Courant number. Obviously, for the case of $\delta t = 10^{-4}s$, the Courant condition is less frequently breached than for the longer time step.

9.1.5 Open spline boundary conditions

End boundary conditions must be set for the spline interpolation. The types of boundary conditions applied for cubic splines are listed in section E.1 of the appendix. The three first types are for open splines, as in the case of the meniscus surface. Since different pairs of boundary conditions may be applied for the spline ends at the mould wall and at the hot-top surface, a total of 9 different combinations of boundary conditions are possible. In the physical

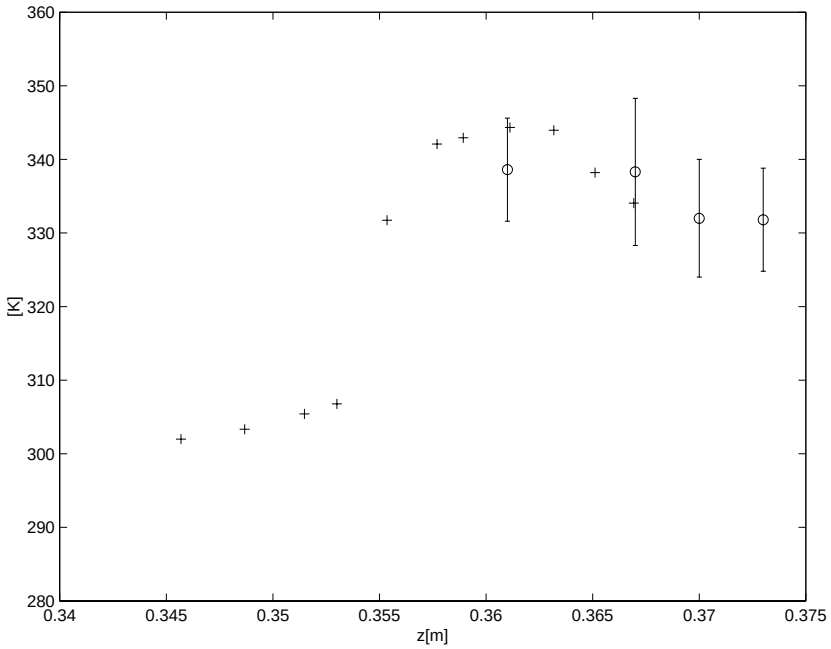

(a) Initial profile. Experimental values (o) for Al6082.

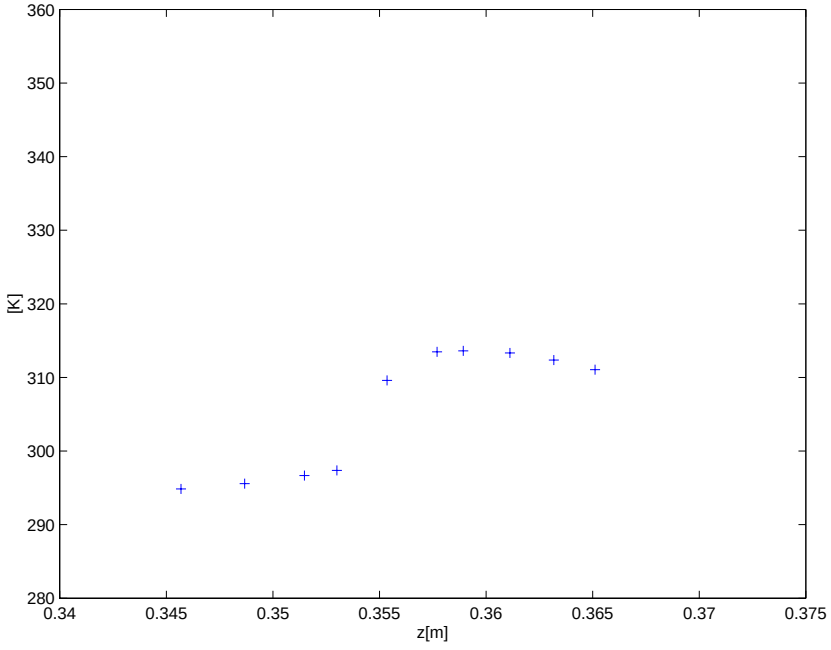

(b) Profile for free hot-top bottom surface (as fig. 9.7).

Figure 9.4: Mould wall temperature profile (+).

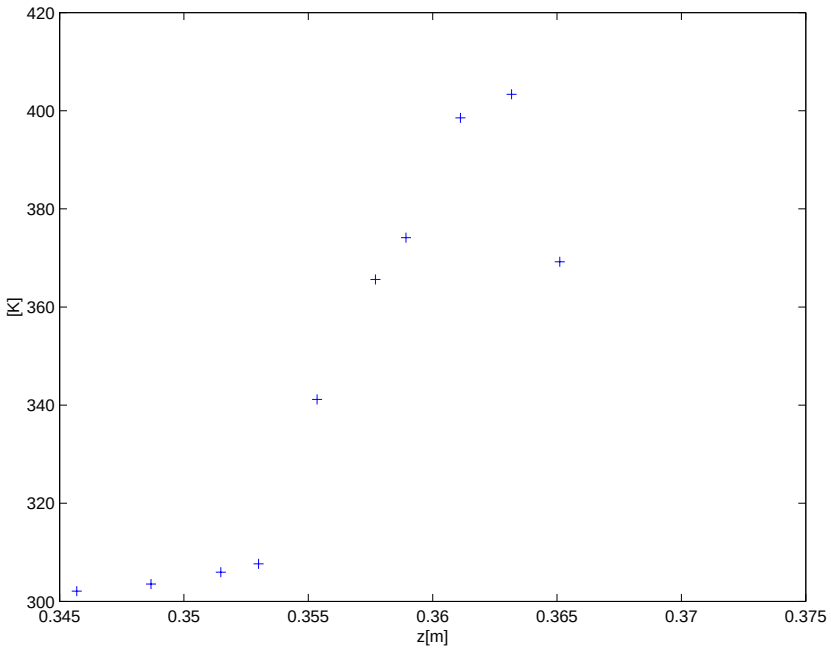

Figure 9.5: Mould wall temperature profile (+). Profile after meniscus collapse (0.361s in fig. 9.10).

fence, both the boundary condition of natural splines with zero curvature and the extrapolated second derivative gives a free wetting angle, while the forced slope boundary condition determines a constant wetting angle.

Natural spline boundary conditions and forced wetting is compared here (figures 9.8 and 9.9). In these tests the contraction model is turned off to improve stability[3]. For the smaller time step, in the case of forced wetting angle in 9.8(b) the meniscus surface is less smooth than for the case with free wetting,9.8(a). Also an extra vortex has developed for the case of forced angle, indicating reduced stability.

The longer time step produces a more unstable flow with spurious currents in both cases. The influence of the different boundary conditions are more difficult to separate, although the simulations with forced wetting seem slightly less stable also in this case. The results suggest that the condition of constant slope is too strong a constraint[4]. Also the boundary condition of interpolated second derivative leads to instabilities, although not to the

[3]The contraction model leads to a thinner solid lip and subsequently greater dynamics in the melt flow.

[4]A forced wetting angle also hinders the possibility of overpressure in the gas pocket, which would lead to a reversal of the meniscus curvature

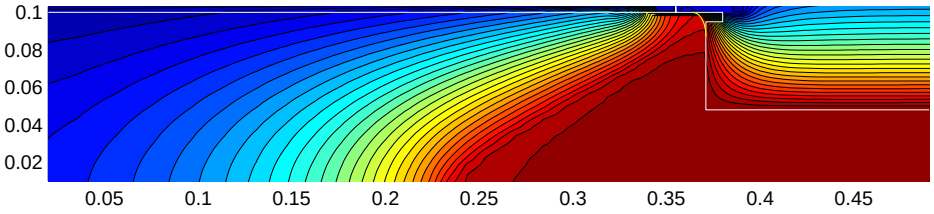

(a) Computational domain

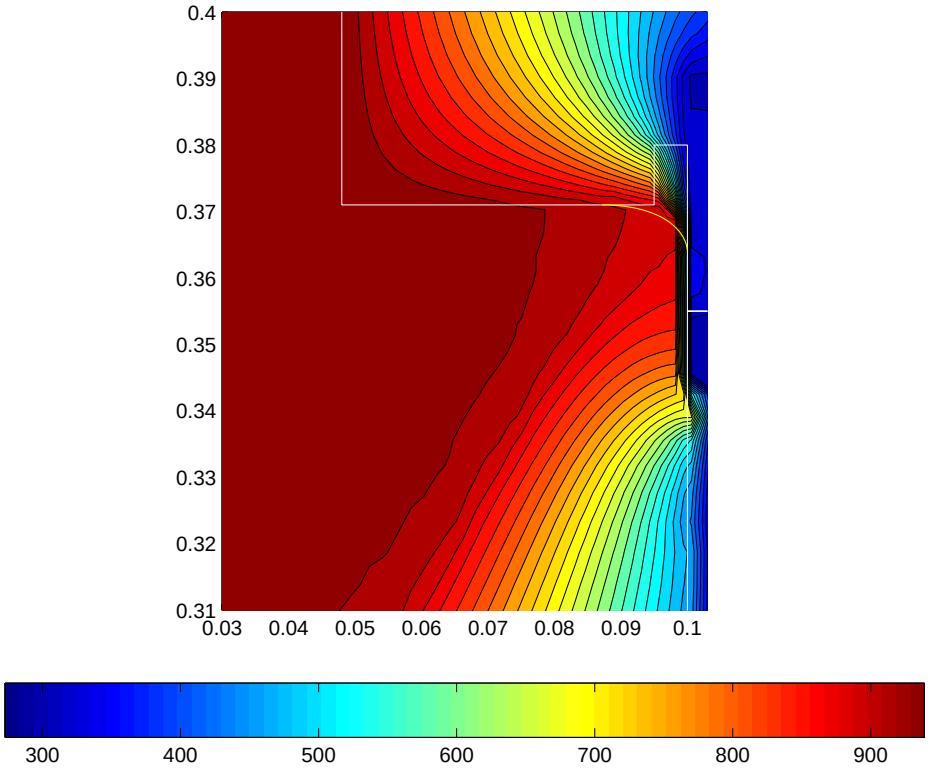

(b) Meniscus region

Figure 9.6: Initial temperature field in Kelvin for Al6082. Initial meniscus in yellow.

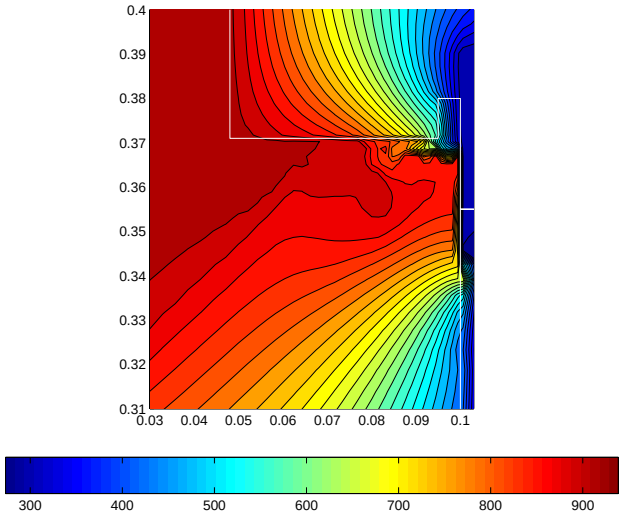

Figure 9.7: Temperature field [K] in meniscus region for free hot top bottom surface. Corresponding to 1s in figure 9.13.

same extent as for the condition of forced slope. Therefore the condition of natural spline, i.e. a free wetting angle with zero end curvature, is applied in the further simulations.

9.1.6 Time step criteria and stability

With a given gridsize the time step determines the degree of flow stability by the constraints on advection and diffusion in (4.17) and (4.18). Here only the Courant condition will be considered. An approximate Courant number may be found for the two different time steps. In the first case, where the time step is $10^{-3}s$, the maximum Courant number[5] is approximately 0.3, while for the second case (with time step $10^{-3}s$) the maximum Courant number is only approximately 0.01, suggesting that the decline of the Courant number with time step is stronger than linear. And comparing figures 9.9 to figures 9.8 it can be seen that the stability is improved considerably. The spurious currents (seen as vortices) occurring for the high Courant number simulations are practically nonexistent in the low Courant number simulations. This result suggests that a small Courant number should be applied in the meniscus simulations, preferably of the order of 10^{-2} or lower.

[5]As described earlier, for a Courant number higher than 0.1, the time step is automatically shortened so that $c = 0.1$.

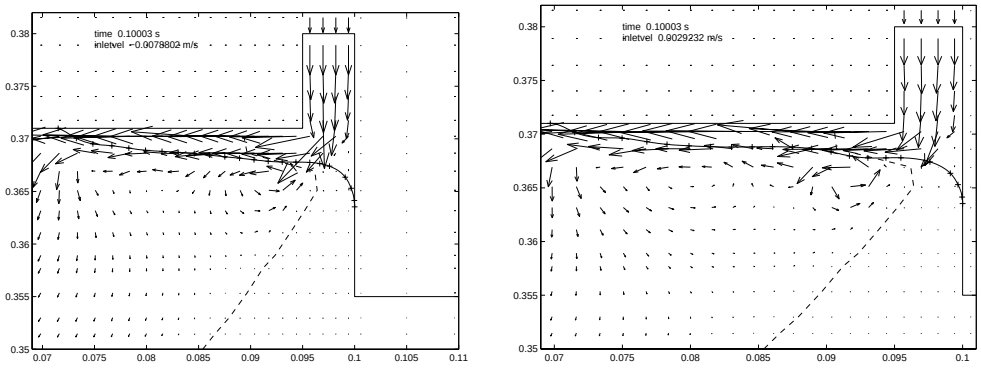

(a) Free hot top wetting angle, natural spline.

(b) Zero hot top wetting angle.

Figure 9.8: Wetting tests for meniscus simulations. Time increment $10^{-4}s$. Velocity field shown. Slip gas inflow at top. Point of onset of rigidity of metal indicated by dashed line. Other parameters as in appendix F.

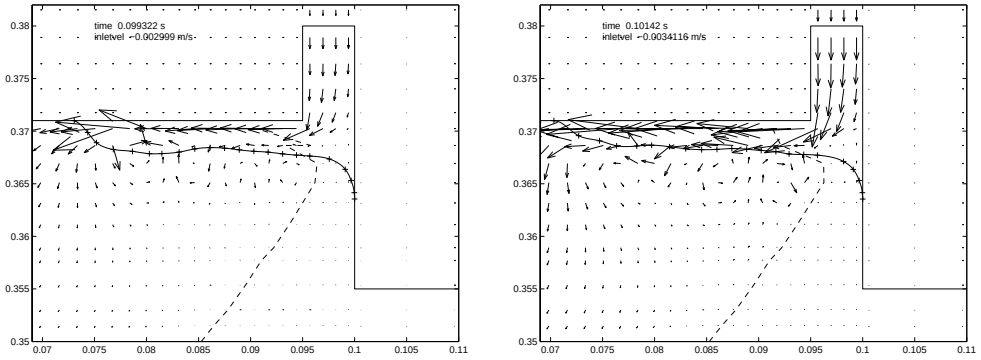

(a) Free hot top wetting angle, natural spline.

(b) Zero hot top wetting angle.

Figure 9.9: Wetting tests for meniscus simulations. Time increment $10^{-3}s$. Velocity field shown. Slip gas inflow at top. Point of onset of rigidity of metal indicated by dashed line. Other parameters as in appendix F.

9.2 Simulations

Results from three different simulations are shown in figures 9.10 to 9.17. All the simulations have been started from the initial conditions described above. Subsequently they have been run for 0.01 seconds with an inlet velocity of 100mm/s to achieve an initial expanded gas pocket. After this the inlet velocity is turned down. In the first case (fig. 9.10) the inlet velocity of the slip gas is low (5mm/s). This inlet velocity provides an inlet volume flow rate of the same order as the gas volume flow rate out through the air gap. A slip gas inlet velocity of approximately 3mm/s would balance the flow in and out of the gas pocket under these conditions. The inlet velocity of the second case (figures 9.12 and 9.12) is higher (25mm/s), resulting in a rapid growth of the gas pocket volume. The third case (fig. 9.17), which is an extension of the high inlet velocity case with the inlet velocity turned down to 10mm/s, shows upward discharge. The mould wall temperature profile at the termination of the cases of low and high inlet velocities are for comparison shown together with the initial profile in figures 9.4 and 9.5.

Low inlet velocity For the low inlet velocity case an inclusion is formed in the form of a bubble (figure 9.10). As the volume of the gas pocket expands the upper contact point of the meniscus moves back to the corner next to the gas pocket, as discussed in section 1.3. The contact point is subsequently locked at this corner by the melt flow[6]. As the air pocket further expands there is a lot of oscillation (0.107s-0.5s), but none of which influences the lower meniscus contact point to a significant extent. The isotherm for 80% solid fraction is also approximately static. Since the air pocket is hindered from extending further downward by the solid region it must extend inwards. When the extent of the meniscus is such that the pressure jump no longer can be balanced by the curvature it collapses (from 0.561s and onwards). The meniscus collapse leads to the formation of an air bubble inside the melt and upward melt flow leading to rapid upward movement of the lower meniscus contact point. Also, the 80% f_s isotherm moves rapidly downwards, due to flow of warmer melt into the meniscus region, which can be seen in figure 9.11.

The inner mould wall temperature profile after the meniscus collapse is shown in figure 9.5. The peak mould wall temperature has moved upwards, as would be expected. A periodically collapsing meniscus (as described in

[6]All the presented simulations apply natural spline boundary conditions. For zero upper contact angle as a boundary condition locking at the gas pocket corner does not occur.

chapter 1) would therefore produce oscillations in mould wall temperature as observed in the casting experiments in 2.1. However, the graphite surface temperature range, $\sim 350K$ to $\sim 400K$, is a lot larger than that measured in the castings for Al6082 (shown in figure 9.4(a)); $\sim 330K$ to $\sim 360K$. If this mechanism of meniscus collapse is causing the experimentally observed oscillations adjustment of the applied thermal boundary conditions are needed.

High inlet velocity In the high velocity case the gas has enough momentum to move the upper meniscus contact point away from the gas pocket corner. After approximately 0.44s a wave forms, which proceeds to move toward the mould wall (see figures 9.15 and 9.16). As the waves moves outwards it is dampened by the solid region under the meniscus until it breaks at the mould wall. Due to the damping effect of the solid region, the momentum of the wave does not significantly influence the position of the lower contact meniscus point. After the initial wave formation the meniscus gradually reaches a semi-steady state (see 9.14), where the upper contact point moves slightly back towards the wall while the volume of the air pocket gradually increases (0.613s to 0.773s). Eventually the situation becomes unstable and a large wave again forms. As this wave approaches the mould wall the upper point of the meniscus commences its inward movement. The wave is again dampened and breaks at the mould wall (0.893s), while a wave moving in the opposite direction breaks at the upper contact point (0.873s). Subsequently the situation becomes more steady as the upper meniscus contact point moves inwards along the bottom of the hot top.

Upward discharge The simulation for high inlet velocity above was continued with reduced velocity to simulate upward bubbling . The result is shown in figure 9.17. As the upper meniscus point passes the melt inflow corner (also discussed in 1.3), a bubble forms (1.15s). This bubble moves up along the wall, proceeding to take the characteristic shape of a bubble with large Eotvos number. Another bubble starts to form at 1.16s and follow the first along the wall. As the bubbles form and the volume of the gas pocket decreases the meniscus surface gradually rises smoothly towards the bottom of the hot top. The instabilities formed here due to the bubble formation do not tend to effect the smoothness of the meniscus at the mould wall. Instabilities are confined to a region close to the corner of melt inflow.

Insufficiencies in the current implementation prevent the simulation of proper bubble separation. The spline surface is at all times connected. Also the effect of gas escaping through the top of the melt and the connected abrupt drop of the melt surface in the mould (as observed in the water model

experiments in appendix B) may not be simulated, since the free surface at the top of the mould is not included in the simulations.

At the termination of the high inlet velocity simulation above, the upper meniscus nearly extends to the corner of the melt inlet, so that the bottom surface of the hot-top is free (again figure 9.13). The inner mould wall temperature for this situation is shown in figure 9.4(b). When the hot top bottom surface is free the temperature profile of the bottom of the hot top corresponds better with the experimental measurements, as explained above. But the temperature profile of the inner graphite surface is significantly lower than for experimental values (figure 9.4(a)). If there is periodic upward discharge of gas coupled with oscillating gas pocket volume, as suggested in chapter 1, the meniscus level at the wall would be varying, subsequently giving oscillations in temperature as observed in the experiments. The low temperature profile for the low point of the meniscus in the simulations indicates either that the thermal boundary conditions are inaccurate, or that the meniscus will not extend this far down under normal conditions. It is believed that the former is the correct explanation.

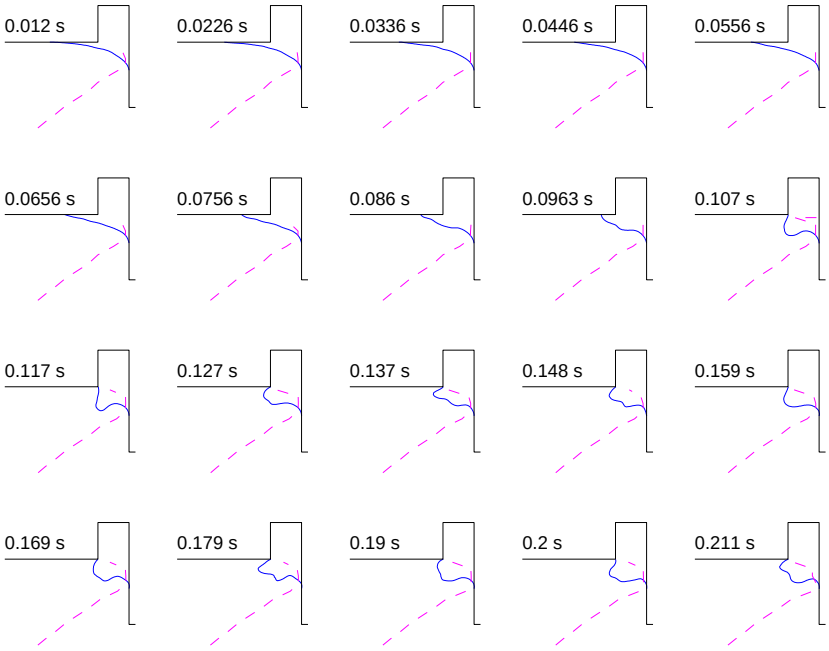

(a)

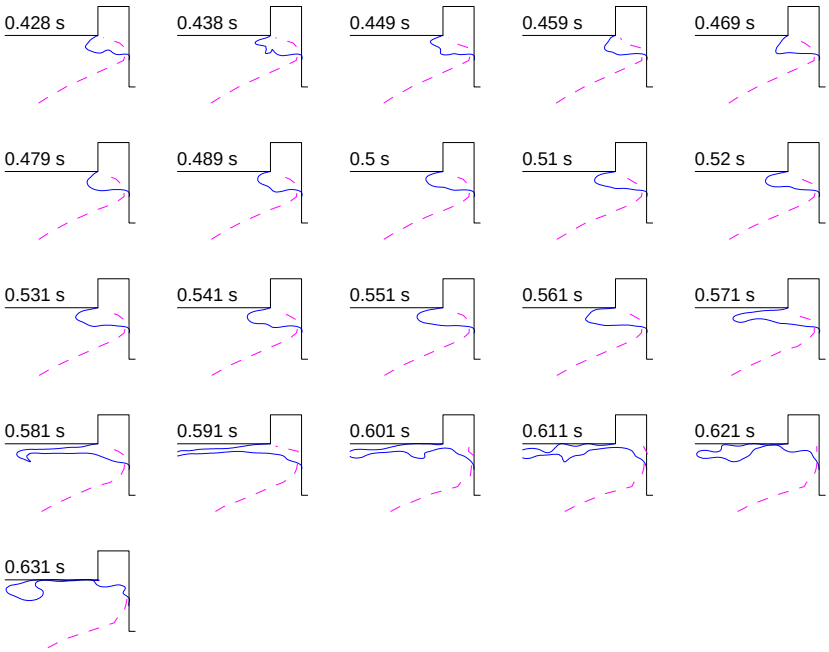

(b)

Figure 9.10: Casting simulation, low slip gas inlet velocity of 5mm/s

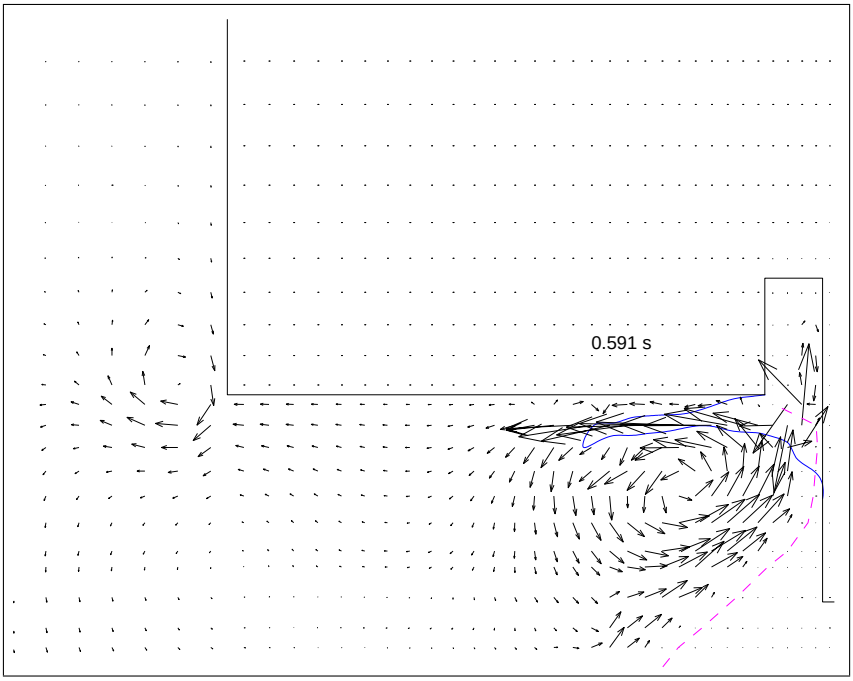

Figure 9.11: Casting simulation, low slip gas inlet velocity of 5mm/s. Vortex formed at meniscus collapse.

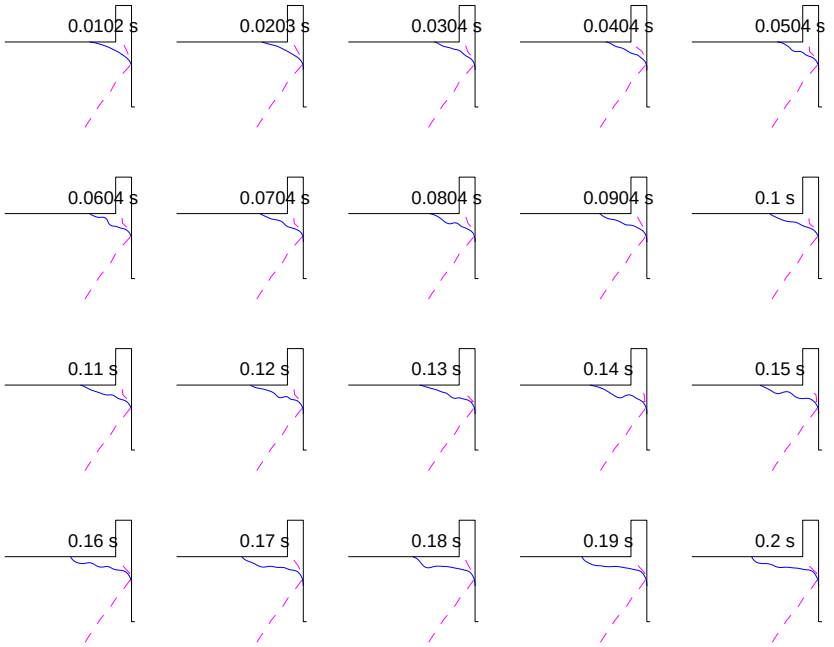

(a)

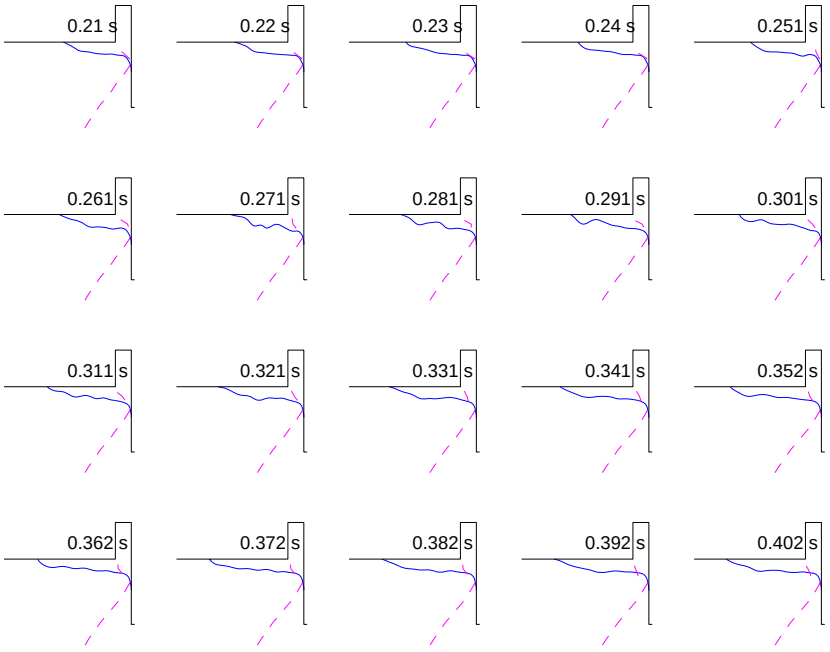

(b)

Figure 9.12: Casting simulation, high slip gas inlet velocity of 25mm/s, first part.

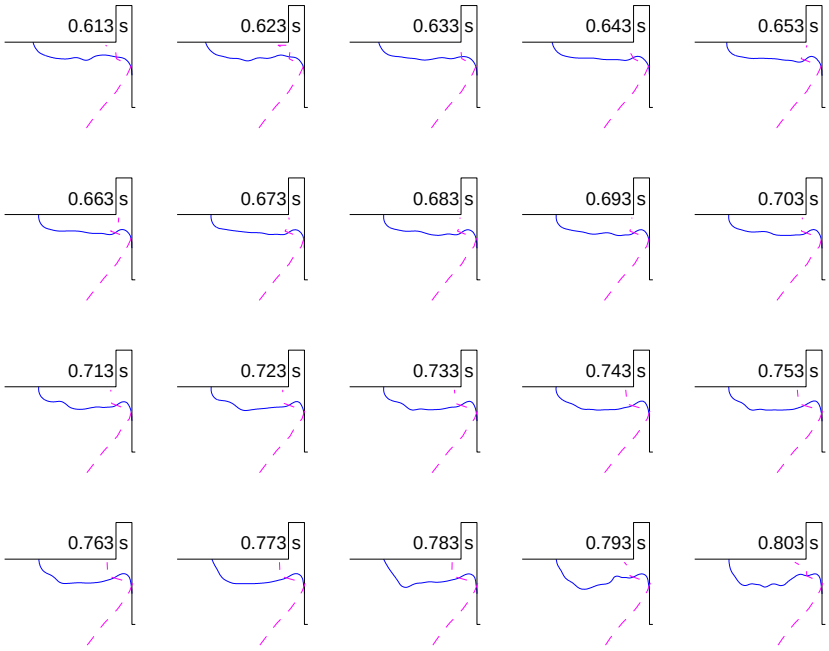

(a)

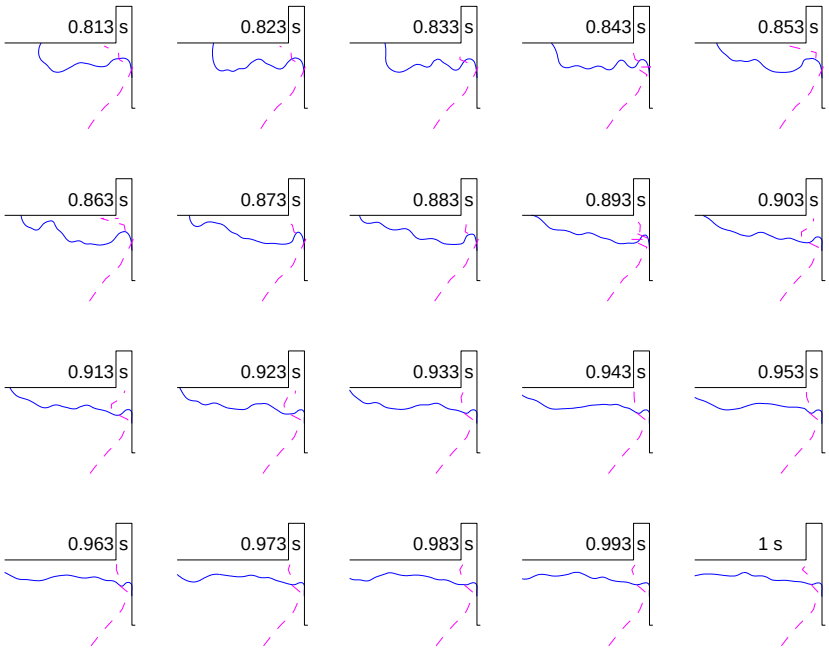

(b)

Figure 9.13: Casting simulation, high slip gas inlet velocity of 25mm/s, second part.

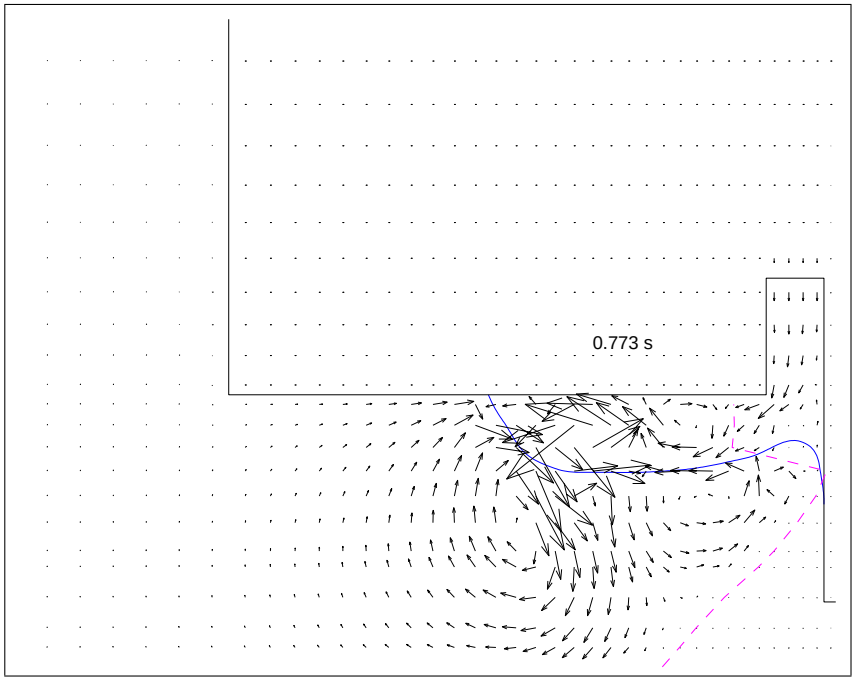

Figure 9.14: Casting simulation, high slip gas inlet velocity of 25mm/s. Semi steady state fluid flow.

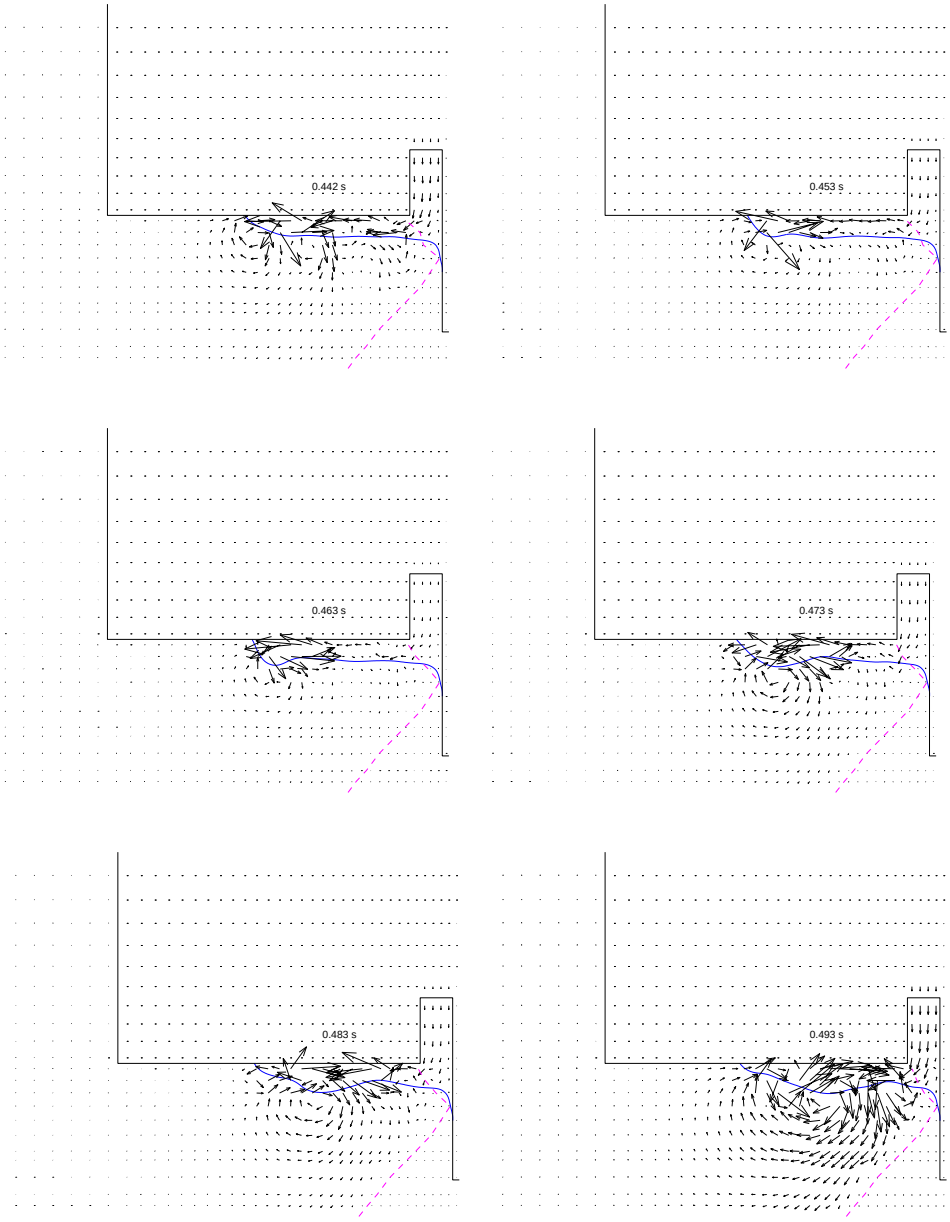

Figure 9.15: Casting simulation, high slip gas inlet velocity of 25mm/s. Wave formation and propagation.

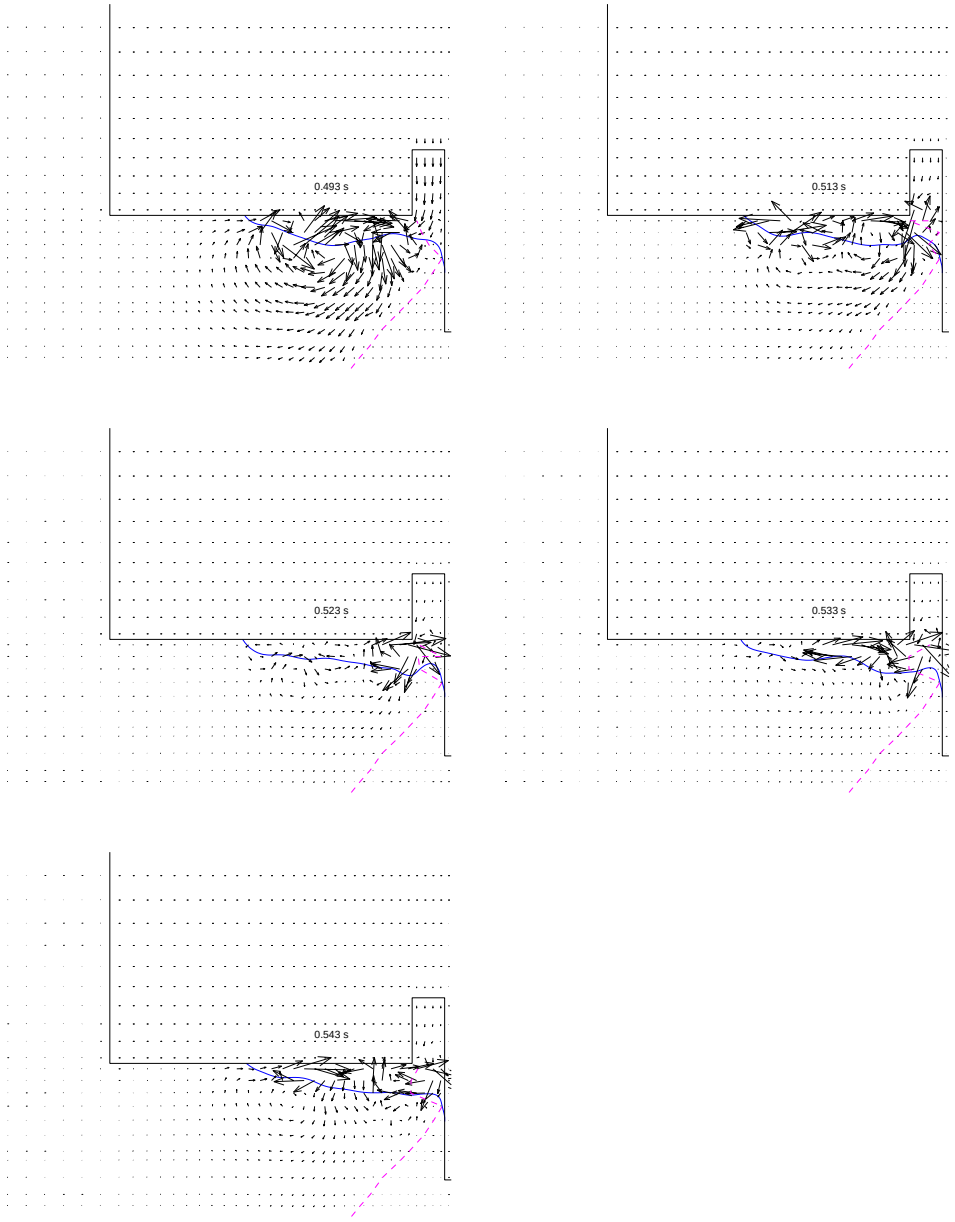

Figure 9.16: Casting simulation, high slip gas inlet velocity of 25mm/s. Wave propagation and breaking.

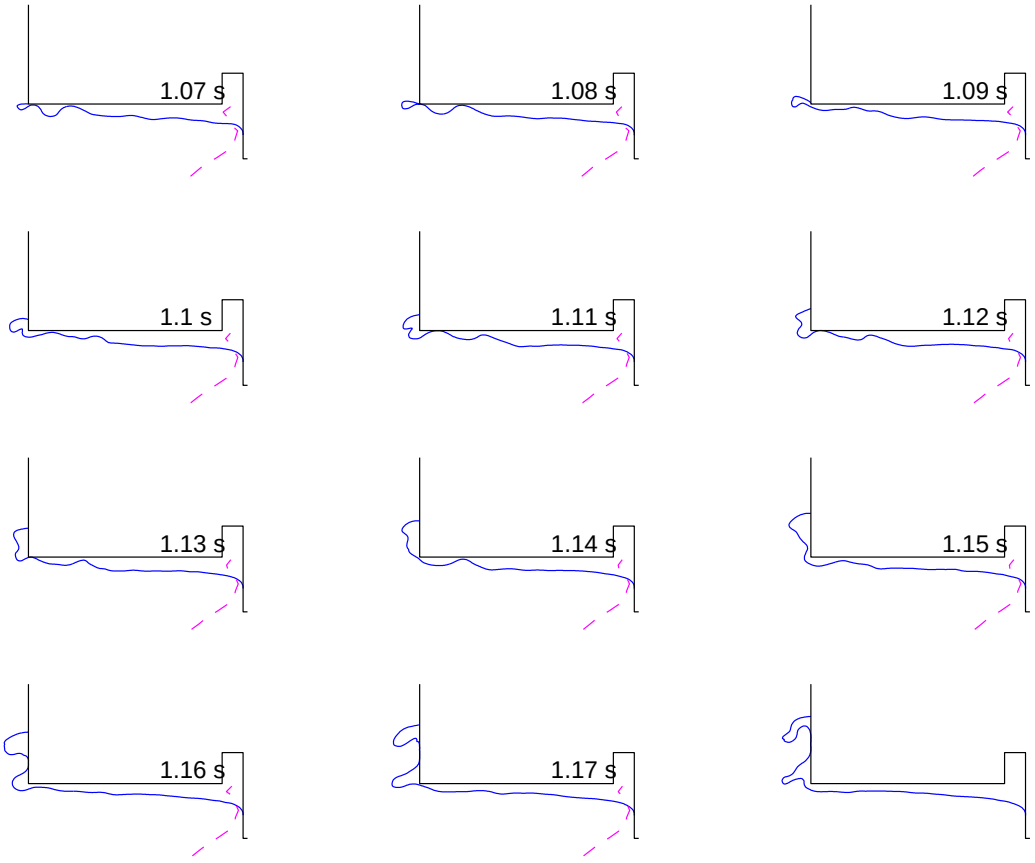

(a)

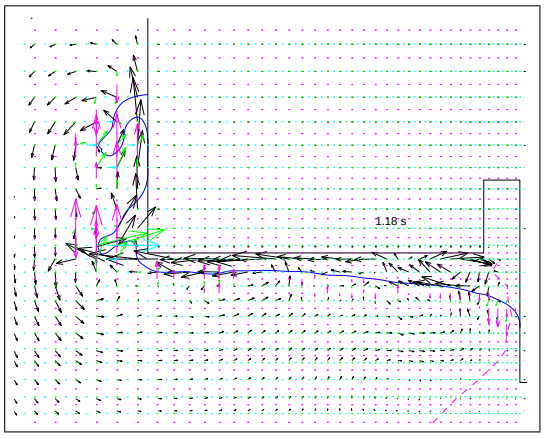

(b) Velocity field and surface tension forces shown.

Figure 9.17: Casting simulation, slip gas inlet velocity of 10mm/s. Upward discharge.

Chapter 10

Summary and Discussion

This work has lead to two important contributions related to analysis of the hot top DC gas slip continuous casting process of aluminium extrusion ingot .

The first is the development of a numerical method for analyzing the meniscus dynamics and its effect on and interaction with solidification. The main part of the development of this numerical method is the adaption of a marker chain free surface modelling technique for simulating the movement of the meniscus surface, which may also be applied to the modelling of any non-disperse two-phase system with a large density ratio.

The second contribution is added insight into the casting process, specifically into the mechanisms and influence of the meniscus behaviour on ingot surface formation during casting. This insight has been gained by modelling the casting process by the use of the developed numerical method, by experimental observations of the casting process and by water model experiments.

10.1 Meniscus Surface Dynamics

A presentation and comparison of methods of free surface modelling on an Eulerian grid were given in chapter 4. Of these methods the Method of Tensions of Popinet and Zaleski [49] was selected for the purpose of modelling the movement of the meniscus free surface. The method was chosen for its advantage of surface smoothness and control, stability in calculation of surface tension forces, and simplicity in application of wetting boundary conditions (see section 4.4). These properties are important in modelling the two-phase Al melt/air system, which is particularly vulnerable to instability due to its large melt/air density ratio (chapter 5).

A cellwise homogeneous model is applied in the numerical simulations.

An analysis of the combination of such a model together with the Method of Tensions for free surface modelling is performed in chapter 5. Here it is pointed out that a certain degree of numerical smoothing of the interface is necessary to avoid large errors in the region of the interface between the air and melt. It is also found that the technique of marker velocity interpolation and surface force distribution must be weighted by density to approximate free surface behaviour. The weighting technique is described in chapter 6, where adaption from the 2D Cartesian MOT to cylindrical coordinates is also presented.

Another stabilizing factor is the redistribution of marker particles. Due to gradients in the velocity field the spacing between marker particles may change during advection. Subsequently marker redistribution is necessary. The marker redistribution also stabilizes the surface by causing smoothing of the surface. The best method of marker redistribution is found to be alternating midway redistribution, presented in section 6.8.3. This technique both smoothes and ensures appropriate marker spacing on a non-uniform grid.

Due to redistribution of markers and inaccuracies in velocity interpolation accurate phase conservation is difficult to achieve in the applied Method of Tensions. Here a method has been developed for accurate phase conservation in the case of a commonly applied advection test case, also presented in section 6.8.3. In this method surface interpolation is performed with alternating regular cubic and cubic B-splines. Further adaption of this method is needed for general application, so it is not applied in the casting simulations.

10.1.1 Waves on meniscus

Several types of wave formation have been considered. In chapter 3 typical frequencies for some types of wave phenomena are calculated. The dispersion relations found for capillary and capillary gravity waves on surfaces segments of constant curvature may be considered to be approximations of meniscus surface behaviour. For typical meniscus dimensions ($\sim 1cm$) the pure capillary waves with boundary conditions for the velocity potential given by condition (3.15), the frequency of oscillations are several orders larger than the typical experimentally observed frequencies (chapter 2). But for the coupled capillary gravity waves, a solution giving frequencies of the order of the ones experimentally observed is possible (section 3.3). The solution for capillary gravity waves is extremely unstable.

The characteristic frequency of gravitational oscillations in the casting column, discussed both in chapter 1 and in section 3.4.1, is of the same order as the experimentally observed frequencies, so this type of oscillation may

be part of the mechanism causing oscillations during casting. This type of oscillation may only occur when the air gap is open, so that slip gas may escape through it. For a closed air gap this type of gravitational oscillation must be coupled with pressure oscillations in the gas pocket, as described in 3.4.1. The gravity pressure oscillations have a characteristic frequency two orders of magnitude larger than those experimentally observed, so this type of oscillation may be assumed to be of lesser importance.

10.1.2 Meniscus stability

In the analysis of capillary and gravity capillary waves the meniscus oscillations are assumed to be small perturbations around a static equilibrium meniscus of constant curvature. This assumption may be a fair approximation for the case when the upper meniscus contact point is at the gas pocket corner, as shown in figure 1.8(b). For the other extreme case (figure 1.8(a)) the static equilibrium meniscus is obviously not of constant curvature. Subsequently the wave analysis above indicates that a meniscus as figure 1.8(b) is very sensitive to small perturbations. The meniscus collapse observed in the numerical simulations with low gas inlet velocity (figures 9.10), also indicates instability for this type of meniscus geometry.

Wave propagation along the meniscus is observed in the numerical simulations, shown in chapter 9, and also in the water model experiments, where some results are shown in appendix B. A typical case of simulated wave formation, propagation and damping/breaking is shown in figures 9.15 and 9.16. Wave propagation with subsequent breaking or folding at the mould wall may be a mechanism of meniscus collapse, as described in chapter 1. Therefore attempts were made to provoke this behaviour in casting simulations. Several simulations were performed to provoke meniscus folding by wave propagation on a similar meniscus geometry as the one shown in figures 9.15 and 9.16 (i.e. with a gas pocket extending quite far inward along the bottom of the hot top). But a folding leading to a significant change in the level of the lower meniscus contact point with the mould wall was not achieved. A dramatic change in the level of the lower meniscus contact point was only achieved for the case with the upper meniscus contact point situated at the gas pocket corner, as shown in figure 9.10. In this case the meniscus collapse is so dramatic that there is danger of the meniscus freezing to the mould wall, so it is a situation that should be avoided[1]. Such a meniscus does however not seem to be common in our casting experiments, as indicated by

[1]This may be achieved by ensuring a high enough slip gas inlet velocity, as explained in chapter 9.

the experimental measurements of the hot top bottom temperature profile (appendix A). This profile indicates a meniscus with significant extension inwards under the hot top, as discussed in 9.1.5.

Also the numerical simulations indicate a meniscus which extends significantly inwards. The meniscus surface becomes increasingly stable as the meniscus extends inwards (compare figures 9.13 and 9.17). In figure 9.17, where the upper meniscus contact point is at the melt inlet corner, the instabilities are all on the inner region of the meniscus. No instabilities seem to propagate out towards the mould wall. The observed meniscus surface in the casting experiments is also very stable in the periods between meniscus collapse, which can be discerned in figure 2.5. Therefore the simulations suggest that a typical meniscus shape in the casting experiments is given by figure 9.17.

10.2 Casting Process

Effects included in the modelling of solidification are increased viscosity and solid state flow(section 7.2.6), solidification contraction with air gap formation, and air gap slip gas flow. Buoyancy and radiation are neglected, since these effects are not believed to influence meniscus dynamics. Radiation is negligible compared to conduction and the time scale of the buoyancy is orders larger than the time scales of the meniscus dynamics.

The latent heat is included in the heat capacity through relation 7.11. On account of the subsequent large gradient in heat capacity smoothing is imposed for stability in the numerical simulation.

The solidification contraction is modelled by a cellwise linear model presented in section 7.2. Here the onset of contraction is assumed to be at a given solid fraction f_s, where the value of f_s is tentatively chosen as 0.8 in subsequent casting simulations. The calculated contraction is linear in f_s, and the resulting radial contraction is the radial sum of cellwise contraction. The calculated radial contraction implies the subsequent air gap width and the necessary change in material parameters for modelling heat flow in the gap (section 7.2.8).

The air gap size is also applied in the calculation of air gap gas flow (section 7.2.5). The flow is assumed to be fully developed Poiseuille flow. An estimate (figures 7.5 and 7.6) shows that this assumption is generally valid for the typical air gap dimensions simulated in the numerical modelling.

10.2.1 Mechanisms of Ingot Surface Formation

In the experiments a characteristic folding or collapse of the meniscus is observed (section 2.2). The lower part of the meniscus rapidly moves back up the mould wall until the meniscus regains equilibrium at a higher level. A similar effect can be seen for the numerical simulations in figure 9.17, where there is upward bubbling. As the bubbles form at the melt inlet the level of the meniscus moves upwards, although the lower contact point of the meniscus remains at the same level (see 1.13s to 1.18s in figure 9.17). This upward bubbling could be linked to the meniscus collapse. As bubbles form and move up the melt inlet the volume of the gas pocket gradually decreases, so the meniscus surface must subsequently move upwards, as described above. Two possible effects may subsequently lead to the meniscus collapse and formation of a new meniscus surface.

Firstly, since the lower meniscus contact point seems to be aproximately static as the gas pocket volume decreases, the shape of the meniscus will gradually change until it becomes unstable and collapses against the mould wall. The momentum of this collapse would induce a spurt of upward bubbling.

Secondly, bubbles escaping from the surface of the melt in the mould would briefly lead to a drop in the mould melt level, where the dropping melt would induce a downward momentum in the mould. The effect may be seen in the water model experiments in appendix B. This added momentum to the melt due to bubble discharge could also lead to destabilizing and subsequent collapse of the meniscus. In this case the spurt of bubbles would be seen escaping from the melt surface briefly before the meniscus collapse.

The mechanism of meniscus collapse could also be a combination of the two effects. Further experiments would have to be performed to ascertain whether spurts of upward bubbling occur directly before or after the meniscus collapse, or both.

These mechanisms, indicated by both the experimental observations and the numerical simulations, indicate that the prevailing effect is the collapsing meniscus model, suggested in chapter 1 (although possibly with a less pronounced solid lip than in figure 1.10), and that the Surface Mark Formation model of Ackerman et al is too much of a simplification to describe the process thoroughly.

The possible gravity waves in the casting column, discussed above, might be coupled with or perhaps induce the meniscus oscillations and collapse. The additional peak in pressure oscillations observed at approximately 1 Hz could indicate this effect, as it is close to the frequency found in the solution for gravity waves in chapter 3, although this observed frequency may also be

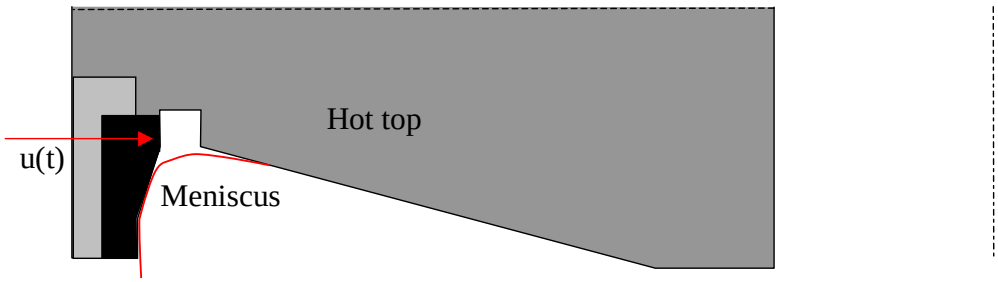

Figure 10.1: Modified mould geometry.

artificial, as suggested in section 2.3.

Although the air gap was open most of the time in the casting simulations, the volumetric flow rate of the slip gas through the air gap was at all times quite low. This would indicate that the contraction due to the solidification would never be sufficient to lead to a large enough air gap gas flow to induce a rapid destabilizing and collapse of the meniscus[2], as suggested in previous models [5], [4]. Of course this result depends to a great extent on the solidification contraction model applied (see section 7.2.4). However, with a greater air gap than the one observed in simulations, the gas flow in the gap would quickly become turbulent, thereby reducing the flow rate (section 7.2.5). Further work should be done on the contraction model to ascertain what dimensions of the air gap can occur, but a substantial increase in the modelled air gap width would be necessary to increase the air gap gas flow rate to a significant extent.

10.2.2 Suggestions for Process Modifications

Wetting The water model experiments (appendix B) show that the violence of the bubble discharge depends to a great extent on the wetting of the Al melt with the hot top; the lower the wetting the gentler the discharge. Since the pulsating discharge process is believed to influence the meniscus collapse it would seem that a low wetting and gentle discharge should be sought. So the wetting should be as low as possible.

The discharge would also be effected by the geometry of the hot top. In the water experiments the lower corner of the melt inlet is a sharp angle. Rounding of this corner would facilitate upward bubbling, thereby leading to a smoother upward bubbling process with a smaller meniscus collapse and a smoother cast ingot surface.

[2] A possible link between pressure variations and meniscus collapse with and without upward bubbling is however suggested in chapter 2.

Geometry With better control of the slip gas flow and modified mould geometry it may be possible to *avoid meniscus collapse*, so that a smooth ingot surface may be achieved. An intersection of a suggested modified mould geometry is shown in figure 10.1. A section is here cut out of the bottom of the hot top so that the meniscus position is raised up above the bottom level of the hot top. The idea is that the meniscus should remain in this position by regulating the gas pocket volume. Regulating the gas pocket volume may be performed by drilling a series of holes through the hot top around its circumference at an appropriate distance from its outer edge. Subsequently the slip gas may escape through these holes to prevent the volume of the gas pocket increasing to a significant extent.

A problem with this geometry might be the small size of the gas pocket. With poor control the ingot might freeze to the hot-top. However, with an excess of injected slip gas this could be avoided. As pointed out above, such a small meniscus might be more unstable than the larger meniscus which normally occurs. However, the meniscus dynamics should be quite smooth, since there would be no upward bubbling through the hot top, and regulating the gas pocket volume should prevent the meniscus from collapsing, as in the case of figure 9.10.

Other problems with the suggested technique may be clogging of the holes in the hot top by oxide or buildup of oxide on the meniscus. The clogging may be a serious problem for small holes. And for too large holes the melt will flow up into them. Therefore the dimension of the holes drilled in the hot top is an important issue. Buildup of oxide on the meniscus seems to be a problem mainly when the meniscus is steady, and not oscillating. This is the case when oxygen is not applied in the slip gas in our experiments (see chapter 2). So some meniscus oscillation may be required to avoid this effect. However, with the suggested technique it should be possible to reduce the oscillations to a minimum, where buildup of oxide is avoided and oscillations are small enough to not significantly affect ingot surface formation.

Another possible alteration is a partly *conically shaped graphite ring*, which would support meniscus surface to avoid collapse. In this case good control of the cooling is necessary to avoid the isotherm of onset of contraction from extending too far upwards, which might lead to a decrease in ingot radius. But as long as the control of the gas pocket volume functioned, the meniscus would be quite stable, resulting in a stable heat flow. Therefore good control of the temperature profile might also be possible.

10.3 Further Development and Analysis

Solidification contraction In the casting modelling the question of whether there is sufficient air gap gas flow to quickly reduce the gas pocket volume is very much determined by the solidification contraction model. To properly determine the air gap width a more accurate contraction model should be applied, preferably including the appropriate rheology and the effect on the air gap of the contraction of the ingot below the primary cooling zone. Perhaps the modelling might be done in parallel with a finite element method simulator such as ALSIM, where contraction modelling is much simpler to perform.

Buoyancy A proper model for buoyancy might be included in the model. Even if the time scale of the buoyancy is orders of magnitude larger than the meniscus dynamics, the buoyancy affects the temperature profile in the ingot, and should therefore be included.

Merging and breakup If the effect of upward discharge is to be properly included in the methods of surface merging and breakup must be included in the free surface model. A thorough presentation of such a technique is given by Shyy [59]. This technique could quite easily be implemented in the Method of Tensions.

Free surface control Several adjustments could be made to further improve the stability and accuracy of the free surface modelling. An independent gas / melt flow model allowing splitting of gas and melt flow velocities might be included. Such a model would incorporate boundary conditions at the phase interface and independent flow equations for the gas and melt. Additional algorithms would also have to be included for advection of gas and melt in the cells containing phase interfaces.

Including the pressure correction method of Popinet and Zaleski (chapter 6) might improve stability and convergence of pressure, although the surface force redistribution technique applied here (also chapter 6) is probably sufficient.

The Power Law is here applied in the discretization of the flow equations (chapter 8). This technique is not influenced by the free surface configuration. Since it is a free surface, the heavier fluid, i.e. the melt, should determine the flow. Therefore the surface configuration should be included in the discretization. So the Power Law should be applied together with an appropriate discretization where interface geometry and stability properties are addressed in the cells with phase interfaces.

For phase conservation further development of the correction technique presented in section 6.8 should be made. Alternatively a higher order spline might be applied to control both surface smoothness and boundary wetting conditions.

Casting developments Both numerical simulations and casting tests should be applied on the suggested *modified mould geometry*. Since the geometry can not be modelled with a orthogonal grid the applied numerical method would have to be adapted to a non orthogonal grid. Subsequent simulations together with casting tests would show whether the suggested modifications could improve the casting process.

The aspect of wetting conditions should definitely be considered and any corners of the hot top geometry should be rounded to achieve as smooth a process as possible.

Appendix A

Analysis of castings: ingot 6

A.1 Statistics

Statistics for ingot 6 in the casting tests are displayed in the following tables. Temperatures in ^oC. The indicated pressure is measured pressure deviation from time average pressure in the gas pocket. The 'temp' temperatures are measured graphite ring temperatures and the 'HT' temperatures are measured hot-top temperatures (see figures 2.2 and 2.3).

$100mm/min$ **casting velocity**

	Pressure (mbar)	temp2	temp4	temp5	temp6
Mean	0	64,53622	78,49369	68,3981	68,59016
Max	0,168947	73,478	89,291	75,554	75,241
Min	-0,35918	54,868	63,846	58,559	59,682
Stdev	0,084008	3,908624	4,783425	3,021095	2,725702

	HT1	HT2	HT3	HT4	MOULD
Mean	597,0166	487,4816	128,7675	120,7548	40,93242
Max	608,82	509,77	157,18	134,32	42,185
Min	577,89	459,38	96,135	105,28	39,739
Stdev	8,487291	14,29764	17,59707	8,261432	0,453548

$120mm/min$ **casting velocity**

	Pressure (mbar)	temp2	temp4	temp5	temp6
Mean	0	65,56731	65,32221	58,95359	58,76375
Max	0,395197	72,486	83,55	72,851	72,851
Min	-0,46355	56,589	60,437	55,953	56,108
Stdev	0,08997	4,09607	1,99704	1,283	1,11119

	HT1	HT2	HT3	HT4	MOULD
Mean	619,8884	473,5051	198,8337	147,2541	38,98327
Max	623,28	509,77	208,44	150,2	40,736
Min	608,82	472,13	157,01	134,16	38,046
Stdev	1,74663	1,51681	5,98003	1,8239	0,37115

$160mm/min$ **casting velocity**

	Pressure (mbar)	temp2	temp4	temp5	temp6
Mean	0	83,21908	74,25397	66,14937	67,04145
Max	0,177697	90,917	80,372	72,388	72,388
Min	-0,11168	78,349	71,162	63,38	64,768
Stdev	0,052974	1,973887	1,604671	1,834478	1,50668

	HT1	HT2	HT3	HT4	MOULD
Mean	597,0166	487,4816	128,7675	120,7548	40,93242
Max	608,82	509,77	157,18	134,32	42,185
Min	577,89	459,38	96,135	105,28	39,739
Stdev	8,487291	14,29764	17,59707	8,261432	0,453548

A.2 Fourier Analysis

The signals were sampled with a sampling frequency $S_f = 14.29Hz$. The DC component of the data was cancelled out. The data were filtered with a transposed low-pass 45th order Kaiser Window FIR filter with cutoff frequency at $0.3S_f$ to avoid aliasing and leakage. A Hanning window was applied to avoid the Gibbs effect and to improve results for the lower frequencies. Finally the discrete Fourier transform was found using a Finite Fourier Transform algorithm. The Fourier Analysis was performed using Matlab.

Plots for *tc2* to *tc6* correspond to temperatures measured in the graphite in figure 2.2 and *al mould* corresponds to the temperature measured in the aluminium part of the mould. Results are again presented only for ingot 6.

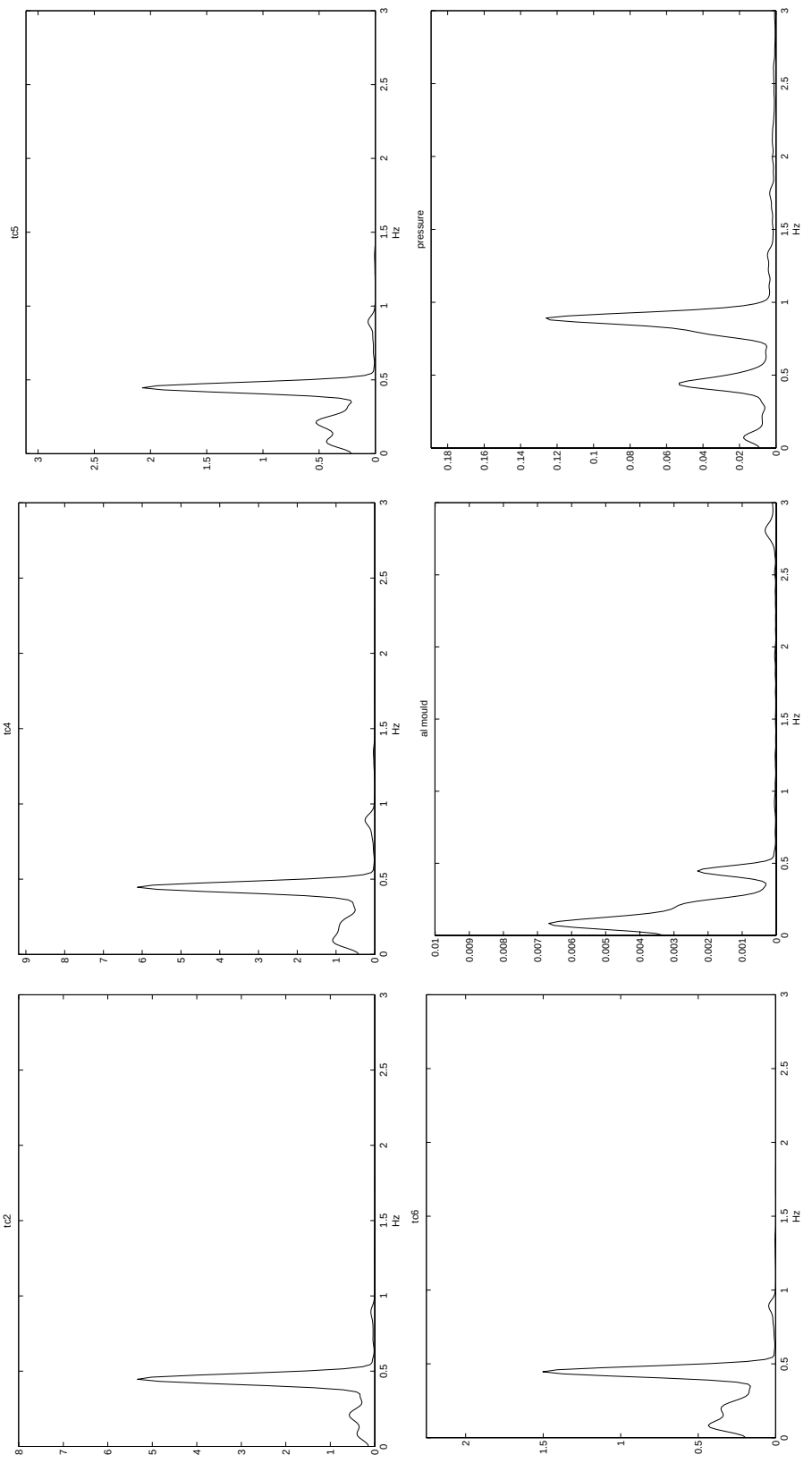

Ingot 6, 100mm/s

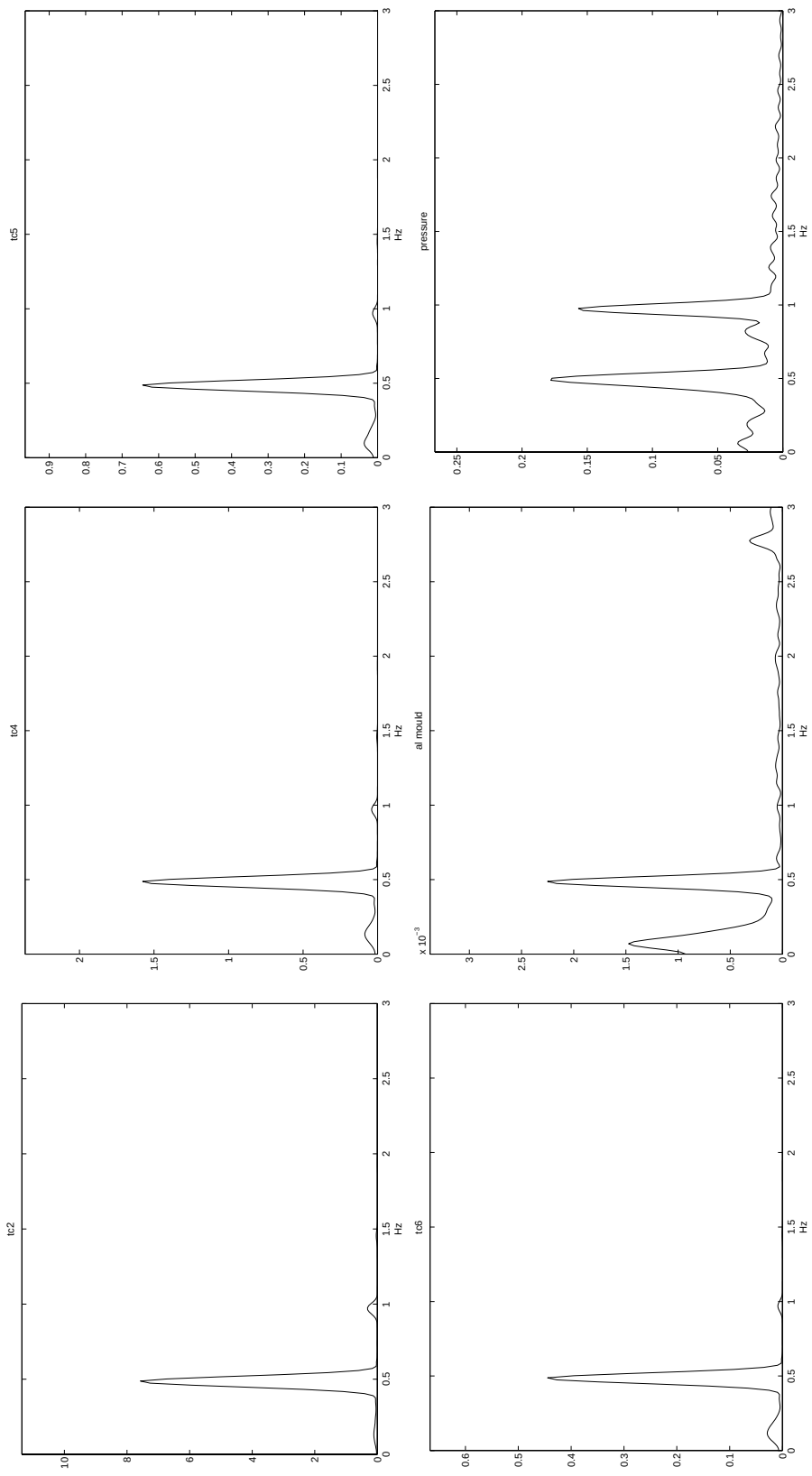

Ingot 6, 120mm/s

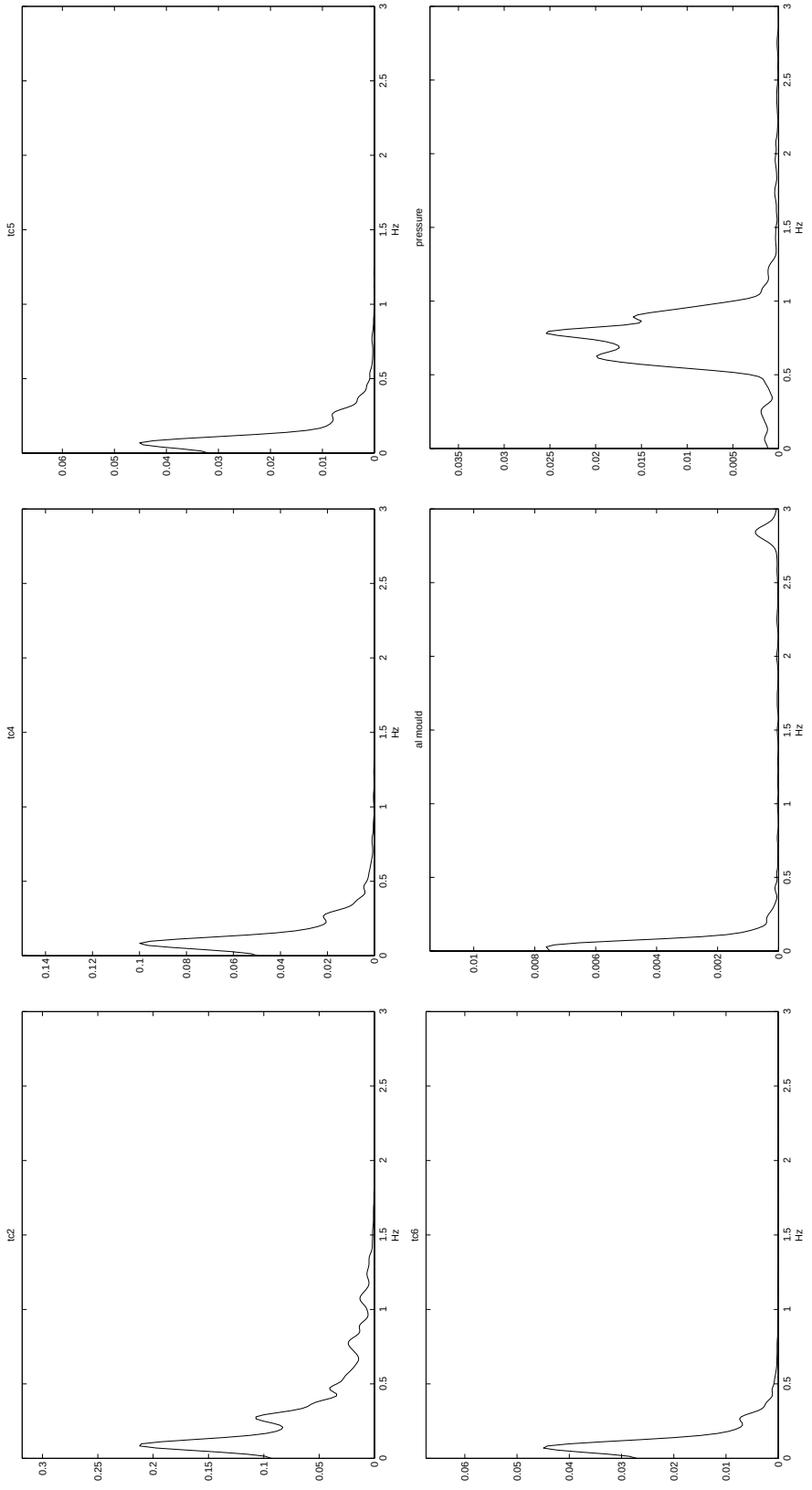

Ingot 6, 160mm/s

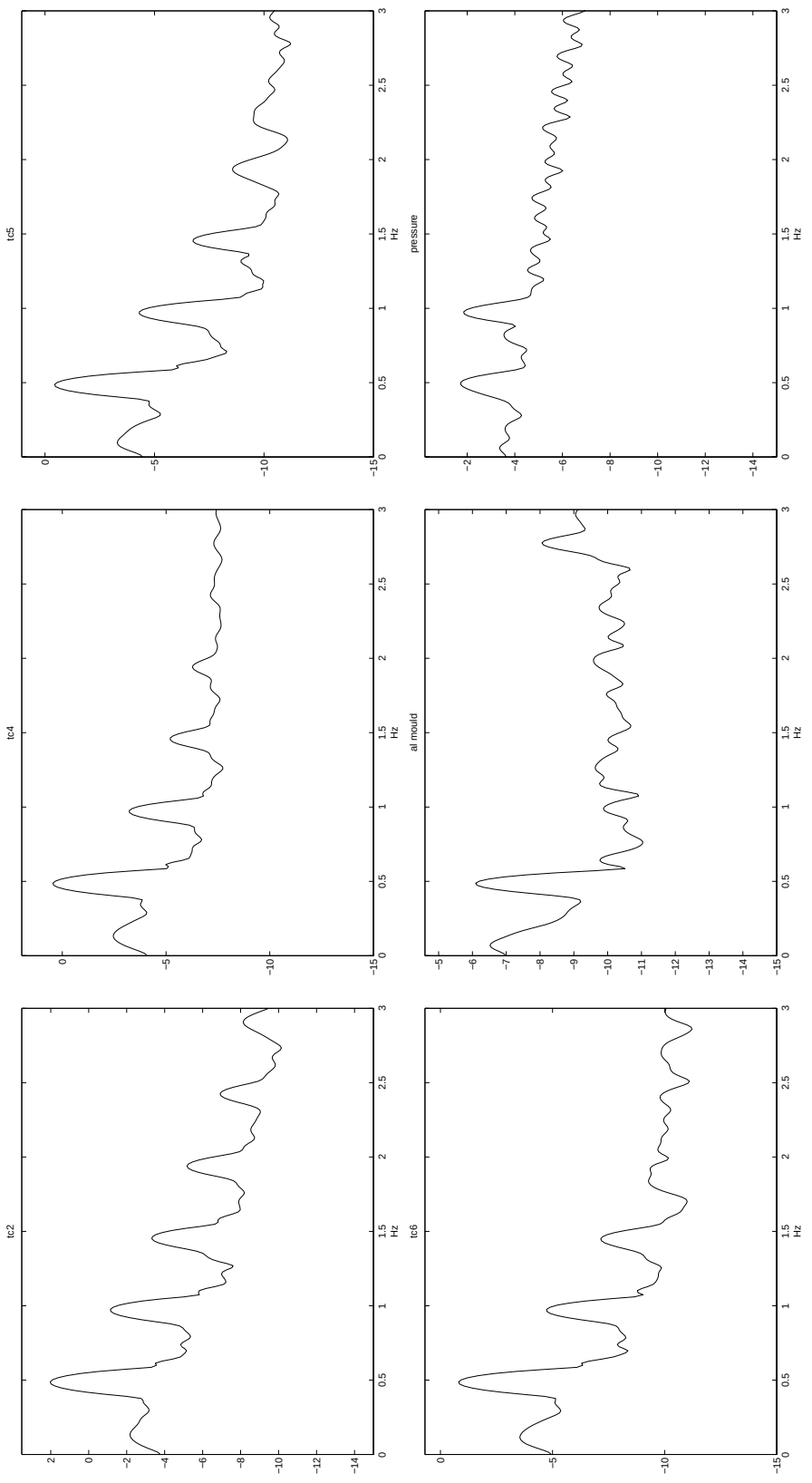

Ingot 6, 120mm/s, logarithmic

Appendix B

Water meniscus experiments

To observe the effect of surface wetting and gas flow rate on the characteristics of meniscus development and on gas discharge up through the melt inlet in a typical casting geometry, a water model experiment was performed.

B.1 Experimental setup

A Plexiglas container in the shape of a half cross-section of the casting was used in the experiment. The geometry is shown in figure B.

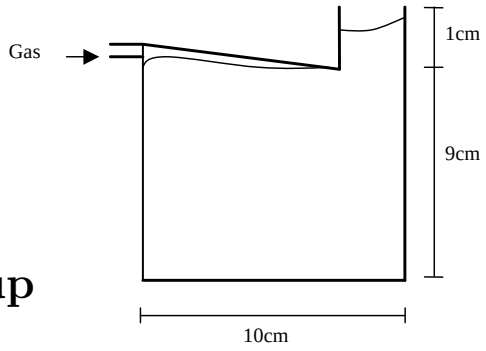

Figure B.1: Experimental geometry for water modelling tests. Water surface and meniscus indicated.

The container was approximately cubic, with dimensions $10cm \times 10cm \times 10cm$. The top lid of the container, corresponding to the hot top in the casting process, was slanted to facilitate creation and observation of the gas pocket and meniscus underneath it.

Gas was let in under pressure through a series of tubes with diameter =3mm along the side of the container, indicated in figure B. The gas would periodically bubble up and escape through the top of the container, to the right in the figure. Initially the Plexiglas surface was untreated, so for the first testrun the wetting was quite high. For subsequent runs the surface was treated with chemicals to achieve decreasingly lower surface wetting.

B.2 Results

Figure B.2 shows three series of tests for a gradually decreasing wetting conditions: from high wetting (B.2(a) to B.2(c)), to medium (B.2(d) to B.2(f)), to low wetting (B.2(g) to B.2(i)). It can be seen that the most pronounced dynamic behaviour occurs in the case of high surface wetting. As the wetting is reduced the gas discharge is less violent and as a consequence the surface of the meniscus is more stable. The gas pocket above the meniscus can fill to a higher extent in the case of high wetting. This can be seen by the difference in minimum and maximum height of the water column. Consequently the dynamics are more violent when the pocket bursts and the gas flows out through the top.

In our water experiment the outlet of gas creates gravity waves. This effect is more pronounced in the case of higher wetting. The gravity waves are damped so that the meniscus surface becomes steady before each gas discharge. In the case of the water model, damping is mainly due to the wall boundaries. Since the circulation caused by waves decreases exponentially downwards the waves will not be notably damped by the bottom of the container. The damping effect of gravity waves in the casting process would depend on the composition and depth of the mushy zone and consequently on the alloy type and casting velocity. The least efficient damping would occur for pure Al at high casting velocity, which would give a deep liquid phase and no mushy zone. Wave damping might be included in mathematical simulations of the process.

In the water model experiments the hydrostatic head increases as the gas pocket above the meniscus increases in volume. This would however not be the case in individual moulds in a casting set-up. The molten metal surface over a mould would not increase notably in height. Gravity would force it toward the average surface level of the molten metal. Therefore the pressure at the meniscus would not vary as much as it does in the case of our water experiment. So the gas discharge through the top of the mould, if it occurs, could be expected to be less violent than the observed discharge in our water model experiments.

In the water model experiments the contact point between the meniscus and the wall is nearly constant in the case of high wetting at the wall beneath the gas inlet. The meniscus sticks to the wall. When the wetting is decreased the contact point can move more freely. Therefore the concept of constant contact angle in modelling is probably most applicable in cases with low wetting. The time to reach equilibrium contact angle apparently decreases with decreasing wetting. A static contact angle might be used when modelling the meniscus movement in the case of low wetting. For cases with higher

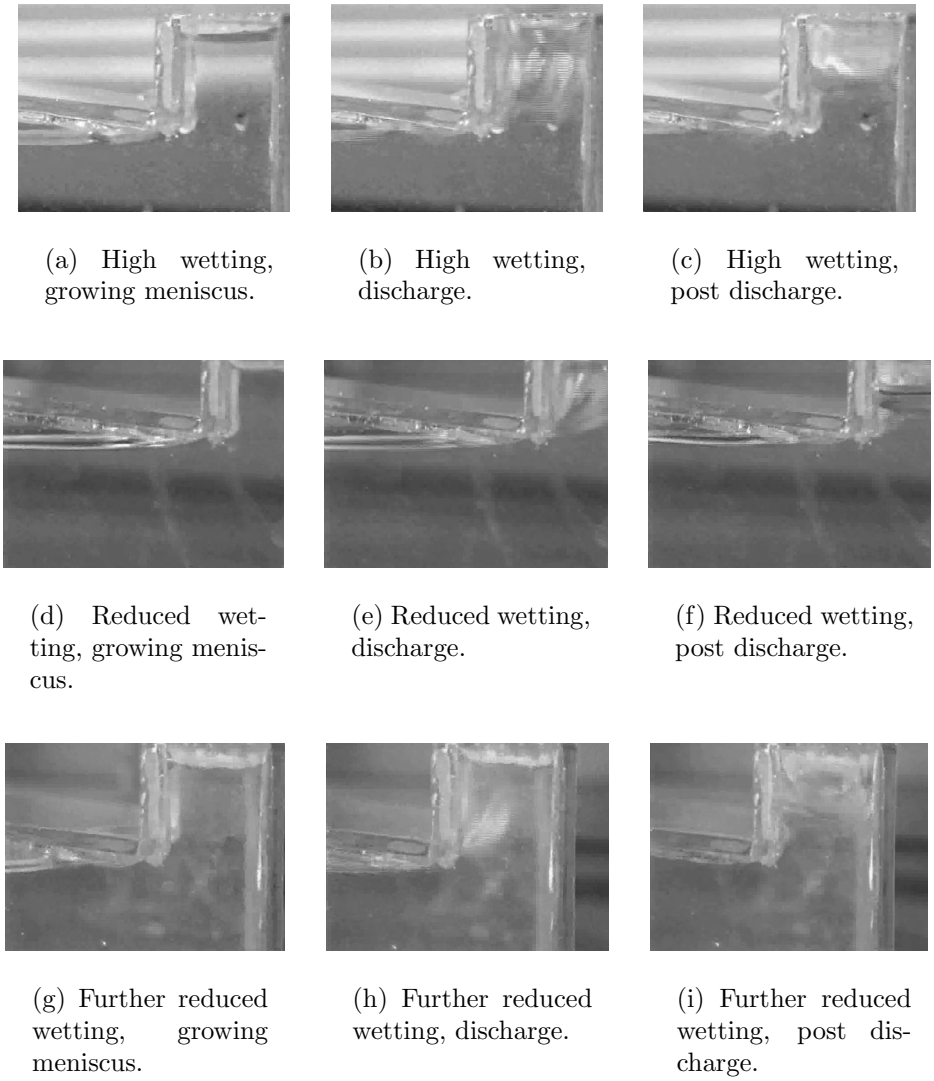

(a) High wetting, growing meniscus.

(b) High wetting, discharge.

(c) High wetting, post discharge.

(d) Reduced wetting, growing meniscus.

(e) Reduced wetting, discharge.

(f) Reduced wetting, post discharge.

(g) Further reduced wetting, growing meniscus.

(h) Further reduced wetting, discharge.

(i) Further reduced wetting, post discharge.

Figure B.2: Water meniscus experiments.

wetting it is necessary to model a dynamic contact angle. The forces driving the contact angle towards its equilibrium point will then decrease with increasing wetting.

Appendix C

VOF phase conservation

Two test examples of the VOF donor acceptor algorithm are presented here to show that flux correction is in general needed to achieve phase conservation when this method is applied.

C.1 Simultaneous advection

Figure C.1 shows the cells used in the VOF donor-acceptor advection algorithm for calculating cell face volume fraction (F) fluxes for a cell (centre). A 2D flow with a regular grid, $\delta x = \delta y = \delta z$, is used and the direction of flow is upwards to the right. The fluxes over the cell faces are calculated according to the donor acceptor model. The value shown in the cells is the cell volume fraction (here also denoted by F). Using the method to calculate the surface direction presented in [26] the result here is that the surface is more vertical than horizontal. Consequently, in the advection in the x direction upwinding is default in the advection, i.e. the acceptor cell gives the initial volume fraction flux. In the y direction downwinding is default.

For $\Delta t > .25\delta x/u_l$ total flux per unit area from the left is

$$\delta F_l = .25\delta x \cdot F_{i,j} + u_l(\Delta t - .25\delta x/u_l) = u_l\Delta t - .05\delta x. \tag{C.1}$$

For $\Delta t > .22\delta x/u_r$ total flux per unit area from the right is

$$\delta F_r = .22\delta x \cdot F_{i+1,j} + u_r(\Delta t - .22\delta x/u_r) = u_r\Delta t - .2\delta x. \tag{C.2}$$

For $\Delta t > .2\delta y/u_r$ total flux per unit area on top is

$$\delta F_t = v_t(\Delta t - .2\delta y/u_t) = v_t\Delta t - .2\delta y. \tag{C.3}$$

The total flux per unit area on the bottom surface is

$$\delta F_b = v_b\Delta t \tag{C.4}$$

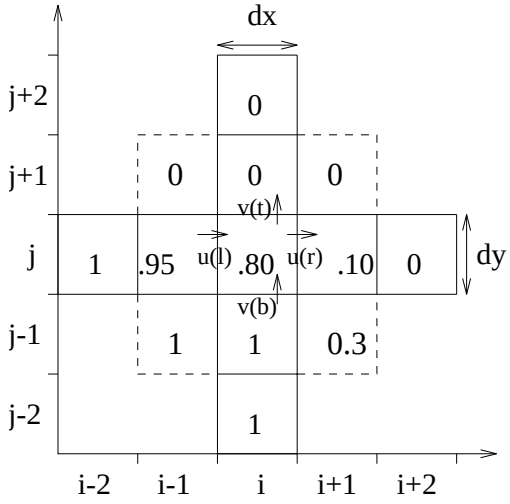

Figure C.1: Cells used in 2D F advection algorithm

The resulting volume fraction in the cell after the time step then becomes

$$F_i^{n+1} = F_i^n + \left(\delta F_l \delta y \delta z - \delta F_r \delta y \delta z + \delta F_b \delta x \delta z - \delta F_t \delta x \delta z\right) / \delta x \delta y \delta z = \quad \text{(C.5)}$$

$$F_i^{n+1} = F_i^n + 0.35 + \Delta t \left(\frac{u_l}{\delta x} + \frac{v_b}{\delta y} - \frac{u_r}{\delta x} - \frac{v_t}{\delta y} \right).$$

Δt is the time increment. This result is achieved by using explicit time integration in derivation of the fluxed values. By incompressibility we have

$$u_l + v_b - u_r - v_t = O(h^3) \approx 0. \quad \text{(C.6)}$$

Therefore the new F_i-value is 1.15, and the cell is overfilled (or underemptied) by 15%. By setting the F-value back to 1, as is suggested in the donor acceptor model, a significant deal of liquid volume is lost. The calculation is also done with the assumption that $\Delta t > \frac{.25dx}{u_{max}}$. For smaller time increment the overfilling is smaller, but with other interface configurations stronger restrictions on Δt could result. Thus the Courant condition could probably be made more restrictive, i.e. even smaller $\frac{\Delta t}{dx}$ should probably be used. Of course decreasing the grid size would also help. However, for folding actions sharp corners like the one in figure C.1 will always occur, independent of grid size.

Using an implicit advection method would probably be natural in this case, and might help with this problem. The nature of the implicit method would however probably have to depend on both the direction of velocity and the configuration of the interface, making the method a lot more complex and more demanding on cpu time.

C.2 Operator splitting

Using operator splitting (sequential flux calculation in x and y directions), with δt large enough:

$$\delta t > \frac{\delta x}{v_t}\left[1 - \left(F_i^n + 0.15 + (u_l - u_r)\frac{\Delta t}{\delta x}\right)\right], \tag{C.7}$$

we get

$$F_i^{n+1} = 1 - \left(\frac{u_l}{\delta x} - \frac{u_r}{\delta x}\right)\Delta t \tag{C.8}$$

when $\delta x = \delta y$. For smaller t the expression becomes more complicated. Error could still occur though. Obviously $F > 1$ for $u_l < u_r$. So flux correction is also needed when operator splitting is applied. But again for small $u\delta t/\delta x$ the error is small. Care must therefore be taken in the discretization if phase conservation is to be achieved with this method.

Appendix D

Some comments on applied simplifications

Buoyancy

Gas pocket flow The density of the gas is dependent on both pressure and temperature through the ideal gas equation:

$$\frac{p}{RT} = \frac{n}{V} \propto \rho. \tag{D.1}$$

The density variation in the gas due to hydrostatic forces is negligible (less than 0.1 Pa). And the small flow velocities in the gas in the simulations (see chapter 9) give very low Mach numbers ($Ma_{max} \sim 10^{-4}$), so compression due to flow is negligible. Therefore the pressure in the gas pocket can be assumed to be approximately homogeneous. Then if the upper contact angle of the meniscus is assumed to be free, with surface tension forces leading to a negligible macroscopic curvature at the contact point, the gas pocket pressure will equal the metallostatic pressure at the bottom surface of the hot-top since there is no pressure jump across the meniscus surface here.

The density / temperature dependence will lead to *natural convection* in the gas pocket. The only other forces influencing the gas flow are due to the inflow pressure, meniscus movement and shear acting on the gas at the free surface meniscus boundary. However, since it is assumed that the meniscus is a free surface, the flow in the gas pocket will have no effect on the liquid metal flow.

Another consideration is increased heat transfer due to natural convection in the gas pocket. The relation between heat transport by convection and heat transport by conduction is given by the product of the Prandtl and Reynolds numbers, also called the Peclet number $Pe = Pr\,Re$. For typical values in the gas pocket $Pe \approx 400U$, where U is the characteristic gas flow

velocity. This suggests that natural convection will contribute significantly to heat transfer across the gas pocket. However, the effect of convection in the gas pocket is assumed negligible compared to heat transfer due to the conduction across the air gap and the direct conduction in contact areas between metal and mould. Subsequently the effect of buoyancy in the gas may be neglected in the simulations.

Compression of the gas in the gas pocket by the movement of the meniscus, may lead to volume change. If the gas has no escape, i.e. the air gap is closed, then the reduction in volume will lead to increased density, and also increased pressure, if constant gas temperature is assumed. With the assumption that the pressure in the gas pocket equals the metallostatic pressure at the bottom of the hot-top, these volume/density variations must be coupled with variations of metallostatic height in the mould. To include this type of gas density variations the ideal gas model would have to be incorporated. However, such variations will not significantly influence meniscus oscillations, as shown in section 3.4.2.

Melt flow The density of the melt is also dependent on temperature. This temperature dependence influences both the melt flow through buoyancy and also the ingot geometry by contraction during solidification. As remarked earlier, the effect of solidification contraction on the meniscus movement is introduced through an independent model. So here we will concentrate on the effect of temperature dependent density on the melt flow, i.e. the effect of natural convection.

The importance of buoyant forces to the flow are given by the relation between buoyancy and inertial forces, expressed by the ratio of the Grashof number to the square of the Reynolds number, which is

$$\frac{Gr}{Re^2} = \frac{\beta g \Delta T L}{U^2} \approx \frac{0.01}{U^2} \tag{D.2}$$

for the simulation parameters. Here the characteristic dimension L is set to the ingot diameter 0.1m, the characteristic temperature difference ΔT is in the order of 100K, and the thermal expansion coefficient β is in the order of 1.0×10^{-3}. The velocity U in the Reynolds number may be interpreted as the mean flow velocity when buoyancy is neglected. In the simulations (chapter 9) the flow velocity in the region of the meniscus is mostly in the order of $0.01m/s$ to $0.1m/s$. In this case boyancy would have an influence, but would not greatly alter the flow. In the bulk of the ingot U is however of the order of the casting velocity for the simulations. Then for a casting velocity of 120mm/min, $U \sim 2.0 \times 10^{-3} m/s$ and $Gr/Re^2 \sim 2500$. So if buoyant forces were included the flow field should be significantly altered.

This would again lead to altered heat flow due to convective heat transport. A buoyancy model should therefore be applied to include these effects. This remains to be done in future work.

In the simulations the thermal boundary conditions are found by iteratively solving the inverse heat transfer problem for a conservative laminar flow field without natural convection. The resultant temperature field is comparable to that found in the experimental measurements. Therefore omitting natural convection in the simulations does not result in an erroneous temperature profile. Also, the meniscus dynamics should not influence the bulk convection in the mould, and vice versa, if it is assumed that the characteristic dimensions of the meniscus are a lot smaller than those of the mould.

Cellwise homogeneous velocity

The cell Reynolds number[1] gives an indication of the validity of the approximation of homogeneous velocity in the two phases in a computational cell. This nondimensional value gives the ratio of inertial to viscous forces in a computational cell. By putting an upper bound on $R_{\Delta x}$ the velocity variation over a cell can be made small compared to the mean velocity. So in the areas of two phases within the computational domain the grid size should fulfill the relation

$$Re_{\Delta x} << 1. \tag{D.3}$$

With typical casting parameters (appendix F) and characteristic velocities in the casting mould in the order of $10^{-2} m/s$, as in the casting simulations (chapter 9), then the condition on grid size becomes

$$\Delta x << 0.001m. \tag{D.4}$$

In our simulations the grid size is of the order of 1mm. Simulations with a smaller grid would be more time consuming, but according to this analysis the accuracy in velocity interpolation at the phase interface for the applied grid size is poor. Accuracy in the discretization of the flow equations at the phase boundary should be greatly improved by refining the grid.

Isotropic conductivity

To correct the error in the heat conduction interface cells caused by using an isotropic conductivity, a directionally dependent, i.e. non-isotropic, conductivity vector $\vec{k}$ could be introduced. Then the conductive term becomes

$$-\nabla \cdot \vec{q} = -\nabla \vec{k} \cdot \nabla T. \tag{D.5}$$

[1] With computational cell dimension Δx the cell Reynolds number is defined as $\frac{\rho U \Delta x}{\mu}$.

The conductivity vector in cells containing both phases can be determined by the geometry of the spline interface in the Method of Tensions. Together with an enthalpy correction method as suggested in 5.1.3 this should produce a stable and more accurate method for calculating the heat flow at the melt surface. The technique remains to be tested out.

Appendix E

Cubic spline interpolation

This is a third order polynomial interpolation method. With the interpolation polynomial for the i^{th} segment a curve parameterized by t (see figure E.1) is expressed as

$$x^{(i)} = a^{(i)}\left(t - t_i\right)^3 + b^{(i)}\left(t - t_i\right)^2 + c^{(i)}\left(t - t_i\right) + d^{(i)}, \tag{E.1}$$

where $x(t) = x^{(i)}(t),\ t\ \epsilon\ (t_i, t_{i+1})$. The condition of continuous second derivative gives

$$a^{(i)} = \frac{S_{i+1} - S_i}{6h_i} \tag{E.2}$$

$$b^{(i)} = \frac{S_i}{2} \tag{E.3}$$

where $S_i = x^{(i)\prime\prime}(t_i) = x^{(i-1)\prime\prime}(t_i)$ and $h_i = t_{i+1} - t_i$.

Since

$$d^{(i)} = x(t_i) \tag{E.4}$$

the polynomial E.1 gives

$$c^{(i)} = \frac{x^{(i)}(t_{i+1}) - x^{(i)}(t_i)}{h_i} - \frac{2S_i + S_{i+1}}{6}h_i. \tag{E.5}$$

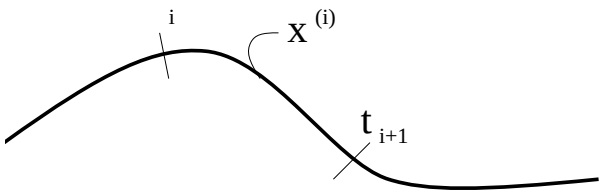

Figure E.1: Segment of curve.

All the values in the expressions for the polynomial coefficients above are known, except the second derivatives, S_i which are found using the condition of continuity of first derivatives, leading to the general set of equations

$$h_{i-1}S_{i-1} + 2(h_i + h_{i-1})S_i + h_i S_{i+1} = h(f_i - f_{i-1}),\ f_i = \frac{x(t_{i+1}) - x(t_i)}{h_i}. \tag{E.6}$$

E.1 Boundary conditions

The types of boundary conditions normally used are

- $S_i = 0$ at the boundaries, natural splines
- extrapolating the second derivative boundary values
- forcing the slope to assume certain values at the boundaries (specified contact angle with the boundary)
- periodic boundary conditions (f. ex. for a bubble)

The three first types of boundary conditions lead to tridiagonal systems which are easily solved (see [21]). The periodic boundary condition leads to a cyclic tridiagonal system, which requires a different solution method.

E.1.1 Periodic boundary conditions

In the following it is shown how to solve the cyclic tridiagonal system using the Sherman-Morrison Formula, described in [50]. With periodic boundary conditions ($x_0|_{t=0} = x_n|_{t=t_n}$, $\frac{dx_0}{dt}|_{t=0} = \frac{dx_n}{dt}|_{t=t_n}$; $\frac{d^2x_0}{dt^2}|_{t=0} = \frac{d^2x_n}{dt^2}|_{t=t_n}$), the cyclic tridiagonal system for the second derivatives becomes:

$$\mathbf{As} = \mathbf{f} \tag{E.7}$$

where $\mathbf{s} = [S_0, S_1, \ldots, S_{n-1}]^T$, $\mathbf{f} = 6\,[f_0 - f_{n-1}, f_1 - f_0, \ldots, f_{n-1} - f_{n-2}]^T$ and

$$\mathbf{A} = \begin{pmatrix} 2(h_0+h_n) & h_0 & 0 & 0 & 0 & h_n \\ h_0 & 2(h_0+h_1) & h_1 & 0 & 0 & 0 \\ 0 & h_1 & 2(h_1+h_2) & h_2 & 0 & 0 \\ \vdots & \ddots & \ddots & \ddots & \ddots & \vdots \\ 0 & 0 & h_{n-3} & 2(h_{n-2}+h_{n-3}) & h_{n-2} & 0 \\ 0 & 0 & 0 & h_{n-2} & 2(h_{n-1}+h_{n-2}) & h_{n-1} \\ h_n & 0 & 0 & 0 & h_{n-1} & 2(h_n+h_{n-1}) \end{pmatrix}$$

Sherman-Morrison Formula

The formula gives the inverse of a matrix

$$\mathbf{A} + \mathbf{u} \otimes \mathbf{v} \tag{E.8}$$

as

$$(\mathbf{A} + \mathbf{u} \otimes \mathbf{v})^{-1} = \mathbf{A}^{-1} - \frac{\mathbf{z} \otimes \mathbf{w}}{1 + \lambda}, \tag{E.9}$$

where
$\lambda = \mathbf{v} \cdot \mathbf{A}^{-1} \cdot \mathbf{u}$, $\mathbf{z} = \mathbf{A}^{-1} \cdot \mathbf{u}$, $\mathbf{w} = \left(\mathbf{A}^{-1}\right)^T \cdot \mathbf{v}$. Since $\frac{1}{1+\lambda}$ is expanded in a power series to derive the formula, is necessary for convergence of the series that $|\lambda| < 1$. So we need

$$|\mathbf{v} \cdot \mathbf{A}^{-1} \cdot \mathbf{u}| < 1. \tag{E.10}$$

Using the Sherman-Morrison formula the solution to the system

$$(\mathbf{A} + \mathbf{u} \otimes \mathbf{v}) \cdot \mathbf{x} = \mathbf{b} \tag{E.11}$$

is

$$\mathbf{x} = \mathbf{y} - \left[\frac{\mathbf{v} \cdot \mathbf{y}}{1 + \mathbf{v} \cdot \mathbf{z}}\right] \mathbf{z} \tag{E.12}$$

where

$$\mathbf{A} \cdot \mathbf{y} = \mathbf{b}, \quad \mathbf{A} \cdot \mathbf{z} = \mathbf{u}. \tag{E.13}$$

Solving E.13 for $\mathbf{y}$ and $\mathbf{z}$ these can be inserted in E.12 to find the solution.

Solution of the cyclic tridiagonal system

We choose

$$\mathbf{B} = \begin{pmatrix} 2(h_0 + h_n) - \gamma & h_0 & 0 & 0 \\ h_0 & 2(h_0 + h_1) & h_1 & 0 \\ \vdots & \ddots & \ddots & \ddots \\ 0 & 0 & h_{n-1} & 2(h_n - h_{n-1}) - h_n^2/\gamma \end{pmatrix}. \tag{E.14}$$

and

$$\mathbf{u} = \begin{bmatrix} \gamma \\ 0 \\ \vdots \\ 0 \\ h_n \end{bmatrix} \quad \mathbf{v} = \begin{bmatrix} 1 \\ 0 \\ \vdots \\ 0 \\ h_n/\gamma \end{bmatrix}. \tag{E.15}$$

Thus $\mathbf{B}+\mathbf{u}\otimes\mathbf{v} = \mathbf{A}$ in E.7. We choose the parameter $\gamma = -2(h_0+h_n)$ to avoid loss off precision. One should still check that the term $2(h_n - h_{n-1}) - h_n^2/\gamma$

is not close to zero.

Subsequently the system E.7 can be solved using the Sherman-Morrison formula:

$$\mathbf{A} \cdot \mathbf{s} = (\mathbf{B} + \mathbf{u} \otimes \mathbf{v}) \cdot \mathbf{s} = \mathbf{f}; \tag{E.16}$$

$$\mathbf{B} \cdot \mathbf{y} = \mathbf{f}, \quad \mathbf{B} \cdot \mathbf{z} = \mathbf{u} \tag{E.17}$$

and finally

$$\mathbf{s} = \mathbf{y} - \left[\frac{\mathbf{v} \cdot \mathbf{y}}{1 + \mathbf{v} \cdot \mathbf{z}} \right] \mathbf{z}. \tag{E.18}$$

Solving the two tridiagonal systems E.17 can be done in $O(N)$ operations, where $N \times N$ is the dimension of the matrix B. Note that one should check that

$$|\mathbf{v} \cdot \mathbf{B}^{-1} \cdot \mathbf{u}| < 1 \tag{E.19}$$

for convergence of the series.

Appendix F

Simulation parameters

F.1 Material parameters

temp [K]	ρ [kg/m^3]	c_p [J/kg K]	k [W/m K]	μ[kg/m s]	f_s
300	2700	900	129		1
600	2700	1036	149		1
811	2700	1139	155		1
828.8	2700	1156	155	100	1
880.0	2700	1917	150	0.1	0.9
898.2	2700	3302	144	0.01	0.8
906.8	2700	5705	139	0.008	0.7
912.0	2700	8251	133	0.005	0.6
915.3	2700	12487	128	0.00324	0.5
917.6	2700	17549	122	0.00162	0.4
919.4	2700	22180	117	0.00162	0.3
920.7	2700	30461	111	0.00135	0.2
921.8	2700	35843	106	0.00135	0.1
922.7	2700	38667	100	0.00135	0.
943	2700	6088	100	0.00135	0.
983	2700	1088	100	0.00135	0.

Table A.1: Material parameters of Al 6082

The simulations were performed with material parameters corresponding to the Al6082 alloy. Material parameters are listed in the table above. The temperature dependence of the solid fraction f_s, conductivity and heat capacity was calculated by ALSTRUC [12]. In the range of solidification (880K-922K) the heat capacity was calculated by the relation for total heat capacity (7.11) in the enthalpy model 7.1.1. The heat capacity curve was

further smoothed to facilitate stability in the numerical simulations. The density was chosen constant to facilitate mass conservation (see 7.2.6). The viscosity was empirically determined based on the viscosity of liquid aluminium (again see section 7.2.6). At complete solidification the viscosity was set to 1. However, above $f_s = 0.8$ the static flow model (7.2.6) is introduced, so in this region the viscosity does not influence the flow.

The material parameters of the air slip gas were chosen to be constant. materials listed below

ρ [kg/m^3]	c_p [J/kg K]	k [W/m K]	μ[kg/m s]
1.0	1.04E3	2.6E-2	1.813E-5

Table A.2: Material parameters of air slip gas.

F.2 Boundary conditions

The computational cells and boundary conditions for simulations of 120mm/min castings of Al6082 are shown on the following pages.

Fluid flow

The inflow velocity (I1-cells) was set to balance the rate of solidified metal movement (I2) out of the computational domain. In addition to the forced inlet conditions two outlet cells were added (O) to facilitate stability in the melt inflow region. Zero boundary velocity was set at the bottom of the hot-top (W2), while the boundary velocity along the solidified ingot surface (W5-W9) was set equal to the casting velocity. The gas inlet was set after initiation of the temperature field in cells (I=52,J=46-49).

Heat flow

Conductive wall conditions (see section 8.1.1) were applied in the hot-top and mould regions (W2,W5,W6,WD,WF and WG). The top of the hot-top region and the outer boundary of the mould wall were insulated (WB,WC). Constant temperature conditions were set at the inlets (I1,I2) and external heat transfer conditions (again 8.1.1) were set for the water cooling (W7,W8,W9,WE) and for air cooling of the hot-top (WA). The heat transfer set at WE models the cooling of the mould wall by the water reservoir.

```
J  I=   2   4   6   8  10  12  14  16  18  20  22  24  26  28  30  32 =I  J
 55  WCWCWCWCWCWCWCWCWCWCWCWCWCWCWCWCWCWCWCWCWCWCWCWCWCWCWCWCWCWCWCWCWC  55
 54  WCWCWCWCWCWCWCWCWCWCWCWCWCWCWCWCWCWCWCWCWCWCWCWCWCWCWCWCWCWCWCWCWC  54
 53  WCWCWCWCWCWCWCWCWCWCWCWCWCWCWCWCWCWCWCWCWCWCWCWCWCWCWCWCWCWCWCWCWC  53
 52  WCWCWCWCWCWCWCWCWCWCWCWCWCWCWCWCWCWCWCWCWCWCWCWCWCWCWCWCWCWCWCWCWC  52
 51  WCWCWCWCWCWCWCWCWCWCWCWCWCWCWCWCWCWCWCWCWCWCWCWCWCWCWCWCWCWCWCWCWC  51
 50  W9W9W9W9W9W9W9W9W9W9W9W9W9W9W9W9W9W9W9W9W9W9W9W9W9W9W9W9W8W8W8W8W7  50
 49  I2 . . . . . . . . . . . . . . . . . . . . . . . . . . . . . . . .  49
 48  I2 . . . . . . . . . . . . . . . . . . . . . . . . . . . . . . . .  48
 47  I2 . . . . . . . . . . . . . . . . . . . . . . . . . . . . . . . .  47
 46  I2 . . . . . . . . . . . . . . . . . . . . . . . . . . . . . . . .  46
 45  I2 . . . . . . . . . . . . . . . . . . . . . . . . . . . . . . . .  45
 44  I2 . . . . . . . . . . . . . . . . . . . . . . . . . . . . . . . .  44
 43  I2 . . . . . . . . . . . . . . . . . . . . . . . . . . . . . . . .  43
 42  I2 . . . . . . . . . . . . . . . . . . . . . . . . . . . . . . . .  42
 41  I2 . . . . . . . . . . . . . . . . . . . . . . . . . . . . . . . .  41
 40  I2 . . . . . . . . . . . . . . . . . . . . . . . . . . . . . . . .  40
 39  I2 . . . . . . . . . . . . . . . . . . . . . . . . . . . . . . . .  39
 38  I2 . . . . . . . . . . . . . . . . . . . . . . . . . . . . . . . .  38
 37  I2 . . . . . . . . . . . . . . . . . . . . . . . . . . . . . . . .  37
 36  I2 . . . . . . . . . . . . . . . . . . . . . . . . . . . . . . . .  36
 35  I2 . . . . . . . . . . . . . . . . . . . . . . . . . . . . . . . .  35
 34  I2 . . . . . . . . . . . . . . . . . . . . . . . . . . . . . . . .  34
 33  I2 . . . . . . . . . . . . . . . . . . . . . . . . . . . . . . . .  33
 32  I2 . . . . . . . . . . . . . . . . . . . . . . . . . . . . . . . .  32
 31  I2 . . . . . . . . . . . . . . . . . . . . . . . . . . . . . . . .  31
 30  I2 . . . . . . . . . . . . . . . . . . . . . . . . . . . . . . . .  30
 29  I2 . . . . . . . . . . . . . . . . . . . . . . . . . . . . . . . .  29
 28  I2 . . . . . . . . . . . . . . . . . . . . . . . . . . . . . . . .  28
 27  I2 . . . . . . . . . . . . . . . . . . . . . . . . . . . . . . . .  27
 26  I2 . . . . . . . . . . . . . . . . . . . . . . . . . . . . . . . .  26
 25  I2 . . . . . . . . . . . . . . . . . . . . . . . . . . . . . . . .  25
 24  I2 . . . . . . . . . . . . . . . . . . . . . . . . . . . . . . . .  24
 23  I2 . . . . . . . . . . . . . . . . . . . . . . . . . . . . . . . .  23
 22  I2 . . . . . . . . . . . . . . . . . . . . . . . . . . . . . . . .  22
 21  I2 . . . . . . . . . . . . . . . . . . . . . . . . . . . . . . . .  21
 20  I2 . . . . . . . . . . . . . . . . . . . . . . . . . . . . . . . .  20
 19  I2 . . . . . . . . . . . . . . . . . . . . . . . . . . . . . . . .  19
 18  I2 . . . . . . . . . . . . . . . . . . . . . . . . . . . . . . . .  18
 17  I2 . . . . . . . . . . . . . . . . . . . . . . . . . . . . . . . .  17
 16  I2 . . . . . . . . . . . . . . . . . . . . . . . . . . . . . . . .  16
 15  I2 . . . . . . . . . . . . . . . . . . . . . . . . . . . . . . . .  15
 14  I2 . . . . . . . . . . . . . . . . . . . . . . . . . . . . . . . .  14
 13  I2 . . . . . . . . . . . . . . . . . . . . . . . . . . . . . . . .  13
 12  I2 . . . . . . . . . . . . . . . . . . . . . . . . . . . . . . . .  12
 11  I2 . . . . . . . . . . . . . . . . . . . . . . . . . . . . . . . .  11
 10  I2 . . . . . . . . . . . . . . . . . . . . . . . . . . . . . . . .  10
  9  I2 . . . . . . . . . . . . . . . . . . . . . . . . . . . . . . . .   9
  8  I2 . . . . . . . . . . . . . . . . . . . . . . . . . . . . . . . .   8
  7  I2 . . . . . . . . . . . . . . . . . . . . . . . . . . . . . . . .   7
  6  I2 . . . . . . . . . . . . . . . . . . . . . . . . . . . . . . . .   6
  5  I2 . . . . . . . . . . . . . . . . . . . . . . . . . . . . . . . .   5
  4  I2 . . . . . . . . . . . . . . . . . . . . . . . . . . . . . . . .   4
  3  I2 . . . . . . . . . . . . . . . . . . . . . . . . . . . . . . . .   3
  2  I2 . . . . . . . . . . . . . . . . . . . . . . . . . . . . . . . .   2
  1   S S S S S S S S S S S S S S S S S S S S S S S S S S S S S S S S   1
J  I=   2   4   6   8  10  12  14  16  18  20  22  24  26  28  30  32 =I  J
```

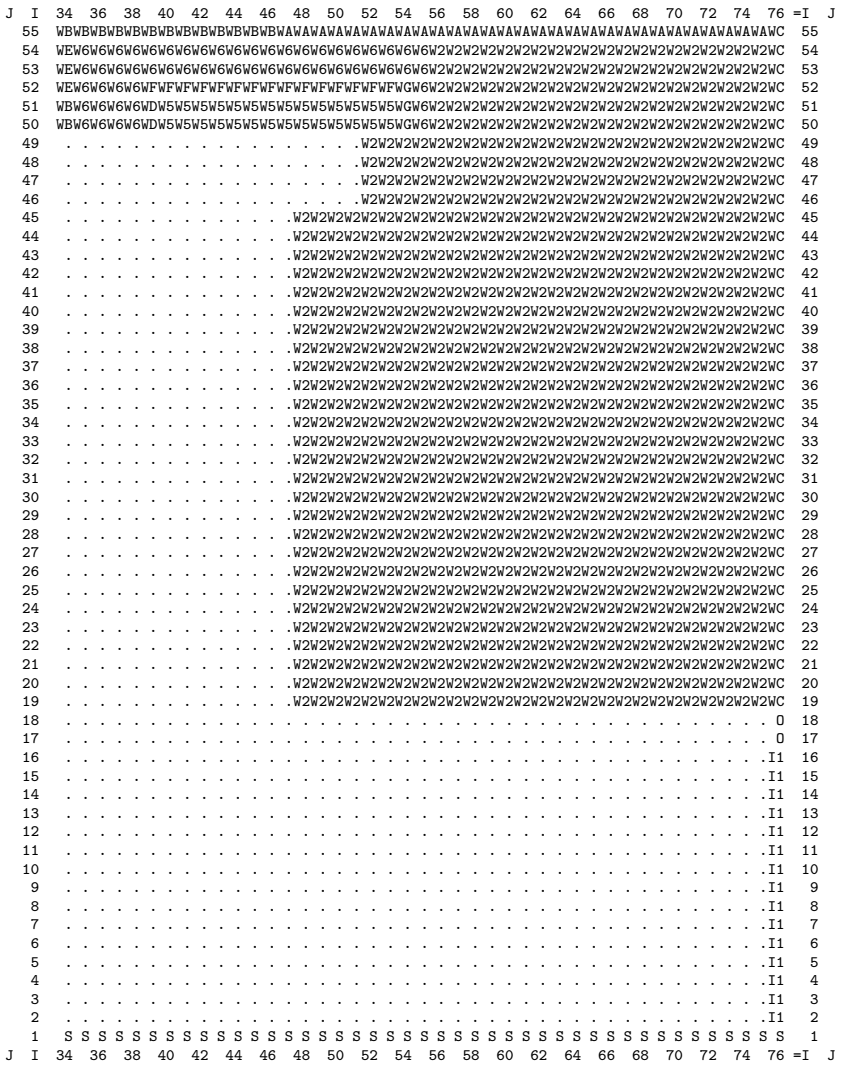
J I 34 36 38 40 42 44 46 48 50 52 54 56 58 60 62 64 66 68 70 72 74 76 =I J
55 WBWBWBWBWBWBWBWBWBWBWBWBWBWAWAWAWAWAWAWAWAWAWAWAWAWAWAWAWAWAWAWAWAWAWAWAWAWAWAWAWAWAWAWC 55
54 WEW6W6W6W6W6W6W6W6W6W6W6W6W6W6W6W6W6W6W6W6W6W6W6W6W6W6W6W6W6W6W6W6W6W6W6W6W6W6W6WC 54
53 WEW6W6W6W6W6W6W6W6W6W6W6W6W6W6W6W6W6W6W6W6W6W6W6W6W6W6W6W6W6W6W6W6W6W6W6W6W6W6WC 53
52 WEW6W6W6W6WFWFWFWFWFWFWFWFWFWFWFWFWFWFWFWGW6W6W6W6W6W6W6W6W6W6W6W6W6W6W6W6W6W6WC 52
51 WBW6W6W6W6WDW5W5W5W5W5W5W5W5W5W5W5W5WGW6W6W6W6W6W6W6W6W6W6W6W6W6W6W6W6W6W6W6W6WC 51
50 WBW6W6W6W6WDW5W5W5W5W5W5W5W5W5W5W5W5WGW6W6W6W6W6W6W6W6W6W6W6W6W6W6W6W6W6W6W6W6WC 50
49 . . . . . .W2W2W2W2W2W2W2W2W2W2W2W2W2W2W2W2W2W2W2W2W2W2W2W2W2W2W2WC 49
48 . . . . . .W2W2W2W2W2W2W2W2W2W2W2W2W2W2W2W2W2W2W2W2W2W2W2W2W2W2W2WC 48
47 . . . . . .W2W2W2W2W2W2W2W2W2W2W2W2W2W2W2W2W2W2W2W2W2W2W2W2W2W2W2WC 47
46 . . . . . .W2W2W2W2W2W2W2W2W2W2W2W2W2W2W2W2W2W2W2W2W2W2W2W2W2W2W2WC 46
45 . . . . . .W2W2W2W2W2W2W2W2W2W2W2W2W2W2W2W2W2W2W2W2W2W2W2W2W2W2W2WC 45
44 . . . . . .W2W2W2W2W2W2W2W2W2W2W2W2W2W2W2W2W2W2W2W2W2W2W2W2W2W2W2WC 44
43 . . . . . .W2W2W2W2W2W2W2W2W2W2W2W2W2W2W2W2W2W2W2W2W2W2W2W2W2W2W2WC 43
42 . . . . . .W2W2W2W2W2W2W2W2W2W2W2W2W2W2W2W2W2W2W2W2W2W2W2W2W2W2W2WC 42
41 . . . . . .W2W2W2W2W2W2W2W2W2W2W2W2W2W2W2W2W2W2W2W2W2W2W2W2W2W2W2WC 41
40 . . . . . .W2W2W2W2W2W2W2W2W2W2W2W2W2W2W2W2W2W2W2W2W2W2W2W2W2W2W2WC 40
39 . . . . . .W2W2W2W2W2W2W2W2W2W2W2W2W2W2W2W2W2W2W2W2W2W2W2W2W2W2W2WC 39
38 . . . . . .W2W2W2W2W2W2W2W2W2W2W2W2W2W2W2W2W2W2W2W2W2W2W2W2W2W2W2WC 38
37 . . . . . .W2W2W2W2W2W2W2W2W2W2W2W2W2W2W2W2W2W2W2W2W2W2W2W2W2W2W2WC 37
36 . . . . . .W2W2W2W2W2W2W2W2W2W2W2W2W2W2W2W2W2W2W2W2W2W2W2W2W2W2W2WC 36
35 . . . . . .W2W2W2W2W2W2W2W2W2W2W2W2W2W2W2W2W2W2W2W2W2W2W2W2W2W2W2WC 35
34 . . . . . .W2W2W2W2W2W2W2W2W2W2W2W2W2W2W2W2W2W2W2W2W2W2W2W2W2W2W2WC 34
33 . . . . . .W2W2W2W2W2W2W2W2W2W2W2W2W2W2W2W2W2W2W2W2W2W2W2W2W2W2W2WC 33
32 . . . . . .W2W2W2W2W2W2W2W2W2W2W2W2W2W2W2W2W2W2W2W2W2W2W2W2W2W2W2WC 32
31 . . . . . .W2W2W2W2W2W2W2W2W2W2W2W2W2W2W2W2W2W2W2W2W2W2W2W2W2W2W2WC 31
30 . . . . . .W2W2W2W2W2W2W2W2W2W2W2W2W2W2W2W2W2W2W2W2W2W2W2W2W2W2W2WC 30
29 . . . . . .W2W2W2W2W2W2W2W2W2W2W2W2W2W2W2W2W2W2W2W2W2W2W2W2W2W2W2WC 29
28 . . . . . .W2W2W2W2W2W2W2W2W2W2W2W2W2W2W2W2W2W2W2W2W2W2W2W2W2W2W2WC 28
27 . . . . . .W2W2W2W2W2W2W2W2W2W2W2W2W2W2W2W2W2W2W2W2W2W2W2W2W2W2W2WC 27
26 . . . . . .W2W2W2W2W2W2W2W2W2W2W2W2W2W2W2W2W2W2W2W2W2W2W2W2W2W2W2WC 26
25 . . . . . .W2W2W2W2W2W2W2W2W2W2W2W2W2W2W2W2W2W2W2W2W2W2W2W2W2W2W2WC 25
24 . . . . . .W2W2W2W2W2W2W2W2W2W2W2W2W2W2W2W2W2W2W2W2W2W2W2W2W2W2W2WC 24
23 . . . . . .W2W2W2W2W2W2W2W2W2W2W2W2W2W2W2W2W2W2W2W2W2W2W2W2W2W2W2WC 23
22 . . . . . .W2W2W2W2W2W2W2W2W2W2W2W2W2W2W2W2W2W2W2W2W2W2W2W2W2W2W2WC 22
21 . . . . . .W2W2W2W2W2W2W2W2W2W2W2W2W2W2W2W2W2W2W2W2W2W2W2W2W2W2W2WC 21
20 . . . . . .W2W2W2W2W2W2W2W2W2W2W2W2W2W2W2W2W2W2W2W2W2W2W2W2W2W2W2WC 20
19 . . . . . .W2W2W2W2W2W2W2W2W2W2W2W2W2W2W2W2W2W2W2W2W2W2W2W2W2W2W2WC 19
18 . . . . . O 18
17 . . . . . O 17
16 . . . . . I1 16
15 . . . . . I1 15
14 . . . . . I1 14
13 . . . . . I1 13
12 . . . . . I1 12
11 . . . . . I1 11
10 . . . . . I1 10
9 . . . . . I1 9
8 . . . . . I1 8
7 . . . . . I1 7
6 . . . . . I1 6
5 . . . . . I1 5
4 . . . . . I1 4
3 . . . . . I1 3
2 . . . . . I1 2
1 S S S S S S S S S S S S S S S S S S S S S S S S S S S S S S S S S S S S S S S S S S S S S S S S S S S S S S S S S 1
J I 34 36 38 40 42 44 46 48 50 52 54 56 58 60 62 64 66 68 70 72 74 76 =I J

- VELOCITY BOUNDARY CONDITIONS -

ZONE	U-VELOCITY	V-VELOCITY
W2	0.0000E+00	0.0000E+00
W5	-2.0000E-03	0.0000E+00
W6	-2.0000E-03	0.0000E+00
W7	-2.0000E-03	0.0000E+00
W8	-2.0000E-03	0.0000E+00
W9	-2.0000E-03	0.0000E+00
WA	0.0000E+00	0.0000E+00
WB	0.0000E+00	0.0000E+00
WC	0.0000E+00	0.0000E+00
WD	0.0000E+00	0.0000E+00
WE	0.0000E+00	0.0000E+00
WF	0.0000E+00	0.0000E+00
WG	0.0000E+00	0.0000E+00
I1	-8.5000E-03	0.0000E+00
I2	-2.0000E-03	0.0000E+00

- TEMPERATURE BOUNDARY CONDITIONS -

ZONE	TEMPERATURE
W2	COND. WALL
W5	COND. WALL
W6	COND. WALL
W7	EXT. H-T
W8	EXT. H-T
W9	EXT. H-T
WA	EXT. H-T
WB	HEAT FLUX
WC	HEAT FLUX
WD	COND. WALL
WE	EXT. H-T
WF	COND. WALL
WG	COND. WALL
I1	9.6100E+02
I2	3.3800E+02

- SPECIAL TEMPERATURE BOUNDARIES -

ZONE	HEAT FLUX BOUNDARY	HEAT FLUX VALUE	EXT. H-T BOUNDARY	EXTERNAL HEAT TRANSFER COEFF.	EXT. TEMP.
W7	N	N/A	Y	1.0000E+02	3.0000E+02
W8	N	N/A	Y	2.0000E+04	2.8500E+02
W9	N	N/A	Y	1.0000E+04	2.8500E+02
WA	N	N/A	Y	1.0000E+03	3.1300E+02
WB	Y	0.0000E+00	N	N/A	N/A
WC	Y	0.0000E+00	N	N/A	N/A
WE	N	N/A	Y	8.0000E+04	2.8500E+02

CONDUCTING WALL ZONE PROPERTIES :

ZONE	THERMAL CONDUCTIVITY	SPECIFIC HEAT	DENSITY	VOLUMETRIC HEAT RATE
W2	1.5500E-01	1.0000E+03	8.3000E+02	0.0000E+00
W5	1.1000E+02	1.3000E+03	1.7400E+03	0.0000E+00
W6	1.8100E+02	9.6300E+02	2.7000E+03	0.0000E+00
WD	9.4000E+00	1.0000E+03	1.0000E+03	0.0000E+00
WF	2.0000E+01	1.0000E+03	1.0000E+03	0.0000E+00
WG	1.2400E+01	1.0000E+03	1.0000E+03	0.0000E+00

Appendix G

Nomenclature

Lower case

c	speed of sound [m/s]
c	colour function
$\tilde{c}$	smoothed colour function
c	Courant number
c_p	constant pressure heat capacity [J/kg K]
c_p^i	constant pressure heat capacity in phase i [J/kg K]
$\tilde{c}_p$	total constant pressure heat capacity [J/kg K]
e	internal energy per unit mass [J/kg]
e	emissivity
f	frequency of harmonic oscillations [Hz]
f_s	solid fraction
f_{SC}	solid fraction at onset of contraction
g	gravitational constant [m/s^2]
g_x, g_y	directional gravitational forces [m/s^2]
$\mathbf{g}$	gravitational force [m/s^2]
h	enthalpy per unit mass (sensible heat) [J/kg]
k	thermal conductivity [W/m K]
k	equilibrium distribution coefficient
m_l	liquidus slope
$\mathbf{n}$	surface unit normal
$\hat{n}, \vec{n}_k$	phase unit normal
p	pressure [Pa]
p^*	initial pressure [Pa]
p'	pressure correction [Pa]
p_0, p_{gp,p_e}	gas pocket pressure [Pa]
p_{atm}, p_0	atmospheric pressure [Pa]
$\vec{q}$	heat flux [W/m^2]

r_S	radius of spline surface [m]
r_{ing}	mean radius of ingot surface [m]
r_m	mould radius [m]
s_{int}	point of intersection
s	arc length parameter [m]
t	time [s]
$\mathbf{t}$	surface unit tangent vector
$\mathbf{u}$	velocity vector [m/s]
$\mathbf{v}$	velocity vector [m/s]
$\vec{u}$	velocity vector [m/s]
$\vec{u}_k$	phase velocity vector [m/s]
$\vec{u}_s$	interface velocity [m/s]
u	velocity in x-direction [m/s]
u^*	initial velocity in x-direction [m/s]
u'	velocity correction in x-direction [m/s]
u_m	density weighted velocity in x-direction [m/s]
v	velocity in y-direction [m/s]
v^*	initial velocity in y-direction [m/s]
v'	velocity correction in y-direction [m/s]
u_i, u_j	velocity components [m/s]
$\tilde{v}_i n$	modified inflow velocity [m/s]
v_r	radial velocity [m/s]
v_θ	angular velocity [rad/s]
v_z	axial velocity [m/s]
$z'(s)$	dz/ds

Upper case

A	area [m^2]
C	phase function
C	Total contraction
C_0	initial concentration
C_l	liquid concentration
C_k	colour function
F	volume fraction
F	view factor
$\mathbf{F}_{SV}$	surface tension volume force [N/m]
$\vec{\mathcal{F}}$	body force N/m^3
$\vec{F}$	phase body force N/m^3
H	total enthalpy per unit mass [J/kg]
H_V	total enthalpy per unit volume [J/m^3]
$\mathbf{I}$	unit tensor

$\mathcal{L}$	convolution kernel
L	characteristic length of liquid column in meniscus [m]
L_{ev}	inlet length [m]
L	computational cell number
L	latent heat of melting J
M	molar mass [kg/mol]
Q	heat flow rate [W]
R, R_i	radii of curvature [m]
R	gas constant [J/K mol]
R	ingot surface radius [m]
S	surface
S_1	melt surface area in mould [m^2]
S_2	meniscus surface area [m^2]
$\mathcal{S}$	energy source term [J/m^3]
S_k	phase energy source term [J/m^3]
$\mathbf{S}$	surface tension volume force [N/m^3]
S_r, S_z	surface tension volume force components [N/m^3]
T	temperature [K]
T_s	solidus temperature [K]
T_l	liquidus temperature [K]
T_{SC}	temperature at onset of contraction [K]
U	mean velocity [m/s]
V	volume (size of averaging volume) [m^3]
V_f	air gap flow rate [m^3/s]
V_k	size of averaging phase volume [m^3]

Greek lower case

α	volume fraction
α_i	phase volume fraction
α	surface tension coefficient [N/m]
δA	Surface area variation [m^2]
δ	variation
$\delta[]$	Dirac delta function
δr	radial contraction
$\delta\rho$	density variation [kg/m^3]
δ_s	delta function across surface s
δS	surface boundary
δt	time step/time increment [s]
$\delta x, \delta y, \delta z$	computational cell dimensions [m]

γ surface force redistribution parameter
κ curvature [1/m]
μ viscosity [kg/m s]
$\hat{\mu}$ harmonic mean viscosity [kg/m s]
ν kinematic viscosity [kg/m s]
ω relaxation coefficient
ϕ normalized pressure p/ρ [N m/kg]
ψ velocity potential [m^2/s]
ρ density [kg/m^3]
ρ_0 equilibrium density [kg/m^3]
σ surface tension coefficient [N/m]
σ Stefan-Bolzman constant [W/m^2K^4]
$\boldsymbol{\tau}$ viscous stress tensor [N/m^2]
$\tau_{i,j}$ viscous stress tensor components [N/m^2]
$\overline{\overline{\tau}}$ stress tensor [N/m^2]
$\overline{\overline{\tau}}_k$ phase stress tensor [N/m^2]
$\vec{\tau}_k$ shear force [N/m^2]
θ_{eq} equilibrium angle of contact [rad]
θ slope of meniscus [rad]
ζ wave amplitude [m]

Greek upper case

Δp	air gap pressure drop [Pa]
Δs	increment of arc length parameter [m]
Δt	time step/time increment [s]
ΔH	latent heat content [J/kg]
$\Gamma_{i,j}$	surface force in cell i,j after force redistribution
Γ	general diffusion coefficient
Ω	averaging volume
Ω_k	phase volume
Π	viscous stress tensor [N/m^2]
Ψ	stream function [m^2/s]
Σ	rz surface intersection of computational cell
$\delta\Sigma$	phase boundary in Σ

Symbols

$<>$	extensive volume average
$^i<>$	intrinsic volume average
$^t<>$	time average

Bibliography

[1] *An introduction to computational fluid dynamics*, Longman, 1995.

[2] P. Ackermann, W. Heinemann, and W. Kurz, *Surface quality and meniscus solidification in pure chill cast metals*, Arch Eisenhuttenwes., 55 (1984), pp. 1–8.

[3] N. Ashgriz and J. Y. Poo, FLAIR*: Flux line-segment model for advection and interface reconstruction*, Journal of Computational Physics, 93 (1991), pp. 449–468.

[4] P. W. Baker and J. F. Grandfield, *The role of surface tension forces in gas pressurized vdc castings*, in 7th Austratlian Asian Pacific Conference, Aluminium Cast House Technology, P. R. Whiteley, ed., TMS, 2001, pp. 195–204.

[5] S. Benum, A. Håkonsen, J. E. Hafsås, and J. Sivertsen, *Mechanisms of surface formation during direct chill (DC) casting of extrusion ingots*, in Light metals 1999, C. E. Eckert, ed., San Diego, February, TMS, pp. 737–742.

[6] S. Benum, D. Mortensen, and H. Fjær, *Prediction of boundary conditions and hot spots during the start-up phase of an extrusion ingot casting*, in Proceedings of Continous Casting, Frankfurt, 2000.

[7] W. J. Bergmann, *Solidification in continuous casting of aluminium*, in TMS-AIME Annual Meeting, no. A 70-27, Denver, February 1970.

[8] Bird, Stewart, and Lightfoot, *Transport phenomena*, Wiley, New York, 1960.

[9] T. F. Bower, D. A. Granger, and J. Keverian, *Solidification*, ASM, Metals Park, Ohio, 1971.

[10] J. Brackbill, D. Kothe, and C. Zemach, *A continuum method for modelling surface tension*, J. Comput. Phys, 100 (1992), pp. 335–354.

[11] W. D. Callister, *Materials Science and Engineering*, Wiley, New York, 4th ed., 1997.

[12] A. L. Dons, E. K. Jensen, Y. Langsrud, E. Trœmborg, and S. Brusethaug, *The alstruc microstructure solidification model for industrial aluminium alloys*, Metallurgical and Materials Transactions A, 30A (1999).

[13] D. A. Drew, *Mathematical modelling of two phase flow*, Ann. Rev. Fluid Mech, (1983), pp. 261–291.

[14] J. M. Ekenes and W. S. Peterson, *Visual observations inside an airslip mold during casting*, in Light Metals 1990, C. M. Vickert, ed., TMS.

[15] J. M. Ekenes and K. W. Storey, *Fiber optics - a new look at airslip casting*, in Light Metals, E. Rooy, ed., 1991, pp. 933–938.

[16] E. F. Emley, Int. Met. Rev., 21 (1976), pp. 75–115.

[17] T. E. F. Frisvold, E Øvrelid, *Casting of extrusion ingots. part* I., tech. report, SINTEF Materialteknologi, 1997. STF24 F97608.

[18] J. H. Ferziger and M. Peric, *Computational methods for fluid dynamics*, Springer, 3rd ed., 2002.

[19] M. C. Flemings, *Solidification processing*, McGraw-Hill, 1974.

[20] M. Fortin, R. Peyert, and R. Temam, *Resolution numerique des equations de navier-stokes puor un fluide incompressible*, J. Mec, 10 (1971), pp. 357–390.

[21] C. F. Gerald and P. O. Wheatley, *Applied numerical analysis*, addison-Wesley, 4th ed., 1992.

[22] H. Gikling, F. Iversen, and J. A. Bakken, *Dc-stping av aluminium*. Prosjektoppgave NTNU, 1999.

[23] H. Goldstein, *Classical Mechanics*, Addison Wesley, 1980.

[24] D. Gueyffier, J. Li, A. Nadim, R. Scardovelli, and S. Zaleski, *Volume-of-fluid interface tracking with smoothed surface stress methods for three-dimensional flows*, Internet source: http://www.lmm.jussieu.fr/˜ zaleski, (1998).

[25] E. Herrmann, *Handbook on Continuous Casting*, Aluminium-Verlag, 1980.

[26] C. W. Hirt and B. C. Nichols, *Volume of fluid (*VOF*) method for the dynamics of free boundaries*, Journal of Computational Physics, 39 (1981), pp. 201–225.

[27] T. Iida and R. I. L. Guthrie, *The Physical Properties of Liquid Metals*, Oxford University Press, New York, 1993.

[28] M. Ishii, *Two fluid model for two phase flow*, Multiphase Sci. Tech., 5 (1990).

[29] J.F.Grandfield, K.Goodall, P.Misic, and X.Zhang, *Water cooling in direct chill casting: Part 2, effect on billet heat flow and solidification*, in Light Metals 1997, R. Huglen, ed., The Minerals, Metals and Materials Society, pp. 1081–1090.

[30] J.J.Monaghan, *Smoothed particle hydrodynamics*, Ann. Rev. Astrophysics, 30 (1992), pp. 543–574.

[31] S. T. Johansen, *A* VOF *(volume of fluid) technique for 3d free surface flows*. SINTEF Materials Technology, N-7034 Trondheim NTNU, Norway.

[32] S. T. Johansen, *Menisksonens fysikk ved dc-støping*, tech. report, SINTEF Materialteknologi, 1998. STF24 F98681.

[33] J.P.Faunce, F.E.Wagstaff, and H.Shaw, *New casting method for improving billet quality*, in Light Metals 1984, E.L.Rooy, ed., The Minerals, Metals and Materials Society, pp. 1145–1158.

[34] L. Katgerman, *Developments in continuous casting of aluminium alloys*, Cast metals, 4 (1991), pp. 133–139.

[35] Kincaid and Cheney, *Numerical analysis*, Brooks/Cole, Pacific Grove, California, 1991.

[36] D. Kothe and R. Mjolsness, *Ripple: A new model for incompressible flows with free surfaces*, AIAA, 30 (1992), pp. 2694–2700.

[37] E. Kreyszig, *Advanced Engineering Mathematics*, vol. 6, Wiley, 1988.

[38] W. Kurz and D. J. Fisher, *Fundamentals of Solidification*, Trans Tech Publications, 1992.

[39] B. Lafaurie, C. Nardone, R. Scardovelli, s. Zaleski, and G. Zanetti, *Modelling merging and fragmentation in multiphase flows with surfer*, Journal of Computational Physics, 113 (1994), pp. 134–147.

[40] L. Landau and E. Lifshitz, *Fluid Mechanics*, vol. 6 of Course of Theoretical Physics, Butterworth-Heinemann, Oxford, 2nd ed., 1987, ch. 7.

[41] B. P. Leonard, *A stable and accurate convective modelling procedure based on quadratic upstream interpolation*, Comput. Methods Appl. Mech. Eng., 19 (1979), pp. 59–98.

[42] E. Lossack, *Practical experience with the use of hot-top moulds in D.C. casting of al-billets*, in Light Metals, 1978, pp. 413–424.

[43] M. O. Lutset, *The development time of boiling crises*, in Third International Conference on Multiphase Flow, Lyon, June 8-12 1998, ICMF.

[44] G. Moritz, *Einfluß der Erstarrungsbedingungen auf das Gefüge beim Aluminiumstrangguß*, Z. Metallkunde, 60 (1969), pp. 742–751.

[45] D. Mortensen, *Matematisk modellering av menisk ved pressbolt hot-top gass-slipp støping*, tech. report, IFE, 1996. IFE/KR/F-96/204.

[46] W. F. Noh and P. Woodward, SLIC *(simple line interface calculation)*, 1976, pp. 330–340.

[47] S. V. Patankar, *Numerical Heat Transfer and Fluid Flow*, Taylor & Francis, 1980.

[48] S. Popinet and S. Zaleski, *Simulation of axisymmetric free surface viscous flow around a non-spherical bubble in the sonoluminescence regime*, in Third International Conference on Multiphase Flows, ICMF'98, 1998.

[49] S. Popinet and S. Zaleski, *A front-tracking algorithm for accurate representation of surface tension*, Int. J. Numer. Meth. Fluids, 30 (1999), pp. 775–793.

[50] W. H. Press, w T Vetterling, S. A. Teukolsky, and B. P. Flannery, *Numerical Recipies in Fortran 77*, Cambridge, 2nd ed., 1992.

[51] J. D. Ramshaw and J. A. Trapp, *A numerical technique for low-speed homogeneous two-phase flows with sharp interfaces*, J. Comput. Physics, 21 (1976), pp. 438–453.

[52] W. J. Rider and D. B. Kothe, *Stretching and tearing interface tracking methods,* AIAA-*95-1717*.

[53] W. J. Rider and D. B. Kothe, *Reconstructing volume tracking*, Journal of Computational Physics, 141 (1998), pp. 112–152.

[54] M. Rieber and A. Frohn, *Navier-stokes simulation of droplet collision dynamics*, 7th ISCFD, Beijing, China, (1997).

[55] M. Rudman, *Volume tracking methods for interfacial flow calculations*. Submitted to the International Journal for Numerical Methods in Fluids, July 1996.

[56] M. Rudman, *A volume-tracking method for incompressible multi-fluid flows with large density variations*, International Journal for Numerical Methods in Fluids, 28 (1998), pp. 357–378.

[57] L. A. Segel and G. H. Handelman, *Mathematics applied to continuum mechanics*, Dover, Toronto, 1987.

[58] D. J. Shaw, *Introduction to Colloid and Surface Chemistry*, Butterworths, 1980.

[59] W. Shyy, H. S. Udaykumar, M. M. Rao, and R. W. Smith, *Computational Fluid Dynamics with Moving Boundaries*, Taylor & Francis, 1996. Series in Computational and Physical Processes in Mechanics and Thermal Sciences.

[60] J. C. Slattery, Ind. Eng. Chem. Fund., 6 (1967), p. 108.

[61] S. L. Soo, *Particulates and Continuum*, Hemisphere publishing corporation, 1989.

[62] H. Steinrück, C. Rudischer, and W. Schneider, *The formation of oscillation marks in continuous casting of steel*, in Modeling of Casting, Welding and Advanced Solidification Processes VIII, B. G. Thomas and C. Beckermann, eds., TMS, 1998.

[63] M. Sussman, P. Smereka, and S. Osher, *A level set approach for computing solutions to incompressible two-phase flow*, Journal of Computational Physics, 114 (1994), pp. 146–159.

[64] M. Syvertsen, *Oxide skin strength measurements*, tech. report, SINTEF, 2000. STF24 F00674.

[65] H. J. Thevik, A. Mo, A. Håkonsen, S. Benum, E. K. Jensen, and B. R. Henriksen, *Measurements and modeling of surface macrosegregation in DC casting*, in Modeling of Casting, Welding and Advanced Solidification Processes VIII, B. G. Thomas and C. Beckermann, eds., TMS, 1998.

[66] L. H. Thomas, *Elliptic problems in linear difference equations over a network*, tech. report, Watson Sci. Conput. Lab., Columbia University, New York, 1949.

[67] H. Tomono, P. Ackermann, W. Kurz, and W. Heinemann, in Solidification technology in the foundry and casthouse, Warwick University, Coventry, September 1980.

[68] H. Tomono, W. Kurz, and W. Heinemann, Metallurgical Transactions, 12 B (1981), pp. 409–411.

[69] S. O. Unverdi and G. Tryggvason, *A front-tracking method for viscous, incompressible, multi-fluid flows*, Journal of Computational Physics, 100 (1992), pp. 25–37.

[70] E. W. Weisstein, *CRC Concise Encyclopedia of Mathematics*, Chapman & Hall/CRC, 1999.

[71] J. E. Welch, F. H. Harlow, J. P. Shannon, and B. H. Daly, *The* MAC *method. a computing technique for solving viscous, incompressible, transient fluid-flow problems involving free surfaces*, tech. report, Los Alamos Scientific Laboratory of the University of California, 1965. Report LA-3425.

[72] S. Whitaker, Ind. Eng. Chem., 61, p. 4.

[73] F. M. White, *Viscous Fluid Flow*, Mechanical Engineering, Mcgraw Hill, Singapore, 2nd ed., 1991.

[74] M. Wörner, W. Sabisch, G. Grötzbach, and D. G. Cacuci, *Volume-averaged conservation equations for volume-of-fluid interface tracking*, Fourth International Conference on Multiphase Flow, (2001). ICMF.

[75] G. Yadigaroglu, *Lecture in multiphase flow short course*, 1989. Zurich.

[76] G. Yadigaroglu and R. T. Lahey, *On the various forms of the conservation equations in two phase flow*, Int. Journal of Multiphase Flow, (1976), pp. 477–494.

[77] D. L. Youngs, *Time-dependent multi-material flow with large fluid distortion*, Num. Meth. for Fluid Dymanics, (1982), pp. 273–285.

[78] S. Zaleski, J. Li, S. Succi, R. Scardovelli, and G. Zanetti, *Direct numerical simulation of flows with interfaces*, 1995.

Index